Elucidating the role of PGR5 and PGRL1 in the regulation of C_4 photosynthesis

Samuel James Nix

June 2026

A thesis submitted for the degree of *Doctor of Philosophy* of

The Australian National University

Research School of Biology



Australian National University

© Copyright by Samuel James Nix 2026, All Rights Reserved

Declaration

This thesis contains no material which has been accepted for the award of any other degree or diploma in any university. To the best of my knowledge, it contains no material previously published or written by another person, except where due reference is made in the text. Chapter 2 is co-authored work; the nature and extent of my contribution, and those of my co-authors, are detailed in the Statement of Contribution at the beginning of that chapter.

Dedication

In loving memory of my namesake and grandfather, Samuel Bacon Nix (1936 – 2020): rancher, Jello enthusiast, and "a farmer of grasses." He spent many years advising ranchers across Texas on rangeland and soil conservation and knew his grasses well. I came to plant science too late for us to share it, but it is yours as much as mine.

Acknowledgements

First and foremost, I thank my supervisory team. To Professor Bob Furbank, for always being available when I needed him; to Dr. Maria Ermakova, for her guidance in experimental design and her enormous help in writing this thesis; to Dr. Kai Chan, for guidance and support throughout the project; and to Dr. Marten Moore, for all things RNA. Their collective expertise shaped both the direction of this work and my development as a researcher.

To my fellow PhD students: Russell Woodford, for teaching me all things spectroscopy and gas exchange; and Suyan Yee, for her help in the lab and for lending me her chemicals. To the others who have helped in one way or another along the way: Davin Wijaya, "Hafiz" Sabah-Ud-Din, Marvin Jin, Jack Weiss, and others. Thank you for the camaraderie, discussions, and good humour that made the lab a better place to work. A special thanks to my fellow lab members, Dr. Jing Zhang, Dr. Kavya Yalamanchili, Dr. Kelly Chapman, and Riya Kuruvilla.

I am also grateful to Dr. Craig Morton from the CSIRO for modelling PGRL1 in the membrane; to Professor Susanne von Caemmerer, for looking over my differential equations and ensuring I wasn't going crazy; to Dr. Andrew Bowerman, for his help and advice on the statistical analysis of my proteomics; and to Dr. Diego Marquez Antivilo, for training me on the LI-COR system.

This work was made possible by funding from the ARC Training Centre for Future Crops Development, with special thanks to Professor Bary Pogson, Professor Tony Millar, Dr. Lauren DuFall, Dr. Julie Leroux, and Dr. Derek Collinge for their help from the Centre. I also thank the Australian Plant Phenomics Network (APPN) for access to the fluctuating-light growth chambers and for general use of their facilities. My thanks to the plant services team, along with Dr. Adam Carroll, Joe Boileau, and Anitha Jeyasingham at the Joint Mass Spectrometry Facility (JMSF), for their technical support on all things proteomics.

Finally, to my family and friends. To my mother, who was always there for me, even though she never wanted me to move to Australia in the first place; and to my father, who has been there for me too, not least in reassuring her that Australia was a safe country. To my siblings,

thank you to my sister and her family for looking after my cat, and to my brother for always being up for a philosophical chat. To my Nana, who was happy to see me carry on my grandfather's legacy. Thank you all for your unwavering encouragement and support. This would not have been possible without you.

Use of Generative AI

The generative AI tools Claude and ChatGPT were used during the preparation of this thesis. Claude assisted with writing and debugging code for data analysis, as cited in the relevant chapters. ChatGPT was used to assist with mathematical derivations in Chapter 3, which I verified independently. Both tools were also used for grammar and spell checking, to suggest phrasing or rephrasing, and to help organise ideas and draft outlines. Beyond these uses, the research, analysis, and intellectual contribution of this thesis are my own.

Abstract

Regulation of C_4 photosynthesis is an elaborate process that requires cell-specific specialisation of the light reactions to match the distinct metabolic energy demands of mesophyll and bundle sheath cells. This balance is further complicated under fluctuating light conditions which require rapid changes in energy production and photoprotection, yet how C_4 plants achieve this has remained poorly defined. PROTON GRADIENT REGULATION 5 (PGR5) and PGR5-LIKE PHOTOSYNTHETIC PHENOTYPE 1 (PGRL1), which keep Photosystem I (PSI) oxidised by regulating PSI photoprotection and proton motive force generation, stood out as the principal candidates, accumulating to higher levels in C_4 species than in their C_3 relatives. This thesis provides novel insights into the evolution and function of the PGR5/PGRL1 system in the C_4 model grass *S. viridis*, showing that it is not simply inherited from C_3 plants but has specialised for the regulatory needs of C_4 photosynthesis.

Phylogenetic analysis revealed that grasses carry two PGRL1 paralogs that diverged following a whole-genome duplication early in grass evolution: the ancestral PGRL1α, conserved across algae and land plants, and a grass-specific PGRL1β. In NADP-ME C_4 grasses these paralogs are expressed in a cell-specific manner, with PGRL1α enriched in mesophyll cells and PGRL1β in bundle sheath cells. Analysis of gene-edited *Setaria viridis* showed that PGRL1β was necessary for faster oxidation of PSI during dark-to-high-light transitions, whereas PGRL1α was required to keep PSI sufficiently oxidised at steady-state high light affording a more dynamic range of photoprotection than in non-grasses.

To address the long-debated mechanism of PGR5, a mass-action kinetic framework was developed to convert in vivo Dark Interval Relaxation Kinetics (DIRK)–NIR redox signals of P700, plastocyanin, and ferredoxin into electron fluxes. This approach confirmed that loss of PGR5 is associated not only with acceptor-side limitation at PSI but also with a substantial donor-side flux deficit at 1 second post low-to-high-light transition that cannot be explained by decreased PSII activity, a restriction at Cytochrome b_6f, or depletion of PSI acceptor capacity, providing new in vivo evidence that suggests PGR5 may regulate cyclic electron flow without concluding that PGR5 definitively participates in a cyclic electron flow pathway.

In C_3 plants, *pgr5* and *pgrl1* mutants are phenotypically identical, but whether this holds in C_4 had not been tested. Unexpectedly, the *S. viridis pgrl1αβ* mutant retained ~6% of wild-type PGR5 under fluctuating light. In result, the mutant showed an intermediate growth and photosynthetic phenotype between wild-type and *pgr5-1*. Because PSI declined as severely as in *pgr5-1*, this residual pool was too low to protect PSI and result in the intermediate growth; instead, it was associated with improved metabolic acclimation via elevated C_4 and

photorespiration enzymes. PGR5 therefore contributes to the coordinated metabolic acclimation of C_4 plants to fluctuating light, a role beyond its established function in PSI photoprotection.

Together, these findings refine the mechanistic understanding of how PGR5 and PGRL1 act in C_4 photosynthesis and identify new directions and priority targets for engineering improved electron transfer in C_4 crops under the fluctuating light of field environments.

Table of Contents

Declaration ii

Dedication iii

Acknowledgements iii

Abstract v

Table of Contents vii

Abbreviations xiii

Chapter 1: General Introduction 1

Introduction 1

1. Light reactions of photosynthesis 1

2. Calvin-Benson cycle 4

3. Carbon Concentrating Mechanisms 5

4. The metabolic C_4 cycle 6

5. Electron transport pathways in C_4 chloroplasts 8

6. Balancing energy supply and demand 9

7. Non-photochemical quenching 11

8. Photosynthetic control 11

9. Proton motive force regulators 12

10. Molecular mechanism of PGR5/PGRL1 13

11. PGR5/PGRL1 in C_4 photosynthesis 14

12. Research questions addressed in the thesis 16

Chapter 2: PGRL1 paralogs provide distinct modes of photoprotection in C_4 photosynthesis 17

Statement of Contribution 17

Introduction 17

Materials & Methods 20

Phylogenetic analysis 20

***PGRL1* expression analyses** 20

Plant growth conditions 20

Mass spectrometry analyses 21

CRISPR-Cas9 mutant generation 21

Leaf spectroscopic and fluorescence analyses 22
Plant phenotyping 23
Gas-exchange analysis 23
Protein modelling 23
Results 24
***PGRL1* paralogs diverged after genome duplication early in grasses evolution** 24
***PGRL1α* and *PGRL1β* have distinct expression patterns** 27
PGRL1α is required for PSI oxidation at high light 29
PGRL1β facilitates faster PSI photoprotection 31
Protein models of PGRL1α and PGRL1β suggest structural basis for functional differences 35
Discussion 37
Conclusion 39
Supplementary materials 41
Chapter 3: C_4 plants provide new evidence for PGR5 involvement in regulation of cyclic electron flow 52
Introduction 52
Material and Methods 56
Experimental approach and quantitative framework: from DIRK–NIR redox signals to flux 56
Mass-action example for electron transfer 56
Working equations and parameter mapping 57
P700: a simple pseudo-first-order decay 57
Plastocyanin: competing PSI oxidation and Cytb_6f-dependent reduction 58
Ferredoxin: combined activity of sinks determines the observed decay constant 60
Measured signals and notation 62
DIRK principle and definition of flux at dark onset 62
DIRK curve fitting and parameter extraction 63
Plant material and growth conditions 65
Saturating pulse analysis of chlorophyll fluorescence and P700 spectroscopy 65

Dual-KLAS-NIR signal deconvolution and experimental protocols 66
Signal deconvolution and differential model plot generation 66
DUAL-KLAS-NIR measurements of P700, PC, and Fd redox changes during induction 67
DIRK measurements of P700, PC, and Fd relaxation kinetics 67
Thylakoid membrane energisation analysis 67
Statistical analysis 68
Data normalisation and preprocessing (Python) 68
Results 70
P700 and PC in *S. viridis pgr5* mutant are oxidised during photosynthetic induction 70
P700 is transiently more oxidised in *pgr5-1* mutant during the photosynthetic induction 72
ECS dynamics show an early deficit in *pmf* generation in *pgr5-1* 75
Fd DIRKs: *pgr5-1* shows lower rate of Fd oxidation 77
P700 DIRKs: P700 flux is decreased in *pgr5-1* with a temporal delay relative to acceptor-side flux 80
PC DIRKs: PC flux is immediately decreased in *pgr5-1* upon light induction 82
Early loss of PC reduction flux in *pgr5-1* is caused by a limitation in electron delivery 85
Lower P700 reduction flux in *pgr5-1* is caused by the PSI donor-side over-reduction 87
PSI donor-side effective rate constant differs between genotypes beyond PC redox effects 89
Discussion 92
Loss of PGR5 produces an immediate acceptor-side flux deficit 92
PC flux reveals early Cyt*f*-dependent delivery limitation 92
Over-reduction of P700 is the dominant cause of decreased PSI flux and *pmf* loss in *pgr5-1* 93
A slower PC to P700 rate constant in *pgr5-1* is consistent with diffusion-limited PC delivery to PSI 95
ATP synthase proton conductivity is altered in *pgr5-1* during induction 96
PGR5-CEF prevents over-reduction of the electron transport chain during rapid light transitions 97

Engineering implications for C_4 electron transport 98
Future work 99
Supplemental Tables and Figures 101
Chapter 3: Supplemental Derivations 106
S1. $P700^+$ reduction kinetics during a DIRK: encounter-complex scheme, quasi–steady state, and integrated pseudo-first-order form 106
S1.1 Rationale and experimental constraint 106
S1.2 Kinetic scheme: light-driven form and DIRK simplification (after Haehnel et al. 1994) 106
S1.3 Mass-action ODEs and quasi–steady-state reduction to an effective second-order law 107
S1.4 Limiting case: $k2,\mathrm{eff} \approx k\mathrm{on}$ when intracomplex ET is fast 108
S1.5 Integration of the mass-action ODE 108
S1.6 Reduction to the familiar exponential form 109
S2. PC oxidation kinetics during a DIRK: forced first-order ODE, integrating-factor solution, and bi-exponential form 110
S2.1 Rationale and connection to the $P700^+$ derivation 110
S2.2 Governing ODE for $PCo(t)$ during the DIRK 110
S2.2.1 Source term: production of PCo by PSI 110
S2.2.2 Sink term: consumption of PCo by Cytb_6f 110
S2.2.3 Combined ODE 111
S2.3 Solution of Eq. (S2.6) by integrating factor 111
S2.3.1 Integrating factor 111
S2.3.2 Integrate from 0 to t 112
S2.3.3 Solve for $PCo(t)$ 112
S2.4 Bi-exponential "two-amplitude" form for fitting 112
S2.5 Summary of symbols 113
S3. Ferredoxin (Fd) DIRK kinetics: parallel-pathway mass action scheme, integrated solution, and pathway-specific k' terms 114
S3.2 Kinetic schema for Fdr oxidation during a DIRK (parallel sinks) 114
S3.3 Mass-action ODE for $Fdr(t)$ and definition of $kobsFd$ 114
S3.4 Integration: exponential decay of $Fdr(t)$ 115
S3.5 Pathway-resolved fluxes and total flux 115

S3.6 Genotype partitioning of the CEF-associated contribution 116

S3.7 What is contained within kF': Michaelis–Menten acceptor dependence embedded in an effective first-order term 116

S4. Why $kobsP700$ contains the time-averaged PCr integral 118

S4.1 Starting point: the integrated $P700^+$ solution makes the "missing time" explicit 118

S4.2 Connection to the fitted single-exponential form 118

S4.3 Interpretation for readers (why "$k \times [PCr]$" is an average, not an instantaneous value) 119

S5. Log decomposition of flux differences into kinetic versus redox contributions 120

S6. Encounter theory links PSI donor-side kinetics and $\mathrm{Cyt}f \rightarrow PC$ delivery: diffusion, pH, and electrostatics (Hope 2000; Haehnel et al. 1994) 121

S6.1 Implication for the *pgr5-1* phenotype from $P700^+$ kinetics 121

S6.2 Smoluchowski-style encounter framework for $k\mathrm{on}$ (Hope 2000) 121

S6.3 Factorization of $Cytf \rightarrow PC$ delivery into pH, diffusion, and electrostatic/docking terms 122

S7. Full species-level donor-side model with PC diffusion and Jacobian reduction 123

S7.2 Species-level kinetic scheme 123

S7.3 State vector and nonlinear ODE system 124

S7.4 Full Jacobian matrix 125

S7.5 Why the full Jacobian implies shared rates 125

S7.6 Reduction to the PSI donor-side interaction block 126

S7.7 PSI diffusion Jacobian 126

S7.8 Diffusion eigenvalues and interpretation 127

S7.9 Interpretation for the present study 128

Chapter 4: Residual PGR5 protects *Setaria viridis pgrl1aβ* mutant under fluctuating light. 129

Introduction 129

Materials and Methods 131

Generation and selection of *S. viridis pgrl1aβ* double mutant lines 131

Plant material and growth conditions 132

Chlorophyll fluorescence and P700 spectroscopy analysis 132

Thylakoid membrane energisation analysis 133
MultispeQ analysis under constant and fluctuating light 133
Phenospex PlantEye measurements 134
Transcript abundance meta-analysis 134
Protein extraction, quantification and digestion 134
LC-MS/MS data acquisition 135
Proteomics data analysis 136
Functional annotation and pathway enrichment analysis 137
Statistical analysis 138
Results 138
Generation of the *pgrl1αβ* double mutant 138
Photosynthesis in plants grown under constant light 140
Growth phenotype under constant and fluctuating light 143
Targeted proteomics of PGR5 and PGRL1 paralogs 146
Quantitative leaf proteomics under constant and fluctuating light 147
Discussion 157
Future directions 160
Conclusion 161
Chapter 5: Conclusions and Future Directions 162
References 165

Abbreviations

2-OG:	2-oxoglutarate
3-PGA:	3-phosphoglycerate
ADK:	Adenylate kinase
ANCOVA:	Analysis of covariance
APPN:	Australian Plant Phenomics Network
ATP:	Adenosine triphosphate
BS:	Bundle sheath (cell)
C_3:	C_3 photosynthesis (three-carbon pathway)
C_4:	C_4 photosynthesis (four-carbon pathway)
CA:	Carbonic anhydrase
CAM:	Crassulacean acid metabolism
CAT:	Catalase
CBC:	Calvin–Benson Cycle
CCM:	Carbon Concentrating Mechanism
CDS:	Coding sequence
CEF:	Cyclic electron flow
Chl:	Chlorophyll
COMT:	Caffeic acid 3-O-methyltransferase
CRISPR:	Clustered Regularly Interspaced Short Palindromic Repeats
Cytb_6f:	Cytochrome b_6f complex
Cyt*f*:	Cytochrome *f*
DDA:	Data-dependent acquisition
DIRK:	Dark Interval Relaxation Kinetics
DMP:	Differential Model Plot
DTT:	Dithiothreitol
ECS:	Electrochromic shift
ECS_{ST}:	Electrochromic shift single-turnover flash amplitude
EDTA:	Ethylenediaminetetraacetic acid
EMS:	Ethyl methanesulfonate
ESI:	Electrospray ionisation

F_O:	Minimum chlorophyll fluorescence
FBPase:	Fructose-1,6-bisphosphatase
Fd:	Ferredoxin
Fd-GOGAT:	Ferredoxin-dependent glutamate synthase (glutamine:2-oxoglutarate aminotransferase)
FeS:	Iron-sulphur (cluster; e.g. Rieske FeS)
FLV:	Flavodiiron protein
F_M:	Maximum chlorophyll fluorescence
FNR:	Ferredoxin-$NADP^+$ oxidoreductase
FQR:	Ferredoxin-plastoquinone reductase
FTMS:	Fourier-transform mass spectrometry
F_V/F_M:	Maximum quantum yield of PSII
G3P:	Glyceraldehyde-3-phosphate
GAPDH:	Glyceraldehyde-3-phosphate dehydrogenase
GDC:	Glycine decarboxylase complex
GGAT:	Glutamate:glyoxylate aminotransferase
g_{H^+}:	Thylakoid membrane proton conductivity
GLYK:	Glycerate kinase
GOX:	Glycolate oxidase
gRNA:	Guide RNA
GS/GOGAT:	Glutamine synthetase / glutamate synthase cycle
GS2:	Glutamine synthetase 2 (chloroplast-localised)
H_2O_2:	Hydrogen peroxide
HCO_3^-:	Bicarbonate
HL:	High light
HPR1:	Hydroxypyruvate reductase
iBAQ:	Intensity-based absolute quantification
IDEAspec:	Integrated spectrophotometer/fluorometer (instrument)
IPMK:	Inositol polyphosphate multikinase
JMSF:	Joint Mass Spectrometry Facility
kDa:	Kilodalton

LC-MS/MS:	Liquid chromatography-tandem mass spectrometry
LEF:	Linear electron flow
LFQ:	Label-free quantification
LHC:	Light-harvesting complex
LHCII:	Light-harvesting complex II
LL:	Low light
M:	Mesophyll (cell)
MDH:	Malate dehydrogenase
ML:	Maximum likelihood (phylogenetics)
MS:	Mass spectrometry; also Murashige and Skoog (growth medium)
MS/MS:	Tandem mass spectrometry
NAD-ME:	NAD-dependent malic enzyme
NADH:	Nicotinamide adenine dinucleotide (reduced)
NADP-ME:	NADP-dependent malic enzyme
$NADP^+$ / NADPH:	Nicotinamide adenine dinucleotide phosphate (oxidised / reduced)
NDH:	Chloroplast NAD(P)H dehydrogenase-like complex
NDVI:	Normalised Difference Vegetation Index
NIR:	Near-infrared
NPCI:	Normalised Pigment Chlorophyll Index
NPQ:	Non-photochemical quenching
OAA:	Oxaloacetate
OEC:	Oxygen-evolving complex
P680:	PSII reaction centre chlorophyll
P700:	PSI reaction centre chlorophyll
PC:	Plastocyanin
PCON:	Photosynthetic control
PEPC:	Phosphoenolpyruvate carboxylase
PEPCK:	Phosphoenolpyruvate carboxykinase
PGK:	3-phosphoglycerate kinase
PGLP:	2-phosphoglycolate phosphatase
PGR5:	PROTON GRADIENT REGULATION 5

PGRL1:	PGR5-LIKE PHOTOSYNTHETIC PHENOTYPE 1
Pheo:	Pheophytin
pLDDT:	Predicted local distance difference test
P_M:	Maximum oxidisable P700
pmf:	Proton motive force
PPDK:	Pyruvate orthophosphate dikinase
PPDK-RP:	Pyruvate orthophosphate dikinase regulatory protein
PQ:	Plastoquinone
PQH_2:	Plastoquinol
PRK:	Phosphoribulokinase
PsbS:	Photosystem II subunit S
PSI:	Photosystem I
PSII:	Photosystem II
PSRI:	Plant Senescence Reflectance Index
qE:	Energy-dependent non-photochemical quenching
qL:	Fraction of open PSII reaction centres
qZ:	Zeaxanthin-dependent quenching
RCA:	Rubisco activase
riBAQ:	Relative intensity-based absolute quantification
RNA-seq:	RNA sequencing
ROS:	Reactive oxygen species
Rubisco:	Ribulose-1,5-bisphosphate carboxylase/oxygenase
RuBP:	Ribulose-1,5-bisphosphate
SBPase:	Sedoheptulose-1,7-bisphosphatase
SDS:	Sodium dodecyl sulfate
SGAT:	Serine:glyoxylate aminotransferase
SHMT:	Serine hydroxymethyltransferase
SP:	Saturating pulse
SPAD:	Relative chlorophyll content (SPAD index)
TCEP:	Tris(2-carboxyethyl)phosphine
TEAB:	Triethylammonium bicarbonate

TPM:	Transcripts per million
triose-P:	Triose phosphate
Tris:	Tris(hydroxymethyl)aminomethane
TROL:	Thylakoid rhodanese-like protein
Trxm4:	Thioredoxin m4
UHPLC:	Ultra-high-performance liquid chromatography
UTR:	Untranslated region
VDE:	Violaxanthin de-epoxidase
vFd:	Initial rate of ferredoxin oxidation
v_{H^+}:	Initial rate of ECS decay
WT:	Wild type
φ_I:	Photochemical yield of PSI
φ_{NA}:	Non-photochemical yield of PSI due to acceptor-side limitation
$\varphi_{ND:}$	Non-photochemical yield of PSI due to donor-side limitation
φ_{II}:	Photochemical yield of PSII
$\varphi_{NPQ:}$	regulated energy dissipation of PSII
$\varphi_{NO:}$	non-regulated energy dissipation of PSII

Chapter 1: General Introduction

Introduction

Photosynthesis is the process of capturing energy from sunlight and using it to fix carbon dioxide from the atmosphere into organic molecules. It serves as the foundation of life on Earth by providing oxygen and food, forming the basis of global food chains, and meeting most of humanity's energy needs via fossilised photosynthetic fuels (Johnson, 2016). Humanity is, however, facing concurrent global challenges. The global population is growing, and food demand is projected to increase by 35-56% by 2050 (van Dijk *et al.*, 2021). Simultaneously, biofuel demand is projected to rise by 43 billion litres to around 237 billion litres per year by 2030, reaching 8% of total transport fuel demand (IEA, 2025). This baseline trend has been further accelerated by the recent 2026 Iran oil shock, an event noted by financial analyses to increase crude prices and alter market dynamics (Goldman Sachs, 2026). This type of shock enhances the competitiveness of biofuels, driving agricultural commodity and feedstock demands even higher through the biofuel production channel (Wei *et al.*, 2024). In addition, climate change stressors, including rising temperatures, drought, flooding, and surface ozone, severely impact crop productivity (Long, 2025).

It is therefore imperative to improve photosynthetic efficiency and crop yields for food and biofuel production within the context of these volatile growing conditions. Balancing the production and consumption of chemical energy in photosynthesis, while avoiding deleterious effects of excess incoming light requires delicate and complex regulation In the field, it takes several minutes for photosynthesis to regain efficiency during both sun-to-shade and shade-to-sun transitions, costing 10% to 40% of potential crop CO_2 assimilation (Long *et al.*, 2022). Consequently, understanding and optimising how the light and dark reactions of photosynthesis adapt to fluctuating light environments is critical. C_4 crops are among the most important biomass producers vital to meeting future food and bioenergy demands, and tuning their photosynthetic capacity is a highly promising target for crop improvement (Ermakova *et al.*, 2026). This thesis explores how C_4 plants regulate photosynthesis to achieve efficient but safe energy production by the light reactions, with a specific focus on the PGR5/PGRL1 pathway.

1. Light reactions of photosynthesis

The light reactions occur on the thylakoid membranes of chloroplasts by four transmembrane complexes: Photosystem II (PSII), the Cytochrome b_6f complex (Cytb_6f), Photosystem I (PSI), and ATP synthase (Fig. 1). In linear electron flow (LEF), these complexes work together to harness the energy of absorbed photons to drive electrons along a chain of redox carriers

while pumping protons into the thylakoid lumen, generating both reducing power in the form of NADPH and a trans-thylakoid proton motive force (*pmf*) that powers the synthesis of ATP. The general structure and function of these four complexes are ancient and highly conserved. LEF first arose in cyanobacteria between 3.8 to 3.5 billion years ago and remained largely unchanged up to terrestrial plants (William Schopf, 2011; Cardona *et al.*, 2019; Sánchez-Baracaldo & Cardona, 2020; Ermakova *et al.*, 2024a).

LEF begins at Photosystem II (PSII). The PSII reaction centre (P680) is a special pair of chlorophyll *a* molecules with an absorption maximum at 680 nm that, upon absorbing a photon, is oxidised to $P680^+$ by rapid electron transfer to the primary electron acceptor of PSII, pheophytin (Pheo). From Pheo, electrons are passed to the bound plastoquinone (PQ) in the Q_A pocket. Then 2 electrons are transferred from Q_A to the mobile PQ in the Q_B pocket, pulling 2 H^+ from the stroma and generating plastoquinol (PQH_2). PQH_2 then dissociates from PSII and migrates into the thylakoid membrane (Imaizumi & Ifuku, 2025). $P680^+$ has a high oxidising potential, strong enough to oxidise water and split it into oxygen and protons (H^+). Water oxidation occurs on the lumenal side of PSII at the oxygen-evolving complex (OEC). OEC binds a Mn_4CaO_5 cluster which, through a four-step cycle, processes 2 water molecules, sequentially releasing 4 electrons to reduce $P680^+$, 4 H^+ into the lumen, and 1 molecule of O_2 as a by-product (Kok *et al.*, 1970).

Oxidation of PQH_2 at Cytb_6f is coupled to translocation of protons to the lumen through the Q cycle. PQH_2 binds to the Qo site of Cytb_6f, releasing 2 H^+ into the lumen as 1 electron is passed through the Rieske FeS and Cytochrome *f* (Cyt*f*) proteins to reduce the soluble lumenal electron carrier Plastocyanin (PC). The second electron from PQH_2 at the Qo site is transferred to oxidised PQ molecule at the Qi site, located on the stromal side of Cytb_6f, generating semiquinone (Sarewicz *et al.*, 2021). When the next PQH_2 binds to the Qo site, again 2 H^+ are transferred into the lumen, and 1 electron reduces PC while the other electron fully reduces semiquinone to PQH_2. This results in the net transfer of 2 H^+ per electron from stroma into lumen. The reduced PC then carries the electron to PSI, to reduce the photo-oxidised reaction centre, $P700^+$ (a second special chlorophyll *a* pair, with an absorption maximum at 700nm). P700 is oxidised when, upon absorbing a photon, electron is transferred to the chlorophyll *a* molecule at the Ao site within PSI. This electron then travels through a series of FeS clusters within PSI until it reaches the stromal soluble carrier Ferredoxin (Fd). Electrons from Fd are finally used to reduce $NADP^+$ to NADPH via Ferredoxin:$NADP^+$ oxidoreductase (FNR; Fig. 1; Kramer & Evans, 2011).

The protons released from the OEC and translocated into the lumen by the Q cycle generate electrochemical potential serving as *pmf* which consists of components: a proton

concentration gradient (ΔpH) and a membrane electric potential (Δψ) across the thylakoid membrane. Protons stored in the lumen move back into the stroma across the electrochemical gradient though the *c*-ring of ATP synthase. Rotation of ATP synthase requires protonation of each *c* subunit, with each full rotation of the *c*-ring yielding 3 ATP. Because higher plants carry 14 *c* subunits, ATP synthase requires 4.67 H^+ per ATP ratio (Turina *et al.*, 2016; Davis & Kramer, 2020). As LEF inputs 12 H^+ into the lumen and produces 2 NADPH per 4 electrons, LEF produces ATP and NADPH at a fixed ATP/NADPH ratio of 2.6:2 (Kramer & Evans, 2011) which could fall short of the metabolic demand typical requiring higher ATP/NADPH (see Calvin cycle section below). To overcome the fixed ratio of ATP:NADPH of LEF, the electron transport chain requires supplementary mechanisms increasing ATP/NADPH produced. This can be accomplished through cyclic electron flow (CEF).

CEF around PSI produces additional ATP without additional NADPH by returning electrons from Fd to the intersystem chain, so they can pass again through Cytb_6f and generate *pmf* (Fig. 1). In plants, there is one accepted pathway, and two proposed pathways: the established chloroplast NADH dehydrogenase-like complex (NDH)-dependent route; the proposed antimycin A-sensitive route regulated by PROTON GRADIENT REGULATION 5 (PGR5) and PGR5-LIKE PHOTOSYNTHETIC PHENOTYPE 1 (PGRL1) (Munekage *et al.*, 2002; DalCorso *et al.*, 2008); and a proposed direct transfer of electrons from FD to Cytb_6f (Malone *et al.*, 2021). These routes differ in energetic yield because NDH itself pumps 2 H^+ per electron from stroma to lumen, bringing the total ratio for NDH-CEF to 4 H^+ per electron and making NDH-CEF the most efficient for additional ATP generation. Other routes are theorised to contribute to *pmf* only through the Cytb_6f Q-cycle at a hypothesised 2 H^+ per electron (Strand *et al.*, 2017; Pan *et al.*, 2020; Zhang *et al.*, 2020). By redirecting electrons from FNR to PQ, CEF allows the generation of additional ATP without changing NADPH generation thereby helping to balance the output of light reactions against the changing requirements of cellular metabolism.

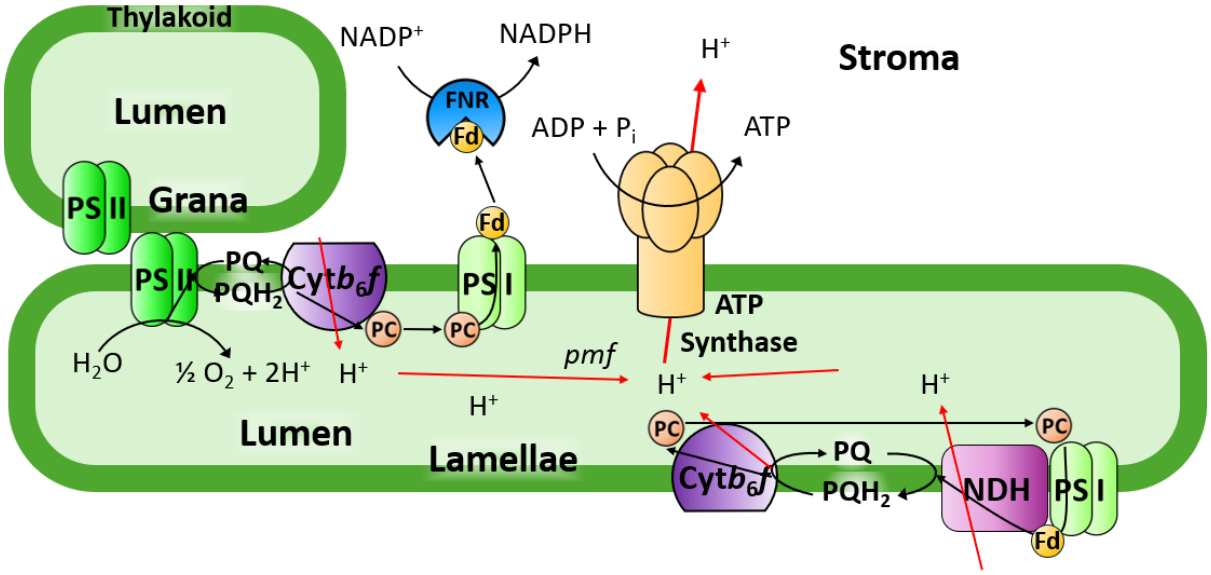

Fig. 1. Chloroplast electron transport. Black arrows denote electron transfer paths, red arrows denote H^+ translocation, diffusion, and efflux pathways. PSII, Photosystem II; PSI, Photosystem I; Cytb_6f, Cytochrome b_6f complex; PC, plastocyanin; PQ, plastoquinone; PQH_2, plastoquinol; Fd, Ferredoxin; FNR, Ferredoxin: $NADP^+$ oxidoreductase; NDH, chloroplast NADH dehydrogenase-like complex; *pmf,* proton motive force; PC, plastocyanin.

2. Calvin-Benson cycle

The Calvin-Benson Cycle (CBC) is the carbon-fixing pathway of all oxygenic phototrophs, fixing CO_2 into sugars. Photosynthetic organisms that exclusively use this pathway for CO_2 fixation are referred to as C_3, as the first product of carboxylation is a 3-C molecule. The cycle begins with the carboxylation phase in which ribulose-1,5-bisphosphate carboxylase/oxygenase (Rubisco) incorporates 1 CO_2 onto the 5-C sugar ribulose-1,5-bisphosphate (RuBP). The resulting 6-C product is unstable, spliting into 2 molecules of 3-phosphoglycerate (3-PGA). In the reduction phase, 3-phosphoglycerate kinase (PGK) phosphorylates each 3-PGA using 2 ATP per each CO_2 fixed. Glyceraldehyde-3-phosphate dehydrogenase (GAPDH) reduces the resulting intermediates using 2 NADPH per CO_2 fixed, yielding 2 molecules of glyceraldehyde-3-phosphate (G3P). 1 out of 6 G3P molecules produced in SBS leaves the cycle as net product while the remainder 5 are regenerated into 3 RuBP through aldolase, fructose-1,6-bisphosphatase (FBPase), transketolase, sedoheptulose-1,7-bisphosphatase (SBPase), ribose-5-phosphate isomerase and ribulose-5-phosphate epimerase, and phosphoribulokinase (PRK) which consumes 1 additional ATP per CO_2 fixed (Raines, 2003; Eisenhut *et al.*, 2019). The full CBC energy cost comes to 3 ATP and 2 NADPH for every CO_2 fixed which already exceeds the ATP/NADPH produced by LEF. However, additional ATP is also required by photorespiration, starch synthesis, and a host of other metabolic processes in the chloroplast (Kramer & Evans, 2011; Strand & Walker, 2023).

In addition to its primary role in fixing CO_2, Rubisco also catalyses oxygenation of RuBP, producing 1 molecule of 3-PGA and 1 molecule of 2-phosphoglycolate (2PG), that inhibits CBC enzymes and must be recycled (Bauwe *et al.*, 2010). The ratio of carboxylation to oxygenation depends on the kinetic properties of the enzyme, temperature, and the CO_2:O_2 ratio at the active site (Eisenhut *et al.*, 2019). For instance, drought facilitates stomatal closure which decreases CO_2:O_2 inside chloroplasts while heat reduces Rubisco's specificity for CO_2, with both conditions thereby increasing the rate of oxygenation. 2PG is recycled by the photorespiratory pathway, which comprises nine enzymatic reactions distributed across the chloroplast, peroxisome and mitochondrion (Bauwe *et al.*, 2010): phosphoglycolate phosphatase (PGLP) acts first in the chloroplast; glycolate oxidase (GOX), catalase (CAT) and glutamate:glyoxylate aminotransferase (GGAT) operate in the peroxisome; glycine decarboxylase (GDC) and serine hydroxymethyltransferase (SHMT) in the mitochondrion; serine:glyoxylate aminotransferase (SGAT) and hydroxypyruvate reductase (HPR1) back in the peroxisome; and glycerate kinase (GLYK) returns 3-PGA to the chloroplast, with intercompartmental flux carried by transporters such as PLGG1 (Pick *et al.*, 2013) and BASS6 (South *et al.*, 2017). The pathway is energetically expensive: mitochondrial glycine decarboxylation by GDC releases previously fixed carbon as CO_2 and nitrogen as NH_3 while consuming ATP and NAD(P)H, and the liberated NH_3 must be re-assimilated by glutamine synthetase (GS2) and ferredoxin-dependent glutamine:oxoglutarate aminotransferase (Fd-GOGAT), each demanding further ATP and reducing power from Fd (Coschigano *et al.*, 1998). This overall process, known as photorespiration, thus inflicts a yield penalty of 20–50% in C_3 plants depending on environmental conditions (Bauwe *et al.*, 2010). However, in multiple instances photosynthetic organisms have developed unique adaptations to circumvent the photorespiration penalty.

3. Carbon Concentrating Mechanisms

Carbon Concentrating Mechanisms (CCMs) share the same principle of elevating CO_2 partial pressure in the vicinity of Rubisco to prioritise carboxylation over oxygenation, but they do so through distinct strategies (Flothow & Küffner, 2026). Cyanobacteria deploy carboxysomes, microcompartments encapsulating Rubisco together with carbonic anhydrase so that bicarbonate imported by dedicated membrane transporters is converted to CO_2 precisely where it is fixed (Huffine *et al.*, 2023; Zimmer *et al.*, 2026). Eukaryotic algae and some non-vascular plants such as hornworts instead organise their Rubisco into condensates called pyrenoids, which, like carboxysomes, co-localise Rubisco and carbonic anhydrase and thereby sustain efficient assimilation with far less enzyme (Adler *et al.*, 2022; Ang *et al.*, 2023). In angiosperms, there are two types of biochemical CCM: C_4 photosynthesis and Crassulacean acid metabolism (CAM) which separate primary carboxylation reaction from the

secondary carboxylation by Rubisco. In, CAM CO_2 is fixed into organic acid at night and stored, then released and re-fixed by Rubisco during the day, so that the two steps occur in the same cells but at different times (Gowik & Westhoff, 2011). C_4 photosynthesis separates the two carboxylation steps across specialised cell types (von Caemmerer & Furbank, 2003).

Of the four CCMs, C_4 photosynthesis is the most promising system for improving C_3 crops. Carboxysomes and pyrenoids evolved only in cyanobacteria and algae, whereas C_4 and CAM arose within the angiosperms themselves, making their genetic and anatomical aspects far more transferable to crop species. Between C_4 and CAM, C_4 is more productive: CAM evolved primarily for water conservation, rather than improved CO_2 assimilation, allowing these species to thrive in dry arid environments at the cost of slow growth (Gowik & Westhoff, 2011), whereas C_4 plants have higher than C_3 CO_2 assimilation with rapid growth. C_4 photosynthesis is one of the most striking examples of convergent evolution in plants, having arisen independently more than sixty times within the angiosperms (Sage *et al.*, 2011). This recurrent origin across unrelated lineages signals strong, repeated selective pressure under the warm, dry, high-light conditions where photorespiration most compromises the C_3 pathway (Sage & Kubien, 2007; Ghannoum *et al.*, 2011; Sage *et al.*, 2012). The resulting productivity is why C_4 species represent some of the most important food and biomass crops: maize (*Zea mays*), sorghum (*Sorghum bicolor*) and sugarcane (*Saccharum* sp.), while the model C_4 grass *Setaria viridis* is widely used to study the pathway. This productivity has driven sustained efforts to engineer C_4 traits into C_3 crops to raise their yield and resource-use efficiency (Ermakova *et al.*, 2021a; Croce *et al.*, 2024).

4. The metabolic C_4 cycle

The C_4 cycle acts like CCM by spatially separating reactions of photosynthesis between mesophyll (M) cells and bundle sheath (BS) cells (Fig. 2). CO_2 first diffuses into the M cytosol where it is hydrated to bicarbonate (HCO_3^-) by carbonic anhydrase (CA). Phosphoenolpyruvate carboxylase (PEPC) incorporates bicarbonate onto PEP to form the 4-carbon acid oxaloacetate (OAA), which is transported into the chloroplast and reduced to malate by malate dehydrogenase (MDH) using NADPH. Malate diffuses to BS cells, where it is decarboxylated, releasing CO_2 to be fixed by Rubisco. High activity of PEPC vs Rubisco allows CO_2 to be concentrated in BS cells well above atmospheric levels (Hatch, 1987; von Caemmerer & Furbank, 2003).

There are three biochemical subtypes of C_4 photosynthesis based on the enzyme primarily used for decarboxylation: NADP-malic enzyme (NADP-ME), NAD-malic enzyme (NAD-ME) and phosphoenolpyruvate carboxykinase (PEPCK; Hatch. 1987). The NADP-ME subtype is characteristic of the major food and energy C_4 crops, including maize, sorghum, sugarcane,

miscanthus and millets (Ermakova *et al.*, 2026). The NADP-ME is also the most studied subtype as it is the simplest in regard to the number of enzymes and involves only chloroplasts in BS cells. Therefore NADP-ME is solely the focus of this thesis. However, these subtypes are not mutually exclusive. Many NADP-ME species operate more than one decarboxylation pathway and can adjust the proportion of flux routed through each pathway according to environmental conditions (Furbank, 2011; Wang *et al.*, 2014). For example, maize commonly supplements NADP-ME with a secondary PEPCK pathway (Walker *et al.*, 1997).

NADP-ME activity results in releasing CO_2, reducing $NADP^+$ and forming pyruvate in BS chloroplasts (Hatch, 1987; von Caemmerer & Furbank, 2003). Pyruvate returns to M cells where it is regenerated into PEP by the enzyme pyruvate orthophosphate dikinase (PPDK) in the chloroplast, concluding the cycle at the cost of 2 ATP. Therefore, the operation of the C_4 cycle at minimum requires 2 ATP in addition to 3 ATP and 2 NADPH for fixing 1 CO_2 through CBC. This energy cost is shared between the two cell types. In BS cells, NADPH obtained though decarboxylation of malate supplies at least half of the reductant required for CBC (Furbank, 2011). The remaining NADPH can be fully, or partially, accounted for through the triose-phosphate (triose-P) shuttle (Fig. 2). In this pathway, a portion of 3-PGA produced in the BS diffuses to M cells, where it is reduced to G3P using 1 ATP and 1 NADPH. G3P then returns to the CBC in BS cells. Thereby, in species operating pure NADP-ME subtype, the energy requirement supplied from chloroplast electron transport per cell type is 3 ATP and 2 NADPH in the M, and 2 ATP and 0 NADPH in the BS (Fig. 2).

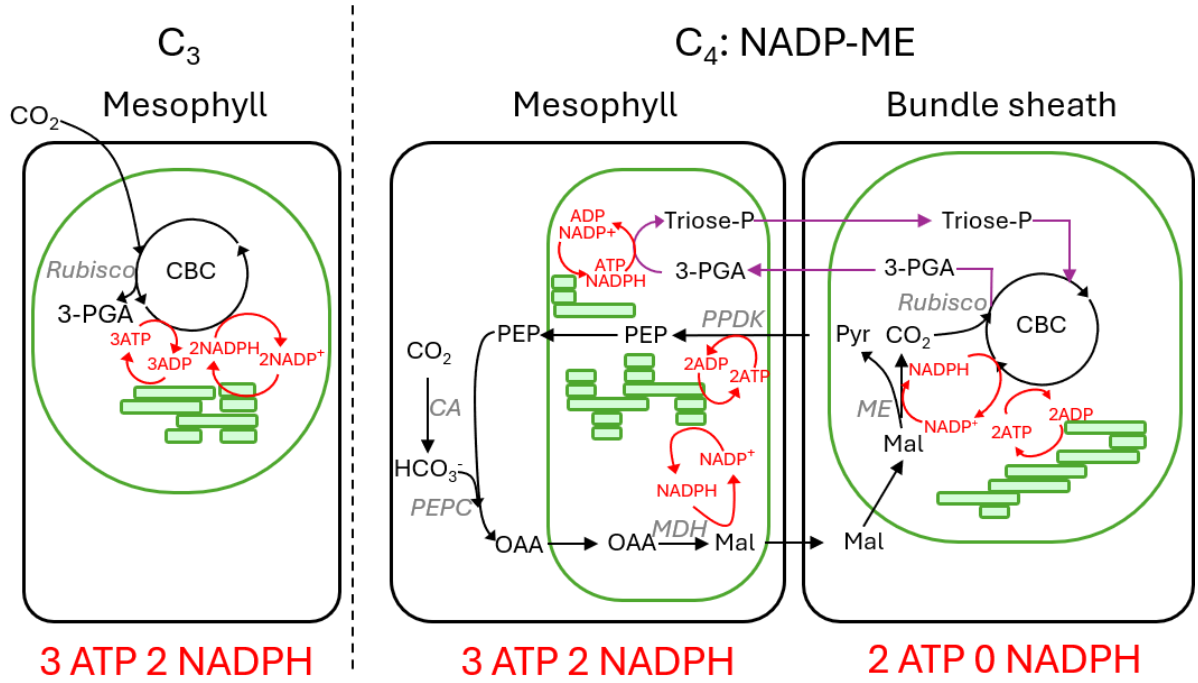

Fig. 2. Metabolic pathway and energy requirements for NADP-ME C_4 photosynthesis. Black arrows show metabolite flux for the C_4 and Calvin-Benson Cycle (CBC) pathways, purple arrows show flux for the triose-phosphate shuttle, red arrows and red font mark reactions consuming ATP and NADPH, with the number of molecules per CO_2 fixed. Enzyme names are in grey italic font. Total ATP and NADPH requirements of each cell are given underneath. CA, carbonic anhydrase; Mal, malate; MDH, malate dehydrogenase; ME, $NADP^+$-dependent malic enzyme; OAA, oxaloacetate; PEP, phosphoenolpyruvate; PEPC, phosphoenolpyruvate carboxylase; 3-PGA, 3-phosphoglycerate; PPDK, pyruvate, phosphate dikinase; Pyr, pyruvate; Rubisco, ribulose-1,5-bisphosphate carboxylase/oxygenase; Triose-P, triose phosphate.

5. Electron transport pathways in C_4 chloroplasts

Different energy requirements between M and BS cells in the NADP-ME subtype result in markedly different electron transport chain composition. M chloroplasts rely predominantly on LEF and therefore retain an equivalent ratio of PSII and PSI, similar to C_3 mesophyll cells, with PSI/PSII ≈ 1.06 in *S. viridis* (Munekage, 2016; Munekage & Taniguchi, 2016; Ermakova *et al.*, 2021b). BS chloroplasts, by contrast, have low NADPH demand which strongly reduce LEF activity and PSII abundance, to 0–30% of that in M cells depending on species and conditions. Sorghum, operating a near-pure NADP-ME subtype, typically has no detectable PSII activity in BS cells, while maize and sugarcane, which operate predominantly NADP-ME but engage PEPCK under stress, experience increased demand for NADPH in BS and increase PSII activity under shade and drought (Ubierna *et al.*, 2013; Cacefo *et al.*, 2019; Sales *et al.*, 2021). In the model NADP-ME grass *S. viridis*, PSII abundance and activity In BS cells is about 10-20% of the M, depending on the ecotype and growth irradiance (Ermakova *et al.*, 2021b; Ermakova *et al.*, 2024a). This functional asymmetry is mirrored structurally as PSII is largely localised to the grana and PSI the lamellae of the thylakoid. M thylakoids form extensive grana stacks to support PSII and LEF, whereas BS thylakoids lack grana and are dominated by lamellae to support CEF (Woo *et al.*, 1970; Danila *et al.*, 2019).

Since BS chloroplasts need to generate primarily ATP, they predominantly require PSI and operate CEF. CEF/LEF ratio in BS cells of *S. viridis* is ~5, versus ~0.1 in M cells (Bellasio & Ermakova, 2022; Ermakova *et al.*, 2024a). Most of CEF in BS cells is operated via NDH (Nakamura *et al.*, 2013; Ermakova *et al.*, 2024b). The NDH complex is markedly more abundant in C_4 than in C_3 plants, and its upregulation is considered an important step in the evolution of C_4 photosynthesis (Nakamura *et al.*, 2013; Munekage, 2016). High abundance of NDH enables generation of extra ATP required for C_4 photosynthesis. This importance is demonstrated in C_4 NDH mutants where a deficiency in, or absence of, NDH significantly reduces electron transport, carbon assimilation, and biomass in maize, *S. viridis* and *Flaveria*

bidentis (Ishikawa *et al.*, 2016; Peterson *et al.*, 2016; Ogawa *et al.*, 2023; Ermakova *et al.*, 2024b; Zhang, Q *et al.*, 2024).

6. Balancing energy supply and demand

Balancing energy supply and demand is important for smooth operation of photosynthesis. When too little ATP or NADPH are produced, metabolism is energy limited and sub-optimal. while excessive production of ATP or NADPH can rapidly lead to accumulation of high energy intermediates causing overreduction of electron transport chain. An over-reduction of electron acceptors leads to the formation of chlorophyll triplet states (^{3}Chl*) in both photosystems, which react with oxygen generating reactive oxygen species (ROS). In PSI, when oxidised Fd is unavailable, the 'Mehler reaction' between the FeS clusters F_A and F_B and O_2 produces superoxide ($^*O_2^-$) which is rapidly dismutated to hydrogen peroxide (H_2O_2) (Murchie & Niyogi, 2011; Das & Roychoudhury, 2014; Lima-Melo *et al.*, 2021). A low level of H_2O_2 is generated continuously, even under favorable conditions and is not inherently harmful. Usually, ROS is promptly detoxified by the chloroplast' scavenging systems, water-water cycle, and ascorbate antioxidant enzymes (Asada, 1999; Miyake, 2010). However, when ROS production exceeds the capacity of the scavenging systems, it damages the thylakoid complexes leading to photoinhibition. Furthermore, as ROS forms part of the retrograde signaling network, excess of ROS signals stress and drives changes in nuclear gene expression (Chan *et al.*, 2016).

Changing environmental conditions, like light, temperature, humidity, etc, alter the energy and substrate inputs for light and dark reactions. Often these changes are very fast, extreme, contrasting or repetitive, making it hard to adapt and requiring continuous adjustments of activity of all involved reactions. In C_4 photosynthesis, it is essential to match energy supply and demand at each cell-level. But furthermore, there an additional layer of balancing of metabolic reactions between the cell types to achieve seamless operation of C_4 photosynthesis on the leaf level. If the C_4 cycle and CBC are uncoordinated, it leads to CO_2 leakage from BS cells and the need to re-fix this CO_2 in M cells, further increasing energy demand (Furbank *et al.*, 1990). While leakage is estimated at 20% at steady-state, it can be as high as 50%, making C_4 photosynthesis very inefficient (Kromdijk *et al.*, 2014; Wang *et al.*, 2022). Indeed, C_4 photosynthesis is known to be sensitive to transient light conditions owing to the thiol- and phosphorylation-based regulation of key enzymes and the need to readjust large metabolite pools when conditions change (Furbank & Walker, 1985; Slattery *et al.*, 2018; Arce Cubas *et al.*, 2023; Arrivault *et al.*, 2025).

In C_4 plants, the activity of photosynthetic enzymes is regulated in a cell-specific manner at transcriptional, translational, and post-translational levels to balance assimilation demand with CO_2 supply. Over long timescales the confinement of Rubisco to the BS and matching its

abundance to assimilation demands is achieved through transcriptional, translational, and post-translational control (Chotewutmontri & Barkan, 2021; Hotto *et al.*, 2021). On the shorter timescale, the activation state of key enzymes, especially Rubisco by Rubisco activase (RCA), is set post-translationally. In addition, with CBC enzymes, NDH, and NADP-ME which are activated by the ferredoxin/thioredoxin system (Ashton *et al.*, 1990; Alvarez *et al.*, 2019), PEPC by PEPC kinase (PEPCPK) reversible phosphorylation (Furumoto *et al.*, 2007), and PPDK by bifunctional PPDK regulatory protein (PPDK-RP) reversible phosphorylation (Om *et al.*, 2022). Finally, flux can be tuned within seconds by allosteric metabolite effectors: C_4 PEPC is activated by glucose-6-phosphate and uncharged amino acids such as glycine, and feedback-inhibited by its downstream products malate and aspartate (Kai *et al.*, 1999; Tovar-Méndez *et al.*, 2000).

Metabolic regulation by altering protein expression is rather slow, from minutes to hours, and plants need to promptly adjust energy supply by regulating activity of light reactions. This includes regulating ATP/NADPH balance but also slowing down electron transport, lowering overall NADPH and ATP production. Several mechanisms are well known and studied in C_3 plants. Among the most important are non-photochemical quenching (NPQ; regulated energy dissipation by PSII antenna remodeling), photosynthetic control (PCON; oxidation of PSI by slowing of electron transfer through Cytb_6f in response to lumen acidification), malate valve (exchanges reducing equivalents NADPH and NADH between the chloroplast and mitochondria), and CEF. Interestingly, the malate valve and CEF, which are considered the main ways to balance ATP/NADPH in C_3 plants at low and high light, respectively (Walker *et al.*, 2020). gained C_4 specific functions. MDH operating in the malate valve in C_3 plants by reducing oxaloacetate to malate to export excess NADPH out of the chloroplast, became the essential part of the C_4 cycle while NDH became critical for high ATP generation in BS cells (Ermakova *et al.*, 2024a).

NPQ, specifically the energy-dependent form qE, and photosynthetic control at Cytb_6f are the most important fast-acting mechanisms minimising light energy or electrons reaching photosystems to protect them from overreduction and photoinhibition (Ruban, 2016; Degen & Johnson, 2024). Both mechanisms respond to the pH component of *pmf* to monitor how energy production compares with energy usage by metabolism. This relies on ATP synthase's usage of finite pools of ADP and P_i for ATP synthesis: if ATP is not consumed by metabolism promptly, ADP or P_i are not regenerated, leaving ATP synthase without substrate (Kramer & Evans, 2011). The *pmf* therefore accumulates and acidifies the lumen. Thus, lumen pH provides a critical signal for adjusting activity of light reactions (Degen & Johnson, 2024).

7. Non-photochemical quenching

When PSII activity outpaces the capacity of downstream metabolism, plants down-regulate light energy reaching PSII reaction centres through NPQ. The light-harvesting complexes switch into a dissipative state that releases a portion of the absorbed energy as heat (Müller *et al.*, 2001; Ruban, 2016). NPQ comprises several distinct forms that differ in their molecular basis and in the timescales over which they act, allowing plants to accommodate both brief fluctuations and sustained increases in irradiance (Müller *et al.*, 2001; Malnoë, 2018). Energy-dependent NPQ (qE) is the most rapid form, engaging and relaxing over seconds to minutes (Müller *et al.*, 2001; Nilkens *et al.*, 2010; Jahns & Holzwarth, 2012). In qE, protonation of Photosystem II subunit S (PsbS) upon lumenal acidification drives a conformational change within light harvesting complex II (LHCII) that promotes energy-dissipation (Malnoë, 2018). In parallel, the lowered lumen pH activates violaxanthin de-epoxidase (VDE), which converts the thylakoid localised carotenoid violaxanthin to zeaxanthin through the xanthophyll cycle. Zeaxanthin helps to quench the excited electron on singlet chlorophyll, preventing the formation of triplet chlorophyll and the reactive oxygen species (Jahns & Holzwarth, 2012).

Zeaxanthin-dependent quenching (qZ) is a distinct form of NPQ that, unlike qE, operates independently of PsbS and lumen pH, relying instead on a slowly interconverting pool of violaxanthin and zeaxanthin, providing photoprotection on a timescale of minutes to hours (Nilkens *et al.*, 2010). In qZ, zeaxanthin promotes the aggregation of LHCII subunits and alters the organisation of the thylakoid membrane to shift the antenna into a more dissipative arrangement (Nilkens *et al.*, 2010; Ruban, 2016; Malnoë, 2018).

8. Photosynthetic control

PSI is uniquely vulnerable to damage because, unlike PSII, damaged PSI cannot be repaired within the assembled complex and must instead be replaced by de novo synthesis and assembly. PSII manages photoinhibition through a repair cycle of the D1 subunit of the reaction-centre allowing the complex to recover its activity within minutes to hours without requiring re-assembly of the whole complex (Tikkanen & Aro, 2014). PSI has no equivalent mechanism: damage to the PSI reaction centre requires the degradation of the damaged complex and the complete *de novo* synthesis and assembly of a replacement complex. This process is energetically expensive and takes hours to days, resulting in a prolonged and costly reduction in photosynthetic capacity (Sonoike, 2011; Degen & Johnson, 2024). Most oxygenic photosynthetic organisms apart from angiosperms mitigate PSI photoinhibition through Flavodiiron proteins (FLVs), which rapidly accept excess electrons from ferredoxin and reduce O_2 directly to water (Yamamoto *et al.*, 2016; Chaux *et al.*, 2017; Storti *et al.*, 2020). Angiosperms, however, lost FLVs early in their evolution, and must instead rely on slowing the

delivery of electrons to PSI to keep PSI oxidised through a phenomenon known as photosynthetic control (PCON).

When the rate of proton translocation across the thylakoid membrane exceeds the rate of proton efflux through ATP synthase, lumen acidification shifts pKa of the Qp site at Cytb_6f from 8 to 6.2 and thus slows the rate of electron transfer from PQ to PC (Rumberg & Siggel, 1969; Soriano *et al.*, 2002; Tikhonov, 2014; Degen & Johnson, 2024). The consequence is that P700 is maintained in an oxidised state, allowing for safe charge recombination (Degen & Johnson, 2024). There are, however, indications that PCON is not simply an intrinsic, pH-dependent property of Cytb_6f. For example, knocking-down Glyceraldehyde 3-phosphate dehydrogenase (GAPDH) or FNR in tobacco both reduce CBC activity. However, while the GAPDH knock-down induces PCON, the FNR knock-down has a normal ΔpH (inferred from qE) but no PCON (Hald *et al.*, 2008). A candidate mechanism for a redox regulation is the conserved C112-C127 disulphide bridge of the Rieske FeS protein, which when reduced by the lumen-facing thioredoxin-like proteins could raise the pKa of the His128 ligand and thereby couple stromal redox state directly to the rate of PQH2 oxidation (Hald *et al.*, 2008; Johnson & Berry, 2021). This means that the sensitivity of Cytb_6f to ΔpH, and therefore PCON, is in principle tuneable and could in principle be relaxed to permit faster electron delivery to PSI in high light without sacrificing PSI protection, as indicated by Rieske FeS overexpression studies that raised electron transport capacity and growth (Ermakova *et al.*, 2019; Ermakova *et al.*, 2023).

9. Proton motive force regulators

The fact that both qE and PCON are both triggered by lumen pH highlights the importance of regulating *pmf* particularly it's pH component. Plants possess multiple mechanisms to change either the amplitude of *pmf* or the ratio between ΔpH and Δψ. There are several thylakoid channels that regulate ion fluxes across the membrane and modulate ΔpH and Δψ. Most notably, KEA3 is a K^+/H^+ antiporter that exports protons from the lumen in exchange for potassium, thereby converting ΔpH into Δψ. By dissipating the ΔpH while preserving the overall *pmf*, KEA3 allows plants to promptly relax NPQ when irradiance falls, redirecting more absorbed energy toward the dark reactions (Uflewski *et al.*, 2024).

PGR5 (PROTON GRADIENT REGULATION 5) and PGRL1 (PGR5-LIKE PHOTOSYNTHETIC PHENOTYPE 1) are the principal regulators that promote ΔpH formation which qE and PCON depend on. PGR5 was first identified in an ethyl methanesulfonate (EMS) mutant screen of *Arabidopsis thaliana* for impaired *pmf* as the *pgr5* mutant displayed lower qE despite an otherwise normal growth phenotype under constant light (Shikanai *et al.*, 1999). Subsequent characterisation revealed increased acceptor-side limitation at PSI (φ_{NA}) and no donor-side limitation of PSI (φ_{ND}) even at high irradiances. This indicated that plants lacking

PGR5 have lower *pmf* and consequently lower qE and diminished PCON (Munekage *et al.*, 2002; Suorsa *et al.*, 2012; Suorsa *et al.*, 2016). Due to an inability to keep PSI oxidised at high irradiances, *pgr5* suffers from PSI photoinhibition (Suorsa *et al.*, 2016).This is especially detrimental during repetitive increases of irradiance. Notably, C_3 *pgr5* mutants grow normally under constant moderate light but suffer severe growth penalties under fluctuating light, where the rapid induction and relaxation of PCON and qE is essential (Tikkanen *et al.*, 2010; Suorsa *et al.*, 2012; Long *et al.*, 2022; Niu *et al.*, 2023).

10. Molecular mechanism of PGR5/PGRL1

PGR5 is a small, soluble stromal protein lacking transmembrane domains and is highly conserved across photosynthetic eukaryotes, consistent with a fundamental role in the light reactions (Munekage *et al.*, 2002). PGR5 operates alongside of PGRL1, an integral transmembrane protein in the thylakoid. The *pgrl1ab* double mutant of *A. thaliana* copies the phenotype of *pgr5*, with the PGR5 protein disappearing from the *pgrl1ab* background alongside PGRL1A/B disappearance suggesting PGR5 requires PGRL1 presence/activity (DalCorso *et al.*, 2008). Biochemical evidence suggests that the two proteins assemble into a heterodimeric complex, although direct structural proof of this complex is lacking (DalCorso *et al.*, 2008; Hertle *et al.*, 2013; Rühle *et al.*, 2021). The activity of this complex appears to be gated by a redox switch on PGRL1 between conserved stromal cysteines (Hertle *et al.*, 2013). Okegawa and Motohashi (2020) identified thioredoxin m4 (Trxm4) as a redox regulator of PGRL1 on the same cysteines involved in dimerisation, providing a mechanism by which the disulphide is reduced and the dimer dissociated. Chaturvedi *et al.* (2024) subsequently resolved the kinetics of this transition in vivo, demonstrating that the oxidised dimer exists in the dark and is reduced to the monomer within seconds of light exposure, which is then hypothesised to permit PGR5 activity.

While Hertle *et al.* (2013) originally proposed that PGRL1 acts as the ferredoxin-plastoquinone reductase (FQR) of CEF, this interpretation has since been challenged (Rühle *et al.*, 2021; Penzler *et al.*, 2022). It is instead more likely that PGR5 is a component that actively regulates *pmf* while PGRL1 serves as its gatekeeper (Rühle *et al.*, 2021). This is supported by the discovery of PGRL2, a structural homolog of PGRL1 that likely promotes the proteolytic degradation of PGR5 in the absence of PGRL1 (Rühle *et al.*, 2021). In the *pgrl1ab pgrl2* triple mutant, PGR5 re-accumulates and indistinguishable from WT under moderate and high light conditions. Under very low light, however, NPQ is significantly elevated and electron transport is significantly decreased relative to WT, consistent with an increased delta pH. This indicates that unregulated PGR5, freed from PGRL1 and PGRL2 regulation, induces photoprotection outside the conditions in which it is beneficial (Rühle *et al.*, 2021).

The mechanism in which PGR5 builds *pmf*, however, remains contested. The long-standing proposal is that PGR5 facilitates the antimycin A-sensitive CEF pathway around PSI, returning electrons from Fd to the PQ pool and thereby driving additional proton translocation through Cytb_6f (Munekage *et al.*, 2002; Suorsa *et al.*, 2012; Yamori & Shikanai, 2016).The primary in vitro support for this comes from isolated thylakoids supplied with NADPH and Fd under very weak light (1 µmol m^{-2} s^{-1}). Electrons from reduced Fd are transferred back to the PQ pool, detected as a rise in chlorophyll fluorescence, and this Fd to PQ reduction is antimycin A-sensitive and diminished in *pgr5* and *pgrl1* mutants (Munekage *et al.*, 2002; Okegawa *et al.*, 2007; DalCorso *et al.*, 2008; Long *et al.*, 2008; Courteille *et al.*, 2012; Nishikawa *et al.*, 2012; Hertle *et al.*, 2013). In vivo, evidence for CEF loss in *pgr5* is circumstantial: increased PSI acceptor side limitations φ_{NA} along with over reduced Fd pools (Suorsa *et al.*, 2016; Yamori *et al.*, 2016; Takagi & Miyake, 2018; Yamamoto & Shikanai, 2018). Stronger in vivo evidence comes from the ATP synthase mutant *hope2*, where constitutively high proton efflux is offset by strongly upregulated PGR5-dependent proton influx which is consistent with CEF (Degen *et al.*, 2023a). Conclusively showing deficiency in CEF in the *pgr5* mutant is however challenging in C_3 plants. The strong acceptor side limitation and lack of PCON prevents the oxidation of P700 in the *pgr5* mutant (Tikkanen *et al.*, 2014). Therefore, $P700^+$ relaxation kinetics cannot be used to follow the re-reduction of an oxidised pool like previously used to measure NDH's contribution to CEF flux (Ermakova *et al.*, 2024b). Generating $P700^+$ in the C_3 *pgr5* mutant requires preventing electron flow from PSII using DCMU, far-red light, or additional mutations that reduce LEF, yet each of these interventions perturbs the very fluxes under investigation and confounds the interpretation (Nandha *et al.*, 2007; Suorsa *et al.*, 2016).

A second alternative hypothesis suggests that PGR5 acts as an electron distributor on the PSI acceptor side, but not through CEF; *pmf* therefore builds through accelerated LEF (Takagi & Miyake, 2018). The loss of PGR5 causing electrons to accumulate on the acceptor side leading to "backpressure" that over reduces the entire electron transport chain (Kappel *et al.*, 2023). A third alternative hypothesis suggests that PGR5 influences *pmf* by regulating the proton efflux through ATP synthase. This is supported by the observation that *pgr5* mutants display elevated thylakoid membrane proton conductivity (g_{H^+}), indicating a higher rate constant of proton efflux though ATP synthase, which does not allow *pmf* to accumulate under high light to upregulate qE and PCON (Avenson *et al.*, 2005a; Nikkanen *et al.*, 2018; Degen *et al.*, 2023b; Nikkanen *et al.*, 2024).

11. PGR5/PGRL1 in C_4 photosynthesis

PGR5 and PGRL1 accumulate to higher levels in C_4 species than in their C_3 relatives. In the genus *Flaveria*, PGR5 expression rises across C_3 to C_3-C_4 intermediate to C_4 transition

(Munekage *et al.*, 2010), and a comparable increase is reported across C_3 to C_4 species in the grass genus Neurachne (Kümpers *et al.*, 2017). This is overall consistent with a requirement for enhanced PSI photoprotection in the high irradiance environments that C_4 species inhabit (Sage, 2004; von Caemmerer & Furbank, 2016). The *S. viridis pgr5* mutant shows that PGR5 is required for WT-levels of *pmf*, PCON, and qE - all necessary for photoprotection under light stress (Woodford *et al.*, 2025b). As PGR5 is distributed equally between M and BS cells (Munekage *et al.*, 2010; Ishikawa *et al.*, 2016; Ermakova *et al.*, 2021b), *pgr5* mutants accumulate ROS in both cell types, indicating that PGR5 is required for PSI photoprotection in both M and BS cells of a C_4 leaf (Woodford *et al.*, 2025b).

The fluctuating light growth phenotype of the *S. viridis pgr5* mutant is notably less severe compared to that of C_3 *pgr5* mutants. Whereas the *A. thaliana pgr5* mutant typically shows a complete absence of φ_{ND}, *S. viridis pgr5* could establish φ_{ND}, albeit still significantly lower than WT (Woodford *et al.*, 2025b). This residual donor-side limitation is most likely supported by the greater activity of NDH CEF in C_4, which lowers lumenal pH sufficiently to trigger qE and photosynthetic control even without PGR5 (Woodford *et al.*, 2025b). In the absence of qE, a slower-relaxing, qZ enabled *S. viridis pgr5* to survive under fluctuating light; however, because qZ relaxes slowly, constitutively high NPQ wastes a substantial fraction of absorbed light during the low-light phases of the fluctuating-light resulting in a growth penalty (Woodford *et al.*, 2025b).

Instantaneous CO_2 assimilation rates of constant-light-grown plants exposed to short-term high light were unaffected in *S. viridis pgr5* mutant prompting Woodford *et al.* (2025b) to conclude that PGR5 is not important for ATP generation in C_4 plants. This conclusion aligns with the results from *F. bidentis* knockdown PGR5 mutants (*pgr5-RNAi*) which also showed lowered NPQ and reduced CO_2 assimilation by around 20%, but no difference in biomass when the plants were grown under constant moderate or high light (Ogawa *et al.*, 2023). PGR5 overexpression of PGR5 in *F. bidentis* lowered PSI acceptor-side limitation upon low-to-high light shift but produced no change in *pmf*, NPQ, growth, or assimilation (Tazoe *et al.*, 2020). Together these data indicate that the primary role of PGR5 in C_4 plants is enabling of photoprotection rather than ATP supply.

The increased ATP demand of C_4 photosynthesis could in principle recruit PGR5 for ATP generation under certain conditions. Evidence that this capacity exists comes from *S. viridis* plants lacking NDH, in which residual CEF in BS cells that could be mediated by PGR5/PGRL1 (Ermakova *et al.*, 2024b). A double PGRL1 NdhO knockdown mutant in *F. bidentis* which has significantly impaired growth compared to NdhO knockdown alone, also indicates that the PGR5/PGRL1 pathway supplies additional ATP when NDH is lost (Nakamura *et al.*, 2026).

Given this potential involvement in both photoprotection and ATP generation, the role of PGR5/PGRL1 in C_4 photosynthesis requires further study.

12. Research questions addressed in the thesis

PGR5 and PGRL1 act as central regulators of *pmf* and PSI photoprotection and this pathway is functionally important in C_4 plants. Yet multiple questions remain: Is PGR5 regulated differently between mesophyll and bundle sheath cells? Can the residual photosynthetic control retained by C_4 *pgr5* mutants resolve PSI electron fluxes? How does PGR5 support adaptation of C_4 photosynthesis to fluctuating light? This thesis addresses these three questions using *S. viridis* as a model C_4 grass.

Chapter 2 explores cell-specific regulation of PGR5. Distinct energy requirements between M and BS cells raise the possibility that regulation of photoprotection is different between the two cell types. In this chapter I resolved cell-specific function of the two PGRL1 paralogs in grasses by combining phylogenetic analysis, structural modelling, and physiological characterisation of CRISPR-generated mutants. I demonstrate that the duplication of PGRL1 diversified the molecular control of photoprotection by selecting one paralog for speed, and the other for capacity to support PSI oxidation in grasses, thereby meeting the specialised needs of cell types in NADP-ME C_4 photosynthesis.

Chapter 3 investigates whether C_4 plants could provide novel insight into the mechanism of PGR5 function. In this chapter I address the three hypotheses laid out in section 10 concerning how PGR5 builds *pmf.* I quantified PSI donor and acceptor-side fluxes by combining dark-interval relaxation kinetics with DUAL KLAS-NIR deconvolution of P700, PC, and Fd redox signals, interpreted through a mass-action kinetic framework. I show that the loss of donor-side flux in the C_4 *pgr5* mutant suggests a loss of electron flux from Cyt*f* to PC during the first second of low light to high light transition, consistent with a role for PGR5 in regulating CEF.

Chapter 4 compares *S. viridis* lacking both PGRL1 paralogs with the *pgr5-1* mutant and explores how residual PGR5 facilitates acclimation of plants to fluctuating light. I find that even 6% of WT PGR5-levels are sufficient to facilitate adaptation of plants to fluctuating light through the upregulation of NDH complex, C_4 cycle enzymes and photorespiratory nitrogen reassimilation, allowing plants to partially mitigate the negative effects of a lack of PGR5 on photosynthesis and growth under fluctuating light.

Chapter 2: PGRL1 paralogs provide distinct modes of photoprotection in C_4 photosynthesis

Statement of Contribution

This chapter is based on a manuscript prepared for publication, co-authored by Samuel J. Nix, Craig J. Morton, Russell Woodford, Robert T. Furbank and Maria Ermakova. It has not been accepted by any journal; an earlier version is available as a preprint on bioRxiv (https://doi.org/10.1101/2024.11.28.625945).

As first author, I designed the study, conducted the experiments, collected and analysed the data, and wrote the manuscript. Russell Woodford assisted with the spectroscopy experiments. Craig J. Morton performed the molecular dynamics simulations modelling PGRL1 folding within the membrane. My supervisors, Maria Ermakova and Robert T. Furbank, provided guidance throughout and contributed to writing and editing the manuscript.

Introduction

Light is essential for photosynthesis, and therefore for plant productivity, but an excess of absorbed light can over-reduce the chloroplast electron transport chain and damage the photosynthetic machinery. Plants have evolved multiple strategies, collectively known as photoprotection, that prevent over-reduction of the chloroplast electron transport chain and help to avoid damage of Photosystem I (PSI), which, unlike damage to Photosystem II (PSII), is very slow to repair (Tikkanen & Aro, 2014; Walker *et al.*, 2020). Trans-thylakoid proton motive force (*pmf*), and specifically the proton gradient (ΔpH) component of *pmf,* plays critical role in regulating photoprotection. *pmf* is established largely by the Cytochrome b_6f complex (Cytb_6f) which couples electron transport with shuttling protons from the chloroplast stroma to the thylakoid lumen. While *pmf* is essential for powering ATP synthase activity to generate ATP, when proton influx exceeds efflux from the lumen, lumen acidification below pH 6 triggers two key mechanisms of photoprotection: energy-dependent non-photochemical quenching (qE) and photosynthetic control (Kramer *et al.*, 1999). qE dissipates excess absorbed light energy as heat in the Photosystem II (PSII) antennae, while photosynthetic control slows down Cytb_6f activity to restrict electron transfer to PSI (Li *et al.*, 2004; Degen & Johnson, 2024).

PROTON GRADIENT REGULATION 5 (PGR5) and PROTON GRADIENT REGULATION 5-LIKE 1 (PGRL1) form a pathway essential for initiating pH-dependent photoprotection by building up *pmf*. Plants lacking either PGR5 or PGRL1 suffer severe PSI damage under

fluctuating light as a result of diminished ability to establish *pmf*, qE and photosynthetic control (Munekage *et al.*, 2002; Suorsa *et al.*, 2012; Yamori *et al.*, 2016; Woodford *et al.*, 2025b). Molecular studies suggest that transmembrane PGRL1 and soluble PGR5 form a heterodimer complex (DalCorso *et al.*, 2008; Hertle *et al.*, 2013). PGR5 appears to regulate electron transport while PGRL1 mainly acts as a gatekeeper of PGR5 function and prevents PGR5's degradation by PGRL2 (Rühle *et al.*, 2021; Chaturvedi *et al.*, 2024). In the dark, PGRL1 is dimerised via a disulphide bond between conserved stromal cysteines which keeps PGR5 inactive, while the reduction of the PGRL1's disulphide bond by Thioredoxin *m*4 (Trxm4) under light is proposed to activate PGR5 (Hertle *et al.*, 2013; Okegawa & Motohashi, 2020; Chaturvedi *et al.*, 2024). Although mechanistic details remain unresolved, the PGR5-PGRL1 pathway is proposed to build up *pmf* by facilitating cyclic electron flow (CEF) around PSI, i.e. directing electrons from Ferredoxin back to Cytb_6f (Munekage *et al.*, 2002; Joliot & Johnson, 2011).

In contrast to most dicots where PGRL1 is encoded by a single gene, some grasses were reported to contain two *PGRL1* homologs (Zhang, T *et al.*, 2024). It is also noted that transcripts of one of these homologs appear to be more abundant in bundle sheath (BS) cells compared to mesophyll (M) cells in *Zea mays* (maize), *Sorghum bicolor* (sorghum), and *Setaria viridis* – grasses that employ NADP-ME subtype of C_4 photosynthesis (Wu & Guo, 2023). C_4 photosynthesis provides a strong advantage over the conventional C_3 photosynthesis in low CO_2, high temperature and dry environments (Sage *et al.*, 2011). This is achieved through operation of the C_4 metabolic cycle across M and BS cells which increases CO_2 partial pressure in BS cells where the main CO_2 fixing enzyme, ribulose-1,5-bisphosphate carboxylase/oxygenase (Rubisco), resides (Hatch, 1987; von Caemmerer & Furbank, 2003). Most agronomically critical C_4 grasses belong to the NADP-ME subtype, predominantly relying on $NADP^+$-dependent malic enzyme for decarboxylation, but two other subtypes, NAD-ME and PCK, as well as combinations of subtypes also exist (Furbank, 2011; Ermakova *et al.*, 2026). A distinct feature of NADP-ME plants is that decarboxylation of malate, produced in M cells with the use of NADPH, generates NADPH in BS chloroplasts. This means that while M chloroplasts require both PSII and PSI, BS chloroplasts have lower PSII activity and mostly rely on PSI (Chapman *et al.*, 1980; Ermakova *et al.*, 2021b).

Here we integrated phylogenetics, structural modelling, cell-specific expression data, and physiological analysis of gene-edited *S. viridis* to identify the roles of the two PGRL1 paralogs. We demonstrate that while functions of PGRL1 paralogs largely overlap, they show unique properties regarding the speed and capacity of PSI oxidation during light stress. Our results suggest that PGRL1 duplication provided an evolutionary opportunity to diversify molecular control of photoprotection and allow for dynamic range of protective responses to

environmental stresses. Employing the two paralogs in cell-specific manner in NADP-ME C_4 photosynthesis conceivably contributed to the broader suite of adaptations of NADP-ME species for growing in high-stress environments.

Materials & Methods

Phylogenetic analysis

All phylogenetic analyses were performed in Geneious Prime (Geneious, 2024). *PGRL1* sequences were obtained from the Phytozome (Goodstein *et al.*, 2011), Gramene (Tello-Ruiz *et al.*, 2022), and CoGe (Lyons & Freeling, 2008) databases. Grass species were selected based on availability of a complete genome assembly and an RNA-seq based transcriptome annotation. *PGRL1* genes were identified using a predicted-protein search. For the phylogenetic tree, coding sequences (CDS) corresponding to the mature protein were utilised. First, peptide sequences were processed using TargetP 2.0 (Almagro Armenteros *et al.*, 2019) to predict chloroplast transit peptides. Mature protein regions were then mapped back to their corresponding CDS. Gene IDs can be found in Table S1.

Protein alignment was conducted using MUSCLE 5.1 with default settings (Edgar, 2022). Multiple sequence alignment of CDS was carried out using the MAFFT v7.490 algorithm (Katoh *et al.*, 2002; Katoh & Standley, 2013) with the BLOSUM62 scoring matrix, a gap open penalty of 1.53, and an offset value of 0.123. The phylogenetic tree was generated using RAxML v8.2.11 (Stamatakis, 2014) based on the MAFFT alignment, with the following parameters: Nucleotide Model: GTR CAT, Algorithm: Rapid Bootstrapping and search for best-scoring ML tree, Number of starting trees: 100, Parsimony random seed: 1. The resulting RaxML bootstrapped tree was finalised and annotated in iTOL (Letunic & Bork, 2021).

PGRL1 expression analyses

Expression of *PGRL1s* and corresponding proteins in *Z. mays*, *S. bicolor*, *S. viridis, Panicum virgatum* and *Oryza sativa* was examined by investigating publicly available RNA-seq (John *et al.*, 2014; Döring *et al.*, 2016; Rao *et al.*, 2016; Denton *et al.*, 2017; Hua *et al.*, 2021; Borba *et al.*, 2023), Ribo-seq (Chotewutmontri & Barkan, 2021), and proteomics (Friso *et al.*, 2010) datasets. Data were manually extracted from supplementary files, and the $\log_2$ of the ratio between *PGRL1α* and *PGRL1β* transcript abundances (*PGRL1α*/*PGRL1β*) or corresponding protein abundances were derived to facilitate comparison between different datasets. Detailed methods on tissue enrichment, RNA extraction and sequencing, and data processing are provided in original publications.

Plant growth conditions

S. viridis plants were germinated on rooting medium as described in Osborn *et al.* (2016), then transferred to soil in 0.5 L pots with seed-raising mix and 5 g L^{-1} of slow-release Osmocote fertiliser (Scotts, Australia). Plants were grown in a chamber with ambient CO_2, temperatures of 28°C (day) and 22°C (night), and 60% humidity, and either a constant light regime (380

μmol m^{-2} s^{-1}, 16 h photoperiod) or a fluctuating light regime. The fluctuating light regime involved a cycle of 5 minutes at 250 μmol m^{-2} s^{-1} followed by 1 minute at 1000 μmol m^{-2} s^{-1} (6-minute cycle), repeating for an entire 16 h photoperiod and giving a total integrated irradiance of 375 μmol m^{-2} s^{-1}. All measurements and analyses were performed on the youngest fully expanded leaves of three-to-four-week-old plants.

Mass spectrometry analyses

To obtain tissue-specific enriched protein fractions from WT *S. viridis*, M-enriched proteins were isolated via the leaf rolling method (Furbank *et al.*, 1985), and BS strands were obtained by differential grinding (Furbank & Badger, 1983), followed by homogenisation with mortar and pestle to extract proteins as described in Ermakova *et al.* (2019). Protein extracts were digested with trypsin following the filter-aided sample preparation protocol (Wiśniewski *et al.*, 2009). Briefly, 10 μg of protein in each sample was suspended in lysis buffer [50 mM tris(hydroxymethyl)aminomethane (Tris), 25 mM NaCl, 20 mM Ethylenediaminetetraacetic acid (EDTA), 1% sodium dodecyl sulfate (SDS), 5 mM dithiothreitol (DTT)], heated to 95°C for 5 minutes, sonicated, and centrifuged at 16,000 g for 5 minutes. Lysate was loaded onto a Amicon Ultra-0.5 Centrifugal Filter (Millipore) with 20 μL of urea buffer (8 M urea, 50 mM ammonium bicarbonate) to retain the total protein. Vacuum was applied to facilitate buffer elution from the columns. Following an initial wash, 15 μL of chloroacetamide was added to the urea buffer, and three additional washes with urea buffer (without chloroacetamide) were performed. Proteins were digested on the filter with 120 μL of 50 mM ammonium bicarbonate and 5 μL of 400 ng μL^{-1} trypsin for 8 h at 37°C. Digested peptides were collected with 50 μL of water. Peptides were then dried using a speed vac, resuspended in 0.1% formic acid, and sonicated. Samples were loaded onto an Orbitrap Fusion Mass Spectrometer (Thermo Fisher Scientific, Waltham, Massachusetts, USA). Data were analysed using MaxQuant software (Cox & Mann, 2008), and relative protein abundances were calculated using the iBAQ method (Schwanhäusser *et al.*, 2011). For each replicate, iBAQ values were normalised by dividing each protein's iBAQ value by the total iBAQ sum in that replicate. Minimal contamination of tissue-enriched fractions was identified using malic enzyme and phosphoenolpyruvate carboxylase as signature proteins for BS and MS cells respectively.

CRISPR-Cas9 mutant generation

S. viridis cv. ME034V-1 plants with null *pgrl1α* and *pgrl1β* alleles were created using CRISPR/Cas9 gene-editing as described in Ermakova *et al.* (2024b). The genomic and coding sequences of *S. viridis* PGRL1α and PGRL1β were obtained from Phytozome and can be found in Supplemental Table 1. Cas9 was targeted to the first exons of each gene using gRNAs selected with CRISPOR (Concordet & Haeussler, 2018) and assembled into a synthetic

polycistronic gene according to Xie *et al.* (2015). The Golden Gate cloning system (Engler *et al.*, 2014) was used to assemble the construct which was transformed into *S. viridis* using *Agrobacterium tumefaciens* strain AGL1 (Osborn *et al.*, 2016). Editing of the target genes was confirmed by sequencing in T_1 plants and the progenies of plants lacking T-DNA with homozygous null alleles were used in all experiments. Multiple independent null alleles for both *pgrl1α* and *pgrl1β* were obtained and verified by sequencing and proteomics.

Leaf spectroscopic and fluorescence analyses

To measure light responses of PSI and PSII quantum yields, simultaneous measurements of chlorophyll fluorescence and P700 redox spectroscopy were performed using a DUAL-PAM/F (Heinz Walz, Effeltrich, Germany) under 635 nm red actinic light with red light saturating pulses (300 ms, 12,000 µmol m^{-2} s^{-1}). P700 redox state was assessed by detecting absorbance of the $P700^+$ at 830 nm with a dual wavelength unit (830/875 nm). Leaves were dark-adapted for 30 min before applying a saturating pulse to determine the maximum (F_M) and minimum (F_0) levels of fluorescence. The maximum quantum yield of PSII (F_V/F_M) was calculated as (F_M - F_0) / F_M. Following this, the maximal $P700^+$ signal (P_M) was recorded by applying a saturating pulse at the end of an 8-s far-red light (720 nm) illumination, with the minimal $P700^+$ signal (P_0) recorded directly following the saturating pulse. After determining dark-adapted parameters, leaves were light-acclimated to 300 µmol m^{-2} s^{-1} for 15 minutes.

Light response curves were recorded by progressively increasing the actinic light from 0 to 2,000 µmol m^{-2} s^{-1} and applying a saturating pulse at the end of every 120-s illumination period. Upon the application of each saturating pulse, F_M' (the maximum level of fluorescence under light) and F (the fluorescence level before the application of a saturating pulse) were recorded. This enabled the monitoring of the partitioning of absorbed light energy within PSII between the photochemical [$\varphi_{II} = (F_M' - F) / F_M'$] and non-photochemical reactions, including the regulated [$\varphi_{NPQ} = (F/F_M' - F/ F_M)$] and non-regulated ($\varphi_{NO} = F / F_M$) fractions (Kramer *et al.*, 2004). The photochemical yield of PSI [$\varphi_I = (P_M' - P) / (P_M - P_0)$], the non-photochemical yield of PSI due to acceptor side limitation [$\varphi_{NA} = (P_M - P_M') / (P_M - P_0)$] and the non-photochemical yield of PSI due to donor side limitation [$\varphi_{ND} = (P - P_0) / (P_M - P_0)$] were calculated as described in Klughammer and Schreiber (2008c).

PSI and PSII quantum yields during the photosynthetic induction were monitored simultaneously using a Dual KLAS-NIR (Heinz Walz, Effeltrich, Germany) under a 635 nm red actinic light with saturating pulses of red light (300 ms, 12,000 µmol m^{-2} s^{-1}). Leaves were dark-adapted for 30 minutes before determining F_V/F_M and P_M. After that, leaves were shifted to high light (1,500 µmol m^{-2} s^{-1}) for 2 minutes, with saturating pulses applied at 10, 30, 60, 90, and 120 s and quantum yields of PSI and PSII calculated as described earlier. To obtain

parameters describing the kinetics of P700 oxidation, $P700^+$ absorbance traces were baseline corrected to 0 and normalised for P_M for each sample. The midpoint (x_0) and slope factor (dx) derived from Boltzmann fits of P700 oxidation kinetics were determined using OriginPro (OriginLab, Northampton, MA).

Plant phenotyping

Rapid phenotyping was performed using MultispeQ V2.0 (PhotosynQ, East Lansing, MI, USA) and the standard Photosynthesis RIDES 2.0 protocol which determines photosynthetic parameters at the incident irradiance (Kuhlgert et al., 2016). MultispeQ measurements were made under ambient conditions on plants grown under either a constant or fluctuating light environment. For fluctuating light, measurements were performed during the low irradiance periods. Digital plant biomass and leaf area was estimated using a PlantEye F600 Multispectral 3D scanner (Phenospex, Heerlen, Netherlands). Whole-plant imaging was performed on four-week-old plants to generate 3D point clouds, with digital biomass then calculated using voxel-based reconstructions.

Gas-exchange analysis

Gas-exchange analysis was performed using the portable gas-exchange system LI-6800 (LICOR, Lincoln, Nebraska USA) equipped with a 6800-01A fluorometer head. For all measurements 90% red/10% blue actinic light was used with 25°C leaf temperature, 55% relative chamber humidity, flow rate of 500 µmol s^{-1}, flow pressure of 0.1 kPa and fan speed of 10,000 RPM. For CO_2 response curves, leaves were clamped into the chamber and equilibrated at 400 µmol mol^{-1} CO_2 on the reference side and 1,000 µmol m^{-2} s^{-1} for 15 minutes. CO_2 assimilation rates were then recorded at CO_2 partial pressures from 0 to 1600 µmol mol^{-1} at 3-minute intervals. For light response curves, leaves were equilibrated at 400 µmol mol^{-1} CO_2 and 1,000 µmol m^{-2} s^{-1} irradiance for 15 minutes. CO_2 assimilation was then recorded with irradiance progressively increasing from 0 to 3000 µmol m^{-2} s^{-1} at 3-minute intervals. CO_2 and light response curves were fit using the biochemical model of C_4 photosynthesis parameterised for *S. viridis* (von Caemmerer, 2021; Woodford *et al.*, 2025a).

Protein modelling

Protein structures of monomers and complexes were built using the AlphaFold3 web server (Abramson *et al.*, 2024). PGR5-PGRL1 heterodimer-dimer structures were modelled using the mature sequences for PGR5, PGRL1α and PGRL1β from *S. viridis* (Gene/Protein IDs found in Table S1) with a single Fe^{2+} ion per PGRL1 monomer and 50 palmitic acid molecules to provide a pseudo-membrane during structure prediction. Specific models were chosen for analysis from the AlphaFold3 output structures based on their pTM and ipTM scores. Model

protein structures were embedded in a DOPC bilayer model as a proxy for a thylakoid membrane using the CHARMM-GUI server and membrane builder (Jo *et al.*, 2008; Wu *et al.*, 2014) and the OPM server (Lomize *et al.*, 2011) to orient the protein with respect to the modelled membrane. Protein-membrane complexes were energy minimised in NAMD (Phillips *et al.*, 2020) and inspected using PyMOL (Schrodinger, 2015).

Results

PGRL1 paralogs diverged after genome duplication early in grasses evolution

To resolve the evolutionary history of PGRL1, we aligned *PGRL1* sequences from publicly available annotated genomes across the grass family, as well as selected monocot and dicot outgroups. The phylogenetic tree of *PGRL1* genes showed two distinct clades within the grass family which were designated as *PGRL1α* and *PGRL1β* (Fig. 1). *PGRL1β* was absent in monocot outgroups *Musa acuminata* and *Joinvillea ascendens*, as well as in eudicot outgroups *A. thaliana*, *Flaveria trinervia*, and *Artemisia annua* (Fig. 1). This indicates that functionally redundant *PGRL1A* and *PGRL1B* in *A. thaliana* both belong to the *PGRL1α* group. *Streptochaeta angustifolia,* which diverged from the main branch of grasses before the evolution of *Pharus latifolius* (Seetharam *et al.*, 2021), also had only *PGRL1α* (Fig. S1). However, *PGRL1β* was present in Pharus, PACMAD, and BOP clades suggesting that *PGRL1β* emerged in the common ancestor of *P. latifolius* and the PACMAD and BOP clades, corresponding with a hypothesised whole-genome duplication event around 98 MYA (Ma *et al.*, 2021).

Among the 34 grass species examined, 24 species had at least one copy of both *PGRL1α* and *PGRL1β* (Fig. 1). In some species, multiple copies of *PGRL1α* or *PGRL1β* were observed, correlating with their genome architecture; for example, three copies of *PGRL1β* in *T. aestivum*, consistent with hexaploidy. However, no *PGRL1α* was found in 11 species and no *PGRL1β* in three species (Fig. 1, Table S1). Subsequent analysis suggested that *PGRL1α* in grasses was lost or rendered non-functional at least six times independently through random mutations in *Urochloa fusca*, *Oropetium thomaeum*, *Leersia perrieri*, *Raddia guianensis*, *Bonia amplexicaulis*, and Triticeae species (Fig. S2a). Potential *PGRL1β* loss-of-function mutations were observed in two woody bamboos (Fig. S3) and *Lolium perrene*, all of which lost functional transit peptides.

Next, we aligned the mature amino acid sequences (lacking chloroplast signal peptide) of PGRL1α and PGRL1β from 39 grass species (Fig. 1). Alignments yielded a pairwise positive BLSM62 score of 89%, with most variation due to single amino acid substitutions scattered across the sequence. However, a short region, previously shown to be exposed to the

thylakoid lumen (DalCorso *et al.*, 2008; Hertle *et al.*, 2013), was consistently different between paralogs (Fig. 1). For PGRL1α this sequence was TYLLE, while for PGRL1β it was NVFQ. Further alignments of PGRL1α sequences from *S. viridis, A. thaliana*, *M. acuminata*, *F. trinerva*, *A. annua*, *Selaginella moellendorfii*, and *Chlamydomonas reinhardtii* showed that the TYLLE sequence was conserved as far back evolutionary as the lycophyte *S. moellendorffii*, with the green alga *C. reinhardtii* also having a similar sequence, TKLVE (Fig. S4). In contrast, the NVFQ sequence of PGRL1β was exclusive to grasses.

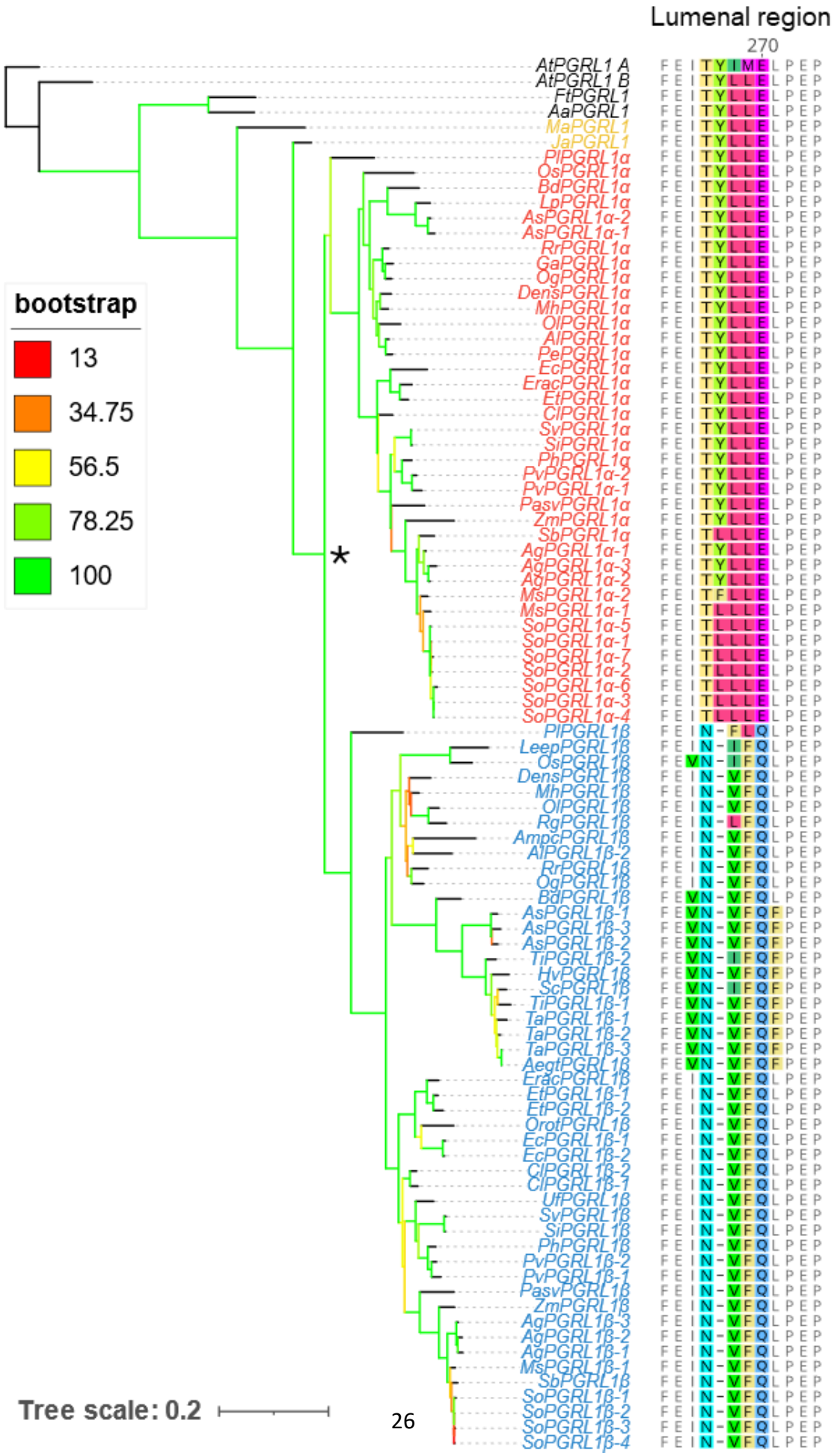
Lumenal region
270
bootstrap
13
34.75
56.5
78.25
100
AtPGRL1 A
AtPGRL1 B
FtPGRL1
AaPGRL1
MaPGRL1
JaPGRL1
PlPGRL1α
OsPGRL1α
BdPGRL1α
LpPGRL1α
AsPGRL1α-2
AsPGRL1α-1
RrPGRL1α
GaPGRL1α
OgPGRL1α
DensPGRL1α
MhPGRL1α
OlPGRL1α
AlPGRL1α
PePGRL1α
EcPGRL1α
EracPGRL1α
EtPGRL1α
ClPGRL1α
SvPGRL1α
SiPGRL1α
PhPGRL1α
PvPGRL1α-2
PvPGRL1α-1
PasvPGRL1α
ZmPGRL1α
SbPGRL1α
AgPGRL1α-1
AgPGRL1α-3
AgPGRL1α-2
MsPGRL1α-2
MsPGRL1α-1
SoPGRL1α-5
SoPGRL1α-1
SoPGRL1α-7
SoPGRL1α-2
SoPGRL1α-6
SoPGRL1α-3
SoPGRL1α-4
PlPGRL1β
LeepPGRL1β
OsPGRL1β
DensPGRL1β
MhPGRL1β
OlPGRL1β
RgPGRL1β
AmpcPGRL1β
AlPGRL1β-2
RrPGRL1β
OgPGRL1β
BdPGRL1β
AsPGRL1β-1
AsPGRL1β-3
AsPGRL1β-2
TiPGRL1β-2
HvPGRL1β
ScPGRL1β
TiPGRL1β-1
TaPGRL1β-1
TaPGRL1β-2
TaPGRL1β-3
AegtPGRL1β
EracPGRL1β
EtPGRL1β-1
EtPGRL1β-2
OrotPGRL1β
EcPGRL1β-1
EcPGRL1β-2
ClPGRL1β-2
ClPGRL1β-1
UfPGRL1β
SvPGRL1β
SiPGRL1β
PhPGRL1β
PvPGRL1β-2
PvPGRL1β-1
PasvPGRL1β
ZmPGRL1β
AgPGRL1β-3
AgPGRL1β-2
AgPGRL1β-1
MsPGRL1β-1
SbPGRL1β
SoPGRL1β-1
SoPGRL1β-2
SoPGRL1β-3
SoPGRL1β-4
Tree scale: 0.2

Fig. 1. Sequence analysis of PGRL1 homologs from grasses and other plant lineages. Phylogenetic tree of *PGRL1* generated through maximum-likelihood analysis based on the coding sequences of the mature proteins. The tree is rooted with *AtPGRL1A*. Bootstrap support values are indicated by the colour gradient as per the legend. The names of the *PGRL1* genes from eudicots are in black, *PGRL1* genes from non-grass monocots in orange, *PGRL1α* from grasses in red and *PGRL1β* from grasses in blue. The asterisk marks the point of divergence between *PGRL1α* and *PGRL1β*. In the alignment of the lumenal regions, highlighted residues indicate sequence divergence among homologs. Additional copies of PGRL1 within a species are suffixed as -1, -2, etc, which were assigned arbitrarily. Aa, *Artesia annua*; Aegt, *Aegilops tauschii*; Ag, *Andropogon gerardii*; Al, *Ampelocalamus luodinaensis*; Ampc, *Ampelocalamus calcareus*; As, *Avena sativa*; At, *Arabidopsis thaliana*; Ba, *Bonia amplexicaulis*; Bd, *Brachypodium distachyon*; Cl, *Chasmanthium laxum*; Dens, *Dendrocalamus sinicus*; Ec, *Eleusine coracana*; Erac, *Eragrostis curvula*; Et, *Eragrostis tef*; Ft, *Flaveria trinerva*; Ga, *Guadua angustifolia*; Hv, *Hordeum vulgare*; Ja, *Joinvillea ascendens*; Leep, *Leersia perrieri*; Lp, *Lolium perenne*; Ma, *Musa acuminata*; Mh, *Melocanna humilis*; Ms, *Miscanthus sinensis*; Og, *Otatea glauca*; Ol, *Olyra latifolia*; Os, *Oryza sativa*; Ot, *Oropetium thomaeum*; Pasv, *Paspalum vaginatum*; Pe, *Phyllostachys edulis*; Ph, *Panicum hallii*; Pl, *Pharus latifolius*; Pv, *Panicum virgatum*; Rg, *Raddia guianensis*; Rr, *Rhipidocladum racemiflorum*; Sb, *Sorghum bicolor*; Sc, *Secale cereale*; Si, *Setaria italica*; So, *Saccharum officinarum*; Sv, *Setaria viridis*; Ta, *Triticum aestivum*; Ti, *Thinopyrum intermedium*; Uf, *Urochloa fusca*; Zm, *Zea mays*.

PGRL1α and *PGRL1β* have distinct expression patterns

To gain insight into the functional differences between *PGRL1α* and *PGRL1β*, we performed a meta-analysis of available RNA-seq datasets of M and BS tissue-enriched fractions from *Oryza sativa* (rice, C_3), *Panicum virgatum* (NAD-ME C_4), *Z. mays*, *S. bicolor*, and *S. viridis* (NADP-ME C_4) (John *et al.*, 2014; Döring *et al.*, 2016; Rao *et al.*, 2016; Denton *et al.*, 2017; Chotewutmontri & Barkan, 2021; Hua *et al.*, 2021). The $\log_2$ of the ratio between *PGRL1α* and *PGRL1β* transcript abundances (*PGRL1α*/*PGRL1β*) or corresponding protein abundances were derived to facilitate comparison between different datasets, with negative values indicating prevalent *PGRL1β* and positive values – *PGRL1α* (Fig. 2a). In *O. sativa* and *P. virgatum*, transcript abundance of *PGRL1β* was greater than *PGRL1α* in both M and BS cells (*O. sativa* M: -1.78, BS: -1.69; *P. virgatum* M: -3.06, BS: -2.80). Interestingly, in all studied NADP-ME grasses, of which *S. viridis* has independently evolved C_4 photosynthesis (Sage *et al.*, 2011), *PGRL1α* was preferentially expressed in M cells, while *PGRL1β* in BS cells (Fig. 2a). *S. bicolor* had the most cell-preferential expression (M: 3.39, BS: -6.30) while *S. viridis* had the least (M: 0.59, BS: -1.63). Transcript abundance of *PGR5* did not differ between M and BS cells in *S. virids*, *Z. mays*, or *S. bicolor* (John *et al.*, 2014; Döring *et al.*, 2016; Denton *et al.*, 2017).

Analysis of cell-specific *Z. mays* Ribo-seq (Chotewutmontri & Barkan, 2021) also revealed cell-preferential translation of *PGRL1α* in M cells and *PGRL1β* in BS cells (M 3.59, BS -3.57).

Furthermore, *Z. mays PGRL1β* transcript has been reported to contain a CACGCAC motif in the 5'-untranslated region (UTR), proposed to upregulate BS-specific translation (Chotewutmontri & Barkan, 2021). In contrast, *Z. mays PGRL1α* has lost a 5'-UTR and likely requires 5'-UTR-independent mechanisms of translational regulation (Majeran & van Wijk, 2009; Hardy & Balcerowicz, 2024). Analysis of cell-specific *Z. mays* proteomics data (Majeran *et al.*, 2008) showed PGRL1α preferentially in M cells (0.82) and PGRL1β preferentially in BS cells (-3.78). Our own mass spectrometry analysis of M and BS cell-enriched fractions from *S. viridis* found PGRL1α dominant in M cells (0.62) and PGRL1β dominant in BS cells (-0.79) (Fig. 2a).

Analysis of publicly available *O. sativa* microarray data (Sato *et al.*, 2011; Sato *et al.*, 2012) revealed a strong diurnal expression pattern of *PGRL1β* but not *PGRL1α* (Fig. 2b). *PGRL1α* was the dominant transcript in the morning and evening while *PGRL1β* was the dominant transcript at midday. Diurnal expression patterns of *PGRL1α* and *PGRL1β* were also distinct in *Z. mays* (Borba *et al.*, 2023) (Fig. 2c). In M cells, *PGRL1α* expression was the lowest at 6 h of illumination and reached the peak at 14 h. In contrast, *PGRL1β* expression in BS cells was at its lowest during the dark period and peaked at 10 h of illumination. Expression of *PGRL1β* in M cells and *PGRL1α* in BS cells in *Z. mays* was consistently low, while PGR5 showed the same diurnal pattern in M and BS cells with a peak at 6 h, though was more abundant in M cells (Fig. 2c).

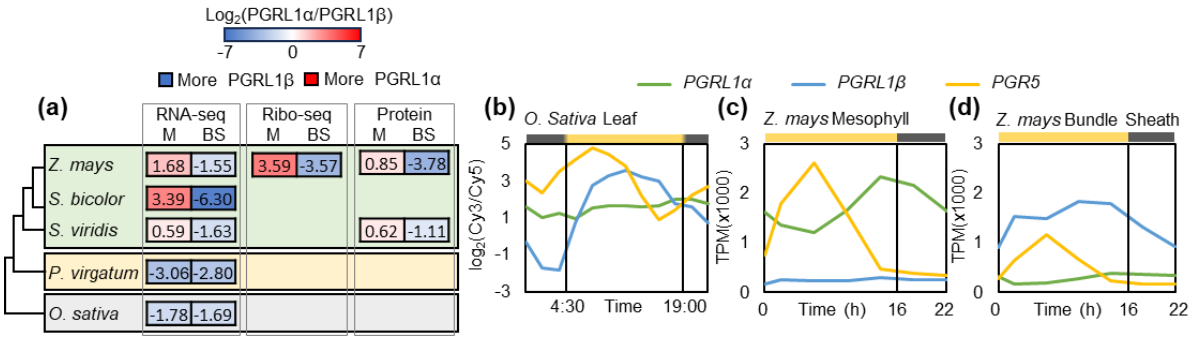

Fig. 2. Expression analysis of *PGRL1α* and *PGRL1β* paralogs in grasses. (**a**) Tissue-specific levels of transcription, translation, and protein abundance in *Zea mays*, *Sorghum bicolor*, *Setaria viridis, Panicum virgatum,* and *Oryza sativa*. Species are organised by the photosynthetic pathway: NADP-ME C_4 (green), NAD-ME (yellow), or C_3 (grey). Expression data are shown as the $\log_2$ of the *PGRL1α*/*PGRL1β* ratio for transcript (or corresponding protein) abundances. Positive values indicate greater *PGRL1α* abundance (red) and negative values indicate greater *PGRL1β* abundance (blue). Transcriptional and translational data are sourced from RNA-seq and Ribo-seq datasets (John *et al.*, 2014; Love *et al.*, 2014; Döring *et al.*, 2016; Rao *et al.*, 2016; Denton *et al.*, 2017; Chotewutmontri & Barkan, 2021; Hua *et al.*, 2021), protein abundances for *Z. mays* are from Majeran *et al.* (2008); values for *S. viridis* were identified in this study. (**b**) Diurnal expression patterns of *PGRL1α*, *PGRL1β*, and *PGR5* in *O. sativa* obtained from the microarray dataset of (Sato *et al.*, 2011; Sato *et al.*, 2012).

Expression levels are shown as log_2 of the Cy3/Cy5 ratios with local sunrise and sunset times indicated. (**c, d**) Diurnal expression of *PGRL1α*, *PGRL1β*, and *PGR5* in mesophyll and bundle sheath enriched fractions of *Z. mays* obtained from the RNA-seq dataset of Borba *et al.* (2023). *PGR5* values shown for *Z. mays* are the sum of the two *PGR5* genes in *Z. mays* genome. TPM, transcripts per million. Light and dark phases are denoted by yellow and grey bars.

PGRL1α is required for PSI oxidation at high light

To investigate specific roles of PGRL1 paralogs, we generated null mutants (hereafter, *pgrl1α* and *pgrl1β)* of *S. viridis* using CRISPR-Cas9. Two null alleles were generated for each gene (*pgrl1α-3*, *pgrl1α-10, pgrl1β-1,* and *pgrl1β-13*) and plants homozygous for each null allele were confirmed by sequencing (Fig. S5). Mass spectrometry analysis confirmed the absence of targeted paralogs in the mutants and showed that mutants appear to compensate for the loss of one paralog with the remaining PGRL1 paralog in both cell types (Fig. 3.) The two null alleles for each paralog exhibited no detectable phenotypic differences in either experiment; therefore, one representative line is shown hereafter.

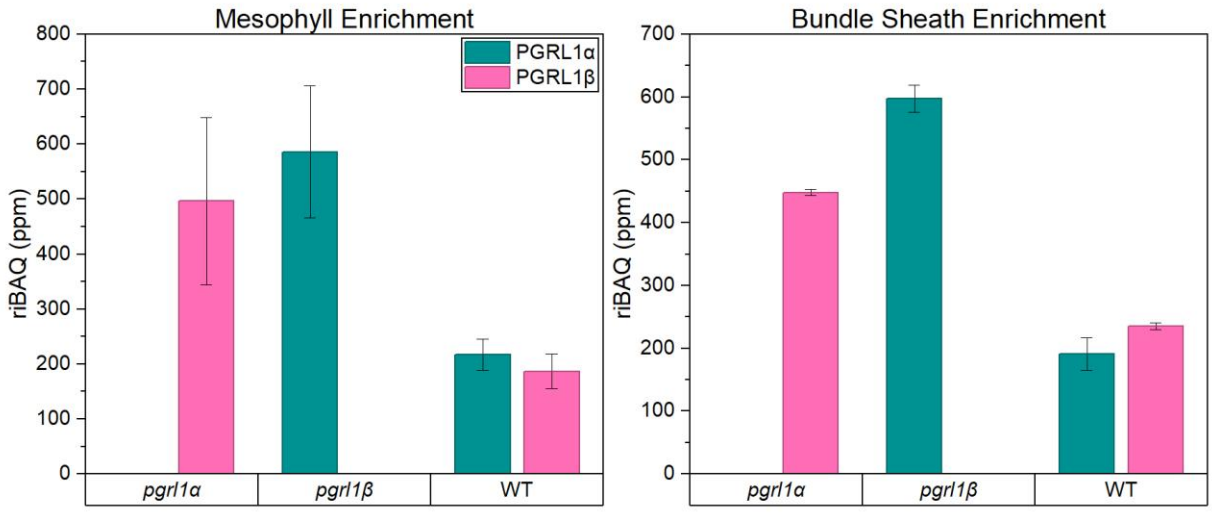

Fig. 3. Relative iBAQ (riBAQ) values for protein abundances of PGRL1 paralogs in the mesophyll-enriched (left) or bundle sheath-enriched (right) fractions from *S. viridis* wild type (WT), *pgrl1α* and *pgrl1β* mutants quantified by mass spectrometry. Mean ± SD, *n* = 2-3 biological replicates.

Overall, growth and photosynthesis of the mutants in optimal conditions under constant daylight were not affected (Fig. 4). No differences in CO_2 assimilation rates or *pmf* were found between genotypes across varying CO_2 partial pressures or irradiances. Fitting of the gas-exchange curves also showed no differences in biochemistry of photosynthesis (Table S2). Analysis of chlorophyll fluorescence showed no differences in photochemical and non-photochemical reactions within PSII at different irradiances between genotypes (Fig. S6). P700 (reaction centre of PSI) redox spectroscopy analysis showed that the quantum yield of photochemical reactions in PSI (φ_I) was similar between all genotypes at all irradiances (Fig.

4g). However, *pgrl1α* had a lower quantum yield of non-photochemical reactions within PSI due to donor side limitation (φ_{ND}), *i.e.* the more reduced PSI, above 800 µmol photons m^{-2} s^{-1}, compared to WT (Fig. 4h). At irradiances above 1300 µmol photons m^{-2} s^{-1}, *pgrl1α* also had significantly higher quantum yield of non-photochemical reactions within PSI due to acceptor side limitation (φ_{NA}) than WT (Fig. 4i).

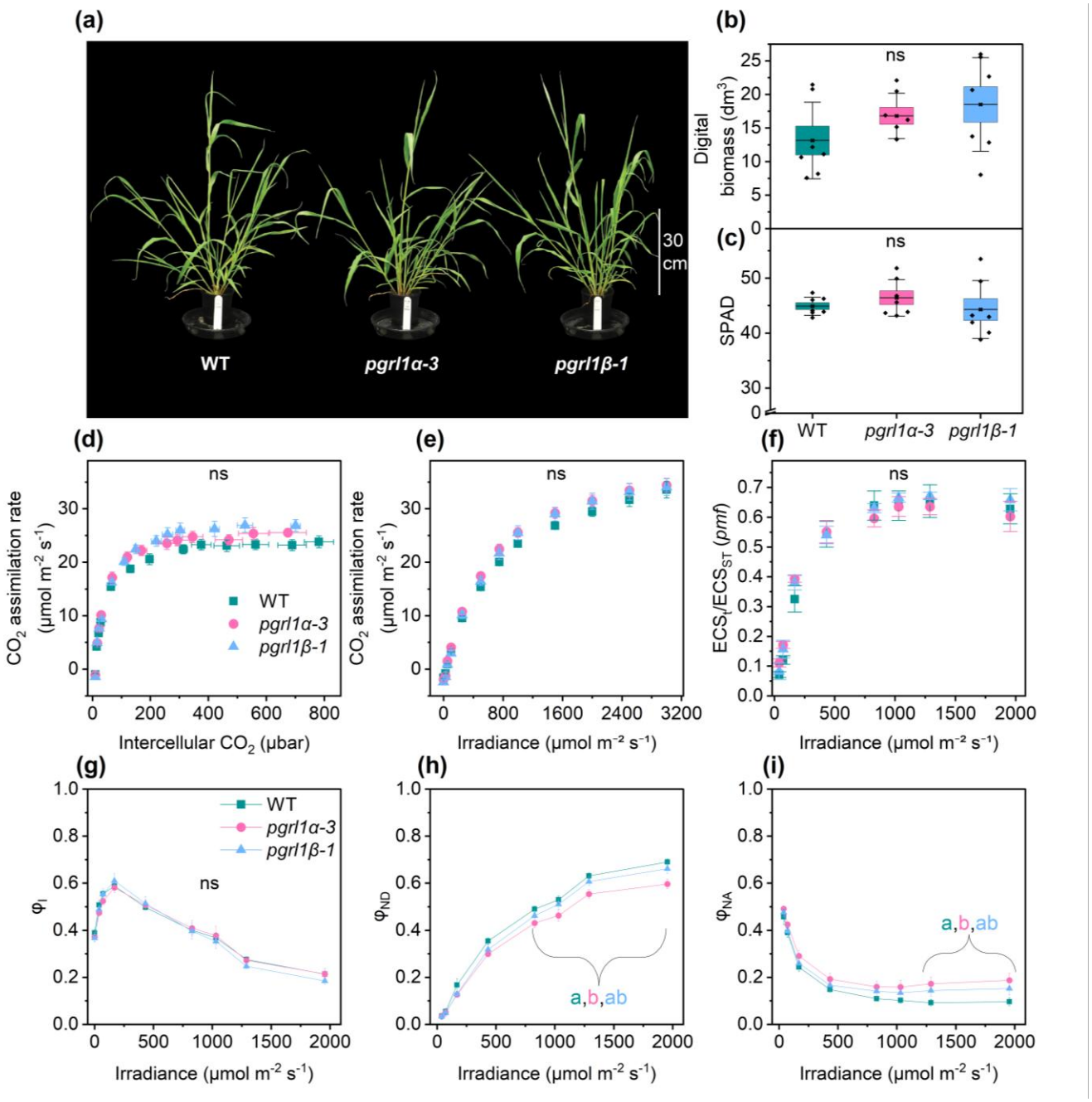

Fig. 4. Growth and photosynthesis of *S. viridis* wild-type (WT), *pgrl1α* and *pgrl1β* mutants grown under constant daylight (380 µmol m^{-2} s^{-1}). (**a**) Growth phenotype, (**b**)

Digital biomass, and (**c**) Relative chlorophyll content of four-week-old plants. (**d–e**) Response of net CO_2 assimilation rate to the intercellular CO_2 partial pressure and irradiance. (**f**) Response of proton motive force (*pmf*) to irradiance. (**g**) Light response of the quantum yield of photochemical reactions in PSI (φ_I). (**h**) Light response of the non-photochemical yield of PSI due to donor side limitation (φ_{ND}). (**i**) Light response of the non-photochemical yield of PSI due to acceptor side limitation (φ_{NA}). (**b, c**) Mean ± SE, n = 7 biological replicates. Letters indicate significant differences between groups; ns, not significant (one-way ANOVA with Tukey's post hoc test at $P < 0.05$). (**d–f**) Mean ± SE, n = 5 biological replicates. Letters indicate significant differences between groups; ns, not significant (two-way repeated measures ANOVA with Tukey's post hoc test at $P < 0.05$). (**g–i**) Mean ± SE, n = 8 biological replicates. Letters indicate significant differences between groups; ns, not significant (two-way repeated measures ANOVA with Tukey's post hoc test at $P < 0.05$).

PGRL1β facilitates faster PSI photoprotection

Next, we studied the speed of photoprotection in *S. viridis* lacking PGRL1 paralogs. For this, we monitored leaf fluorescence and P700 redox state upon the shift of dark-adapted plants to 1,500 µmol photons m^{-2} s^{-1}, i.e. during the induction of photosynthesis (Fig. 5). The maximum quantum efficiency of PSII (F_V/F_M) did not differ between genotypes, and the yields of photochemical and non-photochemical reactions within PSII were similar between the genotypes at 10 s and 60 s of illumination (Fig. 5a-c). The maximum oxidisable P700 (P_M) was also similar between the genotypes but *pgrl1β* had higher φ_{NA} and lower φ_{ND} than both WT and *pgrl1α* at 10 s of illumination (Fig. 5d,e). After 60 s of illumination, PSI parameters were similar between all genotypes (Fig. 5f). Plotting the leaf $P700^+$ signals normalised for P_M showed slower P700 oxidation in *pgrl1β* (Fig. 5g), and boltzmann fitting of the curves revealed that P700 oxidation in *pgrl1β* was delayed for about 5 s compared to WT and *pgrl1α*, based on the lower midpoint parameter (x_0) (Fig. 5h). The slope factor (dx) did not differ between genotypes indicating that the rate of P700 oxidation was similar between genotypes (Fig. 5i).

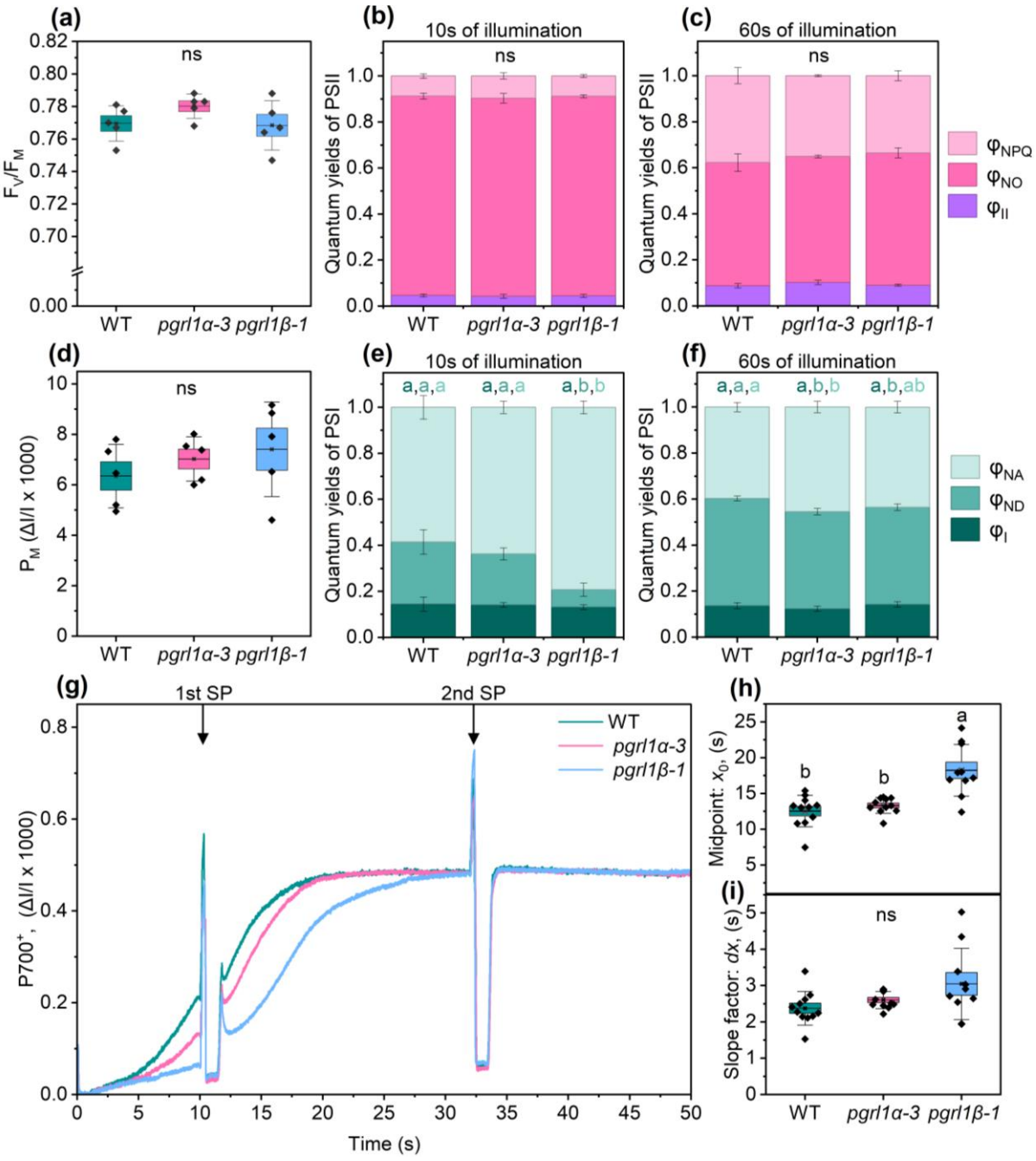

Fig. 5. Induction of photosynthesis in *S. viridis* wild type (WT), *pgrl1α*, and *pgrl1β* mutants following a shift from dark to high light (1,500 µmol m^{-2} s^{-1}). (**a**) Maximum Photosystem II (PSII) efficiency (F_V/F_M). (**b-c**) Partitioning of absorbed light energy within PSII between the effective quantum yield (φ_{II}), the yield of non-regulated non-photochemical reactions (φ_{NO}), and the yield of non-photochemical quenching (φ_{NPQ}) at 10 s (b) and 60 s (c) of the induction. (**d**) P_M, the maximal photo-oxidisable P700, the reaction centre of Photosystem I (PSI). (**e–f**) Partitioning of absorbed light energy within PSI between the photochemical reactions (φ_I), the non-photochemical reactions due to donor side limitation (φ_{ND}) and the non-photochemical reactions due to acceptor side limitation (φ_{NA}) at 10 s (e) and 60 s (f) of the induction. (**g**) $P700^+$ absorbance traces normalised by P_M, arrows indicate saturating pulses (SP) applied; average of 10 biological replicates. (**h-i**) The midpoint (x_0) and the slope factor (dx) derived from Boltzmann fits of curves in (g). (a, d) Boxes show mean, SE,

and SD. *n* = 5 biological replicates; letters indicate significant differences between groups; ns, not significant (one-way ANOVA with Tukey's post hoc test at $P < 0.05$). (b,c,e,f) Stacked bar graphs show Mean ± SE, *n* = 8 biological replicates; letters indicate significant differences between groups; ns, not significant (one-way ANOVA with Tukey's post hoc test at $P < 0.05$). (h, i) Boxes show mean, SE, and SD. *n* = 10 biological replicates; letters indicate significant differences between groups; ns, not significant (one-way ANOVA with Tukey's post hoc test at $P < 0.05$).

We also monitored the $P700^+$ signal in leaves adapted to low light of 300 µmol photons m^{-2} s^{-1} and then shifted to 1,500 µmol photons m^{-2} s^{-1} (Fig. 6a). Plotting the $P700^+$ signals normalised for P_M showed that, after 3 min at high irradiance, the $P700^+$ level in *pgrl1α* was lower compared to WT and *pgrl1β* (Fig. 6a), in line with the lower φ_{ND} at high light seen in the light curve analysis (Fig. 4h). Normalising the curves for the $P700^+$ level at low irradiance (0) and after 45 s at high irradiance (1) to facilitate comparison of the kinetics showed that *pgrl1β* had distinctly slower oxidation rate of PSI compared to WT and *pgrl1α* (Fig. 6b). Next, we tested whether the differences in speed and capacity of P700 oxidation affected growth of the mutants under fluctuating daylight (repeated cycles of 250 µmol photons m^{-2} s^{-1} for 5 min and 1,000 µmol photons m^{-2} s^{-1} for 1 min). No growth phenotype or difference in P_M was detected in those conditions across mutants and WT (Fig. 6c,d)

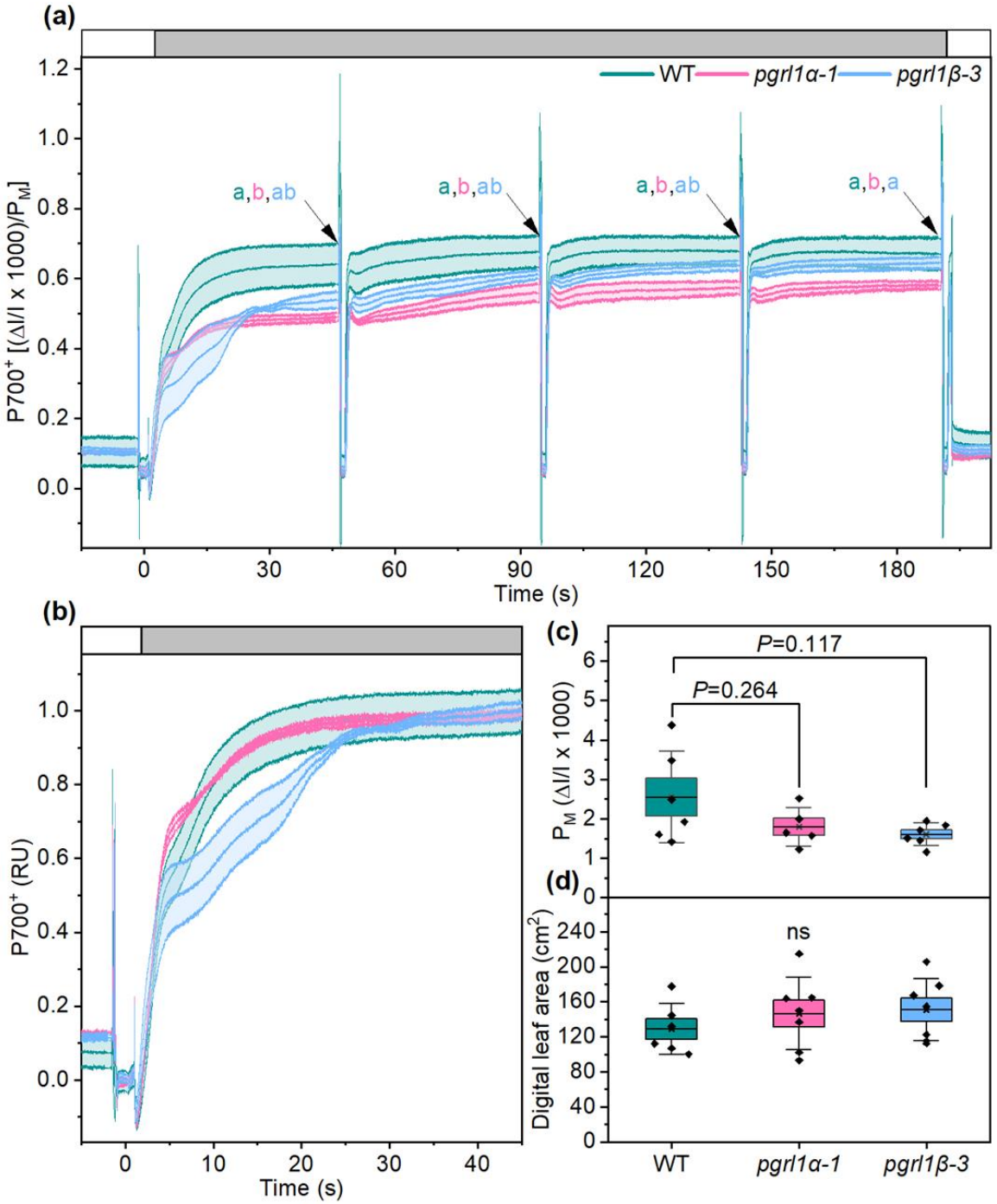

Fig. 6. Responses of *S. viridis* wild type (WT), *pgrl1α* and *pgrl1β* mutants to fluctuating light. (**a**) Leaf $P700^+$ signal normalised for P_M during a shift from low light (300 µmol m^{-2} s^{-1}, white bar on top) to high light (1,500 µmol m^{-2} s^{-1}, grey bar). Arrows indicate saturating pulses. Letters show significant differences between genotypes in φ_{ND}, the yield of non-photochemical reactions in PSI due to donor side limitation, at each SP (two-way repeated measures ANOVA with Tukey's post hoc test, n = 5 biological replicates, $P < 0.05$). (**b**) $P700^+$ induction kinetics from (a) after normalisation (0 = $P700^+$ level at low light; 1 = $P700^+$ at 45 seconds of high light). (**c**) P_M (maximal photo-oxidisable P700) measured from plants grown under fluctuating daylight (repeated cycles of 5 min at 250 µmol m^{-2} s^{-1} followed by 1 min at 1000 µmol m^{-2} s^{-1}, repeated over the photoperiod). (**d**) Digital leaf area of plants grown under fluctuating daylight.

Boxplots show mean, SE and SD; points indicate individual biological replicates (n = 7); ns, not significant (one-way ANOVA with Tukey's post hoc test at $P < 0.05$).

Protein models of PGRL1α and PGRL1β suggest structural basis for functional differences

To understand how PGRL1 paralogs provide distinct modes of photoprotection, we used AlphaFold3 to predict structures of the *S. viridis* PGRL1α and PGRL1β monomers (Fig. 7a). Consistent with prior experimental studies (DalCorso *et al.*, 2008; Hertle *et al.*, 2013), both paralogs had a transmembrane region and a large hydrophilic region on the stromal side. The Trxm4-sensitive cysteines responsible for PGRL1 dimerisation, and a rubredoxin-like domain involved in Fe^{2+} or Zn^{2+} binding, were structurally conserved between PGRL1α and PGRL1β. The key difference was found in the region exposed to lumen, where TYLLE in PGRL1α formed an alpha helix which was not observed in PGRL1β (Fig. 7a).

To gain further insights, we generated AlphaFold3 models of a dimer of the PGR5-PGRL1 heterodimer complex, with either PGRL1α or PGRL1β, at neutral pH and with reduced Trxm4-sensitive cysteines, and assembled these complexes into a model membrane (Fig. 7b). PGRL1 is known to dimerise and interact with PGR5, providing rationale for modelling PGR5–PGRL1 heterodimer-dimers *in silico* (DalCorso *et al.*, 2008; Rühle *et al.*, 2021; Chaturvedi *et al.*, 2024). Heterodimer-dimers formed a T-shaped structure, with each PGR5 binding in a hydrophobic pocket beneath the rubredoxin-like domain of one PGRL1 monomer, covered by the alpha helix ‘arm’ of the other PGRL1 monomer. This configuration was similar for both paralogs (Fig. 7b). The distances between the rubredoxin-like domains of the two PGRL1 monomers, however, were markedly different between paralogs. In PGRL1α, the domains were positioned side by side, 17.1 angstroms apart, whereas in PGRL1β, the domains faced each other with a shorter distance of 10.7 angstroms.

Both heterodimer-dimer models showed interactions between the lumen regions of PGRL1 monomers (Fig. 7c). In PGRL1α, hydrogen bonds were predicted between E-177 of monomer #1 and T-173 of monomer #2, and between E-177 of monomer #1 and Y-174 of monomer #2. In PGRL1β, no hydrogen bonds were observed, but F-173 of the NVFQ regions formed hydrophobic interactions between monomers. A transverse view showed that the PGRL1α and PGRL1β heterodimer-dimers had a different packing arrangement (Fig. 7d), and that the key differing regions were accessible from the thylakoid lumen (Fig. S7).

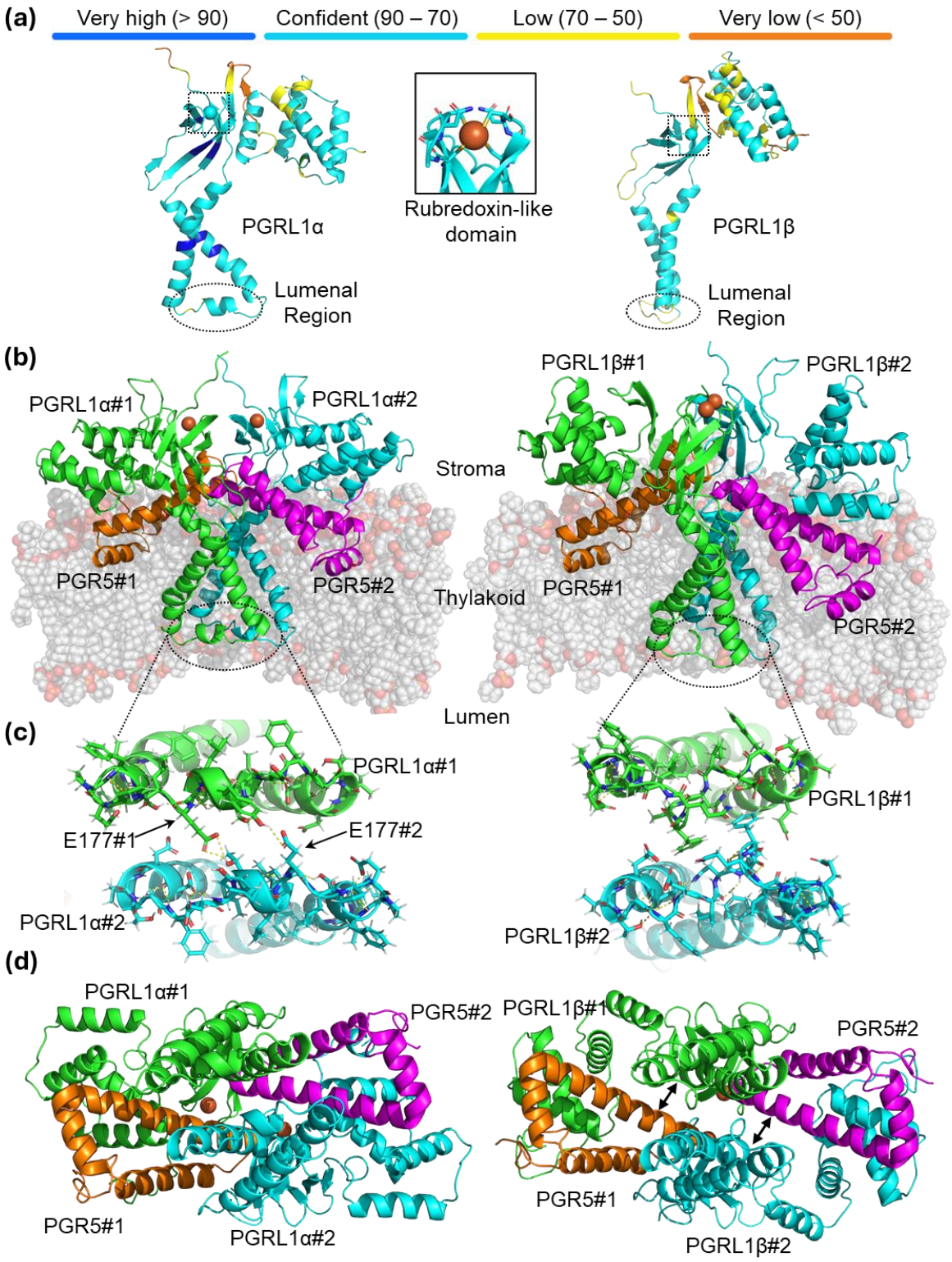

Fig. 7. Structural models of PGRL1α and PGRL1β. (**a**) Predicted structures of PGRL1α and PGRL1β generated by AlphaFold3, with the rubredoxin-like domain in the inset. Predicted local distance difference test (pLDDT) confidence levels for each residue are indicated by colour as per the legend, representing per-atom confidence on a scale from 0 to 100. (**b**) Membrane association models of PGR5-PGRL1α heterodimer-dimer (left) and PGR5-PGRL1β heterodimer-dimer (right). (**c**) Lumen and transverse view of the interface between

PGRL1 monomers in PGR5-PGRL1α (left) and PGR5-PGRL1β (right) heterodimer-dimers. Hydrogen bonds are shown in yellow. E177 residues of each PGRL1α monomer are indicated. (**d**) Lumen view of PGR5-PGRL1α heterodimer-dimer (left) and PGR5-PGRL1β heterodimer-dimer (right) without the membrane. Arrows indicate a gap between the monomers.

Discussion

C_4 photosynthesis has independently evolved over 60 times (Sage *et al.*, 2011). Because C_4 confers substantial advantages over conventional C_3 photosynthesis in hot and dry conditions, there is strong interest in the evolutionary processes that led to its emergence (Sun *et al.*, 2026). Different C_4 subtypes achieve similarly high assimilation rates despite notable biochemical differences, highlighting the flexibility of C_4 metabolism (Furbank, 2011; Fan *et al.*, 2025). However, NADP-ME is the most efficient subtype under optimal conditions (Ehleringer & Pearcy, 1983; Arce Cubas *et al.*, 2023) and is also the most studied. Consequently, NADP-ME is a common target for efforts to engineer C_4 photosynthesis into C_3 crops (Ermakova *et al.*, 2021a). Achieving this goal requires a deeper understanding of the functional rationale and molecular mechanisms underlying cell-differentiation of photosynthetic processes. Interestingly, all three NADP-ME grasses studied here, representing two independent origins of C_4 photosynthesis, have convergently evolved cell-specific expression of *PGRL1* paralogs (Fig. 2), strongly suggesting an advantage of this arrangement for C_4 function.

To test whether the cell-specific arrangement of PGRL1α and PGRL1β is beneficial for C_4 photosynthesis, we generated *S. viridis* mutants lacking either paralog. Cell-level proteomics analysis confirmed that the *pgrl1α* mutants expressed only PGRL1β in both M and BS cells, while the *pgrl1β* mutants expressed only PGRL1α in both cell types. The abundance of PGRL1 was similar in both M and BS cells between mutants, and both mutants compensated for the loss of one PGRL1 paralog in both cell types to achieve similar total PGRL1 levels to WT (Fig. 3). Additionally, *pmf* and φ_{NPQ} in both *pgrl1α* and *pgrl1β* were similar to WT levels (Fig. 4f, Fig. S6) confirming that either paralog was competent in regulating PGR5 and establishing low lumen pH to facilitate qE. Further supporting this conclusion, both mutants maintained WT-like growth under the fluctuating light regime which drastically reduces the growth of the *S. viridis pgr5* mutant (Woodford *et al.*, 2025b).

Despite similar levels of qE, PGRL1α and PGRL1β paralogs each provide a distinct speed and capacity of PSI oxidation. The lower φ_{ND}, the fraction of PSI in the oxidised state, in *pgrl1α* under steady-state high irradiance (Fig. 4h) indicated that PGRL1α in mesophyll cells was necessary for keeping PSI sufficiently oxidised at continuous high light. In contrast, the lower

φ_{ND} at 10 seconds of illumination and the delay in P700 oxidation in *pgrl1β* during the induction of photosynthesis (Fig. 5e,g), as well as the slower P700 oxidation kinetics during the shift from low to high light (Fig. 6b), showed that PGRL1β was required in BS cells for prompt PSI oxidation. Although the relationship between φ_{ND} and photosynthetic control is complex (Degen & Johnson, 2024), based on the strong link between PGR5-PGRL1 and photosynthetic control, we suggest that observed variations in φ_{ND} in the mutants could be attributed to differences in the regulation of photosynthetic control. A more intricate tuning of photosynthetic control than by lumen pH alone has been proposed, with regulation also thought to involve stromal redox state (Degen & Johnson, 2024). This is seen in tobacco plants with Ferredoxin:$NADP^+$ oxidoreductase knock-down, which show uncoupling of qE (and by extension lumen pH) and photosynthetic control (Hald *et al.*, 2008). The similar decoupling seen here in PGRL1 mutants indicates that PGRL1 paralogs may differentially modulate photosynthetic control beyond just lowering lumen pH.

Differences in cell-type-specific electron transport provide clues into why distinct modes of PSI photoprotection conferred by PGRL1 paralogs are required in M and BS cells of NADP-ME grasses. M cells have a high abundance and activity of PSII and therefore predominantly operate linear electron flow (LEF), while BS cells have lower PSII activity and instead operate high CEF through the NDH complex (Ermakova *et al.*, 2021b; Ermakova *et al.*, 2024b). In CEF-dominant systems, while the overall rate of electron transport can be high, it is conceivable that the electron flux on the donor side does not substantially exceed the electron flux the acceptor sides of PSI, meaning that the limitation in electron acceptors is unlikely. Comparatively, in LEF-dominant systems, the capacity of the PSI acceptor side is largely governed by the activity of stromal metabolic reactions, which may be limited, for example, during increases in irradiance due to the time required for enzyme activation (Wang *et al.*, 2021). Therefore, in M cells, if a sudden increase in irradiance stimulates PSII activity, electron influx on the donor side of PSI can significantly exceed the capacity of the acceptor side. Notably, however, this electron influx likely occurs more slowly in LEF than in CEF, as electrons must move from PSII, which resides in stacked grana, to PSI residing in the lamellae (Wójtowicz *et al.*, 2025). Consequently, fast but low capacity photoprotection conferred by PGRL1β is advantageous in CEF-dominant BS cells, whereas high-capacity protection conferred by PGRL1α is preferable in M cells to account for high electron flux from PSII, even at the expense of lower speed. Interestingly, the ratio of *PGRL1β* vs *PGRL1α* transcript abundance in BS cells also correlated well with the relative PSII abundance between species (Fig. 2): it was highest in sorghum with lowest PSII content and lowest in *S. viridis* with highest PSII content (Meierhoff & Westhoff, 1993; Ermakova *et al.*, 2021b), further supporting that the ratio is tuned to the photosystems' composition.

The lumen-exposed sequences of PGRL1α and PGRL1β may underlie the distinct modes of photoprotection conferred by the paralogs. Our protein models suggested that the lumen regions of PGRL1α monomers were linked via hydrogen bonds formed by the negatively charged Glu-177 (Fig. 7c), potentially stabilising the dimer. If this is the case, activation of PGR5 could require not only reduction of the stromal cysteines by Trxm4 but also lumen acidification to protonate the glutamates. This putative pH-sensing role is reminiscent of the function of lumen-exposed glutamates in PsbS that facilitate structural changes under low pH to trigger qE (Krishnan-Schmieden *et al.*, 2021). In contrast, lumen regions of PGRL1β lack the corresponding glutamate and appear to be linked by hydrophobic interactions (Fig. 7c). During increases in irradiance, *pmf* is initially dominated by the electric potential before equilibrating toward a proton gradient (Davis *et al.*, 2017; Wilson *et al.*, 2021), suggesting that responses of reactions depending on lumen pH might be slightly delayed. Therefore, lumen pH-independent PGRL1β might enable faster photoprotection under light transients compared to PGRL1α.

Having both PGRL1 paralogs enabling distinct modes of photosynthetic control is evolutionary advantageous. Our phylogenetic analysis suggests a duplication event after the origin of grasses gave rise to PGRL1β. While whole-genome duplications are common in plants, non-essential duplicates are often lost during subsequent speciation or through random mutations (Rieseberg & Willis, 2007). The persistence of both PGRL1α and PGRL1β in most grasses for up to ~98 million years therefore implies a selective benefit of the dual system. Consistent with this, analysis of *S. viridis* mutants indicates that the paralogs confer complementary functions and together provide both fast and high-capacity photoprotection at the leaf level. Cooperative systems with complementary functions in regard to speed/capacity or affinity/flux are common in biological systems and provide broader operational range; a typical example is membrane transporters (Levy *et al.*, 2011). Notably, however, some grasses have lost one paralog. A prominent example is the group that includes wheat, rye, and barley. It will be important to determine how the absence of PGRL1α in these species shapes the regulation of photosynthetic control relative to C_3 grasses that retain both paralogs.

Conclusion

The duplication of PGRL1 in grasses enabled functional divergence, with PGRL1β evolving as a rapid-response regulator of photoprotection, while PGRL1α retained its ancestral role in slower but high-capacity protection. These differences in function likely arose from a divergence in PGRL1's lumen region, with PGRL1α activity dependent on pH regulation of a conserved glutamate, which is absent in PGRL1β. The co-option of PGRL1 paralogs into M and BS cells by NADP-ME C_4 grasses supports distinct modes of photoprotection offered by

the PGRL1 paralogs and suggests that it's a requirement for efficient NADP-ME C_4 photosynthesis. As modern agriculture relies on open-field environments with high and fluctuating irradiance, introducing PGRL1β into non-grass crops such as canola, potato and soybean might offer enhanced resilience to light stress, presenting a new potential avenue for crop improvement.

Supplementary materials

Table S1. Accessions numbers of *PGRL1* genes studied in this work.

Acronym	Species	Gene	Gene ID	Gene	Gene ID
Aa	*Artesia annua*	*PGRL1*	Chromosome 7; 44,765-49,699		
Aegt	*Aegilops tauschii*			*PGRL1β*	AET5Gv21221900.2
Ag	*Andropogon gerardii*	*PGRL1α-1*	AndgeH1.02BG087800.1	*PGRL1β-1*	AndgeH1.01BG004300.1
		PGRL1α-2	AndgeH1.02AG108200.1	*PGRL1β-2*	AndgeH1.01AG004100.1
		PGRL1α-3	AndgeH1.02CG092200.1	*PGRL1β-3*	AndgeH1.01CG004700.1
Al	*Ampelocalamus luodinaensis*	*PGRL1α*	Alu07Dg10900.2	*PGRL1β-1*	Alu03Cg00420.1
				PGRL1β-2	Alu03Dg30180.2
Ampc	*Ampelocalamus calcareus*	*PGRL1α*	Hca03Dg11500.3	*PGRL1β*	Hca03Dg00380.1
As	*Avena sativa*	*PGRL1α-1*	AVESA.00001b.r3.2Cg0001548.1	*PGRL1β-1*	AVESA.00001b.r3.Ung000396.1
		PGRL1α-2	AVESA.00001b.r3.2Dg0003409.1	*PGRL1β-2*	AVESA.00001b.r3.7Cg000037.1
				PGRL1β-3	AVESA.00001b.r3.4Dg0002573.3
At	*Arabidopsis thaliana*	*PGRL1A*	AT4G22890		
		PGRL1B	AT4G11960		
Ba	*Bonia Amplexicaulis*	*PGRL1α*	Bam07Ag07840.1	*PGRL1β*	Bam03Ag19370.1
Bd	*Brachypodium distachyon*	*PGRL1α*	Bradi1g52550.12	*PGRL1β*	Bradi1g00940.1
Cl	*Chasmanthium laxum*	*PGRL1α*	Chala.10G086100.1	*PGRL1β-1*	Chala.03G290600.1
				PGRL1β-2	Chala.12G040300.1
Cr	*Chlamydomonoas reinhardtii*	*PGRL1*	Cre07.g340200.t1.1		
Da	*Dioscorea alata*	*PGRL1*	Dioal.16G045900.1		
Dens	*Dendrocalamus sinicus*	*PGRL1α*	Dsi07Ag08820.1	*PGRL1β*	Dsi03Ag00220.2
Ec	*Eleusine coracana*	*PGRL1α*	ELECO.r07.7BG0597380.1	*PGRL1β1*	ELECO.r07.3BG0252680.1
				PGRL1β2	ELECO.r07.3AG0207630.1
Erac	*Eragrostis curvula*	*PGRL1α*	EJB05_12845	*PGRL1β*	EJB05_03684
Et	*Eragrostis tef*	*PGRL1α-1*	Et_5B_043645	*PGRL1β-1*	Et_4B_038547
		PGRL1α-2	Et_5A_040970	*PGRL1β-2*	Et_4A_034424
Ft	*Flaveria trinerva*	*PGRL1*	Chromosome 7; 5,778,300 - 5,722,381 (reverse)		

Ga	*Guadua angustifolia*	*PGRL1α*	Gan07Bg09810.2	*PGRL1β*	Gan05Bg00110.1
Hv	*Hordeum vulgare*			*PGRL1β*	HORVU5Hr1G124210.5
Ja	*Joinvillea ascendens*	*PGRL1*	Joasc.10G046600		
Leep	*Leersia perrieri*	*PGRL1α*	LPERR08G08870	*PGRL1β*	LPERR03G35530.1
Lp	*Lolium perenne*	*PGRL1α*	KYUSg_chr2.31374	*PGRL1β*	KYUSg_chr4.681
Ma	*Musa acuminata*	*PGRL1*	GSMUA_Achr4T28830_001		
Mh	*Melocanna humilis*	*PGRL1α*	Mhu07Ag04200.1	*PGRL1β*	Mhu03Bg00260.2
Ms	*Miscanthus sinensis*	*PGRL1α-1*	MisinT443400	*PGRL1β-1*	Misin16G024900
		PGRL1α-2	Misin04G108900	*PGRL1β-2*	MisinT360900
Og	*Otatea glauca*	*PGRL1α*	Ogl07Bg10220.1	*PGRL1β*	Ogl03Cg23350.1
Ol	*Olyra latifolia*	*PGRL1α*	Ol07g09230.1	*PGRL1β*	Ol03g30000.1
Ot	*Oropetium thomaeum*			*PGRL1β*	Oropetium_20150105_23595
Os	*Oryza sativa*	*PGRL1α*	LOC_Os08g41460	*PGRL1β*	LOC_Os03g64020
		PGR5	LOC_Os08g45190		
Pasv	*Paspalum vaginatum*	*PGRL1α*	Pavag02G081500	*PGRL1β*	Pavag01G004100
Pe	*Phyllostachys edulis*	*PGRL1α*	Ped07Dg06700.1	*PGRL1β*	Ped03Cg00420.1
Ph	*Panicum hallii*	*PGRL1α*	Pahal.2G103600	*PGRL1β*	Pahal.9G004200
Pl	*Pharus latifolius*	*PGRL1α*	Phala.03G097200	*PGRL1β*	Phala.01G006700
Pv	*Panicum virgatum*	*PGRL1α-1*	Pavir.2KG249300	*PGRL1β-1*	Pavir.9KG015400
		PGRL1α-2	Pavir.2NG289400	*PGRL1β-2*	Pavir.9NG016300
Rg	*Raddia guianensis*	*PGRL1α*	Rgu07g15140.1	*PGRL1β*	Rgu03g28870.3
Rr	*Rhipidocladum racemiflorum*	*PGRL1α*	Rhi07Bg10380.1	*PGRL1β*	Rhi03Cg00320.1
Sa	*Streptochaeta angustifolia*	*PGRL1α*	Scaffold_1550; 66,500 – 69,500		
Sb	*Sorghum bicolor*	*PGRL1α*	Sobic.002G112400.6	*PGRL1β*	Sobic.001G005200
Sc	*Secale cereale*			*PGRL1β*	SECCE7Rv1G0454960
Si	*Setaria italica*	*PGRL1α*	Seita.2G109800	*PGRL1β*	Seita.9G004200
Sm	*Sellaginella moellendorfii*	*PGRL1*	66389		
So	*Saccharum officinarum*	*PGRL1α-1*	SoffiXsponR570.05Ag111900.1	*PGRL1β-1*	SoffiXsponR570.01Bg004900.1
		PGRL1α-2	SoffiXsponR570.5_9Ag316600.1	*PGRL1β-2*	SoffiXsponR570.01Eg004400.1
		PGRL1α-3	SoffiXsponR570.05Bg100500.1	*PGRL1β-3*	SoffiXsponR570.01Cg005200.1
		PGRL1α-4	SoffiXsponR570.05Bg101000.1	*PGRL1β-4*	SoffiXsponR570.01Ag004400.1
		PGRL1α-5	SoffiXsponR570.05Cg105400.1		

		PGRL1α-6	SoffiXsponR570.05Eg088400.1		
		PGRL1α-7	SoffiXsponR570.05Gg110600.1		
Sv	*Setaria viridis*	*PGRL1α*	Sevir.2G115600	*PGRL1β*	Sevir.9G004600
Ta	*Triticum asetivum*			*PGRL1β-1*	Traes_4AL_A9E7CD7B8
				PGRL1β-2	Traes_5BL_283D01C08
				PGRL1β-3	Traes_5DL_89CF8AFCE
Ti	*Thinopryum intermedium*	*PGRL1α-1*	Thint.V1438200	*PGRL1β-1*	Thint.14G0565500
		PGRL1α-2	Thint.14G0072400	*PGRL1β-2*	Thint.14G0583200
		PGRL1α-3	Thint.V1087200		
		PGRL1α-4	Thint.V1459800		
Uf	*Urochloa fusca*			*PGRL1β*	Urofu.9G004000.1
Zm	*Zea mays*	*PGRL1α*	Zm00001d019454	*PGRL1β*	Zm00001d034900
		PGR5A	Zm00001d031850	*PGR5B*	Zm00001d049883

Table S2. Photosynthetic parameters of wild type (WT), *pgrl1α* and *pgrl1β S. viridis* plants fit from the CO_2 response curves of CO_2 assimilation (Fig. 4d). V_{pmax}, PEPC activity; V_{cmax}, Rubisco activity; *J*, electron transport rate required to sustain the measured CO_2 assimilation rate (see details in Woodford *et al.* (2025a)). Mean ± SE, *n* = 5 biological replicates. No statistically significant differences were found between genotypes (one-way ANOVA with Tukey's post hoc test at $P < 0.05$).

Parameter	**WT**	***pgrl1α-3***	***pgrl1β-1***
J	96.5	103.2	109.4
(μmol m^{-2} s^{-1})	±4.5	±3.5	±4.6
$\boldsymbol{V_{pmax}}$	62.0	70.6	60.1
(μmol m^{-2} s^{-1})	±5.5	±8.5	±3.2
$\boldsymbol{V_{cmax}}$	30.0	32.3	35.7
(μmol m^{-2} s^{-1})	±2.0	±2.5	±2.4

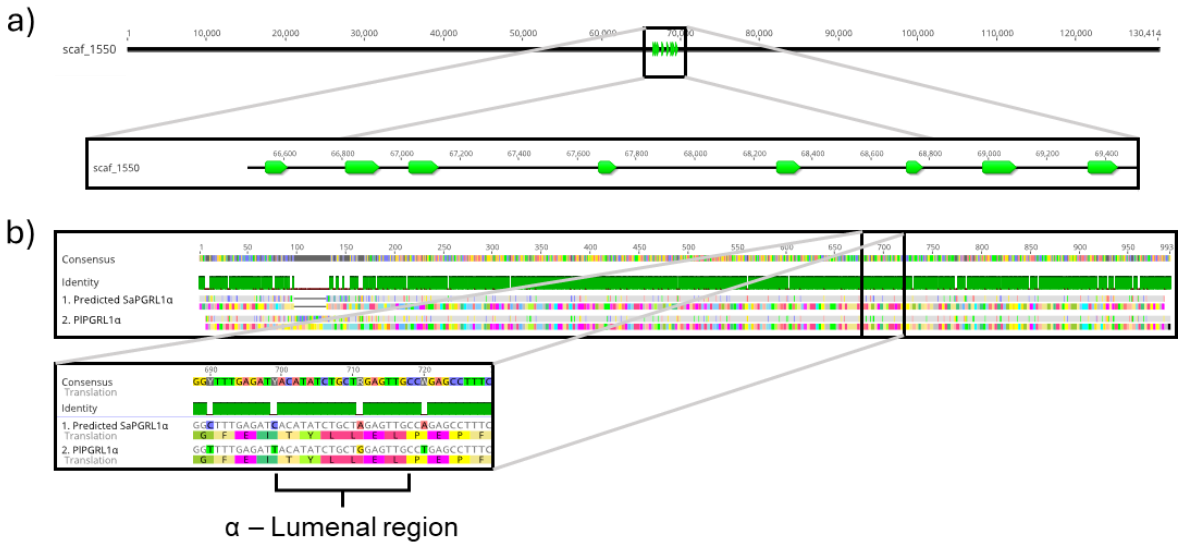

Fig. S1. Alignment of the predicted *PGRL1* gene from *Streptochaeta angustifolia* (Sa). (a) Alignment of *Pharus latifolius* (Pl) *PGRL1α* against the scaffold assembly of Sa. **(b)** MUSCLE alignment of the predicted Sa *PGRL1α* and Pl *PGRL1α*, highlighting the amino acid sequence of the lumenal region characteristic of PGRL1α.

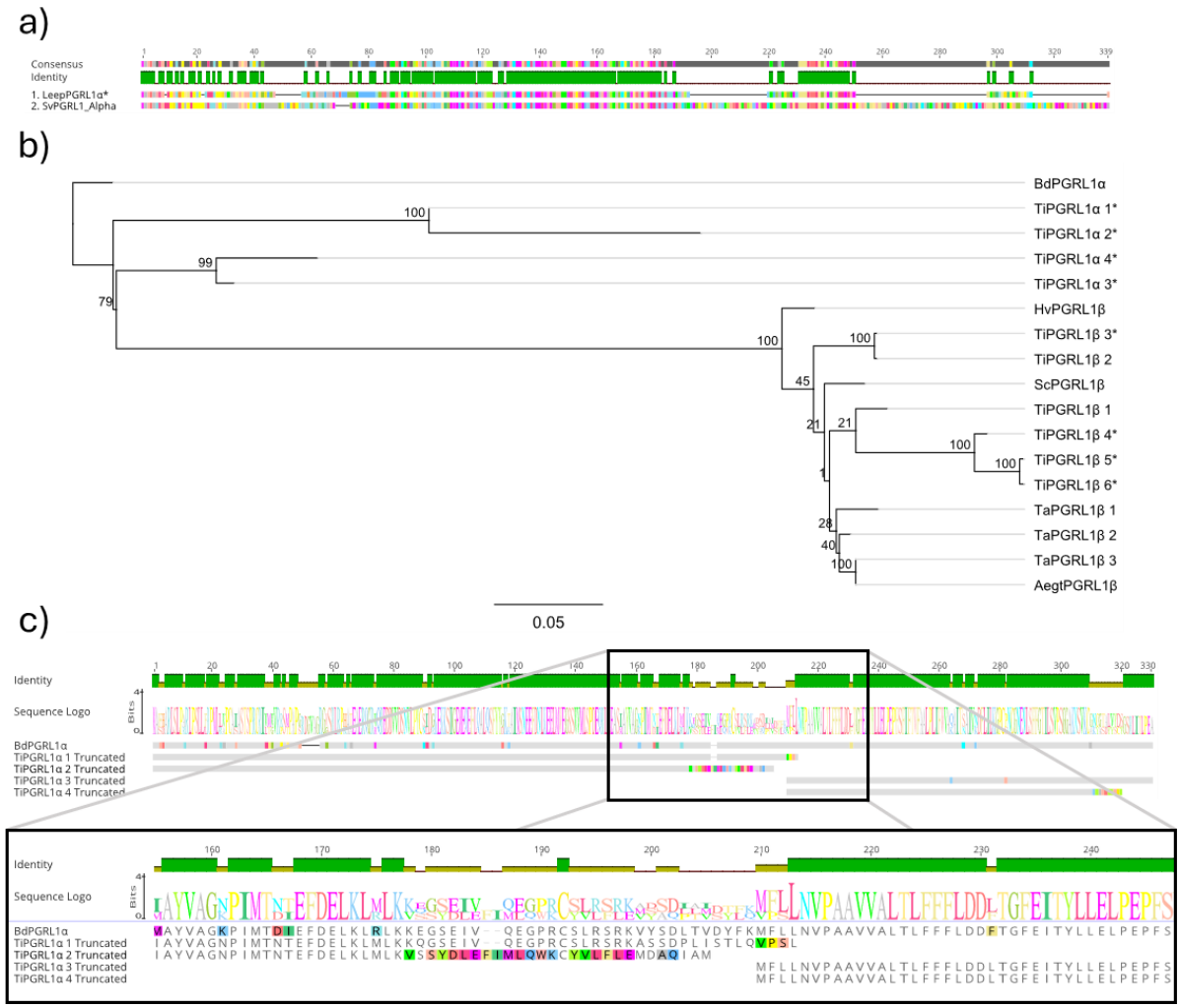

Fig. S2. Loss of functional *PGRL1α* genes across the Poaceae family. *PGRL1α* was lost or rendered non-functional at least six times independently in *Urochloa fusca*, *Oropetium thomaeum*, *Leersia perrieri*, *Raddia guianensis*, *Bonia amplexicaulis*, and all members of the Triticeae subfamily. In *U. fusca* (PEPCK C_4 subtype) and *O. thomaeum* (NAD-ME C_4 subtype), the absence of *PGRL1α* was determined by the lack of RNA-seq annotated sequences. **(a)** Alignment of *L. perrieri* (Leep) and *Setaria viridis* (Sv) PGRL1α amino acid sequences. The chloroplast transit peptide (mapped by TargetP 2.0) and multiple sections of the mature protein are missing in Leep PGRL1α. **(b)** Analysis of *PGRL1α* genes from the Triticeae: *Aegilops tauschii* (Aegt), *Hordeum vulgare* (Hv), *Secale cereale* (Sc), *Triticum aestivum* (Ta), and *Thinopyrum intermedium* (Ti). RAxML phylogenetic tree generated from MAFFT-aligned *PGRL1* genes within Triticeae, with *Brachypodium distachyon* (Bd) as an outgroup. Bootstrap values are shown at each node. Genes that do not encode a functional mature peptide are marked by asterisks. **(c)** Alignment of Ti PGRL1α showing incomplete protein sequences. The incomplete protein sequences were unlikely to be an artifact of poor RNA-seq annotation, as the genes belonged to different genomic regions: TiPGRL1α-2 (*Thint.14G0072400.1*) at Chr14:53647416..53649826 (reverse); TiPGRL1α-1 (*Thint.V1438200.1*) at ChrUN:119455789..119461794 (reverse); TiPGRL1α-3 (*Thint.V1087200.1*) at

scaffold_698:425178..427956 (forward); TiPGRL1α-4 (*Thint.V1459800.1*) at ChrUN:137199120..137203790 (reverse).

a)

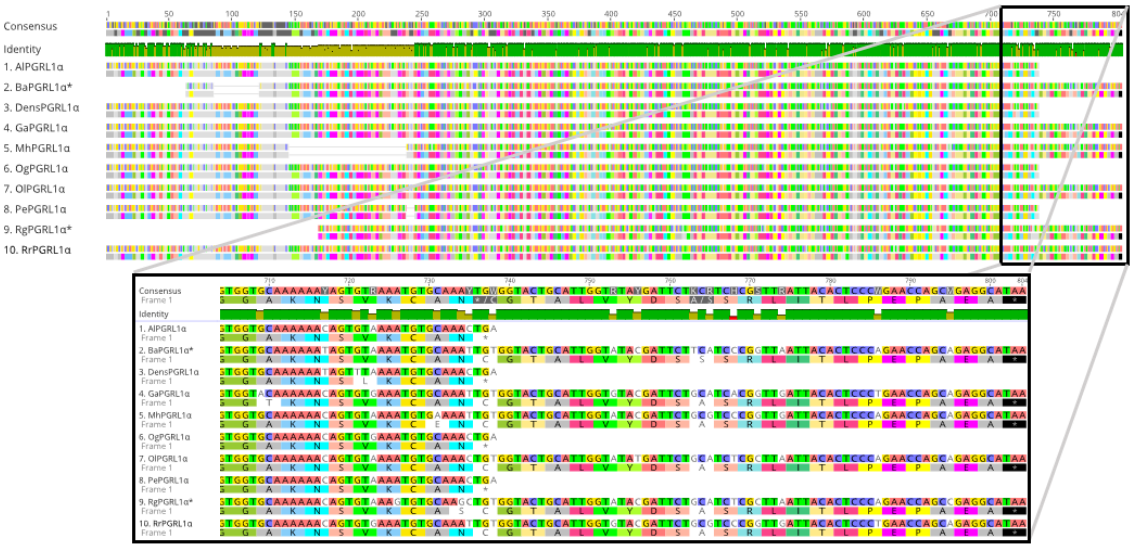

b)



c)

TargetP 2.0 Output						
# ID	Prediction	OTHER	SP	mTP	cTP	lTP
DensPGRL1β	OTHER	0.995417	0.000038	0.003241	0.001303	0.000001
GaPGRL1β	OTHER	0.937145	0.003687	0.03305	0.021813	0.004304

Fig. S3. Loss of functional *PGRL1* genes in the Bambusoideae subfamily. (a) MAFFT alignment of the *PGRL1α* genes and the corresponding amino acid sequences. Asterisks indicate genes that have lost functional chloroplast transit peptides. In *Melocanna humilis* (Mh) *PGRL1α*, a part of the coding sequence (CDS) in the beginning of the gene is missing, including the first cysteine involved in dimerization. *Raddia guianensis* (Rg) and *Bonia amplexicaulis* (Ba) PGRL1α lack chloroplast transit peptides, suggesting that they are not localised to the chloroplast. *Ampelocalamus luodianensis* (Al), *Phyllostachys edulis* (Pe), *Dendrocalamus sinicus* (Dens), and *Otatea glauca* (Og) PGRL1α have premature stop codons and lack the final cysteine in the rubredoxin domain. According to Hertle et al. (2013), mutations at this cysteine do not affect iron binding in recombinant PGRL1 proteins, indicating that these proteins may retain some functional activity. **(b)** MAFFT alignment of the *PGRL1β* genes and the corresponding amino acid sequences. Asterisks indicate genes that have lost functional chloroplast transit peptides. Al and Pe PGRL1β lack chloroplast transit peptides due to later start codons, suggesting these proteins are not present in the chloroplast. Ba and Ga PGRL1β have premature stop codons and lack the final cysteine in the rubredoxin domain. **(c)** TargetP 2.0 outputs for Ga and Dens PGRL1β listed as probabilities, 1 being absolute certainty, 0 being no probability. TargetP 2.0 showed that both Ga and Rr *PGRL1β* lost a functional transit peptide, suggesting these proteins are not present in the chloroplast. OTHER – no signal peptide discovered, SP – signal peptide, mTP – mitochondrial transfer peptide, cTP – chloroplast transfer peptide, lTP – thylakoid lumen transfer peptide.

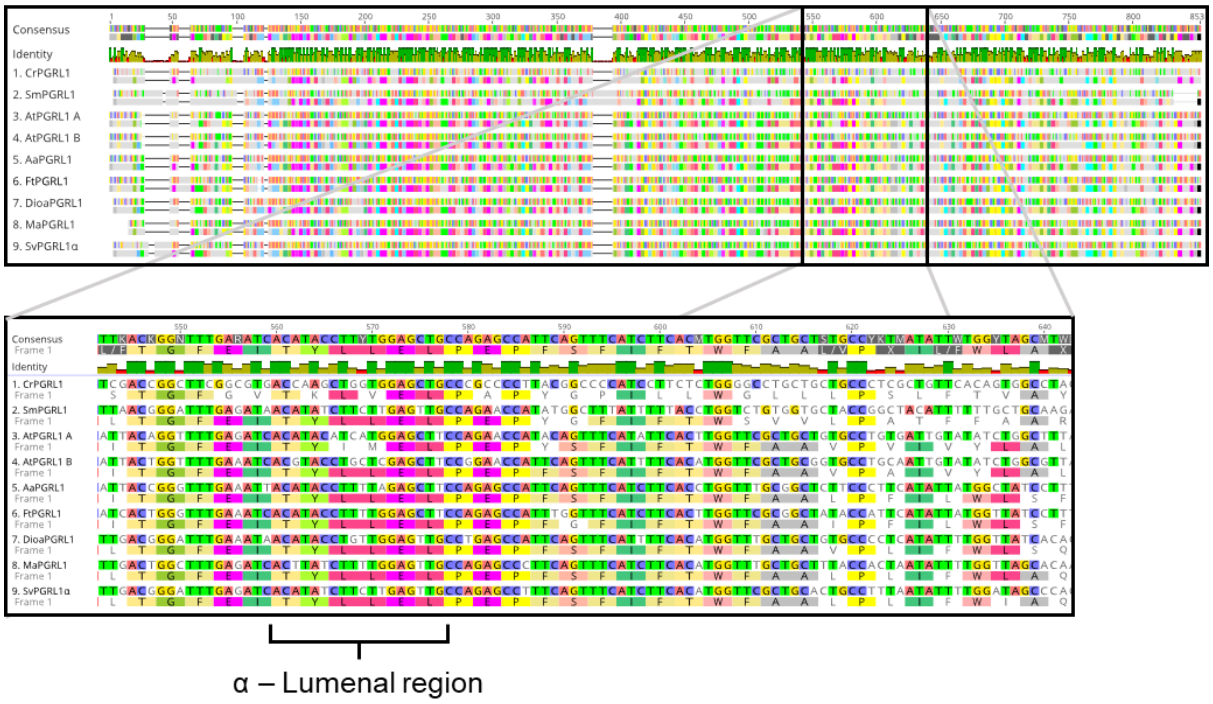

Fig. S4. MAFFT alignment of *PGRL1α* mature coding sequences and corresponding protein sequences from *Chlamydomonas reinhardtii* (Cr), *Sellaginella moellendorfii* (Sm), *Arabidopsis thaliana* (At), *Artesia annua* (Aa), *Flaveria trinerva* (Ft), *Dioscorea alata* (Dioa) and *Musa acuminata* (Ma) to *Setaria viridis* (Sv).

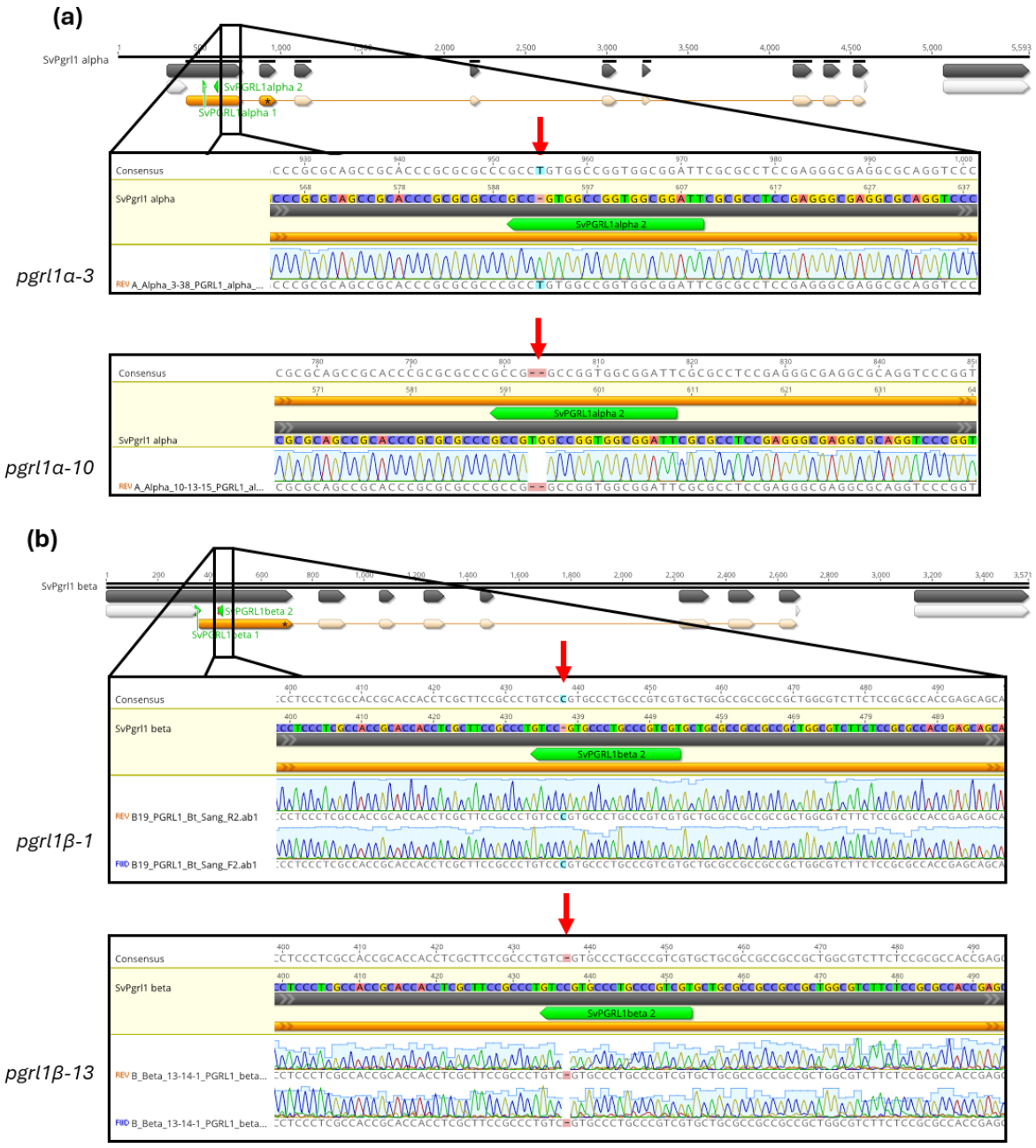

Fig. S5. Cas9-induced mutations in *pgrl1α-3, pgrl1α-10, pgrl1β-1* and *pgrl1β-13*. Gene models of *pgrl1α* (**a**) and *pgrl1β* (**b**) in *S. viridis* with coding sequence (CDS) annotated in orange. The introduced single nucleotide insertion, single deletion, or double deletion caused a frameshift which resulted in a premature stop codon. Sanger sequencing histograms confirm the introduced mutations.

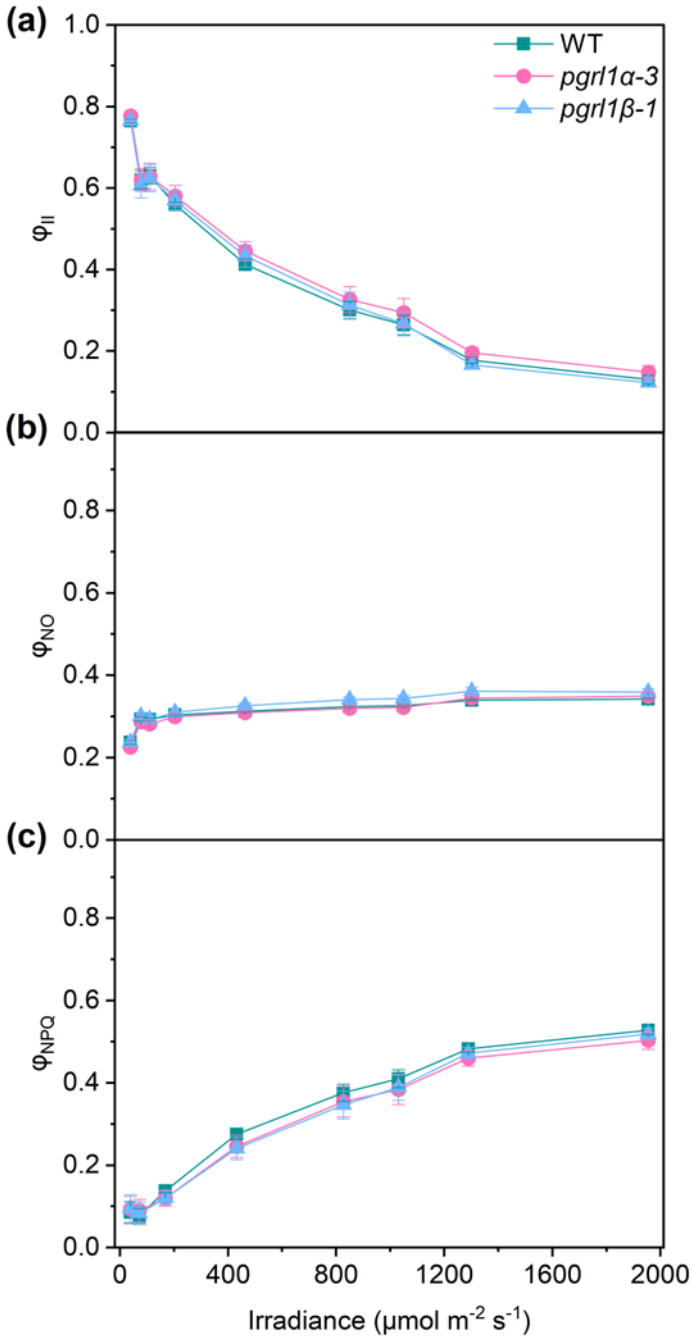

Fig. S6. Light-responses of the effective quantum yield of PSII (φ_{II}), the yield of non-regulated non-photochemical energy dissipation (φ_{NO}), the yield of non-photochemical quenching (φ_{NPQ}) in *S. viridis* wild type (WT), *pgrl1α* and *pgrl1β* mutant plants. Mean ± SE, *n* = 5 biological replicates; two-way repeated measures ANOVA found no statistical differences between genotypes.

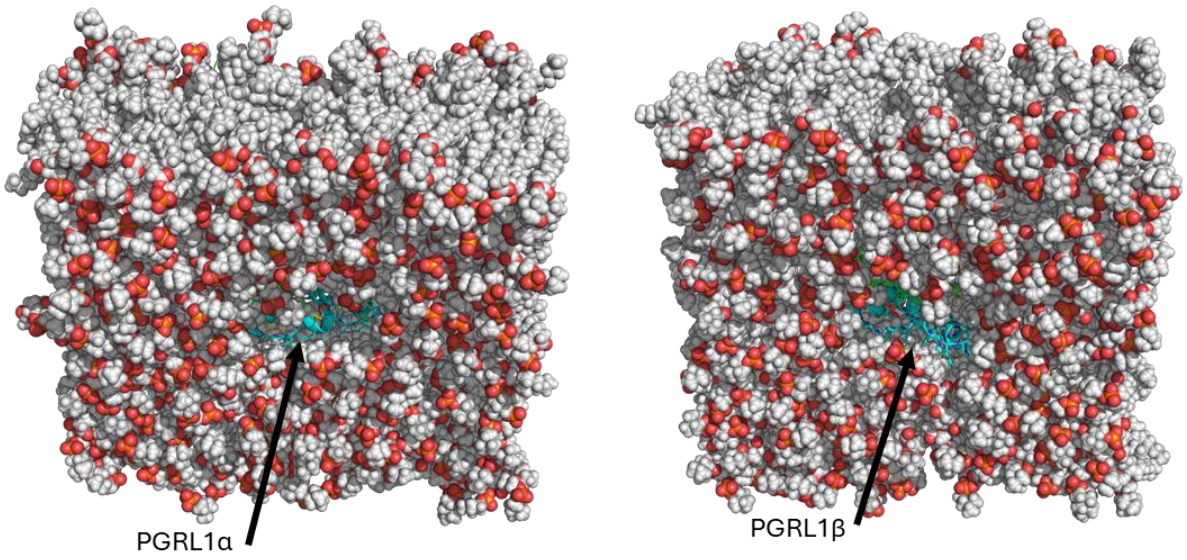

Fig. S7. View of PGRL1α-PGR5 and PGRL1β-PGR5 heterodimer-dimers modelled in the membrane from the lumen.

Chapter 3: C_4 plants provide new evidence for PGR5 involvement in regulation of cyclic electron flow

Introduction

Cyclic electron flow (CEF) around photosystem I (PSI) is postulated to be essential for survival of photosynthetic organisms as it helps to adjust the ratio of ATP to NADPH, produced by the light reactions, to match the metabolic demands of cellular processes (Kramer & Evans, 2011; Degen *et al.*, 2023b). Moreover, CEF is also essential for building up proton motive force (*pmf*), along with linear electron flow (LEF), to lower lumenal pH which triggers photoprotective processes like energy-dependent NPQ (qE) and photosynthetic control (PCON), critical for prompt responses of photosynthetic organisms to light fluctuations (Kramer *et al.*, 2003; Tikhonov, 2013; Degen & Johnson, 2024). In angiosperm C_3 leaves, the PGR5-associated, antimycin A–sensitive CET route is generally considered the major pathway of CEF, whereas in NADP-ME C_4 bundle sheath chloroplasts NDH-mediated CEF is strongly enriched and represents the main cyclic route (Shikanai, 2014; Ishikawa *et al.*, 2016; Ermakova *et al.*, 2024b).

Involvement of PROTON GRADIENT REGULATION 5 (PGR5) in AA-sensitive CEF has been suggested for decades (Munekage *et al.*, 2002; Okegawa *et al.*, 2007; Suorsa *et al.*, 2012). However, while the lack of PGR5 unequivocally results in lower *pmf* and decreased activity of associated photoprotective reactions (Suorsa *et al.*, 2012), whether this is due to a lack of CEF is still unclear. The lack of CEF in a mutant should be seen as a loss of electron flux on both donor and acceptor sides of PSI. While the acceptor side limitation has been confirmed, ambiguity regarding the mechanism largely persists due to inability to assess the electron flux on the donor side of PSI. $P700^+$ is the oxidised fraction of the PSI reaction centre which can be reduced, and the rate of $P700^+$ reduction during light-to-dark shift is typically used to estimate the flux of electrons to PSI (Degen & Johnson, 2024; Ermakova *et al.*, 2024b). However, utilising it in C_3 *pgr5* mutants is not possible because the lack of photosynthetic control (seen as a complete the lack of φ_{ND}) in *pgr5* prevents oxidation of PSI (Nishikawa *et al.*, 2012; Tikkanen *et al.*, 2014). Oxidation of PSI in *pgr5* mutant of C_3 plant *Arabidopsis thaliana* is observed only when PSII activity is slowed through mutagenesis (Suorsa *et al.*, 2016), addition of DCMU or using far-red light (Nandha *et al.*, 2007) - all resulting in lack of electrons for CEF in the WT and confounding the interpretation of results.

Because donor-side electron flux could not be quantified in C_3 *pgr5* mutants, alternative mechanisms by which PGR5 builds-up *pmf* were proposed. One possibility is that PGR5

distributes part of electrons from PSI to other processes so the electrons do not return to PSI. In this hypothesis, PGR5 provides additional sink for electrons from PSI and thus builds up *pmf* by accelerating LEF (Takagi & Miyake, 2018; Kappel *et al.*, 2023). If that is the mechanism, a lack of PGR5 would increase PSI acceptor side limitation and stromal redox carriers would be more reduced. In addition to this debate, it was argued that PGR5 could influence *pmf* by regulating proton conductivity of the thylakoid membrane (g_{H^+}), i.e., the proton efflux through ATP synthase (Avenson *et al.*, 2005a; Nikkanen *et al.*, 2018; Degen *et al.*, 2023a; Nikkanen *et al.*, 2024). In this scenario, lack of PGR5 causes inability to downregulate g_{H^+} at high light and consequently plants cannot build-up *pmf* and establish PCON. Importantly, this ATP synthase regulatory hypothesis is not mutually exclusive with either a role of PGR5 in regulating CEF or an acceptor-side regulator role, because altered proton conductivity could act in parallel with changes in electron transfer. As a result, despite the clear phenotype of lowered *pmf* and impaired photoprotection in C_3 *pgr5* mutants, the primary role of PGR5 as either CEF regulator, acceptor-side distributor, a g_{H^+} regulator, or some combination of these functions, has remained unresolved.

We recently showed that the model C_4 grass *Setaria viridis* lacking PGR5 has significant donor-side limitation of PSI (φ_{ND}) under high light suggesting substantial level of PSI oxidation (Woodford *et al.*, 2025b). This was attributed to the presence of PCON likely due to the high activity of NDH-dependent CEF in C_4 plants (Ermakova *et al.*, 2024b). This key difference between C_3 and C_4 *pgr5* mutants provides an opportunity to quantify how loss of PGR5 affects electron fluxes on the donor side of PSI. In this chapter, I test competing models of PGR5 function by assessing donor- and acceptor-side PSI electron fluxes during photosynthetic induction.

Hypothesis 1: PGR5 is involved in regulation of CEF. Loss of PGR5 decreases electron recycling from ferredoxin (Fd) back to the plastoquinone (PQ) pool. Therefore, electron withdrawal from Fd and the electron delivery to PSI should both decrease.

Hypothesis 2: PGR5 acts as an electron distributor on the PSI acceptor side, but not through CEF. Loss of PGR5 impairs PSI acceptor availability causing electrons to accumulate on the acceptor side. Therefore, electron flux from Fd should decrease, while any reduction in donor-side flux could occur secondarily due to acceptor-side “backpressure” rather than loss of CEF per se (Kappel *et al.*, 2023).

Hypothesis 3: PGR5 affects *pmf* mainly by regulating g_{H^+}, i.e., the proton efflux through ATP synthase. Loss of PGR5 lowers *pmf* through increased proton efflux via ATP synthase rather

than changing electron transfer capacities. This function could potentially co-exist with Hypothesis 1 or 2.

To test these hypotheses, I combined several spectroscopic techniques for studying electron and proton fluxes in leaves, including saturating pulse method for assessing quantum yields in PSI and PSII, electrochromic shift for *pmf* measurements, and dark-interval relaxation kinetics (DIRKs) to quantify electron fluxes through Fd, P700, and plastocyanin (PC). DIRKs briefly interrupt actinic illumination (300ms) and record the subsequent relaxation of redox signals during a short dark interval (Sacksteder & Kramer, 2000). DIRKs are well suited for more frequent probing of electron transport compared to saturating pulses that transiently over-saturate electron transport chain which, upon frequent application, can cause photodamage in light-sensitive mutants like *pgr5*.

Recently developed near-infrared (NIR) spectroscopy, analysed with the DUAL-KLAS/NIR (DKN), allows to deconvolute signals from P700, PC, and Fd. The instrument records four pulse-modulated dual-wavelength difference signals (785–840, 810–870, 870–970, and 795–970 nm) and deconvolutes these mixed signals using empirically derived Differential Model Plots (DMPs) for Fd, P700, and PC. Using the DMP "fingerprints," the software resolves the best combination of component amplitudes at each time point, generating time-resolved traces for P700, PC, and Fd (Klughammer & Schreiber, 2016).

DIRK-based analyses combined with near-infrared (NIR) deconvolution of P700, PC, and Fd signals have been used previously to quantify PSI-associated electron flow and to estimate the contribution of CEF to electron flow through PSI in plants (Kadota *et al.*, 2019; Furutani *et al.*, 2020; Hepworth *et al.*, 2021; Ohnishi *et al.*, 2023; Maekawa *et al.*, 2024; Satoh *et al.*, 2025) and cyanobacteria (Theune *et al.*, 2021; Appel *et al.*, 2022; Hubáček *et al.*, 2024; Ortega-Martínez *et al.*, 2024). In cyanobacterium *Synechocystis sp* PCC 6803, DIRK-based P700 and PC electron flow has been used to estimate CEF and to highlight method-dependent discrepancies in inferred CEF fractions (Theune *et al.*, 2021; Hubáček *et al.*, 2024; Ortega-Martínez *et al.*, 2024). Maekawa *et al.* (2024) applied this to the Fd signal to infer PGR5-dependent contributions to PSI electron transport.

While DIRKs can recover kinetic information relevant to CEF in vivo, DIRK parameters are often reported as empirical metrics (e.g., initial slopes, half-times, or effective rate constants) without explicitly connecting fitted decay parameters to mechanistic rate expressions for PC, P700, and Fd. In practice, 'flux' is commonly approximated as the initial slope of the relaxation (short-window linear regression at dark onset) and/or summarised by parameters derived from exponential curve fitting, rather than derived from explicitly stated differential equations for

interacting redox couples like PC and P700 (Kadota *et al.*, 2019; Hepworth *et al.*, 2021; Theune *et al.*, 2021). A few studies explicitly defined the initial rate of Fd oxidation (vFd) as the product of the observed rate constant of the exponential decay fitting and the concentration of reduced Fd at time 0 (Maekawa *et al.*, 2024; Satoh *et al.*, 2025). However, these studies estimate vFd from short-window linear regression at dark onset rather than from the derivative of a fitted decay function and therefore stop short of using this relationship to attribute changes in vFd to specific kinetic components.

Here, I build on the DIRK and NIR framework by introducing a mass-action kinetic basis for the relaxation of P700, PC, and Fd (Waage & Gulberg, 1864; 1986). The rate expressions used here are grounded in biochemical kinetic measurements that support mass-action descriptions of electron-transfer reactions involving P700 (Haehnel *et al.*, 1994), PC (Haehnel *et al.*, 1994; Hope, 2000), and Fd (Cassan *et al.*, 2005; Hald *et al.*, 2008; Zhu *et al.*, 2013; Kimata-Ariga *et al.*, 2019). I use the initial rate of a signal decay at the onset of darkness (t = 0) as a metric for flux and then use the fitted kinetic components underlying this initial rate to diagnose which step(s) constrain electron delivery to PSI and electron withdrawal from PSI. The initial rate is obtained as the derivative at t = 0 for consistency across carriers. This provides an explicit mapping between the measured DIRK traces, fitted decay parameters, and underlying flux terms, enabling interpretation of whether changes in flux reflect (i) changes in the availability of reduced donors or oxidised acceptors at DIRK onset (signal amplitudes), (ii) changes in effective rate constants reflecting altered turnover/encounter kinetics, or (iii) loss or activation of specific electron sinks that withdraw electrons from Fd.

The new quantitative framework enables to estimate electron fluxes through cytochrome *f* (Cyt*f*) of the Cytochrome b_6f complex (Cytb_6f) via PC kinetics, PSI via P700/PC kinetics, and Fd-dependent pathways via Fd kinetics, during photosynthetic induction in C_4 *S. viridis* lacking PGR5 (Woodford *et al.*, 2025b). Using this approach, I show that loss of PGR5 is associated not only with acceptor-side limitation at PSI, but also with a substantial loss of electron flux on the donor side of PSI. Importantly, the observed donor-side flux deficit cannot be explained by decreased PSII activity, a kinetic restriction at Cytb_6f, or depletion of PSI acceptor capacity under the conditions analysed. The remaining explanation is that Cyt*f* is transiently less reduced in the *pgr5* mutant, implying that fewer electrons reach Cyt*f* from a source other than LEF. This points to a loss of electron recycling into the PQ pool, consistent with a role of PGR5 in regulating CEF. Together, these results provide new in vivo evidence that PGR5-CEF is required to sustain efficient PSI turnover during increases in irradiance and to facilitate photoprotective reactions.

Material and Methods

Experimental approach and quantitative framework: from DIRK–NIR redox signals to flux

This section defines the quantitative framework used to convert DIRK–NIR redox signals into fluxes and to interpret genotype-dependent changes in terms of (i) carrier availability at dark onset, (ii) effective rate constants, and (iii) competing electron sinks. Full derivations of the working equations are provided in the Supplemental Derivations; here I introduce the final expressions and the parameters used throughout the Results.

Mass-action example for electron transfer

For an elementary bimolecular electron-transfer step, where an electron is transferred from a reduced species B^- to an oxidised species A^+,

K 3.1 $$A^+ + B^- \xrightarrow{k} A^- + B^+,$$

the law of mass action gives the instantaneous rate (v):

Eq. 3.1 $$v = \frac{d[A^-]}{dt} = k[A^+][B^-].$$

Where the instantaneous rate is equal to the product of the rate constant (k), and the concentrations of the reactants [A^+] and [B^-]. Over the short DIRK fitting window, one reactant can often be treated as approximately constant (or represented by a time-averaged value, $\langle \mathrm{X} \rangle$), so the reaction becomes pseudo–first-order for the other reactant. For example, if $[B^-] \approx \langle B^- \rangle$, then:

Eq. 3.2 $$\frac{d[A^+]}{dt} = -k\langle B^- \rangle [A^+] \equiv -k_{\mathrm{obs}}[A^+],$$

where $k_{\mathrm{obs}} = k\langle B^- \rangle$. Integrating yields:

Eq. 3.3 $$[A^+(t)] = [A^+(0)]e^{-k_{\mathrm{obs}}t} + C.$$

Thus, the fitted k_{obs} captures both an intrinsic kinetic term (k) and the effective availability of the reaction partner ($\langle B^- \rangle$). The flux (J) is the initial slope/rate at dark onset (t = 0), with sign convention depending on the plotted trace:

Eq. 3.4 $$J(0) = \frac{d[A^+]}{dt}\Big|_{t=0} = k_{\mathrm{obs}}[A^+(0)]$$

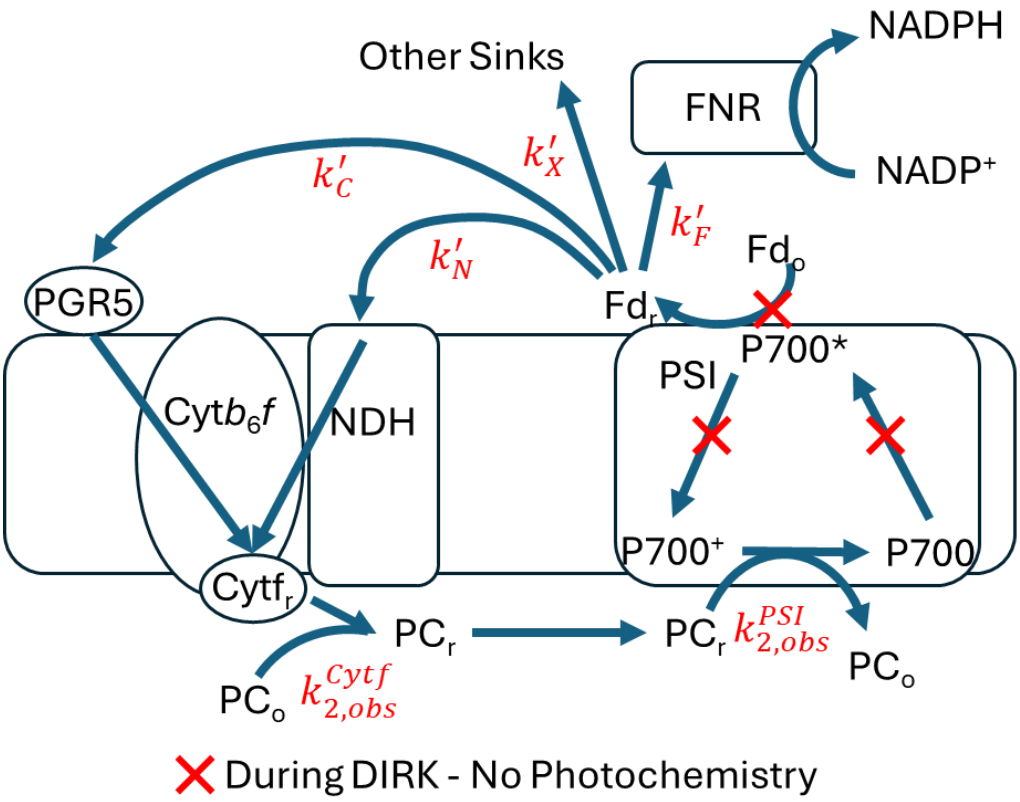

Fig. 1. Working model linking measured DIRK redox kinetics to rate constants of electron transport reactions. Schematic showing electron-transfer pathways between Cytochrome *b*$_6$*f* (Cyt*b*$_6$*f*), cytochrome *f* ($Cytf_r$), plastocyanin (PC_o/PC_r), PSI (P700/P700$^+$), and ferredoxin (Fd_o/Fd_r), including major downstream withdrawal of Fd_r by ferredoxin:NADP$^+$ oxidoreductase (FNR). Red boxes indicate the fitted or inferred rate parameters assigned to each pathway. Red X symbols denote light-driven processes suppressed during the DIRK; consequently, DIRK kinetics report relaxation of the pre-existing redox states via dark reactions, including reduction of P700$^+$ by PC_r and oxidation of Fd_r by competing sinks (FNR, PGR5-dependent pathways, NDH, and other sinks).

Working equations and parameter mapping

P700: a simple pseudo-first-order decay

During a DIRK, the reduction of oxidised P700 ($P700^+$) is driven by electron donation from reduced PC (PC_r) (Fig. 1). This interaction can be summarised by the kinetic schema:

K. 3.2 $$PC_r + P700^+ \overset{k_{2,eff}^{PSI}}{\rightarrow} PC_o + P700$$

Which is the simplified kinetic schema shown in vivo by Haehnel *et al.* (1994).

Here, $k_{2,\mathrm{eff}}^{PSI}$ is an effective second-order term that lumps encounter, dissociation, and electron-transfer steps (see Supplemental Derivations, PSI section).

The corresponding mass-action expression for the rate of $P700^+$ reduction is:

Eq. 3.5 $$J_{P700} = k_{2,eff}^{PSI}[PC_r][P700^+]$$

Over the short DIRK fitting window, $[PC_r]$ can be treated as approximately constant or represented by a time-averaged value $\langle PC_r \rangle_{0\to t}$, giving a pseudo–first-order form:

Eq. 3.6 $$[P700^+](\mathrm{t}) = [P700^+](0)e^{-k_{2,obs}^{PSI}t} + y0p$$

where $y0p$ is the offset/baseline value approached by the decay.

Eq. 3.7 $$k_{2,obs}^{PSI} = k_{2,eff}^{PSI}\,\langle PC_r \rangle_{0\to \mathrm{t}}$$

Thus, for P700⁺ DIRKs, the fitted $k_{2,\mathrm{obs}}^{PSI}$ reports an effective PSI turnover term scaled by the availability of reduced PC over the decay window. The flux of P700 at DIRK onset is obtained directly from the derivative of the fitted decay function (Eq. 3.6), evaluated at $t = 0$:

Eq. 3.8 $$J_{P700}(0) = \frac{d}{dt}\left([P700^+](0)e^{-k_{2,obs}^{PSI}t}\right)|_{t=0} = k_{2,obs}^{PSI}\,[P700^+](0).$$

Accordingly, the DIRK-derived P700 reduction flux scales with the fitted rate constant and the level of oxidised P700 at the start of the DIRK, $P700^+(0)$, with the negative sign indicating reduction of $P700^+$, as $P700^+$ is plotted on an oxidation scale. Full derivations and assumptions are provided in the Supplemental Derivations, PSI section.

Plastocyanin: competing PSI oxidation and Cyt*b*$_6$*f*-dependent reduction

During a DIRK, the reduction of oxidised PC (PC_o) is driven by electron donation from reduced Cyt*f* ($Cytf_r$) (Fig. 1). This interaction can be summarised by the kinetic schema (Hope, 2000):

K.3.3 $$Cytf_r + PC_o \overset{k_{2,eff}^{PSI}}{\rightarrow} Cytf_o + PC_r$$

This reaction is occurring simultaneously with the oxidation of PC by PSI (K. 3.2). Therefore, unlike P700, the PC signal during a DIRK reflects two opposing processes: oxidation of PC by PSI (K. 3.2 and Eq.3.5; Haehnel et al., 1994) and reduction of PC by Cyt*f* (Fig. 1; Hope, 2000). The net PC flux is written as:

Eq. 3.9 $$J_{PC} = -J_{PCo} + J_{PCr}$$

The oxidation and reduction terms are expressed as second-order mass-action processes:

Eq. 3.10 $$J_{PCo} = k_{2,eff}^{PSI}[PC_r][P700^+] = -J_{P700}$$

Eq. 3.11 $$J_{PCr} = k_{2,eff}^{Cytf}[Cytf_r][PC_o]$$

Under the assumptions detailed in the Supplemental Derivations, integration of this coupled form yields a biphasic pseudo-first-order solution for the oxidised PC signal:

Eq. 3.12 $$[PC_o](t) = ([PC_o](0) - B)e^{-k_{2,obs}^{Cytf}t} + Be^{-k_{2,obs}^{PSI}t} + y0c$$

where B is the amplitude of the component governed by the PSI-linked time constant and $y0c$ is the offset/baseline value approached by the decay.

. The $Cytf$-dependent observed rate constant is:

Eq. 3.13 $$k_{2,obs}^{Cytf} = k_{2,eff}^{Cytf}\langle Cytf_r\rangle_{0\to t}$$

This form provides a direct mapping from the fitted PC DIRK to two separable kinetic components: a PSI-linked component (parameterised by B and $k_{2,\mathrm{obs}}^{PSI}$) and a Cyt*f*-linked component (parameterised by $k_{2,\mathrm{obs}}^{Cytf}$ and $PC_{ox}(0) - B$). Because for every P700 reduced, an equivalent amount of PC_o is produced, observed rate constants for P700 and PC are identical (see Supplemental Derivations); the rate constant is therefore shared and defined as the slowest rate for the whole reaction (Kustin ***et al.***, 1965).

Flux proxies at DIRK onset are calculated from the derivative of each fitted component in Eq. 3.12, evaluated at $t = 0$. The Cyt*f*-dependent reduction component corresponds to the term with amplitude $(PC_{ox}(0) - B)$ and time constant $k_{2,\mathrm{obs}}^{Cytf}$, giving:

Eq. 3.14 $$J_{PCr}(0) = \frac{d}{dt}(([PC_o](0) - B)e^{-k_{2,\mathrm{obs}}^{Cytf}t})\,|_{t=0} = k_{2,\mathrm{obs}}^{Cytf}\,([PC_o](0) - B).$$

The PSI-linked oxidation component corresponds to the term with amplitude B and time constant $k_{2,\mathrm{obs}}^{PSI}$, giving:

Eq. 3.15 $$J_{PCo}(0) = \frac{d}{dt}(Be^{-k_{2,\mathrm{obs}}^{PSI}t})\,|_{t=0} = k_{2,\mathrm{obs}}^{PSI}\,B.$$

In this convention, both derivatives are negative because each component decays over the DIRK window. The component flux magnitudes at $t = 0$ are therefore determined by the product of the fitted rate constant and the corresponding component amplitude, and the net

PC flux follows Eq. 3.11 (with sign determined by oxidation versus reduction). Full derivations and parameter definitions are provided in the Supplemental Derivations, PC/P700 coupling section.

Ferredoxin: combined activity of sinks determines the observed decay constant

During the DIRK, reduced ferredoxin ($[Fd_r]$) is oxidised by multiple sinks (Zhu *et al.*, 2013), potentially including PGR5- and NDH-mediated CEF (Fig. 1).

K. 3.4 $Fd_r \xrightarrow{k'_F} FNR;\quad Fd_r \xrightarrow{k'_C} CEF_{PGR5};\quad Fd_r \xrightarrow{k'_N} CEF_{NDH};\quad Fd_r \xrightarrow{\varepsilon k'_x}$ other sinks

The net withdrawal flux from $[Fd_r]$ is written as a first-order mass-action expression:

Eq. 3.16 $$J_{Fd} = (k'_F + k'_C + k'_N + \varepsilon k'_x)[Fd_r].$$

Here, k'_F represents FNR-associated oxidation of Fd, k'_C represents the pseudo-first-order PGR5-CEF-associated sink, k'_N represents the pseudo-first-order NDH-CEF-associated sink, and $\varepsilon k'_x$ represents additional sinks that oxidise Fd (such as thioredoxin, nitrogen metabolism, etc). It should be noted that k'_F is best characterised by the Michaelis-Menton equation which doesn't match to an exponential decay function (Cassan *et al.*, 2005; Hald *et al.*, 2008; Kimata-Ariga *et al.*, 2019). However, for this analysis, where FNR-associated oxidation is clumped with the exponential functions of CEF, Fd signal it best described the in pseudo-first-order terms (Zhu *et al.*, 2013).

Integrating Eq. 3.16 yields a pseudo-first-order exponential decay:

Eq. 3.17 $$[Fd](t) = [Fd](0)e^{-k_{obs}^{Fd}t} + y0f$$

where $y0f$ is the asymptotic upper baseline, that is, the value approached by the rising $[Fd_{red}]$ trace.

Eq. 3.18 $$k_{obs}^{Fd} = k'_F + k'_C + k'_N + \varepsilon k'_x$$

Thus, for Fd DIRKs, k_{obs}^{Fd} reports the summed first-order sink activity withdrawing electrons from reduced Fd, independent of signal amplitude. The flux at DIRK onset is obtained directly from the derivative of the fitted decay function (Eq. 3.17), evaluated at $t = 0$:

Eq. 3.19 $$J_{Fd}(0) = \frac{d}{dt}\left([Fd](0)e^{-k_{\mathrm{obs}}^{Fd}t}\right)|_{t=0} = k_{\mathrm{obs}}^{Fd}\,[Fd](0).$$

Accordingly, the DIRK-derived Fd flux scales with the product of the fitted rate constant and the reduced Fd level at the start of the DIRK, $Fd(0)$(with the positive sign indicating oxidation of Fd_r, as Fd_r is plotted on an oxidation scale). Full derivations and assumptions are provided in the Supplemental Derivations, Fd section.

Measured signals and notation

NIR absorbance measurements made using DKN are spectrally deconvolved to yield time-resolved component traces for P700, PC, and Fd (Fig. 2a; see also M&M section on DKN). These component traces report relative changes in redox state over time and are treated as the state variables $P700^+(t)$, $PC_o(t)$, and $Fd_r(t)$ in the kinetic analysis. Absolute pool sizes are not required for the comparative analyses in this chapter because fluxes are derived from within-trace amplitudes and fitted rate constants obtained from the DIRK relaxation itself (Fig. 2b).

DIRK principle and definition of flux at dark onset

In a DIRK, actinic light is briefly interrupted, and the relaxation of redox signals is recorded during a short dark interval (Sacksteder & Kramer, 2000). As illustrated in Fig. 2b with example of $P700^+$, shutter closure causes oxidation to cease, and the pre-existing oxidised fraction relaxes (reduces) rapidly toward the dark steady-state levels. The initial relaxation rate at dark onset (t = 0) best reflects the operating electron-transfer flux immediately before illumination was interrupted. Accordingly, for any carrier signal, the DIRK-derived flux is defined as the slope at t = 0 (Eq. 3.8). For a single-exponential decay case of $P700^+$ (Eq. 3.6), the initial slope is defined as (Eq. 3.8):

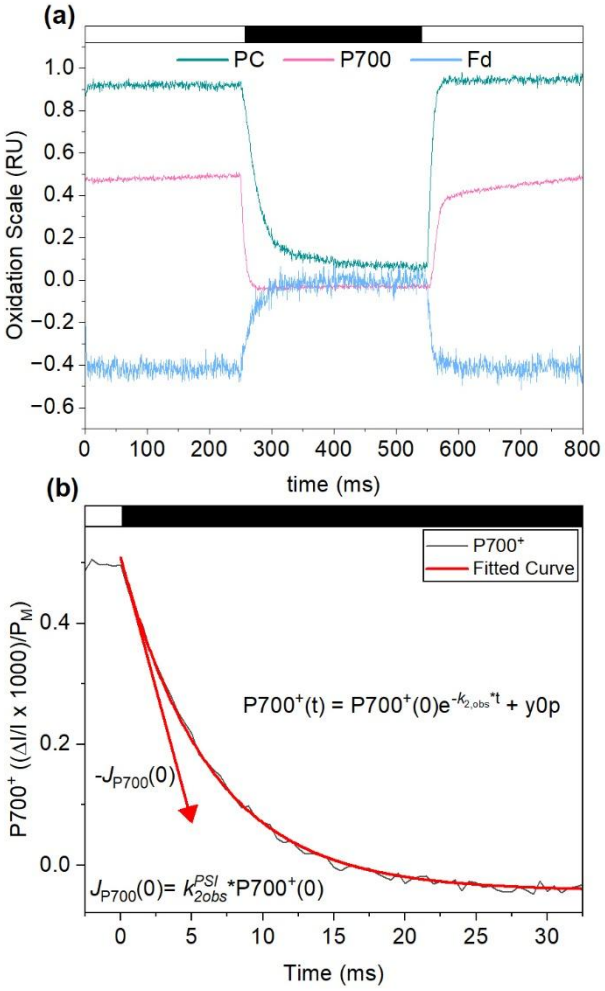

Figure 2. DIRK principle and extraction of flux from relaxation kinetics. (a) Representative DKN DIRK traces showing the redox-state changes of plastocyanin (PC; green), P700 (magenta), and ferredoxin (Fd; blue) during a brief dark interval (black bar). Signals are shown on a relative oxidation scale (RU) with increasing numbers meaning more oxidised, illustrating rapid relaxation toward dark redox equilibria upon shutter closure and recovery after re-illumination. **(b)** Example $P700^+$ DIRK (black) during the first 30 ms of the 300-ms DIRK with a single-exponential fit (red). The flux is the initial slope of the relaxation curve, defined as the derivative at t = 0.

$$J_{P700}(0) = k_{2,obs}^{PSI}\,[P700^+](0)$$

DIRK curve fitting and parameter extraction

For each genotype and time point, the relevant redox relaxation curves were fitted in OriginPro 2025b to pseudo-first-order exponential models derived from the mass-action formulations. Fd DIRKs were fitted as a single exponential decay, yielding k_{obs} as a compact descriptor of the combined sink activity withdrawing electrons from reduced Fd (Eq. 3.17).

While $P700^{+}$ relaxation was fitted as a single exponential decay to obtain the rate constant for $P700^{+}$ reduction (Eq. 3.6), PC reduction required a biphasic model reflecting the superposition of PSI-linked oxidation and Cyt*f*-dependent reduction (Eq. 3.12), as the rate constants for P700 reduction and PC oxidation are shared. To constrain the PSI-linked kinetic component of PC oxidation, P700 and PC traces were fitted jointly (Fig. 3). This approach exploits the shared PSI-linked oxidation time constant present in both P700 and the PSI oxidation component of PC (See supplemental derivations PC section). Joint fitting anchors the oxidation component and improves separation of the PC reduction term attributable to Cyt*f*-dependent electron delivery to PC and the PC oxidation term attributable to PSI oxidation of PC (Fig. 3c).

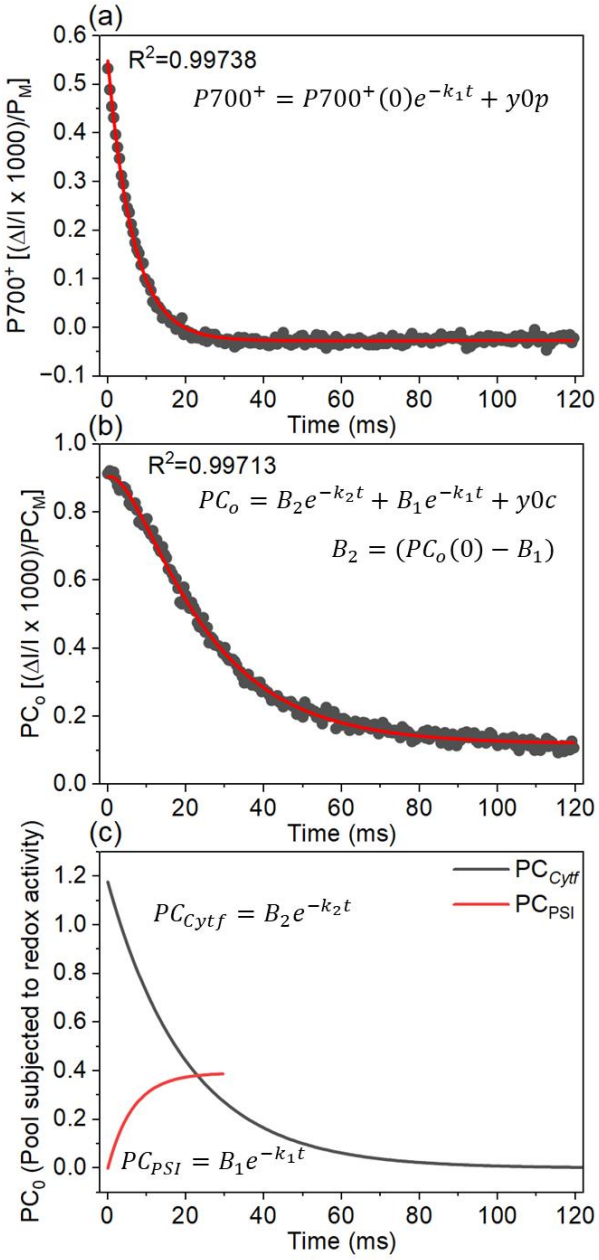

Fig. 3. Joint fitting of P700 and PC DIRK traces to constrain the PSI-linked component of PC oxidation. To separate PSI-driven oxidation of PC from Cyt*f*-dependent PC reduction, P700 and PC traces were fitted jointly using a shared PSI-linked time constant (k_1). Time is shown on the DIRK timescale (t = 0 ms denotes the start of the dark interval). (**a**) Example $P700^+$ DIRK fit using a single exponential decay, $P700^+(t) = P700^+(0)e^{-k_1 t} + y_{0p}$. (**b**) Example PC_o DIRK fit using a constrained biphasic function, $PC_o(t) = B_2 e^{-k_2 t} + B_1 e^{-k_1 t} + y_{0c}$, with $B_2 = (PC_o(0) - B_1)$, k_1 in the PC fit was simultaneously shared with the k_1 parameter in the P700 fit. (**c**) Decomposition of the fitted PC_o trace into the Cyt*f*-linked delivery term, $PC_{Cytf} = B_2 e^{-k_2 t}$, and the PSI-linked oxidation term, $PC_{PSI} = B_1 e^{-k_1 t}$.

Plant material and growth conditions

S. viridis ecotype ME034V-1 WT and the *pgr5-1* line lacking functional PGR5, generated using CRISPR/Cas9 gene-editing as described by Woodford *et al.* (2025b), were used in this study. Only the *pgr5-1* line was used in this study as Woodford *et al.* (2025b) reported no significant difference between *pgr5-1* and *pgr5-3* lines. *S. viridis* seeds were germinated directly on soil in communal pots containing seed-raising mix (Debco, Tyabb, Australia) supplemented with 5 g L^{-1} of slow-release fertiliser (Osmocote, Scotts, Bella Vista, Australia). One week after germination, individual seedlings were transferred to 0.5 L pots containing the same soil and fertilizer mixture, with one plant per pot. For chlorophyll fluorescence, P700 absorption spectroscopy and ECS measurements, plants were grown in a controlled environment room at 28°C day / 22°C night under a 16 h photoperiod, irradiance of 380 µmol photons m^{-2} s^{-1} and 60% humidity. For Dual-KLAS-NIR measurements, plants were grown in a Conviron GEN1000-ECO growth chamber under the same conditions. Measurements were performed on the youngest fully expanded leaves of plants at 3–4 weeks of age.

Saturating pulse analysis of chlorophyll fluorescence and P700 spectroscopy

PSII and PSI quantum yields were monitored concurrently using chlorophyll fluorescence and P700 redox spectroscopy with a DUAL-PAM/F (Heinz Walz GmbH, Effeltrich, Germany) under 635 nm red actinic light with red-light saturating pulses (300 ms, 12,000 µmol photons m^{-2} s^{-1}). The redox state of P700 was assessed using a dual-wavelength unit (830/875 nm). Leaves were dark-adapted for 30 min before measurement and a saturating pulse was first applied to determine the maximum (F_M) and minimum (F_0) fluorescence levels, after which the maximal $P700^+$ signal (P_M) was recorded by applying a saturating pulse at the end of an 8-s far-red illumination (720 nm), with the minimal $P700^+$ signal (P_0) recorded directly following the saturating pulse. Leaves were then acclimated to low-light (LL, 50 µmol m^{-2} s^{-1}) for 15 min before actinic irradiance was increased to high-light (HL, 1,500 µmol m^{-2} s^{-1}) for 1 min, with t = 0 defined as the LL-HL transition, initiating photosynthetic induction.

Saturating pulses were applied at 2, 5, 10, 15, 20, 30, and 60 s during photosynthetic induction to analyse light energy-partitioning within PSI and PSII. To minimise perturbation of induction kinetics by repeated saturating pulses, the time points were divided between two measurements (2, 10, 20, and 60 s in one; 5, 15, and 30 s in the other), which were then combined to obtain the full series.

For PSII, the effective quantum yield was calculated as $\varphi_{II} = (F_M' - F)/F_M'$, where F is the steady-state fluorescence immediately prior to the saturating pulse and F_M' is the maximal

fluorescence during the saturating pulse. The yields of regulated and non-regulated energy dissipation were calculated as $\varphi_{NPQ} = F/F_M' - F/F_M$ and $\varphi_{NO} = F/F_M$, respectively (Kramer *et al.*, 2004; Klughammer & Schreiber, 2008a). The fraction of open PSII reaction centres (qL), providing a proxy for the redox state of the plastoquinone pool, was calculated according to the lake model as $qL = ((F_M' - F)/(F_M' - F_0')) \times (F_0'/F)$ (Klughammer & Schreiber, 2008a).

For PSI, the photochemical yield (φ_I) and the yields of non-photochemical reactions due donor (φ_{ND})- or acceptor (φ_{NA})-side limitation were calculated from P700 absorbance signals as $\varphi_I = (P_M' - P)/(P_M - P_0)$, $\varphi_{ND} = (P - P_0)/(P_M - P_0)$, and $\varphi_{NA} = (P_M - P_M')/(P_M - P_0)$, where P is the steady-state $P700^+$ signal immediately prior to the saturating pulse, P_M' is the maximal $P700^+$ signal during the saturating pulse under light (Klughammer & Schreiber, 2008c).

Dual-KLAS-NIR signal deconvolution and experimental protocols

Signal deconvolution and differential model plot generation

Near-infrared (NIR) absorbance changes attributable to P700, PC, and Fd were measured using the DUAL-KLAS-NIR (Heinz Walz, Effeltrich, Germany). The instrument records four pulse-modulated dual-wavelength transmittance difference signals in the NIR region, corresponding to the wavelength pairs 785–840, 810–870, 870–970, and 795–970 nm. These signals were deconvoluted in the DUAL-KLAS software using differential model plots (DMPs) for Fd, P700, and PC to obtain time-resolved traces for each component (Klughammer & Schreiber, 2016).

DMPs generated for *pgr5-1* were similar in shape and deconvolution to WT (Table S1). Therefore, DMPs generated for WT leaves were applied to all measurements. To generate DMPs, the raw wavelength-pair signals were first balanced using the "NIR Bal." function to bring the baseline close to zero and to minimise offsets across channels. Reference protocols supplied with the Dual-KLAS software were then used to elicit single component-dominated transients for P700, PC, and Fd respectively. For each reference protocol, the averaged transient was transferred to the fitting interface and two fitting intervals were defined: a baseline interval and a component-selective interval. The component model spectrum was extracted using "Get Model Spectrum", then normalised by scaling the largest extracted differential value to 1.0 and proportionally scaling the remaining wavelength-pair values, and saved as a component-specific .KMS file (Klughammer & Schreiber, 2016). Component model spectra were calculated from the mean of 10 averaged spectra for Fd, 25 averaged spectra for P700, and 6 averaged spectra for PC. These model spectra were then imported into the

"Deconvolution" panel for online separation of P700, PC, and Fd signals during all subsequent measurements.

DUAL-KLAS-NIR measurements of P700, PC, and Fd redox changes during induction

To visualise genotype-dependent redox changes in P700, PC, and Fd during induction without perturbation by saturating pulses or dark-interval relaxations, leaves were first dark-adapted for 30 min and maximum deconvoluted signal amplitudes for P700, PC, and Fd were determined using the automated “NIRmax” routine. The maximum quantum efficiency of PSII was then determined as $F_V/ F_{M =} (F_M – F_0)/F_{M.}$ Leaves were subsequently illuminated at LL for 15 min before actinic irradiance was increased to HL for 60 s, with t = 0 defined as the irradiance transition. Deconvoluted traces of P700, PC, and Fd were recorded and later normalised to their respective NIR maxima. At the end of the measurement, P_M was measured again to confirm that no substantial PSI photodamage had occurred over the course of the experiment. For each biological replicate, these traces were then normalised to the corresponding per-sample NIRmax values for P700, PC, and Fd to express the signals in relative units.

DIRK measurements of P700, PC, and Fd relaxation kinetics

For the DIRK protocol, leaves were first dark-adapted for 30 min and maximum deconvoluted signal amplitudes for P700, PC, and Fd were determined using the automated NIRmax routine in the dark-adapted state prior to induction measurements. Leaves were then illuminated at LL for 15 min, after which actinic irradiance was increased to HL for 60 s, with t = 0 defined as the irradiance transition. During the high-light period, dark-interval relaxation kinetics (DIRKs) were imposed using a fast-kinetics trigger file to apply 300 ms dark intervals every 1 s for the first 10 s and every 5 s thereafter. Because occasional software-triggering failures occurred at the final scheduled time point, DIRK datasets were analysed through 55 s.

Thylakoid membrane energisation analysis

Electrochromic shift (ECS) was measured using a Dual-PAM-100 (Heinz Walz, Effeltrich, Germany) equipped with the P515/535 emitter-detector module, following the general ECS measurement framework described for this module by Klughammer and Schreiber (2008b). ECS signals were recorded as absorbance changes between 550 and 520 nm and normalised to the amplitude of the ECS response to a 20 µs saturating pulse at 14,000 µmol m^{-2} s^{-1} applied to dark-adapted leaves (ECS_{ST}).

Leaves were dark-adapted for 30 min prior to measurement, then acclimated at LL for 15 min before actinic irradiance was increased to HL for 60 s, with t = 0 defined as the irradiance transition. At the onset of the irradiance increase, ECS decay kinetics were measured using a fast-kinetics trigger file with the clock function in the ECS software to impose repeated 300 ms dark intervals. Dark intervals were applied every 1 s for the first 10 s following the irradiance step, then every 5 s thereafter, matching the DIRK approach used for the DKN measurements. Each dark interval was fit with a first-order exponential decay in OriginPro (OriginLab, Northampton, MA, USA). The amplitude of the fitted ECS decay was used as a relative estimate of proton motive force (*pmf*), and proton conductivity of the thylakoid membrane (g_{H^+}) was calculated as the inverse time constant of the decay (1/τ) (Cruz *et al.*, 2001). The initial rate of ECS relaxation at dark onset was calculated from the derivative of the fitted exponential at t = 0 and is reported here as v_{H^+} (Avenson *et al.*, 2005b).

Statistical analysis

Statistical analyses were performed in OriginPro 2025b (OriginLab, Northampton, MA, USA). Induction time-course data were analysed by repeated-measures ANOVA, with genotype and time treated as factors as appropriate. Endpoint comparisons, including measurements such as F_V/F_M and changes in P_M, were analysed by one-way ANOVA. When both variables were continuous, relationships between measured parameters were analysed by analysis of covariance (ANCOVA). Where ANOVA or ANCOVA indicated a significant effect, pairwise comparisons were assessed using Tukey's post hoc test. Statistical significance was accepted at $P < 0.05$. Number of biological replicates for each analysis is indicated in figure legends.

Data normalisation and preprocessing (Python)

Raw DIRK and induction datasets were normalised and pre-processed in Python using custom Jupyter notebooks executed in VS Code. These scripts were developed with the aid of ChatGPT (GPT-4 and 5) and were primarily designed to robustly import Walz-exported files and standardize trace formatting prior to downstream fitting.

Walz exports were batch-collated and sample metadata (e.g., genotype and replicate identifiers) were parsed from folder and file names during import. Raw tables were imported using routines compatible with Walz "Western European" formatting (semicolon-delimited files and comma decimal separators), and non-data header/preamble lines were removed where present. Column headers were standardised, numeric columns were coerced to numeric values (invalid entries converted to missing data), and incomplete or malformed rows were

excluded. Time axes were then harmonised by detecting the exported time field (e.g., time/ms or time/s) and converting all traces to a consistent time base prior to export.

Per-sample maxima ($P700_M$, PC_M, and Fd_M) were extracted from the corresponding Walz report outputs and used to scale deconvoluted P700, PC, and Fd traces to relative units (signal/$P700_M$, signal/PC_M, signal/Fd_M) before baseline correction. Normalised traces were then baseline-corrected by subtracting the mean of the first 4s in the dark before measurements. For DIRK-derived summary metrics, standardised time windows were used to calculate mean values for the baseline and dark-interval segments, with sign conventions applied where needed to maintain consistent oxidation/reduction polarity across channels. Finally, all cleaned and normalised traces were exported as consistently formatted trace tables for downstream kinetic fitting and plotting in OriginPro 2025b.

Results

P700 and PC in *S. viridis pgr5* mutant are oxidised during photosynthetic induction

To establish whether the electron transfer kinetics of PSI and its electron donor and acceptor can be resolved in the absence of PGR5 in *S. viridis*, I first examined the max redox levels for P700, PC, and Fd. Following NIR calibration, maximum redox amplitudes for P700, PC, and Fd were determined for each biological replicate, and all signals were normalised to their respective maxima to enable quantitative comparison of redox dynamics during the photosynthetic induction.

Next, I studied the redox behaviour of the P700, PC, and Fd during the transition from LL to HL. Both WT and *pgr5-1* exhibited oxidation of P700 and PC upon the LL-HL transition, seen as an increase in the levels of $P700^+$ and PC_o signals (Fig. 4a,b). Steady-state oxidation levels (50-60s) were significantly different between genotypes, with PC stabilising at 30% of its maximum in *pgr5-1* vs 60% in WT, and P700 stabilising at 40% of its maximum in *pgr5-1* vs 65% in WT (Fig. 4a,b). In addition, Fd became significantly more reduced in *pgr5-1*, reaching 60% of its max signal compared with 40% in WT (Fig. 4c). Importantly, the maximum quantum efficiency of PSII photochemistry (F_V/F_M) was also similar between WT and *pgr5-1* before measurements (Fig. 4d). The maximal photo-oxidisable P700 (P_M) signal, reflecting functional PSI, measured before and after the HL treatment was similar between WT and *pgr5-1*, indicating that no significant difference PSI photodamage over the duration of these measurements occurred (Fig 4e).

These results indicate that, in contrast to the C_3 *pgr5* mutants, where PSI is persistently over-reduced (Tikkanen *et al.*, 2014; Yamori *et al.*, 2016), significant levels of oxidised P700 and PC in *S. viridis pgr5-1* mutant could enable necessary dynamic range for redox kinetics analysis to quantify electron fluxes on the donor and acceptor sides of PSI.

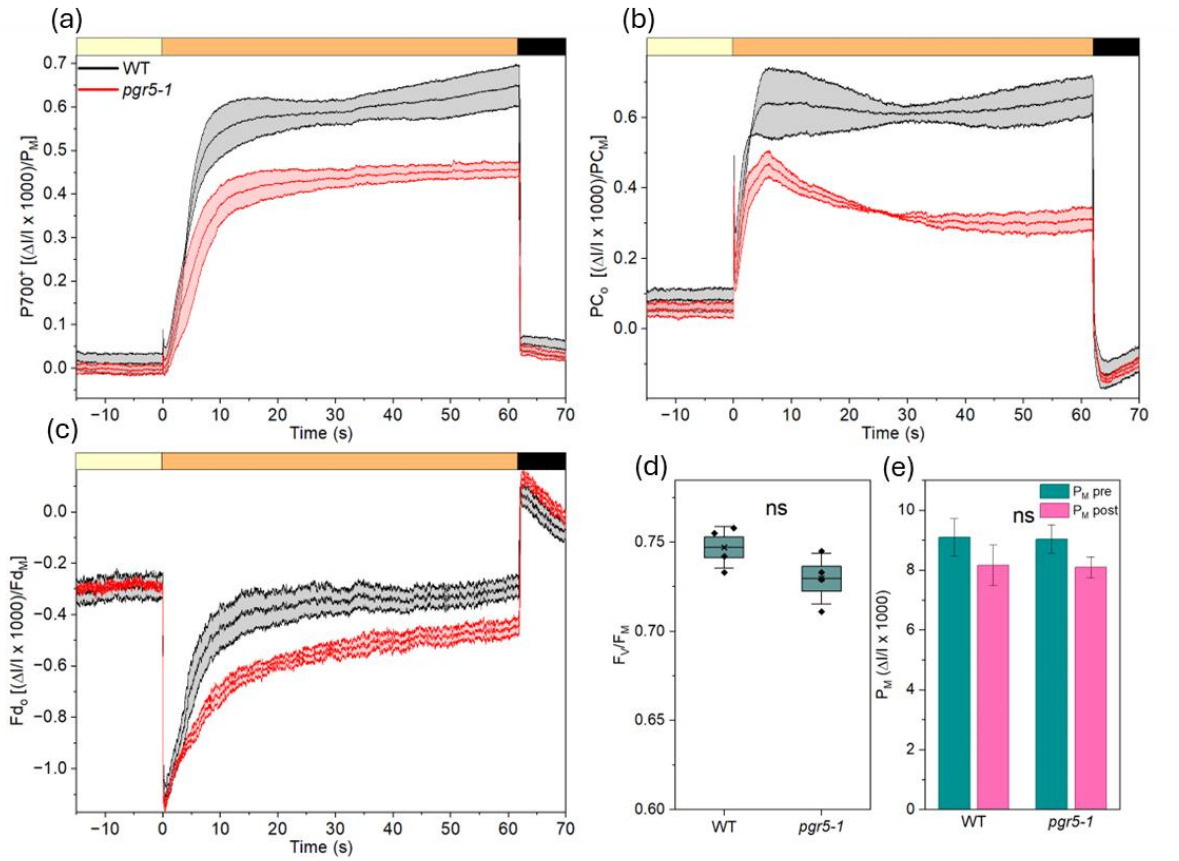

Fig. 4. Redox responses of P700, PC and Fd during a 50 (LL) to 1,500 (HL) µmol photons m^{-2} s^{-1} transition. LL-HL transition occurs at 0 seconds (**a-c**). Coloured bars above panels (**a–c**) indicate the actinic light regime: pale yellow, 50 µmol m^{-2} s^{-1}; light orange, 1,500 µmol m^{-2} s^{-1}; and black, light off. Deconvoluted signal traces of P700 (**a**), PC (**b**), and Fd (**c**) during illumination, normalised to their respective NIR maxima and plotted on an oxidation scale. Traces show the mean (n=4), with shaded bands indicating SE. For the late illumination phase, mean values over 50–60 s were calculated for each biological replicate and compared between genotypes. P700, PC and Fd were significantly more reduced in *pgr5-1* than in WT during this interval (Welch's t-test; P700, P = 0.047; PC, P = 0.0135; Fd, P = 0.0252). d) Maximum PSII efficiency (F_V/F_M) measured from the same plants. (**e**) P_M (maximal photo-oxidisable P700) measured before (pre) and after (post) the light treatment. (**d**) Box plots show the median (centre line), interquartile range (box), whiskers indicating the full range, and individual points (n = 4); (**e**) Bars show means ± SE (n = 4); *ns*, no significant difference (one-way ANOVA, P = 0.05).

P700 is transiently more oxidised in *pgr5-1* mutant during the photosynthetic induction

To monitor how light absorbed by PSI and PSII is partitioned between the photochemical and non-photochemical reactions in WT and *pgr5-1* during photosynthetic induction, we performed saturating-pulse (SP) analysis upon the transition from LL-HL (Fig. 5). PSII parameters were significantly different between genotypes (Fig. 5a-c). φ_{II}, the PSII photochemical yield, dropped sharply in both genotypes upon the LL-HL shift and remained low, with *pgr5-1* significantly lower than WT (Fig. 5a). φ_{NO}, the yield of non-regulated energy dissipation, rose rapidly upon the transition and then gradually declined, remaining significantly higher in *pgr5-1* compared to WT (Fig. 5b). φ_{NPQ}, the yield of regulated energy dissipation, increased upon the transition but was significantly lower in *pgr5-1* than WT (Fig. 5c).

The PSI photochemical yield, φ_I, was similar between genotypes at low light and decreased sharply upon the shift to high light in both genotypes (Fig. 5e). At 2 s, φ_I was similar in WT and *pgr5-1*, whereas after 2 s, WT maintained higher φ_I than *pgr5-1* for the remainder of the high-light period (Fig. 5e). φ_{ND}, the fraction of P700 which is oxidised due to limited by electron supply, increased under high light in both genotypes (Fig. 5f). However, at 2 s, *pgr5-1* had significantly higher φ_{ND} than WT, while at 5-60 s of HL, *pgr5-1* showed significantly lower φ_{ND} than WT. WT and *pgr5-1* also showed a gradual decrease in PSI acceptor-side limitation, φ_{NA} reflecting the fraction of PSI which is reduced due to lack of acceptor availability (Fig. 5g). However, at 2 s, *pgr5-1* leaves exhibited significantly lower φ_{NA} and, at 5-60 s of HL, significantly higher φ_{NA} compared to WT (Fig. 5g). qL, an estimate of the redox state of Q_A and the PQ pool, showed no significant differences at 2 s, however *pgr5-1* was significantly lower than WT from 5-60 s indicating an over-reduction of the PQ pool (Fig. 5d)

Together, these SP-derived parameters indicate that *pgr5-1* undergoes a brief phase in which PSI is more oxidised than in WT, followed by the characteristic more reduced PSI later during induction. A more oxidised PSI in *pgr5-1* at 2 s post high-light transition might present a transient window in which the effects of PGR5 loss of electron fluxes in PSI can be resolved without the confounding factors like the electron congestion at the acceptor side of PSI.

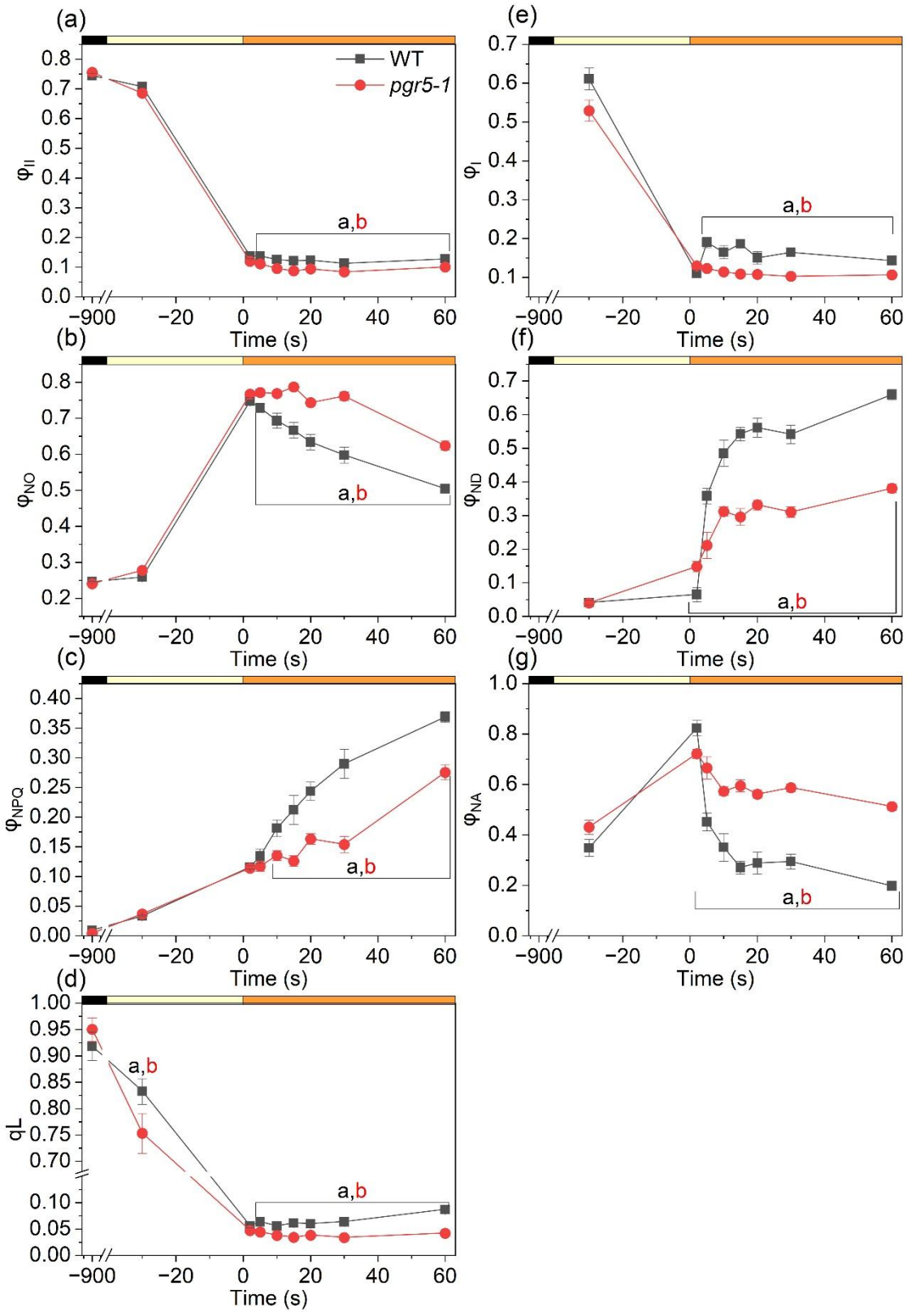

Fig. 5. Quantum yields within PSI and PSII upon LL-HL transition in *S. viridis* WT and *pgr5-1*. Leaves were first dark adapted (Light off; black bars) then acclimated at LL (50 µmol m^{-2} s^{-1}; light yellow bars) and shifted to HL (1,500 µmol m^{-2} s^{-1}; light orange bars), and the

yields were probed with saturating pulses throughout the induction. (**a**) Effective PSII quantum yield, φ_{II}. (**b**) Non-regulated energy dissipation in PSII, φ_{NO}. (**c**) Regulated energy dissipation in PSII, φ_{NPQ}. (**d**) qL (lake model) during induction, shown here as a proxy for the redox state of the plastoquinone pool. (**e**) Effective PSI quantum yield, φ_{I}. (**f**) Donor-side limitation of PSI, φ_{ND}. (**g**) Acceptor-side limitation of PSI, φ_{NA}. PSI quantum yields (e–g) were not determined in dark-adapted leaves and are therefore reported from the LL phase onward. Mean ± SE, n = 5. Different letters denote significant differences between genotypes within the indicated time window (two-way repeated-measures ANOVA with post-hoc Tukey test, $P = 0.05$).

ECS dynamics show an early deficit in *pmf* generation in *pgr5-1*

ECS measurements were used to assess *pmf* and proton fluxes during the LL-HL transition. *pmf* increased rapidly under HL in both genotypes but was significantly lower in *pgr5-1* than WT from 2 s onward (Fig. 6a). g_{H^+}, reporting on the proton conductivity of ATP synthase, was significantly different at 7-20 s and 45-55 s (Fig. 6b); however, there was no genotype × time interaction (Greenhouse–Geisser: F (1.75,8.75) = 1.47, P = 0.277), indicating no evidence that over the time course the g_{H^+} response was differed between WT and *pgr5-1*.

Together, these measurements showed impaired *pmf* generation in *pgr5-1* starting from 2 s of the induction, which was not due to lower proton conductivity and could instead be caused by lower proton influx into the lumen. While the derivative of the ECS exponential decay, v_{H^+}, is conventionally used to estimate proton flux under steady-state conditions, this experiment was conducted during photosynthetic induction rather than steady-state, violating the assumption required for this interpretation (Avenson *et al.*, 2005b). v_{H^+} is assumed to be efflux and did not differ between genotypes across induction (Fig. 6c).

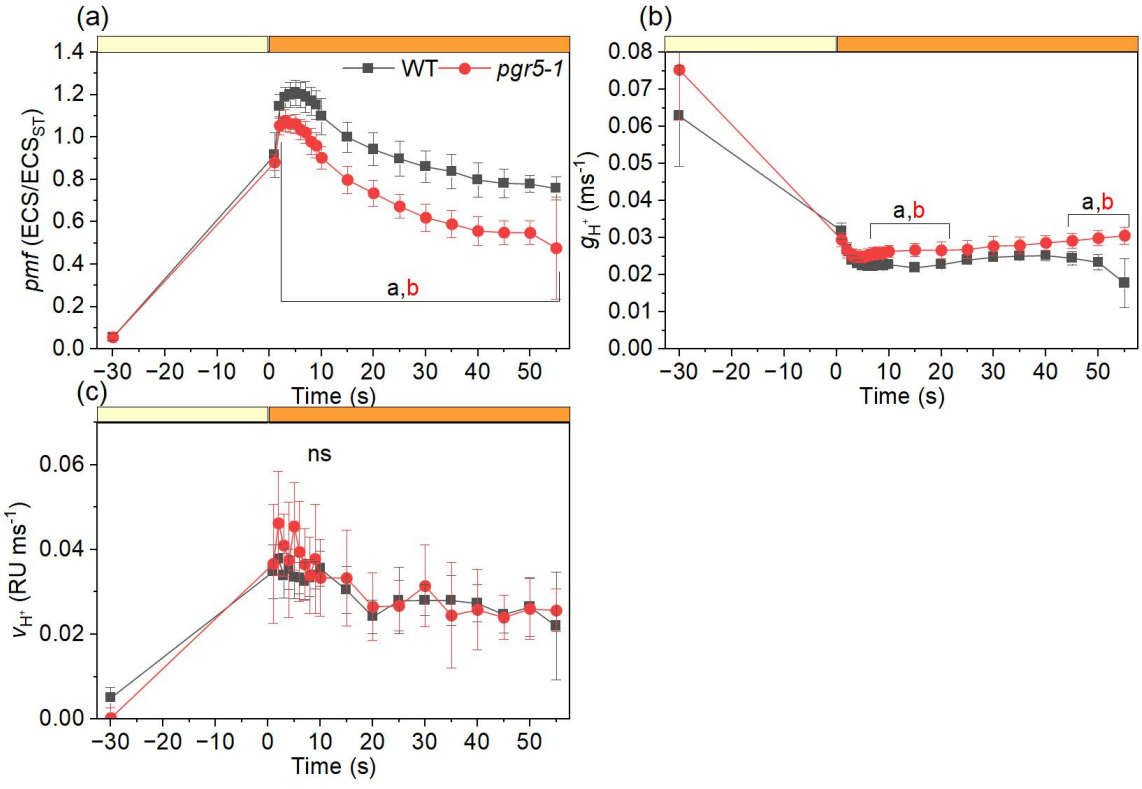

Fig. 6. ECS dynamics during photosynthetic induction in *S. viridis* WT and *pgr5-1*. Plants were LL (50 µmol m^{-2} s^{-1}; light yellow bars) adapted for 15 mins prior to HL (1,500 µmol m^{-2} s^{-1}; light orange bars). Time at 0 represents the start of the HL phase. (**a**) Proton motive force (*pmf*) estimated from ECS amplitude normalised by the maximum ECS amplitude of a single-turnover flash in the dark (ECS_{ST}). (**b**) g_{H^+}, proton conductivity of the thylakoid membrane. (**c**)

v_{H^+} calculated as the initial rate of ATP synthase proton efflux. Data are shown as Mean ± SE, n = 6. Brackets and letters denote significant genotype differences within the indicated time window (two-way repeated-measures ANOVA with Tukey's post hoc test; *P* =0.05); ns, not significant.

Fd DIRKs: *pgr5-1* shows lower rate of Fd oxidation

To test how loss of PGR5 alters electron withdrawal from PSI during the induction, Fd DIRKs were measured during the LL-HL transition (Fig. 7a). Fd oxidation kinetics during the DIRK (Fig. 7a,b) were fitted to obtain fluxes as defined in the Experimental approach and quantitative framework (Eq. 3.16 and Eq. 3.17). Traces in Fig. 7a and 7b are plotted on an oxidation scale (Fd_o), as output from the DKN deconvolution; where the reduction state of the total Fd pool is reported (Fig. 7d), the signal is inverted ($Fd_r = -Fd_o$) such that increasing values reflect greater Fd reduction.

Fd DIRKs were well described by a single exponential decay (Eq. 3.17; residual diagnostics in Fig. S1), where the fitted decay constant, k_{obs}^{Fd}, reports the summed effective sink activity withdrawing electrons from Fd_r and is independent of signal amplitude (Eq. 3.18). Across induction, k_{obs}^{Fd} was lower in *pgr5-1* relative to WT, consistent with a decreased effective capacity for electron withdrawal from Fd_r (Fig. 7c). Because k_{obs}^{Fd} represents a composite of multiple sinks, an empirical $\Delta k_{\mathrm{obs}}^{Fd_r} \equiv k_{\mathrm{obs}}^{\mathrm{WT}} - k_{\mathrm{obs}}^{\mathrm{pgr5}}$ shows the difference between genotypes (Fig. 7c). The reduced fraction of Fd at DIRK onset, $Fd_r(0)$ (reported on a relative scale where 0 as oxidised ground state and 1 is fully reduced pool) was significantly higher in *pgr5-1* from 1 s onward, indicating more reduced Fd pool throughout induction (Fig. 7d). The Fd oxidation flux (J_{Fd}) was defined as the initial rate of Fd oxidation at DIRK onset (t = 0). At 1 s, *pgr5-1* showed significantly lower J_{Fd} than WT (Fig. 7e) but, after 1 s, J_{Fd} was not different between genotypes.

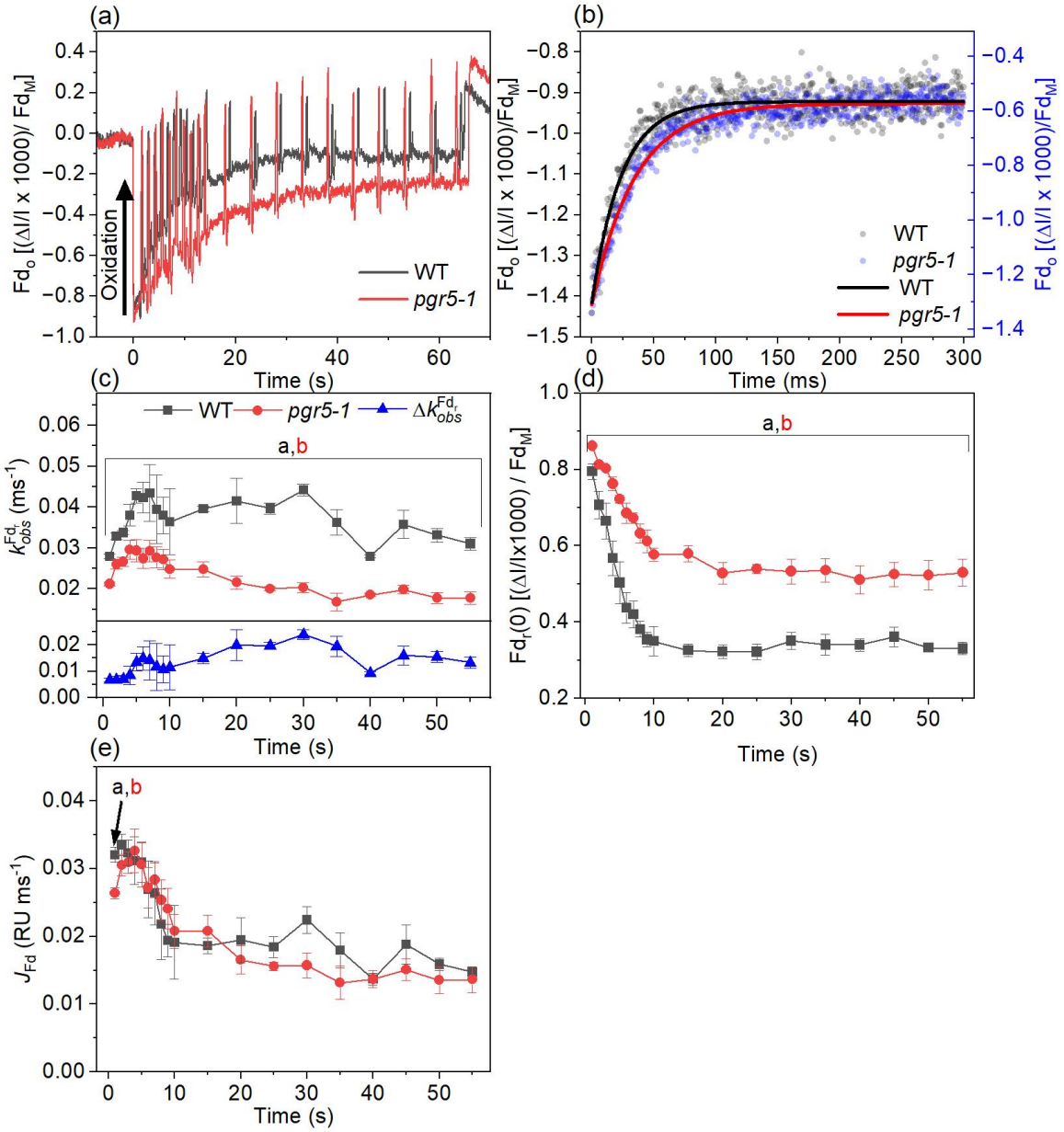

Fig. 7. Ferredoxin DIRK kinetics in *S. viridis* WT and *pgr5-1*. Plants were LL (50 µmol m^{-2} s^{-1}) acclimated for 15 min prior to the HL (1,500 µmol m^{-2} s^{-1}) transition. (**a**) Representative raw Fd_o DIRK trace from WT and *pgr5-1*, normalised to Fd$_M$ (plotted on an oxidation scale as output from DKN deconvolution; arrow indicates the direction of oxidation). Time t = 0 s denotes the start of the HL phase. (**b**) Representative fits from a single WT and *pgr5-1* replicate at the 5 s DIRK, shown on the DIRK timescale (t = 0 denotes the start of the dark interval). Traces were modelled using a single-exponential function (Eq. 3.17) and overlaid after scaling to the same start and end points for visual comparison of kinetics; WT (left y-axis; black) and *pgr5-1* (right y-axis; blue). (**c**) Observed first-order decay constant for Fd oxidation, k^{Fd}_{obs}; the lower panel shows $\Delta k_{obs} = k^{Fd}_{obs,WT} - k^{Fd}_{obs,pgr5}$. (**d**) The reduced fraction of Fd at t = 0 during a DIRK, $Fd_r(0)$ ($Fd_r = -Fd_o$; plotted on a reduction scale such that increasing values reflect greater Fd reduction). (**e**) Fd oxidation flux. (**c–e**) time is reported as cumulative actinic time (excluding the 300 ms dark intervals). Mean ± SE, n = 3. Letters denote significant genotype differences

within the indicated time window (two-way repeated-measures ANOVA with Tukey's post hoc test; $P = 0.05$).

P700 DIRKs: P700 flux is decreased in *pgr5-1* with a temporal delay relative to acceptor-side flux

P700 redox kinetics were analysed to determine whether loss of PGR5 alters PSI electron delivery during the induction. $P700^+$ DIRK relaxations were modelled with a single-exponential function (Fig. 8a,b; residual diagnostics in Fig. S2) and the fitted parameters were used to obtain the observed pseudo-first-order decay constant for $P700^+$ reduction, $k_{2,obs}^{PSI}$, the oxidised fraction of P700 at DIRK onset, $P700^+(0)$, and $P700^+$ reduction flux, J_{P700}, as defined in the Experimental approach and quantitative framework (Eq. 3.6 and Eq. 3.8; Fig. 8c–e).

P700 DIRK kinetics were similar between genotypes at the earliest time points of HL but, from 4 s onward, $k_{2,obs}^{PSI}$ was significantly lower in *pgr5-1* than in WT (Fig. 8c). This kinetic slowing coincided with lower $P700^+(0)$ in the mutant from 4 s onward (Fig. 8d). As a result, J_{P700} was lower in the mutant from 4 s onward (Fig. 8e).

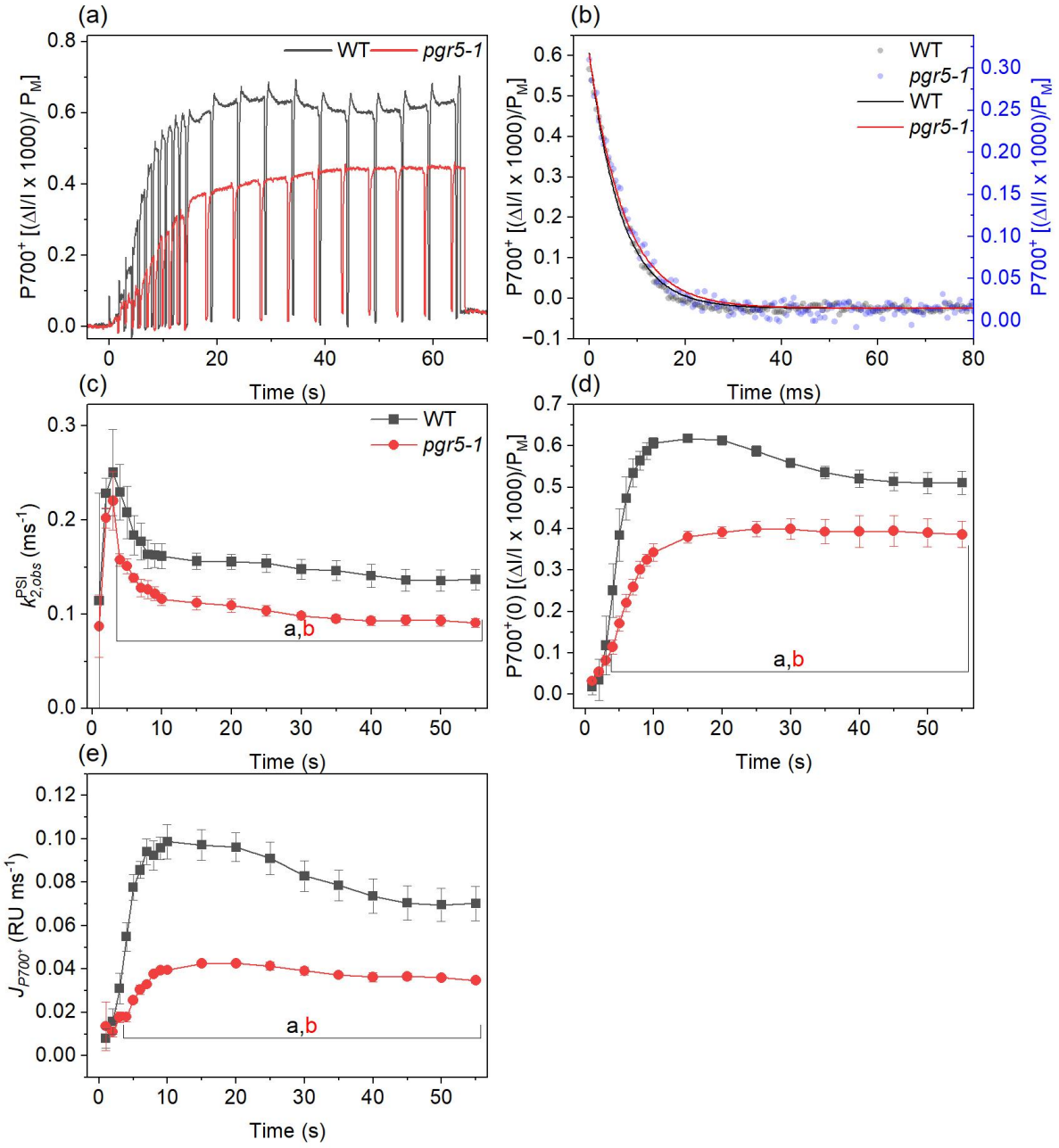

Fig. 8. P700 DIRK kinetics in *S. viridis* in WT and *pgr5-1*. Plants were LL (50 µmol m^{-2} s^{-1}) acclimated for 15 min prior to the HL (1,500 µmol m^{-2} s^{-1}) transition. Time t = 0 s denotes the start of the HL phase. (**a**) Representative raw $P700^+$ DIRK trace from WT and *pgr5-1*, normalised to P_M. (**b**) Representative DIRK fits from a single WT and *pgr5-1* replicate at the 10 s (t = 0 ms denotes the start of the dark interval). Traces were modelled using a single-exponential function (Eq. 3.6) and overlaid after scaling to the same start and end points for visual comparison of kinetics; WT (left y-axis, black) and *pgr5-1* (right y-axis, blue) (**c**) Observed first-order decay constant for $P700^+$ reduction, $k_{2,obs}^{PSI}$. (**d**) The oxidised fraction of P700 at t = 0 during a DIRK, $P700^+(0)$. (**e**) $P700^+$ reduction flux, J_{P700}. (**c–e**) time is reported as cumulative actinic time (excluding the 300 ms dark intervals of each DIRK). Data are shown as Mean ± SE, n=3. Letters denote significant genotype differences within the indicated time window (two-way repeated-measures ANOVA with Tukey's post hoc test; P = 0.05).

PC DIRKs: PC flux is immediately decreased in *pgr5-1* upon light induction

PC redox kinetics were analysed to determine whether loss of PGR5 affects electron flux from Cyt*f* to PC during the induction. PC DIRKs were fit with the constrained biphasic function, in which the PSI-linked rate constant was shared with the corresponding P700 DIRK fit (Eq. 3.12 and Eq. 3.13; Fig. 9a,b; residual diagnostics in Fig. S3). Under this constraint, the fitted Cyt*f*-dependent term reported PC reduction kinetics ($k_{2,obs}^{Cytf}$) and enabled calculation of the PC reduction flux at DIRK onset, J_{PCr} (Eq. 3.14; Fig. 9c,d,e).

Across the induction, $k_{2,obs}^{Cytf}$ was lower in *pgr5-1* than in WT, but the genotype difference was significant only at 1 s and at 25–55 s (Fig. 9c). $PC_o(0)$, the oxidised fraction of the PC pool at DIRK onset, was significantly lower in *pgr5-1* than in WT starting from 2 s (Fig. 9d). The resulting flux, J_{PCr}, was significantly lower in *pgr5-1* at all measured time points (Fig. 9e), consistent with a sustained decrease in Cyt*f*-dependent electron delivery to PC throughout the induction. This PC reduction flux deficit at 1 s of HL mirrored the acceptor-side phenotype inferred from the Fd data and preceded the later slowing of flux to PSI detected in P700 DIRKs and in the PC DIRKs J_{PCo} (Fig. 9f). Although J_{PCo} and $-J_{P700}$ are equal biologically (Eq. 3.10), the independently derived J_{PCo} showed a systematic offset during induction (Fig. S4); because this offset followed a similar time-dependent trajectory in both genotypes, it is most consistent with a shared time-dependent distortion from incomplete deconvolution of the PC signal that likely underestimates PC redox changes, rather than a genotype-specific proportional optical scaling error, and therefore does not alter the interpretation of genotype-dependent differences in PC redox kinetics.

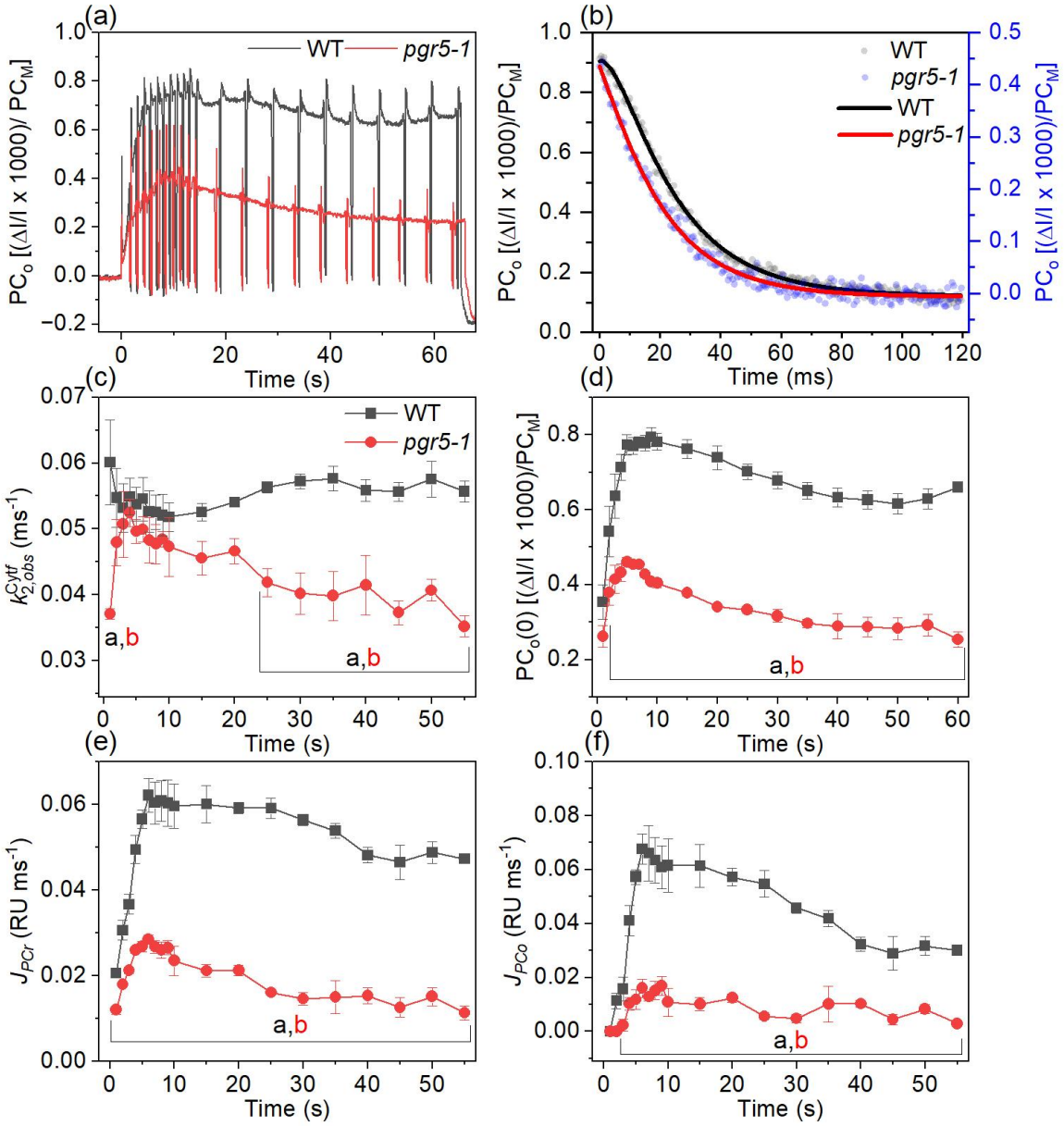

Fig. 9. Plastocyanin DIRK kinetics in *S. viridis* WT and *pgr5-1*. Plants were LL (50 µmol m^{-2} s^{-1}) acclimated for 15 min prior to the HL (1,500 µmol m^{-2} s^{-1}) transition. Time t = 0 s denotes the start of the HL phase. (**a**) Representative raw PC_o DIRK trace from WT and *pgr5-1*, normalised to PC_M. (**b**) Representative DIRK fits from a single WT and *pgr5-1* replicate at the 5 s DIRK (t = 0 ms denotes the start of the dark interval). Traces were modelled using a biphasic exponential function (Eq. 3.12) and overlaid after scaling to the same start and end points for visual comparison of kinetics; WT (left y-axis; black) and *pgr5-1* (right y-axis; blue). PC_o reduction was fitted with a constrained biphasic function in which the fast rate constant was shared with the corresponding P700 DIRK fit. (**c**) Apparent decay constant reporting PC reduction kinetics ($k^{cytf}_{2,obs}$). (**d**) The oxidised fraction of PC at t=0 during a DIRK, PC_o. (**e**) PC reduction flux, J_{PCr}. (**f**) PC oxidation flux, J_{PCo} (**c–f**) time is reported as cumulative actinic time (excluding the 300 ms dark intervals of each DIRK). Mean ± SE, n=3. Letters denote significant

genotype differences within the indicated time window (two-way repeated-measures ANOVA with Tukey's post hoc test, $P = 0.05$).

Early loss of PC reduction flux in *pgr5-1* is caused by a limitation in electron delivery

To distinguish whether the PC flux deficit is caused by the decreased Cyt*f*-dependent electron delivery or a change in PC_o availability, PC reduction flux at DIRK onset was written as a product of the Cyt*f*-linked observed rate term and the PC_o available for reduction (Eq. 3.14), with the Cyt*f*-linked observed rate constant defined as the product of the effective rate constant of Cyt*f* reduction of PC and the time averaged integral of available PC_o (Eq. 3.13). Genotype effects on flux were then decomposed into kinetic and redox contributions by expressing the *pgr5-1* versus WT flux ratio as the product of a $k_{2,obs}^{Cytf}$ ratio and a PC_o ratio:

Eq. 3.20
$$\frac{J_{pgr5}(0)}{J_{WT}(0)} = \frac{k_{2,obs,pgr5}^{Cytf}}{k_{2,obs,WT}^{Cytf}} \cdot \frac{([PC_o](0)-B)_{pgr5}}{([PC_o](0)-B)_{WT}}$$

and separating these terms using a natural log transform:

Eq. 3.21
$$\ln\left(\frac{J_{pgr5}(0)}{J_{WT}(0)}\right) = \ln\left(\frac{k_{2,obs,pgr5}^{Cytf}}{k_{2,obs,WT}^{Cytf}}\right) + \ln\left(\frac{([PC_o](0)-B)_{pgr5}}{([PC_o](0)-B)_{WT}}\right)$$

This decomposition showed that, at 1 s of HL, most of the PC reduction flux loss in *pgr5-1* was attributable to the kinetic component, with a smaller contribution from PC redox availability (Fig. 10). From 2 s onward, the flux deficit became progressively dominated by the PC availability term, consistent with increasing limitation in availability of PC_o during the induction (Fig. 10).

To interpret the origin of the early kinetic limitation, Cyt*f*-dependent electron transfer was framed in terms of factors that can modulate the intrinsic electron transfer frate from Cyt*f* to PC rate:

Eq. 3.22
$$k_{2,eff}^{Cytf} = f(\Delta pH, \eta, D)$$

where ΔpH is lumen acidification, D reflects effective diffusional/encounter limitation of PC within the lumen, and η captures local electrostatic or docking efficiency governing productive PC–Cyt*f* interactions (see Supplemental Derivations). Based on pH dependency of Cyt*f* electron transfer (Hope *et al.*, 1994), a twofold reduction in $k_{2,eff}^{Cytf}$ in *pgr5-1* would require an approximately two-unit decrease in lumen pH, corresponding to a ~100-fold increase in proton concentration, which is unlikely and not supported by *pmf* from ECS measurements (Fig. 6a).

Diffusion (D) and electrostatics (η) are the remaining contributions which could account for the early reduction in $k_{2,eff}^{Cytf}$.

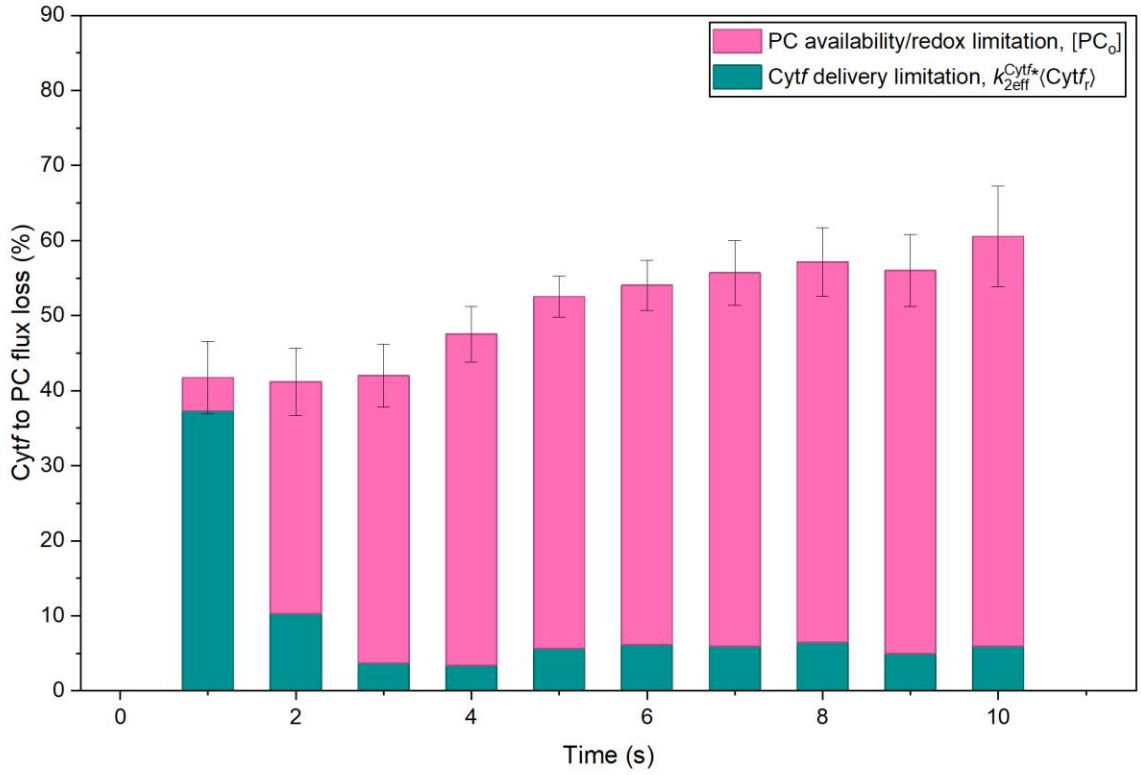

Fig. 10. Partitioning of Cyt*f* to PC flux loss in *pgr5-1* versus WT into kinetic (Cyt*f* delivery) and redox (oxidised plastocyanin availability) limitations over the first 10 s of LL-HL transition. Sum of the stacked bars is Mean ± SE, n=3, of the percent total flux loss; stacked bars show mean of each component's loss.

Lower P700 reduction flux in *pgr5-1* is caused by the PSI donor-side over-reduction

P700 DIRKs were analysed to determine why electron delivery to PSI becomes limited in *pgr5-1* during the induction. At the onset of each DIRK, the genotype effect on P700 reduction flux can be written as the product of a kinetic term ratio and a redox availability ratio:

Eq. 3.23 $$\frac{J_{pgr5}(0)}{J_{WT}(0)} = \frac{k_{2,obs,pgr5}}{k_{2,obs,WT}} \cdot \frac{[P700^{+}(0)]_{pgr5}}{[P700^{+}(0)]_{WT}}$$

and separated into additive contributions using a log transform:

Eq. 3.24. $$\ln\left(\frac{J_{pgr5}(0)}{J_{WT}(0)}\right) = \ln\left(\frac{k_{2,obs,pgr5}}{k_{2,obs,WT}}\right) + \ln\left(\frac{[P700^{+}]_{pgr5}}{[P700^{+}]_{WT}}\right)$$

This decomposition provided a direct way to evaluate how much of the flux deficit arises from changes in the effective rate constant versus changes in available $P700^{+}$.

P700 reduction flux is similar between WT and *pgr5-1* at 1-4 s of HL (Fig. 8e). However, from 5 s onward, the increasing separation in $P700^{+}(0)$ accounted for most of the flux deficit, indicating that donor-side over-reduction decreased the fraction of available PSI reaction centres (Fig. 11). The contribution from changes in the effective rate constant was comparatively small.

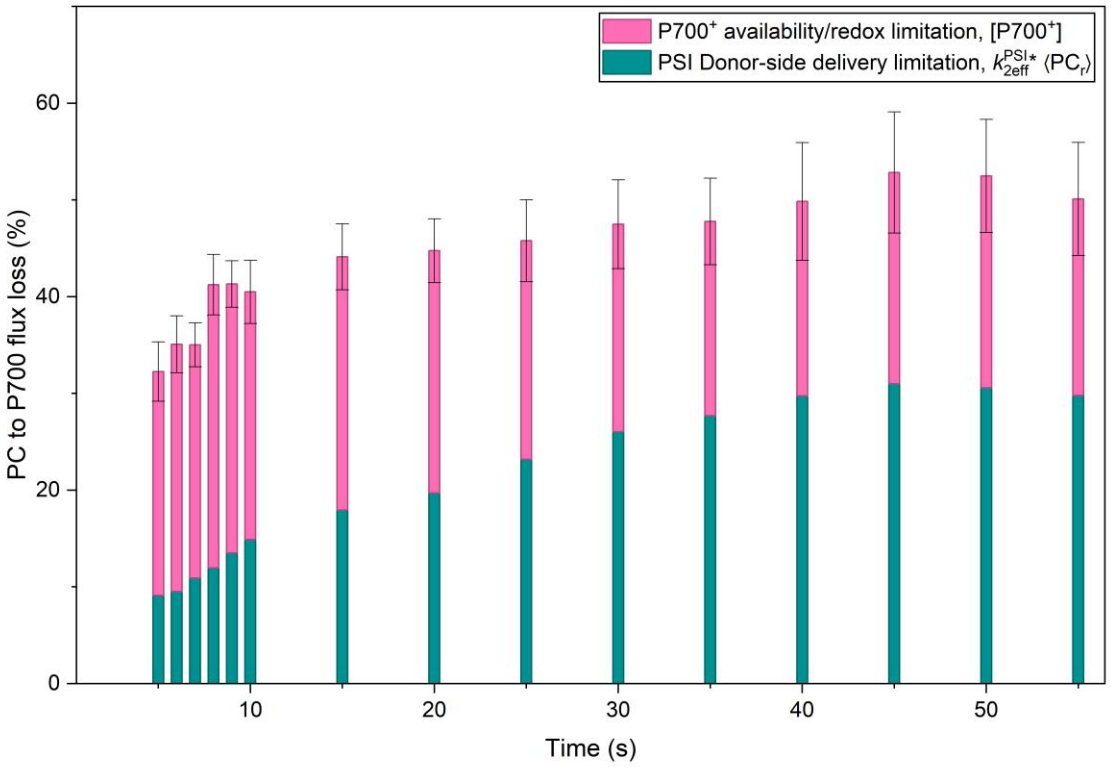

Fig. 11. Partitioning of PC to P700 flux loss in *pgr5-1* versus WT into donor-side delivery ($k_{2,eff}^{PSI} * \langle PC_r \rangle$) and P700 over-reduction components ($[P700^+]$). Sum of the stacked bars is Mean ± SE, n=3, of the percent total flux loss; stacked bars show mean of each component's loss.

PSI donor-side effective rate constant differs between genotypes beyond PC redox effects

Could the slower P700 DIRK kinetics in *pgr5-1* be explained solely by differences in PC_r availability or by an additional change in the effective PSI donor-side rate constant? In the donor-side framework used here, the observed pseudo-first-order constant for P700⁺ reduction is dominated by the effective association step between PC_r and oxidised PSI centres, because this encounter step is rate limiting over the DIRK window (see Supplemental Derivations). Accordingly, the donor-side term can be written as:

Eq. 3.25 $$k_{2,obs}^{PSI} \approx k_{on}^{PSI} \; ; k_{2,obs}^{PSI} = k_{on}^{PSI} \, \langle PC_r \rangle_{0\rightarrow \mathrm{t}}$$

where k_{on}^{PSI} is an effective second-order association constant that contains the encounter and docking efficiency at the PSI donor side, and multiplied by $\langle PC_r \rangle_{0\rightarrow T}$, the time-averaged integral of PC_r abundance at the whole leaf level, this was estimated from the optical PC signal over the corresponding P700 decay window (T = 5 × τ_{P700}), as the actual molar concentration would be necessary for the true determination of k_{on}^{PSI}.

If k_{on}^{PSI} were constant, then $k_{2,obs}^{PSI}$ would be expected to increase with increasing $\langle PC_r \rangle$. Instead, WT and *pgr5-1* showed a strong shared relationship in which $k_{2,obs}^{PSI}$ decreased as $\langle PC_r \rangle$ increased at later induction time points (Fig. 12a). A clear deviation was also apparent during early induction, where *pgr5-1* remained separated from WT despite comparable $\langle PC_r \rangle$ values (Fig. 12a). Together, these patterns indicate that $k_{2,obs}^{PSI}$ is not captured by $\langle PC_r \rangle$ alone. An additional term is constraining either PC_r availability or altering the underlying kinetics of PSI activity. To further explore what defines the genotype difference in $k_{2,obs}^{PSI}$, the observed rate constant was normalised by $\langle PC_r \rangle$ over the same decay window (Eq. 3.14) to obtain $k_{2,eff}^{*}$, a proxy for the effective PSI donor-side encounter term after controlling for $\langle PC_r \rangle$ availability. Because PC delivery to PSI depends on multiple physical parameters, the effective term was framed as:

Eq. 3.26 $$k_{2,eff}^{*} = f(\Delta\mathrm{pH},\, \mathcal{E},\, D)$$

where ΔpH represents lumen acidification, $\mathcal{E}$ denotes local electric field effects that can influence electrostatic steering of PC toward PSI, and D captures diffusional and encounter limitations that set how frequently productive PC–PSI collisions occur. In the absence of direct ΔpH measurements, ECS provides *pmf*, which reflects contributions from both ΔpH and Δ*ψ* (Cruz et al., 2001). Accordingly, $k_{2,eff}^{*}$ was compared against *pmf* to test whether lumen

acidification alone could account for the observed genotype separation (Fig. 12b). Because these variables co-vary during induction, these relationships are treated as exploratory trajectory plots rather than steady-state response curves.

Although $k^*_{2,eff}$ increased with *pmf* in both genotypes, *pgr5-1* remained consistently lower than WT across the overlapping *pmf* range (Fig. 12b). Weighted ANCOVA detected no genotype × *pmf* interaction ($P = 0.198$), but a significant genotype offset persisted in the minimised additive model ($P < 0.001$), consistent with a vertical separation between genotypes that is not explained by differences in *pmf* alone. Plotting $k^*_{2,eff}$ against time also showed that WT was significantly faster than *pgr5*-1 at 2-55 s, consistent with the *pmf* analysis (Fig. 12c). Within the framework of Eq. 3.26, this persistent offset implies that the decrease of $k^*_{2,eff}$ in *pgr5-1* arises from a *pmf*-independent term, most consistent with either decreased effective PC diffusion/encounter frequency at PSI or altered electrostatic/docking interactions governing productive PC–P700 electron transfer.

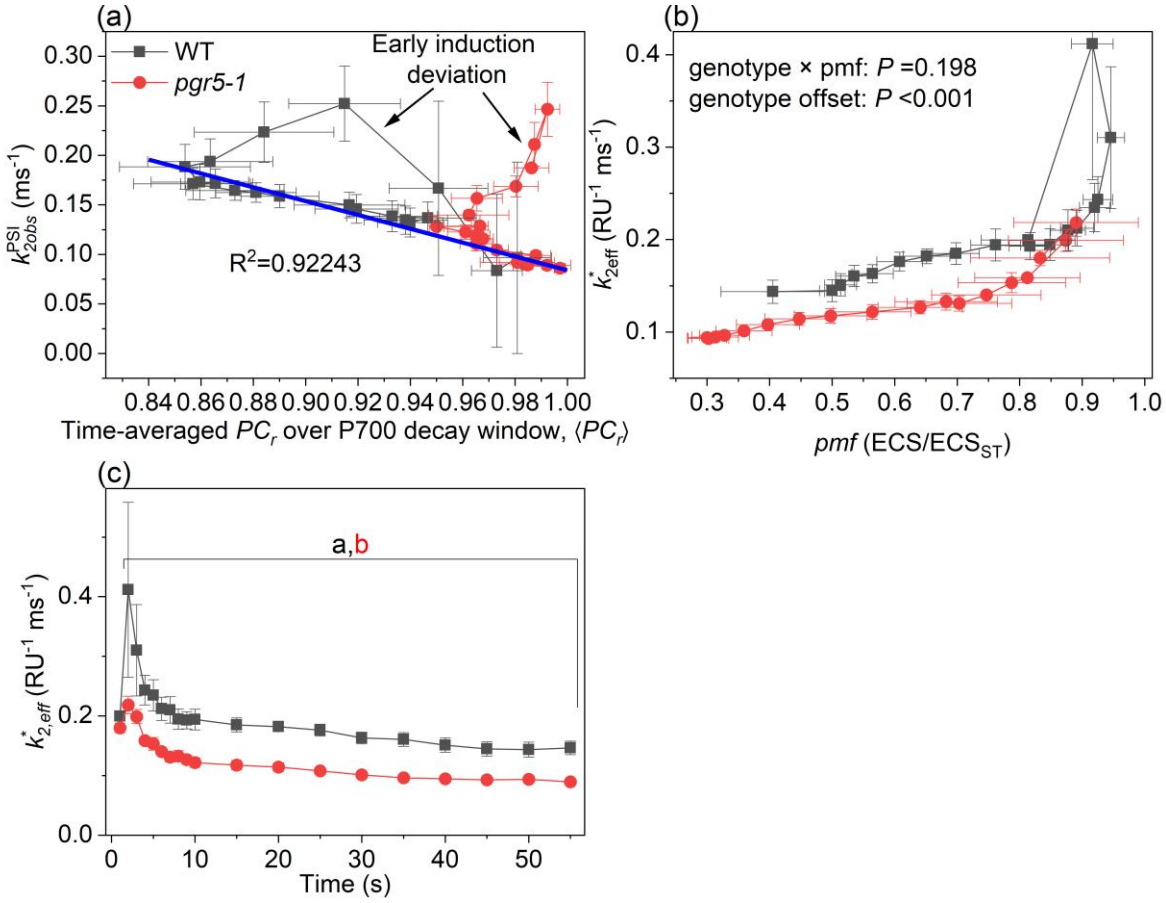

Fig. 12. Exploratory relationships between apparent PSI donor-side kinetics, PC redox availability, and *pmf* during induction. (**a**) The apparent $P700^{+}$ reduction rate constant ($k_{2,obs}^{PSI}$) plotted against the time-averaged PC redox availability proxy over the corresponding P700 DIRK decay window ($\langle PC_r \rangle$). Here, $\langle PC_r \rangle$ is estimated from the optical PC integral (rather than an absolute $[PC_r]$ concentration). A linear regression fitted over the shared region (8–55 s) captures the common dependence of $k_{2,obs}^{PSI}$ on $\langle PC_r \rangle$ in WT and *pgr5-1* (R^2 shown), while points outside this window highlight an early-induction deviation. (**b**) The effective donor-side parameter, $k_{2,eff}^{*}$, plotted against *pmf*. Weighted ANCOVA on genotype-time means detected no genotype × *pmf* interaction (*P* = 0.198), but a significant genotype offset remained in the minimised additive model (*P* < 0.001). (**c**) Time course of $k_{2,eff}^{*}$ during the induction, shown to visualise differences between genotypes; letters denote significant genotype differences within the indicated time window (two-way repeated-measures ANOVA with Tukey's post hoc test; *P* = 0.05). Mean ± SE, n =3.

Discussion

Previous studies demonstrated the utility of P700 redox kinetics for dissecting PSI limitations under fluctuating light (Kono *et al.*, 2017; Yamamoto & Shikanai, 2018), but flux partitioning for PC, P700 and Fd in *pgr5* has not previously been possible. In C_4 plants like *S. viridis*, PSI oxidation is driven by two mechanisms: elevated abundance of the NDH complex in bundle sheath chloroplasts sustains high CEF while, in mesophyll cells, high PEPC activity and the consequent rapid consumption of NADPH by malate dehydrogenase helps maintain oxidation of PSI (Ermakova *et al.*, 2024b). This provides a unique opportunity to detect the immediate consequences of PGR5 loss that is not accessible in C_3 *pgr5* backgrounds. The oxidation of PSI observed in *S. viridis pgr5-1* (Fig. 4a) enabled a DIRK-based, differential-equation framework to extract pathway-specific fluxes and interpret how changes in effective rate terms map onto physiological electron-transfer constraints.

Loss of PGR5 produces an immediate acceptor-side flux deficit

Throughout induction, *pgr5-1* showed a decrease in the summed capacity for electron withdrawal from Fd_r indicating a persistent decrease in the rate of electron withdrawal from the PSI acceptor side compared to WT (Fig. 7c), A modest fraction of this deficit is consistent with ~25% lower NDH content in *pgr5-1* (Woodford *et al.*, 2025b). Furthermore, Woodford *et al.* (2025b) showed that CO_2 assimilation in *S. viridis pgr5-1* is unaffected unless the plants are subjected to prolonged high light exposure causing photodamage, suggesting that FNR-related sink capacity is similar between genotypes in this experiment. Therefore, I hypothesise that most of Δk_{obs}^{Fd} is caused by the loss of the PGR5.

Previous works in *A. thaliana pgr5* also reported altered Fd relaxation kinetic and higher reduction of the Fd pool under steady-state illumination (Maekawa *et al.*, 2024; Satoh *et al.*, 2025). In steady-state measurements, apparent relaxation kinetics conflate changes in sink activity with changes in redox availability, such that a more reduced Fd pool can alter observed decay behaviour without implying a faster rate constant for Fd oxidation (Eqs. 1–2; Suppl. Deriv. S3). By contrast, the DIRK approach during the induction used here resolved k_{obs}^{Fd} and $Fd_r(0)$ explicitly during the light-shift window (Fig. 7a), allowing separation of a persistent sink-capacity deficit from increase in Fd_r.

PC flux reveals early Cyt*f*-dependent delivery limitation

At 1 s of the HL transition, *pgr5-1* showed lower electron flux to PC despite no significant difference in the oxidised fraction of the PC pool, $PC_o(0)$ (Fig. 9d). This represented a distinct

kinetic defect before progressive over-reduction of PC pool becomes dominant (see next part) and is likely caused by the lower Cyt*f*-dependent electron delivery to PC (Fig. 10). It is unlikely that this difference in the observed rate is due to different optical scaling of PC between genotypes, as both WT and *pgr5-1* shared the same offsets between PC oxidation and P700 reduction flux values (Fig. S4). Furthermore, this early flux loss is unlikely to be explained by ΔpH due to similar *pmf* (Fig. 12). Although *pmf* comprises both Δ*ψ* and ΔpH, the ECS-based method for partitioning of these components is not reliable because the signal is confounded by overlapping absorbance changes associated with qE and zeaxanthin formation (Wilson *et al.*, 2021). High-time-resolution modelling based on real ECS traces during light shifts indicates that Δ*ψ* rises rapidly at light onset but relaxes within the first second, so that, over the subsequent induction window, *pmf* is dominated by ΔpH (Lyu & Lazár, 2017). Assuming Δ*ψ* contribution to *pmf* is the same in the *pgr5* mutant, we therefore use *pmf* as a proxy for ΔpH.

In principle, the remaining determinants of Cyt*f* to PC electron transfer within the encounter framework are encounter/docking efficiency (η) and diffusion/encounter constraints (D). However, a lumen-wide shift in either D or η would be expected to impose a parallel constraint on PSI donor-side kinetics, whereas no reduction in intrinsic PSI turnover is observed during the 1–3 s window (Fig. 8c). The simplest explanation consistent with these constraints is that Cyt*f* is more oxidised in *pgr5-1* at 1 s, lowering the effective availability of the reduced Cyt*f* donor for PC reduction.

Although direct PSII measurements at 1 s of HL are unavailable, PSII photochemical activity at 2 s of the HL shift does not differ between genotypes (Fig 5a-c), and qL shows no early genotype effect (Fig 5d), arguing against impaired LEF as the cause of decreased electron flux to PC. Together, these observations support the interpretation that the PC flux deficit at 1 s of HL reflects a transient Cyt*f* delivery limitation arising from decreased electron supply to the Cytb_6f complex not linked to LEF (Fig 13 a,b). This links the early reduction in J_{Fd} to the coincident limitation in electron delivery to Cytb_6f consistent with the loss of PGR5-CEF and with hypothesis 1.

Over-reduction of P700 is the dominant cause of decreased PSI flux and *pmf* loss in *pgr5-1*

The major decline in PSI flux in *pgr5-1* beyond 4 s of the induction arouse from lower availability of oxidised reaction centres (Figure 11). This behaviour follows directly from the mass-action framework: as fewer oxidised P700 are available as reaction partners for PC to P700 electron transfer, the reaction rate slows down even if the intrinsic encounter kinetics

are unchanged. In the classical PCON framework, PSI is protected when donor-side flux from Cyt*f*/PC to P700 is downregulated so that it does not exceed acceptor-side flux from P700 to Fd and downstream sinks (Degen & Johnson, 2024). In *pgr5-1*, PCON cannot oxidise P700 at light onset because the earliest defect is decreased acceptor-side withdrawal from Fd to CEF, while PC and P700 are already largely reduced; oxidised partners (PC_o and $P700^+$) are therefore regenerated too slowly to provide space for continued electron delivery from Cytb_6f, and P700 stays in the reduced state. Thus, the acceptor-side withdrawal deficit at 1 s of HL quickly propagates into over-reduction of PSI, which becomes the dominant constraint on PSI flux, consistent with Hypothesis 2.

A loss of oxidant throughout the electron transport chain also explains the decrease in Cyt*f* to PC flux after 2 s of induction (Fig. 10). Following the transient Cyt*f* delivery limitation at 1 s of HL, PC becomes progressively more reduced in *pgr5-1* (Fig. 9d), constraining Cyt*f*-PC electron transfer (Fig. 10). Once PC_o becomes limiting, Cytb_6f activity slows down, providing a direct mechanistic basis for the delayed *pmf* decrease that emerges after 2 s (Fig. 6). Although Cyt*f* to PC flux is lower in *pgr5-1* at all time points, a significant difference in *pmf* is not detected until after 2 s. ECS signals in NADP-ME C_4 leaves are biased toward mesophyll cells, since the ECS signal is predominantly associated with PSII pigments, and PSII abundance is markedly lower in bundle sheath strands than in mesophyll cells of NADP-ME C_4 species (Olsen *et al.*, 1981; Ermakova *et al.*, 2024). The *pmf* measurements reported here therefore predominantly reflect mesophyll cell contributions. PGR5-dependent CEF is likely less engaged in mesophyll cells relative to bundle sheath cells (Ermakova *et al.*, 2024b; Woodford *et al.*, 2025b), the early loss of CEF-driven proton pumping might be underrepresented in the bulk ECS signal. As the induction proceeds and the deficit in Cytb_6f throughput accumulates, the difference in *pmf* between genotypes becomes apparent. The lowered *pmf* phenotype of *pgr5-1* is therefore initiated by the loss of PGR5-dependent CEF, but is then largely defined by progressive over-reduction of PC slowing Cytb_6f activity (Fig. 13 c,d).

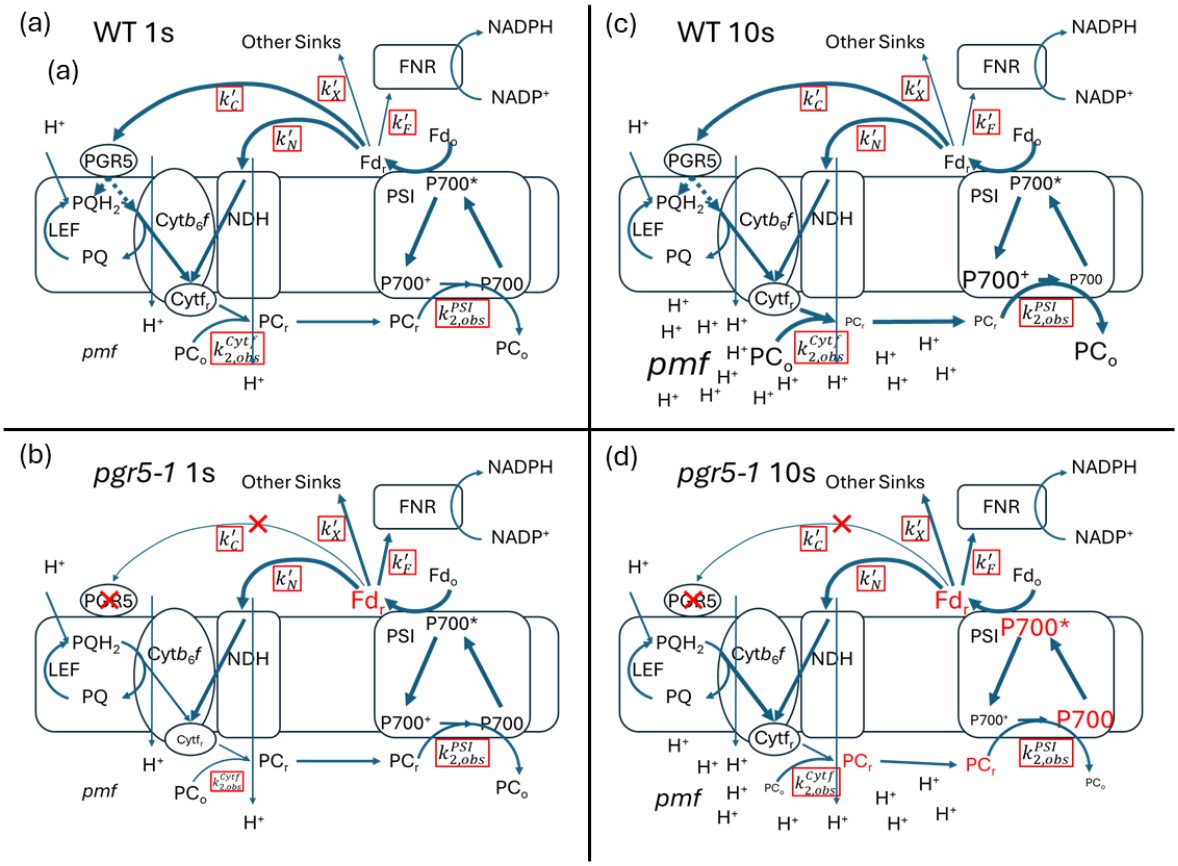

Fig. 13. Scheme for how the loss of PGR5 CEF is visible at 1 second and leads to the over reduction of the electron transport chain in *S. viridis*. For all panels, electrons from PSII are simply denoted by LEF on the left side of the membrane. (**a,b**) WT and *pgr5-1* at 1 s after the shift to high light. Blue arrows indicate the major directions of electron flow and red boxes indicate the effective rate terms used to interpret the kinetic changes. At 1 s, loss of PGR5-dependent CEF in *pgr5-1* decreases flux out of Fd, consistent with lowered acceptor-side electron withdrawal. This is associated with a transient limitation in reduced Cyt*f* electron delivery to PC, lowering flux into PC_o, while P700 has not yet become over-reduced. (**c,d**) WT and *pgr5-1* at 10 s after the shift to high light. Sustained loss of CEF in *pgr5-1* leads to progressive over-reduction of Fd, PC, and P700, such that redox backpressure and carrier-pool saturation become the dominant constraints on electron transport. *pmf* is still generated through LEF and compensatory NDH activity, but lower flux through Cytb_6f is predicted to decrease the rate of *pmf* formation.

A slower PC to P700 rate constant in *pgr5-1* is consistent with diffusion-limited PC delivery to PSI

The effective PSI donor-side rate term is lower in *pgr5-1*, consistent with slower PC delivery to PSI. In a well-mixed system, the observed PSI donor-side rate constant should increase as the available reduced PC pool increases. However, plotting $k_{2,obs}^{PSI}$ against $\langle PC_r \rangle$ shows a weakly negative trend from 7 to 55 s (Fig. 12a), indicating that the effective donor-side kinetic rate is not constant over induction. Normalising $k_{2,obs}^{PSI}$ to $\langle PC_r \rangle$ and comparing $k_{2,obs}^{PSI}$ against

pmf (used here as a proxy for ΔpH) likewise does not remove the genotype separation. While, as mentioned above, ECS signals are biased towards mesophyll cells and P700 is not, the offset between the genotypes is in the y ($k_{2,obs}^{PSI}$) axis and a correction of *pmf* to account for the BS discrepancy would not address the offset. Within the known dynamics controlling PSI donor-side electron transfer rates, the remaining explanation is that *pgr5-1* has lower effective PC delivery to PSI.

An alteration in PC diffusion is expected to limit PSI donor-side electron transfer rates because, in a coupled reaction sequence, the slowest step determines the observed relaxation rate (Kustin et al., 1965). Physiological support for PC diffusion defining the rate constant for PSI comes from thylakoid architecture mutants in which grana reorganisation increases the effective distance PC must traverse between Cyt*b*$_6$*f* and PSI and slows donor-side PSI kinetics, consistent with PC delivery becoming diffusion-limited (Höhner et al., 2020). In the simplified donor-side formulation used initially, diffusion and docking effects are absorbed into a single effective association term (k_{on}), so changes in pathlength are not expressed explicitly. A diffusion-aware formulation that separates encounter rates from transport/distance rates, and that distinguishes local PC pools proximal to Cyt*b*$_6$*f* versus PSI (Supplemental Derivations S7), provides a better model for why diffusion constrains the availability of PC_r at PSI and therefore slows the observed P700 relaxation rate.

This framework is also useful for interpreting why a single, well-mixed $\langle PC_r \rangle$ pool does not predict $k_{2,obs}^{PSI}$. If PC delivery to PSI draws from spatially distinct routes, then the kinetically accessible PC pool at PSI reflects a weighted contribution of routes with different average delivery distances set by thylakoid organisation (stacking state, lumen geometry, and protein packing) (Gu et al., 2022). In this view, loss of the short-path CEF contribution in *pgr5-1* would shift the effective delivery distance toward longer routes and depress $k_{2,eff}^{PSI}$, even if bulk $\langle PC_r \rangle$ is similar. This explains why $k_{2,obs}^{PSI}$ does not necessarily scale with bulk $\langle PC_r \rangle$: when PC is not well mixed, the rate is set by the locally accessible PC pool at PSI rather than by the total $\langle PC_r \rangle$.

ATP synthase proton conductivity is altered in *pgr5-1* during induction

ATP synthase proton conductivity is altered in *pgr5-1* during induction, indicating that ATP synthase regulation can contribute to the *pmf* phenotype and providing partial support for Hypothesis 3. Under the conventional ECS framework, *pmf* reflects the balance between proton flux into the lumen (proton pumping) and proton flux out through ATP synthase, so changes in ATP synthase conductivity influence *pmf* (Avenson *et al.*, 2005b). In our induction

measurements, however, the difference in g_{H^+} between the genotypes does not fully explain the difference in *pmf* (Fig. 6). This indicates that changes in net proton influx associated with electron-transfer also contribute to the difference in *pmf*. Similarly, Woodford *et al.* (2025b) observed higher g_{H^+}in *pgr5-1* at steady state, but that difference did not scale with the *pmf* deficit, consistent with additional limitations on proton influx contributing to lower *pmf*.

The initial ECS decay, v_{H^+} , is usually used as an estimate of proton influx, but because these measurements were made during induction rather than steady state, v_{H^+} as proton influx should be interpreted cautiously (Baker *et al.*, 2007), and therefore here only reports on the instantaneous proton efflux through ATP synthase, which was not different between genotypes (Fig. 6c). Taken together, the ECS results are consistent with a model in which both ATP synthase regulation (Hypothesis 3) and reduced proton pumping linked to more oxidised Cyt*f* throughput either by the loss of CEF (Hypotheses 1) or the over-reduction of the electron transport chain (Hypothesis 2) act together to shape the observed *pmf* phenotype.

PGR5-CEF prevents over-reduction of the electron transport chain during rapid light transitions

Together, these results support a unified interpretation in which the three hypotheses capture different layers of the *pgr5-1* phenotype. The earliest measurable effects support Hypothesis 1: an immediate acceptor-side withdrawal deficit, evidenced by lowered Fd oxidation capacity and a transient Cyt*f* delivery limitation indicate a loss of PGR5-CEF. These deficits then propagate into the dominant phenotype described by Hypothesis 2. Progressive chain-wide over-reduction limits the availability of oxidised PSI and PC, becoming the major driver of lower electron fluxes and *pmf*. In parallel, changes in ATP synthase proton conductivity indicate that PGR5-linked ATP synthase regulation can also modulate *pmf* during induction as described in Hypothesis 3, however, acting alongside the electron-transfer constraints. In this framework, the loss of PGR5-CEF initiates the backpressure because an over-reduced Fd pool limits productive electron transfer out of PSI, reducing $P700^+$ availability, and causing electrons to accumulate in the carrier pools, thereby constraining electron transport (Fig. 13).

By resolving induction kinetics in-planta, under physiological conditions, this work strengthens and extends chloroplast-based evidence for a PGR5-dependent CEF pathway. Prior support for PGR5-CEF came from isolated thylakoids and additions of recombinant Fd and NADPH exceeding physiological concentrations (Nishikawa *et al.*, 2012). Suorsa *et al.* (2016) used far-red excitation with ECS measurements to estimate relative contributions of LEF and CEF, concluding that CEF capacity is reduced in *pgr5* backgrounds; however, this was done under far-red light in the absence of PSII activity lacking physiological relevance. The in-planta

induction flux analysis presented here provides a comprehensive analysis under the physiologically relevant conditions. At 1 s, the 38% lower Cyt*f* to PC observed rate constant in *pgr5-1* is most consistent with Cyt*f* being 38% less reduced than in WT and, assuming that other internal effective rate constants for Cytb_6f are unchanged at this time point, implies an approximately 38% decrease in electron flux into Cytb_6f due to loss of PGR5-dependent CEF contribution during the earliest phase of HL induction. This estimate exceeds the 15% contribution previously attributed to PGR5 under steady-state conditions (Woodford *et al.*, 2025b), indicating that PGR5 contributes proportionally more to electron flux during the LL-to-HL transition than under steady-state illumination. Detecting a PGR5-dependent CEF component within the first second of induction shows how loss of this rapid return capacity can initiate acceptor-side backpressure by 2 s and lead to the subsequent over-reduced state that characterises later the *pgr5* phenotype at steady state.

Engineering implications for C_4 electron transport

The result that a lack of oxidisable electron carrier can slow down electron transfer in the high potential chain highlight mobile carrier availability as a complementary engineering target in C_4 leaves, particularly within the first second after a high-light transition. Increasing the pool of PC is expected to improve Cyt*f* to PC electron transfer by maintaining PC_o availability and reducing diffusion/encounter limitation, thereby sustaining Cytb_6f throughput during this earliest phase of induction. Because Cytb_6f translocates protons, this strategy should support rapid *pmf* formation and photoprotective capacity at light onset, rather than altering intrinsic PSI photochemistry.

Electron transport capacity limits C_4 photosynthesis and relieving this constraint can improve productivity. Overexpression of the Rieske FeS subunit increased Cytb_6f content in *S. viridis* and improved CO_2 assimilation at high light, consistent with Cytb_6f acting as a limiting step in electron transfer (Ermakova *et al.*, 2019). Rieske FeS overexpression in sorghum also increased biomass but likely through improved CEF and improved assimilation under light induction (Ermakova *et al.*, 2023). Separately, boosting mobile electron-carrier capacity has also delivered gains in C_3 tobacco: expression of algal cytochrome c_6 alongside enhanced ribulose 1,5-bisphosphate regeneration (by over-expression of either fructose-1,6-bisphosphatase / sedoheptulose-1,7-bisphosphatase or sedoheptulose-1,7-bisphosphatase) increased photosynthetic assimilation and biomass in tobacco, demonstrating that stimulating electron transport and downstream metabolism together can increase productivity (López-Calcagno *et al.*, 2020). Combining strategies that increase Cytb_6f capacity with strategies that increase mobile donor availability (PC/ c_6) is a testable route to improve CO_2 assimilation and biomass.

Future work

The present results indicate that Cyt*f* is under-reduced in *pgr5-1* at 1 s, consistent with a transient electron delivery limitation at PSI donor-side, and this can be tested directly by performing Cyt*f* absorption spectroscopy analysis over the same induction window. The Cyt*f* absorption band (~554–556 nm) can be characterised, for example, an Integrated Diode Emitter Array spectrophotometer/fluorometer (IDEAspec) with special Cyt*f* filters (Hall *et al.*, 2013) or JTS-150 which can measure Cyt*f*, PC, P700, and ECS simultaneously (BioLogic, Seyssinet-Pariset, France). Resolving biphasic Cyt*f* kinetics during DIRKs would then require estimating the shared kinetic constants (e.g., by averaging fitted rates within genotype across replicate traces) and using these constraints to infer the corresponding upstream Cytb_6f kinetic rate constants. This would extend the same shared-rate logic applied here to additional steps in the high-potential chain, consistent with precedent from isolated-system kinetic analyses (Sujak *et al.*, 2004). With constraints and an explicit depiction of the shared-rate decomposition (Fig. 14), this approach could provide a fully resolved kinetic description of high-potential chain control as originally envisioned by Sacksteder and Kramer (2000).

In this work, DIRK measurements were acquired at the whole-leaf level in a NADP-ME C_4 species and therefore integrate signals from both mesophyll and bundle sheath chloroplasts. Because LEF is dominant in mesophyll cells whereas CEF is dominant in bundle sheath cells, whole-leaf DIRKs report the averaged sum of the effective kinetics. This mixing does not invalidate significant genotype differences: under the standard linear mixing rule for absorbance-based signals, a mixed-signal difference cannot be generated if neither component signal differs (Mayerhöfer & Popp, 2020). Instead, mixing primarily dilutes compartment-specific effects, reducing sensitivity and increasing the risk of false negatives (attenuation) and does not create false positives (Allen, 2017). A significant whole-leaf difference therefore indicates a real genotype effect on the measured kinetics, but it does not specify whether that effect is shared between mesophyll and bundle sheath or driven predominantly by one cell type. Because CEF-linked effects are expected to be bundle sheath-enriched, whole-leaf measurements are likely to underestimate the magnitude of bundle sheath-specific kinetic differences by averaging them with mesophyll kinetics. Cell-type-resolved measurements (e.g., isolated bundle sheath strands or mesophyll preparations) are therefore needed to localise the effect, not to validate whether it exists. This experiment may also provide further support for diffusion limitation arguments, as comparing WT mesophyll and bundle sheath P700 rate constants should yield different rates, as more CEF in bundle sheath should lead to faster averaged rate constants, whereas more LEF in mesophyll should lead to slower averaged rate constants. Additionally, this diffusion effect could be tested in

isolated mesophyll cells by inhibiting PSII with DCMU to suppress LEF and isolate PSI-driven electron flow; under these conditions, any change in P700 relaxation should be interpreted together with PC redox availability, because reduced PC supply can itself slow the observed donor-side kinetics.

$$Q\ cycle \overset{k_3}{\rightarrow} Cytf \overset{k_2}{\rightarrow} PC \overset{k_1}{\rightarrow} P700$$

$$P700^{+}(t) = A_1 e^{-k_1 t}$$

$$PC_{ox}(t) = A_2 e^{-k_1 t} + A_3 e^{-k_2 t}$$

$$Cytf_{ox}(t) = A_4 e^{-k_2 t} + A_5 e^{-k_3 t}$$

Figure 14. Shared-rate decomposition for resolving donor-side kinetics in the high-potential chain. Idealised schematic showing how simultaneous measurements can be used to separate overlapping steps in donor-side relaxation kinetics. In this framework, the P700 relaxation defines the PC-dependent rate constant, and the PC rate constant can then be used to isolate the Cyt*f* reduction rate associated with internal Cytb_6f electron transfer.

Supplemental Tables and Figures

Table S1. Differential model plot (DMP) coefficients for WT and *pgr5-1* and rationale for using WT-derived spectra for deconvolution. DMP coefficients at each NIR peak wavelength (800, 845, 902 and 915.5 nm) are shown for Fd, P700 and PC generated independently from WT and *pgr5-1* following the DMP generation protocol. Spectra deconvoluted with the DMPs were not meaningfully different in shape or in the resulting deconvolution between genotypes. Coefficients were calculated from the mean of 10 (Fd), 25 (P700) and 6 (PC) averaged spectra; no SE is reported for this calculation.

Signal	Fd		P700		PC	
(nm)	*pgr5-1*	WT	*pgr5-1*	WT	*pgr5-1*	WT
800	0.5437	0.5752	0.0076	0.0055	0.1074	0.0879
845	0.7206	0.6994	0.868	0.8817	0.4664	0.4875
902	1	1	1	1	1	1
915.5	0.4553	0.4627	0.3234	0.3358	0.5457	0.5511

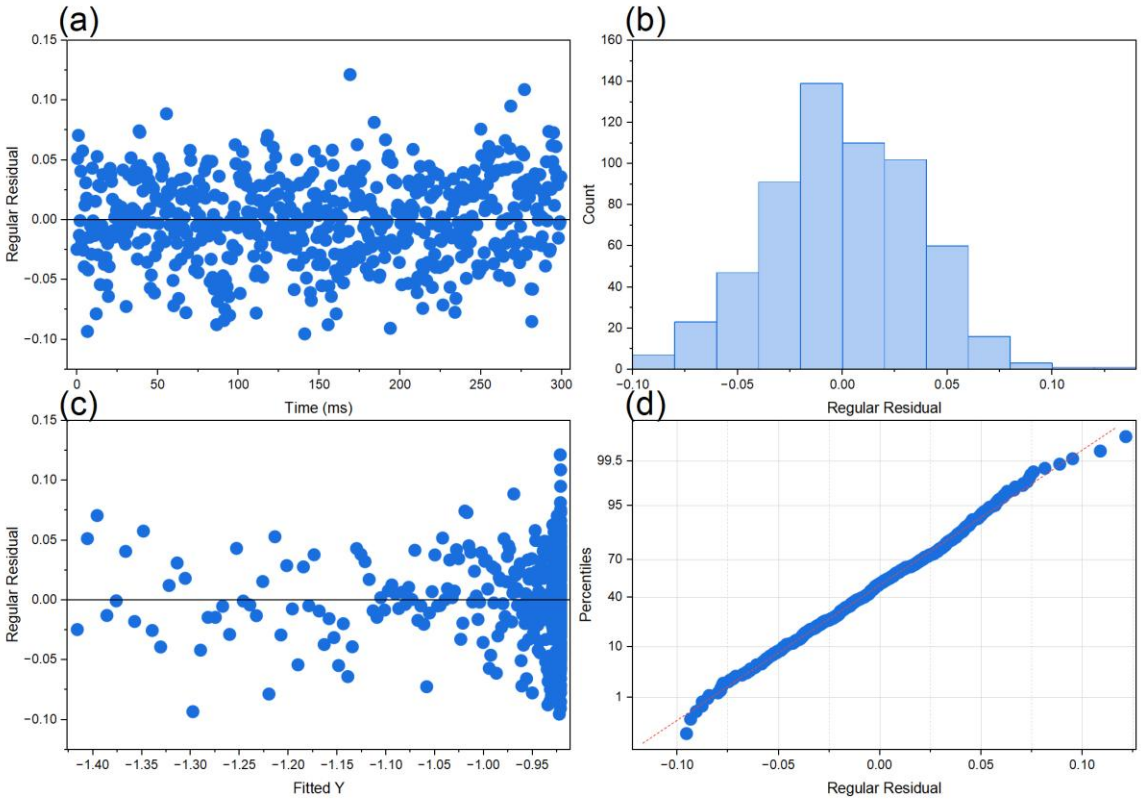

Fig. S1 Residual diagnostics for the single-exponential Fd DIRK decay fit (WT, 5 s). Residual plots from fitting a single-exponential decay model to the Fd DIRK relaxation trace for a representative WT replicate at 5 s of illumination. (**a**) Residuals versus time, showing no systematic trend across the fit window, consistent with adequate model specification. (**b**) Histogram of regular residuals, showing an approximately symmetric, unimodal distribution centred near zero. (**c**) Residuals versus fitted Y, revealing a modest funnel structure in which residual variance increases at higher fitted values (less negative fitted Y, corresponding to the tail of the decay). This heteroscedasticity (unequal residual variance in which residuals are more scattered at low fitted values and more tightly clustered at high fitted values) reflects the increasing signal-to-noise ratio at early time points within the DIRK window and is a known feature of exponential decay fitting to optical relaxation data. (**d**) Normal Q-Q plot of regular residuals, showing close adherence to the theoretical normal distribution (dashed line) across the central quantile range, with minor heavy-tail deviations at the extremes.

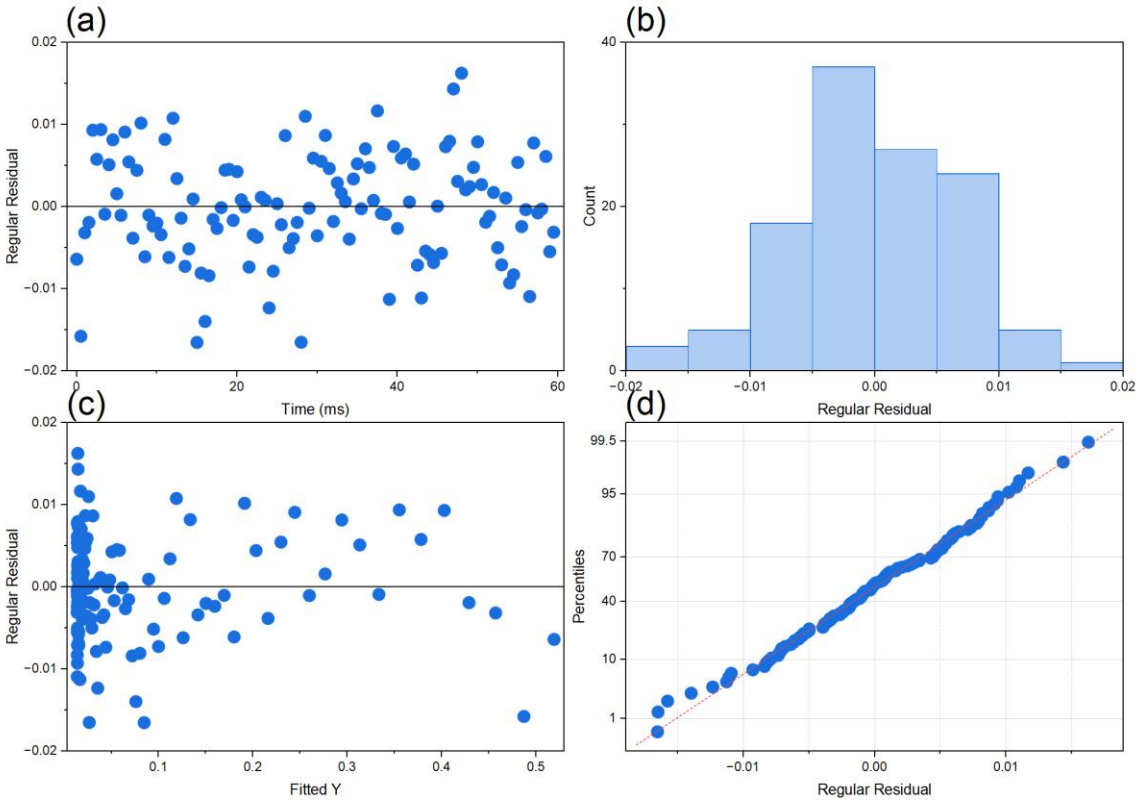

Fig. S2 Residual diagnostics for the single-exponential P700⁺ DIRK decay fit (WT, 10 s). Residual plots from fitting a single-exponential decay model to the P700⁺ DIRK relaxation trace for a representative WT replicate at 10 s of illumination. (**a**) Residuals versus time, showing no systematic trend across the fit window. (**b**) Histogram of regular residuals, showing an approximately symmetric, unimodal distribution centred near zero with a modest positive tail. (**c**) Residuals versus fitted Y, revealing pronounced heteroscedasticity: residual variance is highest at low fitted values corresponding to the early decay window, where the P700⁺ signal is small in amplitude, and decreases substantially at higher fitted values corresponding to the tail of the relaxation. This pattern is consistent with signal-amplitude-dependent noise in optical relaxation data and does not indicate systematic model misspecification. (**d**) Normal Q-Q plot

of regular residuals, showing close adherence to the theoretical normal distribution across the full quantile range.

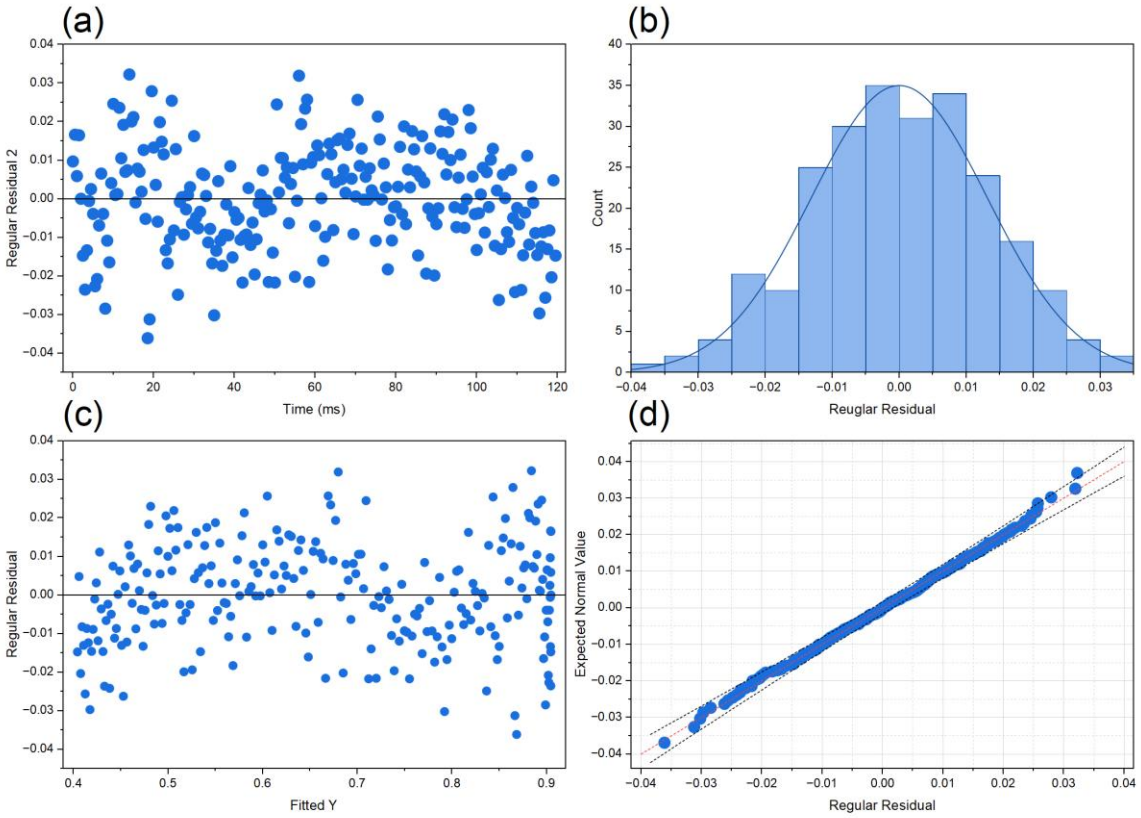

Fig. S3 Residual diagnostics for the biphasic PC DIRK decay fit (WT, 5 s). Residual plots from fitting a biphasic exponential decay model to the PC oxidation DIRK relaxation trace for a representative WT replicate at 5 s of illumination. (**a**) Residuals versus time, showing no systematic trend across the fit window and approximately uniform scatter around zero. (**b**) Histogram of regular residuals, showing close agreement with a normal distribution (overlaid curve), with a symmetric, unimodal shape centred near zero. (**c**) Residuals versus fitted Y, showing homogeneous variance across the full range of fitted values (0.4–0.9), with no evidence of the funnel structure observed in the single-exponential Fd and P700 fits. (**d**) Normal Q-Q plot of regular residuals, showing close adherence to the theoretical normal distribution (dashed reference line with 95% confidence band) across the central quantile range, with minor deviation at the lower tail.

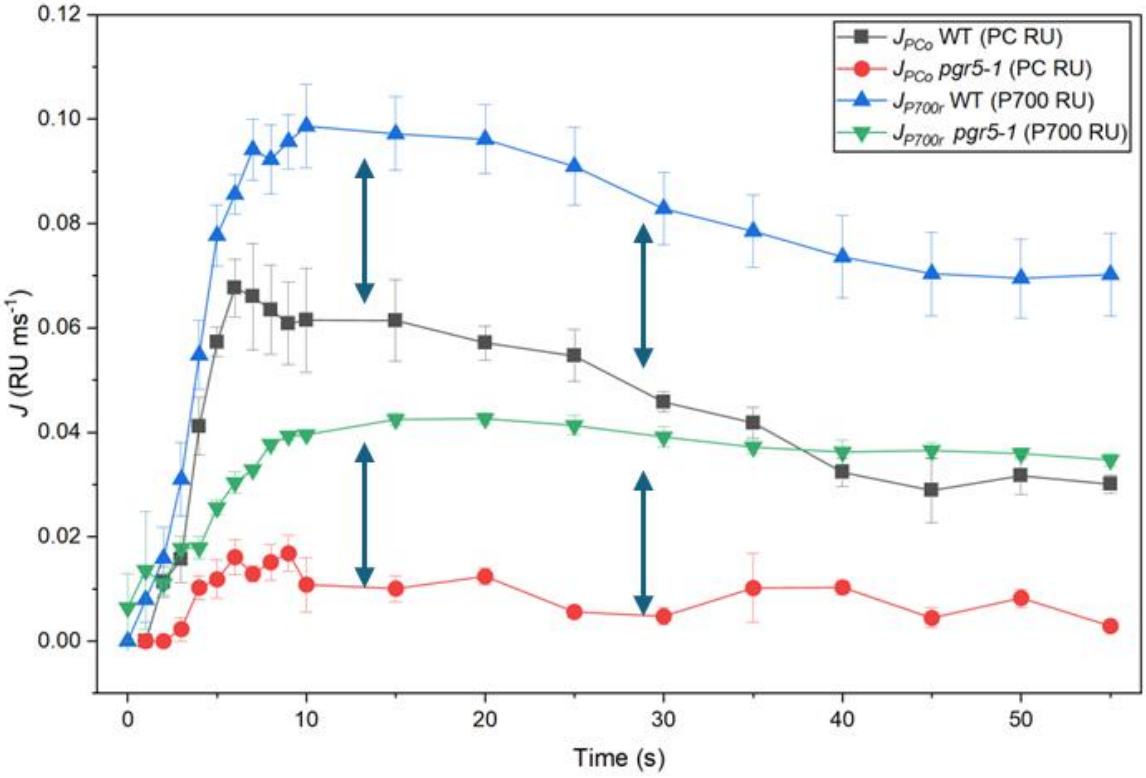

Fig. S4. Shared, time-dependent divergence between PSI flux proxies derived from PC oxidation and P700 reduction during induction. PSI flux estimates calculated independently from PC oxidation (J_{PCo}) and P700 reduction (J_{P700r}) during the LL–HL transition in WT and *pgr5-1*. The systematic separation between the two flux proxies emerges during induction but follows a qualitatively similar trajectory in both genotypes, consistent with a shared time-dependent distortion rather than a genotype-specific biological effect. To quantify this relationship, J_{P700r} was related to J_{PCo} and induction time using an empirical planar surface:

$$J_{P700r} = a + b\,J_{PCo} + c\,t + d J_{PCo} t$$

where b represents a static proportional scaling between the two flux proxies, c captures a time-dependent offset, and d captures a time-dependent interaction between flux magnitude and induction time. The planar model described WT data well (R^2 = 0.97) but fit *pgr5-1* with substantially lower fidelity (R^2 = 0.56), precluding formal quantitative comparison of fitted parameters between genotypes. The qualitative similarity of the divergence trajectories in both genotypes nonetheless indicates that the distortion between J_{PCo} and J_{P700r} is not a genotype-specific optical artefact, and that relative differences in derived PSI flux between WT and *pgr5-1* are not attributable to differential signal deconvolution. Traces show means; shaded bands indicate SE (n = 3).

Chapter 3: Supplemental Derivations

S1. $P700^+$ reduction kinetics during a DIRK: encounter-complex scheme, quasi–steady state, and integrated pseudo-first-order form

S1.1 Rationale and experimental constraint

DIRK relaxations during induction do not occur on a static background: donor availability, acceptor availability, and pathway engagement can all change on the same timescale as the relaxation itself. Under such conditions, a fitted DIRK time constant is best interpreted as an effective outcome of instantaneous flux capacity and pool accessibility, rather than a direct readout of a single intrinsic "slowdown" at Cytb_6f (Sacksteder & Kramer, 2000). This is most transparent when DIRKs are framed using established mobile-carrier kinetics for the PC to PSI donor reaction.

Importantly, in our measurements the deconvoluted P700 signal during DIRKs is well described by a clean single-exponential decay over the fitting windows used (i.e., no systematic curvature in semi-log plots and no structured residuals), providing experimental validation that a pseudo-first-order description is appropriate for the window over which parameters are extracted (see Results). This validation is essential because the derivation below shows explicitly that the "first-order" behaviour is emergent and conditional.

S1.2 Kinetic scheme: light-driven form and DIRK simplification (after Haehnel et al. 1994)

Haehnel et al. (1994) describe PC-mediated reduction of PSI using an encounter-complex scheme in which excitation regenerates $P700^+$. In compact form:

$$PC_r + P700 \underset{k_{\mathrm{off}}}{\overset{k_{\mathrm{on}}}{\rightleftharpoons}} (PC_r{:}P700) \overset{h\nu}{\rightarrow} (PC_r{:}P700^+) \overset{k_{\mathrm{et}}}{\rightarrow} PC_o + P700$$

where

- PC_r, PC_o: reduced and oxidised plastocyanin
- $P700$, $P700^+$: ground-state and oxidised PSI donor
- k_{on}: productive association (docking/encounter)
- k_{off}: dissociation (undocking)
- $h\nu$: excitation step regenerating $P700^+$under illumination

- k_{et}: intracomplex electron transfer once docked

During a DIRK, there is no light excitation ($h\nu$ absent). The relevant reduction step is therefore:

Eq. S1.1 $$PC_r + P700^+ \underset{k_{\mathrm{off}}}{\overset{k_{\mathrm{on}}}{\rightleftharpoons}} (PC_r{:}P700^+) \overset{k_{\mathrm{et}}}{\rightarrow} PC_o + P700$$

S1.3 Mass-action ODEs and quasi–steady-state reduction to an effective second-order law

Let the encounter complex concentration be

$$X(t) \equiv [PC_r{:}P700^+]$$

Mass-action formation and loss terms are:

- Formation: $k_{\mathrm{on}}[PC_r][P700^+]$
- Loss by dissociation: $k_{\mathrm{off}}X$
- Loss by electron transfer: $k_{\mathrm{et}}X$

Thus:

Eq. S1.2 $$\frac{dX}{dt} = k_{\mathrm{on}}[PC_r][P700^+] - (k_{\mathrm{off}} + k_{\mathrm{et}})X$$

Electron transfer within the complex reduces $P700^+$:

Eq. S1.3 $$\frac{d[P700^+]}{dt} = -k_{\mathrm{et}}X$$

Under the standard quasi–steady-state approximation for the encounter complex (Haehnel et al. 1994), set $dX/dt \approx 0$ over the DIRK fitting window:

$$0 = k_{\mathrm{on}}[PC_r][P700^+] - (k_{\mathrm{off}} + k_{\mathrm{et}})X$$

so

Eq. S1.4 $$X = \frac{k_{\mathrm{on}}}{k_{\mathrm{off}}+k_{\mathrm{et}}}\,[PC_r][P700^+]$$

Substitute (S1.4) into (S1.3):

$$\frac{d[P700^+]}{dt} = -k_{\mathrm{et}}\left(\frac{k_{\mathrm{on}}}{k_{\mathrm{off}} + k_{\mathrm{et}}}\right)[PC_r][P700^+]$$

Define an effective second-order constant:

Eq. S1.5 $$k_{2,eff}^{PSI} \equiv \frac{k_{\mathrm{on}} k_{\mathrm{et}}}{k_{\mathrm{off}} + k_{\mathrm{et}}}$$

giving the governing mass-action law for $P700^+$ reduction:

Eq. S1.6 $$\boxed{\frac{d[P700^+(t)]}{dt} = -\,k_{2,eff}^{PSI}\,[PC_r(t)]\,[P700^+(t)]}$$

S1.4 Limiting case: $k_{2,\mathrm{eff}} \approx k_{\mathrm{on}}$ when intracomplex ET is fast

Haehnel et al. (1994) show that intracomplex ET is fast once docking is achieved, motivating $k_{\mathrm{et}} \gg k_{\mathrm{off}}$. In this limit:

Eq. S1.7 $$k_{2,eff}^{PSI} = \frac{k_{\mathrm{on}} k_{\mathrm{et}}}{k_{\mathrm{off}} + k_{\mathrm{et}}} \approx k_{\mathrm{on}}$$

Thus, under DIRK conditions the effective second-order term reports primarily the productive association rate.

S1.5 Integration of the mass-action ODE

Define:

$$P(t) \equiv [P700^+(t)], \qquad C(t) \equiv [PC_r(t)]$$

so:

Eq. S1.8 $$\frac{dP}{dt} = -k_{2,eff}^{PSI}\,C(t)\,P(t)$$

Separate variables:

Eq. S1.9 $$\frac{dP}{P(t)} = -k_{2,eff}^{PSI}\,C(t)\,dt$$

Integrate:

$$\int_{P(0)}^{P(t)} \frac{dP}{P} = -k_{2,eff}^{PSI} \int_0^t C(s)\,ds$$

Eq. S1.10 $$\ln\left(\frac{P(t)}{P(0)}\right) = -k_{2,eff}^{PSI} \int_0^t C(s)\,ds$$

Exponentiate:

Eq. S1.11 $$P(t) = P(0)\,e^{-k_{2,\mathrm{eff}} \int_0^t C(s)\,ds}$$

Restoring full notation:

Eq. S1.12 $$\boxed{[P700^{+}(t)] = [P700^{+}(0)]e^{-k_{2,eff}^{PSI}\int_0^t [PC_r(s)]\,ds}}$$

S1.6 Reduction to the familiar exponential form

If $[PC_r]$is approximately constant over the fitting window:

Eq. S1.13 $$[P700^{+}(t)] = [P700^{+}(0)]e^{-k_{2,eff}^{PSI}[PC_r]t}$$

Thus:

Eq. S1.14 $$\boxed{k_{2,\mathrm{obs}}^{P700} = k_{2,eff}^{PSI}\,[PC_r]}$$

Eq. S1.15 $$\tau_{P700} = \frac{1}{k_{\mathrm{obs}}^{P700}} = \frac{1}{k_{2,eff}^{PSI}\,[PC_r]}$$

S2. PC oxidation kinetics during a DIRK: forced first-order ODE, integrating-factor solution, and bi-exponential form

S2.1 Rationale and connection to the P700⁺ derivation

During a DIRK, the observed PC signal reflects the balance of two concurrent processes operating on the same timescale as the relaxation: (i) PSI-driven oxidation of PC as P700⁺ is reduced, and (ii) Cyt*b*$_6$*f* -driven reduction of PC_o back toward PC_r. As in the P700⁺ derivation, the goal here is to obtain a closed-form expression that can be fit to DIRK traces and interpreted in terms of physically meaningful rate constants and amplitudes.

Throughout this section, $[PC_o]$ denotes the oxidised PC pool, and $P(t) \equiv [P700^+(t)]$ is the oxidised PSI donor pool defined in Section S1.

S2.2 Governing ODE for $[PC_o(t)]$ during the DIRK

S2.2.1 Source term: production of PC_o by PSI

Each reduction event of P700⁺ by PC_r produces one PC_o. Therefore, the rate of PC_o production equals the rate of P700⁺ disappearance:

Eq. S2.1
$$\left(\frac{d[PC_o]}{dt}\right)^{PSI} = -\frac{d[P700^+]}{dt}$$

In the DIRK window used for parameterization, the P700⁺ relaxation is experimentally well described by a single exponential (Results), so we write:

Eq. S2.2
$$P(t) = P_0 e^{-k_1 t} \Rightarrow -\frac{dP}{dt} = k_1 P_0 e^{-k_1 t} = k_1 P(t)$$

$$k_1 = k_{2,\text{obs}}^{P700} = k_{2,\text{eff}}[PC_r]$$

Substituting into (S2.1):

Eq. S2.3
$$\left(\frac{d[PC_o]}{dt}\right)^{PSI} = k_1 P(t)$$

S2.2.2 Sink term: consumption of PC_o by Cyt*b*$_6$*f*

We represent Cyt*b*$_6$*f* -driven reduction of PC_o as an effective pseudo-first-order sink over the DIRK fitting window:

Eq. S2.4
$$\left(\frac{d[PC_o]}{dt}\right)^{Cytf} = -\,k_2\,[PC_o(t)]$$

where k_2(s^{-1}) is the effective first-order rate constant describing the reduction of PC_o during the DIRK (potentially reflecting lumen pH, Cyt*f* redox poise, encounter/docking efficiency, and other factors).

$$k_2 = k_{2,eff}^{Cytf}[Cytf_r]$$

S2.2.3 Combined ODE

Combining the PSI source (S2.3) and the Cytb_6f sink (S2.4) yields:

Eq. S2.5 $$\frac{d[PC_o(t)]}{dt} = k_1 P(t) - k_2[PC_o(t)]$$

Substituting $P(t) = P_0 e^{-k_1 t}$ from (S2.2) gives a linear first-order ODE:

Eq. S2.6 $$\boxed{\frac{d[PC_o(t)]}{dt} + k_2[PC_o(t)] = k_1 P_0 e^{-k_1 t}}$$

Equation (S2.6) states that $[PC_o]$ is "forced" upward by PSI (through the relaxing P700$^+$ pool) while simultaneously being removed as Cytb_6f reduces PC_o back toward PC_r.

S2.3 Solution of Eq. (S2.6) by integrating factor

Equation (S2.6) has the standard form:

$$\frac{dy}{dt} + ay = f(t),$$

with $y = [PC_o(t)]$, $a = k_2$, and $f(t) = k_1 P_0 e^{-k_1 t}$.

S2.3.1 Integrating factor

The integrating factor is:

Eq. S2.7 $$\mu(t) = e^{\int k_2\, dt} = e^{k_2 t}$$

Multiply both sides of (S2.6) by $e^{k_2 t}$:

Eq. S2.8 $$e^{k_2 t}\frac{d[PC_o(t)]}{dt} + k_2 e^{k_2 t}[PC_o(t)] = k_1 P_0 e^{(k_2 - k_1)t}$$

Recognize the left-hand side as a product derivative:

Eq. S2.9 $$\frac{d}{dt}([PC_o(t)]e^{k_2 t}) = k_1 P_0 e^{(k_2 - k_1)t}$$

Integration factor explanation for non-math people:

Equation (S2.6) contains both (i) the instantaneous change in PC_o (the derivative) and (ii) a term proportional to PC_o itself ($k_2 PC_o$), which represents continuous removal of PC_o by Cyt*b*$_6$*f*. Because of this "self-decay" term, the equation cannot be integrated directly by treating the right-hand side as the only driver. The integrating factor $e^{k_2 t}$ is chosen specifically because it cancels the $k_2 PC_o$ decay term and converts the left-hand side into the derivative of a single quantity, $\frac{d}{dt}(PC_o(t)e^{k_2 t})$. This step is simply a bookkeeping change that allows integration of the equation in one line, while keeping the same physical meaning: PC_o is produced by PSI and simultaneously consumed by Cyt*b*$_6$*f*.

S2.3.2 Integrate from 0 to t

Integrate both sides from 0 to t, using a dummy variable s inside the integral:

Eq. S2.10 $$[PC_o(t)]e^{k_2 t} - [PC_o(0)] = k_1 P_0 \int_0^t e^{(k_2 - k_1)s}\, ds$$

Eq. S2.11 $$\int_0^t e^{(k_2 - k_1)s}\, ds = \left[\frac{e^{(k_2 - k_1)s}}{k_2 - k_1}\right]_0^t = \frac{e^{(k_2 - k_1)t} - 1}{k_2 - k_1}$$

Substituting (S2.11) into (S2.10) gives:

Eq. S2.12 $$[PC_o(t)]e^{k_2 t} = [PC_o(0)] + \frac{k_1 P_0}{k_2 - k_1}(e^{(k_2 - k_1)t} - 1)$$

S2.3.3 Solve for $[PC_o(t)]$

Multiply through by $e^{-k_2 t}$:

Eq. S2.13 $$[PC_o(t)] = [PC_o(0)]e^{-k_2 t} + \frac{k_1 P_0}{k_2 - k_1}(e^{-k_1 t} - e^{-k_2 t})$$

This is the desired closed-form expression: a sum of two exponentials with rate constants k_1 and k_2. The $e^{-k_1 t}$ term is the decay forcing imposed by PSI via the relaxing $P700^+$pool (oxidation of PC), whereas the $e^{-k_2 t}$ term reflects the decay of the initial PC oxidation state (reduction) caused by $Cytf$.

S2.4 Bi-exponential "two-amplitude" form for fitting

Equation (S2.13) can be rearranged to make explicit the fitted amplitudes multiplying each exponential. Collect terms in $e^{-k_2 t}$ and $e^{-k_1 t}$:

Eq. S2.14 $$[PC_o(t)] = \left([PC_o(0)] - \frac{k_1 P_0}{k_2 - k_1}\right)e^{-k_2 t} + \left(\frac{k_1 P_0}{k_2 - k_1}\right)e^{-k_1 t}$$

Define:

Eq. S2.15 $$B \equiv \frac{k_1 P_0}{k_2 - k_1}$$

so the fit form is:

Eq. S2.16 $$\boxed{[PC_o(t)] = ([PC_o(0)] - B)e^{-k_2 t} + Be^{-k_1 t}}$$

This form is convenient for global fitting because k_1 can be shared (from the independently fitted P700⁺ DIRK), leaving k_2 and B to be estimated from the PC trace. Here, k_2 sets the time constant for Cyt*f*-driven reduction of PC_o (the $e^{-k_2 t}$ decay). The parameter B quantifies the magnitude of the PSI-imposed term (the component of $PC_o(t)$ that follows the $e^{-k_1 t}$ decay of P700⁺), while $[PC_{ox}(0)] - B$ is simply the amplitude assigned to the Cyt*f* reduction of PC ($e^{-k_2 t}$) component. Although this shared-k_1 form is useful for fitting, it is derived from a reduced lumped model and therefore creates an apparent contradiction when interpreted too literally as $k_{2,\mathrm{eff}}\langle PC_r\rangle = k_{2,\mathrm{eff}}\langle P700\rangle$, because the shared rate is assigned to terms representing different effective donor pools. This issue is resolved in Section S7 by reintroducing PC diffusion and treating the donor-side kinetics as a coupled Jacobian system, in which the shared rate emerges as a common eigenmode rather than from direct equality of the scalar terms.

S2.5 Summary of symbols

- $[PC_o(t)]$: oxidised plastocyanin fraction (or concentration) during the DIRK
- $[PC_o(0)]$: oxidised plastocyanin fraction at $t = 0$
- $P(t) \equiv [P700^+(t)]$: oxidised PSI donor pool during the DIRK
- $P_0 \equiv [P700^+(0)]$: oxidised PSI donor pool at $t = 0$
- k_1(s^{-1}): observed first-order rate constant of P700⁺ relaxation (from DIRK fit)
- k_2(s^{-1}): effective first-order rate constant of PC_o reduction ($Cytb_6f \rightarrow PC$) during the DIRK
- B: fitted amplitudes multiplying the $e^{-k_1 t}$ and $e^{-k_2 t}$ components of $[PC_o(t)]$

S3. Ferredoxin (Fd) DIRK kinetics: parallel-pathway mass action scheme, integrated solution, and pathway-specific k' terms

S3.1 Rationale

Ferredoxin provides a direct readout of PSI acceptor-side electron throughput during induction because the DIRK relaxation of Fd_r reports the net withdrawal of electrons into downstream sinks. In contrast to $P700^+$ (Section S1), oxidation of Fd_r during a DIRK is intrinsically multi-pathway, because several sinks operate in parallel and compete for the same reduced pool. Consequently, the fitted DIRK rate constant is not an intrinsic single-enzyme parameter, but a composite reflecting the summed withdrawal capacity of concurrent pathways at that moment.

S3.2 Kinetic schema for Fd_r oxidation during a DIRK (parallel sinks)

During a DIRK, reduced ferredoxin relaxes as electrons are withdrawn through multiple pathways. Using the pathway partitioning defined in the manuscript, we represent three effective sinks:

Eq. S3.1 $$Fd_r \overset{k'_C}{\rightarrow} Fd_{ox},\ Fd_r \overset{k'_F}{\rightarrow} Fd_{ox},\ Fd_r \overset{k'_X}{\rightarrow} Fd_{ox}$$

where

- k'_C: effective first-order withdrawal constant (s^{-1}) for CEF-associated sinks
- k'_F: effective first-order withdrawal constant (s^{-1}) for FNR-associated withdrawal to $NADP^+$
- k'_X: effective first-order withdrawal constant (s^{-1}) for the remaining Fd-dependent pathways

---

S3.3 Mass-action ODE for $[Fd_r(t)]$ and definition of k_{obs}^{Fd}

Let:

$$F(t) \equiv [Fd_r(t)]$$

Each sink contributes a first-order loss term in $F(t)$, so the total withdrawal flux is:

Eq. S3.2 $$-\frac{dF}{dt} = k'_C F(t) + k'_F F(t) + k'_X F(t)$$

or:

Eq. S3.3 $$\frac{dF}{dt} = -(k'_C + k'_F + k'_X)\, F(t)$$

Define the observed Fd DIRK constant:

Eq. S3.4 $$k_{obs}^{Fd} \equiv k'_C + k'_F + k'_X$$

giving:

Eq. S3.5 $$\boxed{\frac{d[Fd_r(t)]}{dt} = -\, k_{obs}^{Fd}\, [Fd_r(t)]}$$

S3.4 Integration: exponential decay of $[\boldsymbol{Fd_r(t)}]$

Divide by $[Fd_r(t)]$ and multiply by dt:

Eq. S3.6 $$\frac{d[Fd_r(t)]}{[Fd_r(t)]} = -\, k_{obs}^{Fd}\, dt$$

Integrate from 0 to t:

Eq. S3.7 $$\ln\left(\frac{[Fd_r(t)]}{[Fd_r(0)]}\right) = -\, k_{obs}^{Fd} t$$

Exponentiating:

Eq. S3.8 $$\boxed{[Fd_r(t)] = [Fd_r(0)]\, e^{-k_{obs}^{Fd} t}}$$

However, the residuals (Fig. S1) show that the decay is not perfectly captured by a single exponential, consistent with the underlying kinetics being more complex than a pure first-order relaxation.

S3.5 Pathway-resolved fluxes and total flux

Because each pathway is first order in $[Fd_r]$, the instantaneous pathway fluxes are:

Eq. S3.9 $$J_C(t) \equiv k'_C[Fd_r(t)],\ J_F(t) \equiv k'_F[Fd_r(t)],\ J_X(t) \equiv k'_X[Fd_r(t)]$$

The total flux out of $Fd_r$is:

Eq. S3.10 $$J_{Fd}(t) \equiv -\frac{d[Fd_r(t)]}{dt} = k_{obs}^{Fd}[Fd_r(t)]$$

and at DIRK onset ($t = 0$):

$$J_C(0) = k'_C[Fd_r(0)], \qquad J_F(0) = k'_F[Fd_r(0)], \qquad J_X(0) = k'_X[Fd_r(0)],$$

Eq. S3.11 $$J_{Fd}(0) = k_{obs}^{Fd}[Fd_r(0)]$$

S3.6 Genotype partitioning of the CEF-associated contribution

For two genotypes (WT and *pgr5-1*), the observed Fd DIRK constants can be written:

Eq. S3.12 $$k_{obs}^{Fd,WT} = k_C'^{WT} + k_F'^{WT} + k_X'^{WT}$$

Eq. S3.13 $$k_{obs}^{Fd,pgr5} = k_C'^{pgr5} + k_F'^{pgr5} + k_X'^{pgr5}$$

If loss of PGR5 primarily removes the CEF-associated withdrawal term, then the CEF-associated contribution can be estimated by subtraction:

Eq. S3.14 $$\boxed{k_C' \approx k_{obs}^{Fd,WT} - k_{obs}^{Fd,pgr5}}$$

This subtraction applies at the level of effective rate constants (independent of signal amplitude). Fluxes are then obtained by multiplying by $[Fd_r(0)]$ as in Eq. (S3.11).

Consistent with established over-reduction of the PQ pool in *pgr5-1*, it is reasonable to expect that NDH-dependent CEF is also slowed, because NDH ultimately depends on availability of oxidised acceptors in the intersystem chain. Conversely, if stromal acceptor limitation is not dramatically altered (i.e., $NADP^+$ availability is not grossly different), then the higher steady-state reduction pressure upstream of PSI could increase the *potential* for FNR turnover (through increased reduced Fd availability), even if this is partially counteracted by acceptor-side constraints.

Under these assumptions, the genotype difference

$$\Delta k \equiv k_{\mathrm{obs}}^{\mathrm{WT}} - k_{\mathrm{obs}}^{pgr5}$$

most plausibly reflects a dominant contribution from loss of PGR5-dependent CEF, plus a smaller and less constrained contribution from altered NDH-dependent flux and/or other sinks. Δk is therefore presented as an empirical Δk_{obs} (or $\Delta k_{\mathrm{PGR5,app}}$) rather than ascribing it entirely to a single pathway (e.g., k_C'), because the partitioning among sinks cannot be uniquely resolved from the DIRK decay alone.

S3.7 What is contained within k_F': Michaelis–Menten acceptor dependence embedded in an effective first-order term

To make explicit what is contained within k_F', the FNR-mediated withdrawal of electrons from Fd_r is written as a Michaelis–Menten function of the oxidised acceptor pool $[NADP^+]$. Over a

DIRK fitting window, $[NADP^+]$ can be treated as an acceptor-availability factor that modulates withdrawal capacity, while the observed Fd decay is approximated as first order in $[Fd_r]$.

A minimal expression for the FNR-associated flux is:

Eq. S3.15 $$J_F(t) = \frac{V_{\max}\,[\mathrm{NADP^+}(t)]}{K_M^{FNR}+[\mathrm{NADP^+}(t)]}\ \frac{[Fd_r(t)]}{K_M^{Fd}+[Fd_r(t)]}$$

where $V_{\max}$ is the maximal catalytic capacity of the FNR reaction, K_M^{FNR} is an effective Michaelis constant describing dependence on $[NADP^+]$, and K_M^{Fd} is an effective Michaelis constant describing dependence on $[Fd_r]$.

In the regime where the decay is approximately first order in $[Fd_r]$ over the fitting window:

Eq. S3.16 $$[Fd_r(t)] \ll K_M^{Fd} \Rightarrow \frac{[Fd_r(t)]}{K_M^{Fd}+[Fd_r(t)]} \approx \frac{[Fd_r(t)]}{K_M^{Fd}}$$

Substituting (S3.16) into (S3.15) gives:

Eq. S3.17 $$J_F(t) \approx \left(\frac{V_{\max}}{K_M^{Fd}}\right)\frac{[NADP^+(t)]}{K_M^{FNR}+[NADP^+(t)]}\ [Fd_r(t)]$$

Comparing (S3.17) to the first-order sink form $J_F(t) = k'_F(t)[Fd_r(t)]$, we identify:

Eq. S3.18 $$\boxed{k'_F(t) = \left(\frac{V_{\max}}{K_M^{Fd}}\right)\frac{[NADP^+(t)]}{K_M^{FNR}+[NADP^+(t)]}}$$

Thus, k'_F is an effective first-order constant that embeds both catalytic capacity and a Michaelis–Menten acceptor-availability factor. Early in induction, when $[NADP^+]$ is relatively large, the acceptor factor approaches unity and $k'_F(t)$ approaches $\left(V_{\max}/K_M^{Fd}\right)$; as $[NADP^+]$ becomes reduced, the acceptor factor decreases, reducing the effective withdrawal capacity reflected in the fitted Fd DIRK constant.

S4. Why k_{obs}^{P700} contains the time-averaged $[PC_r]$ integral

S4.1 Starting point: the integrated P700⁺ solution makes the "missing time" explicit

From Section S1, the governing mass-action law for P700⁺ reduction during a DIRK is:

Eq. S4.1 $$\frac{d[P700^+(t)]}{dt} = -k_{2,\text{eff}}\,[PC_r(t)]\,[P700^+(t)]$$

After separating variables and integrating, the exact solution is:

Eq. S4.2 $$[P700^+(t)] = [P700^+(0)]e^{-k_{2,\text{eff}}\int_0^t [PC_r(s)]\,ds}$$

Equation (S4.2) shows why it can appear that "time is missing" in the original differential form when the equation is discussed only in terms of $[PC_r]$: the time dependence enters through the integral $\int_0^t [P\,C_r(s)]ds$. Time is therefore present, but it is contained inside the integrated donor-availability term.

S4.2 Connection to the fitted single-exponential form

Experimentally, the P700⁺ DIRK is well described over the fitting window by:

Eq. S4.3 $$[P700^+(t)] \approx [P700^+(0)]e^{-k_{obs}^{P700}t}$$

Comparing Eq. (S4.3) to the exact integrated form (S4.2), the exponents must match over the fitting window. This motivates:

Eq. S4.4 $$k_{obs}^{P700}t \;\approx\; k_{2,\text{eff}}\int_0^t [P\,C_r(s)]\,ds$$

Dividing both sides by t gives:

Eq. S4.5 $$k_{obs}^{P700} \;\approx\; k_{2,\text{eff}}\left(\frac{1}{t}\int_0^t [\,PC_r(s)]\,ds\right)$$

The term in parentheses is the time-averaged donor availability over the window:

Eq. S4.6 $$\langle [PC_r] \rangle_t \equiv \frac{1}{t}\int_0^t [P\,C_r(s)]\,ds$$

Thus:

Eq. S4.7 $$\boxed{k_{obs}^{P700} \;\approx\; k_{2,\text{eff}}\,\langle [PC_r] \rangle_t}$$

S4.3 Interpretation for readers (why "$k \times [PC_r]$" is an average, not an instantaneous value)

In the special case where $[PC_r]$ is constant across the fitting window, $\langle [PC_r] \rangle_t = [PC_r]$ and Eq. (S4.7) reduces to the familiar heuristic $k_{obs}^{P700} = k_{2,\mathrm{eff}}[PC_r]$.

However, during induction $[PC_r(t)]$ can vary measurably within the same window used to fit the P700⁺ DIRK. In that case, the fitted exponential coefficient k_{obs}^{P700} does not correspond to an instantaneous $[PC_r]$ at any single time point. Rather, because the fit is performed to a function of the form e^{-kt}, the fitted k necessarily captures the average donor availability over the window, i.e. $k_{obs}^{P700}/k_{2,\mathrm{eff}}$ is the time-averaged integral term $\frac{1}{t}\int_0^t [P\,C_r(s)]ds$.

Importantly, this averaging result is derived from the reduced lumped formulation in Section S1, where donor availability is represented by a single effective PC_r term. As shown later in Section S7, a fuller diffusion-aware treatment resolves this donor term into spatially and kinetically coupled sub-pools, such that the fitted $\langle PC_r \rangle$ should be interpreted as an effective lumped donor-availability descriptor of the dominant relaxation mode, rather than necessarily the instantaneous PSI-proximal reduced PC pool itself.

S5. Log decomposition of flux differences into kinetic versus redox contributions

As derived in Section S1, the instantaneous P700⁺ reduction flux is proportional to the product of (i) an effective kinetic term describing encounter/turnover capacity and (ii) the availability of the reacting redox pools. Evaluated at DIRK onset ($t = 0$):

Eq. S5.1 $$J_{P700}(0) = k_{2,\mathrm{eff}}\,[PC_r(0)]\,[P700^+(0)]$$

To compare genotypes, we take the ratio of the onset fluxes (mutant relative to WT):

Eq. S5.2 $$\frac{J^{mut}}{J^{WT}} = \frac{k_{2,\mathrm{eff}}^{mut}}{k_{2,\mathrm{eff}}^{WT}} \cdot \frac{[PC_r]^{mut}}{[PC_r]^{WT}} \cdot \frac{[P700^+]^{mut}}{[P700^+]^{WT}}$$

Taking natural logarithms converts this multiplicative relationship into an additive decomposition:

Eq. S5.3 $$\ln\left(\frac{J^{mut}}{J^{WT}}\right) = \ln\left(\frac{k_{2,\mathrm{eff}}^{mut}}{k_{2,\mathrm{eff}}^{WT}}\right) + \ln\left(\frac{[PC_r]^{mut}}{[PC_r]^{WT}}\right) + \ln\left(\frac{[P700^+]^{mut}}{[P700^+]^{WT}}\right)$$

Equation (S5.3) is used in the Results to partition the observed change in J_{P700} into separable contributions arising from altered kinetic capacity ($k_{2,\mathrm{eff}}$) versus altered redox-state availability of the donor and acceptor pools ($[PC_r]$ and $[P700^+]$).

S6. Encounter theory links PSI donor-side kinetics and $\mathrm{Cyt}f \rightarrow PC$ delivery: diffusion, pH, and electrostatics (Hope 2000; Haehnel et al. 1994)

S6.1 Implication for the *pgr5-1* phenotype from P700$^+$ kinetics

Experimentally, the PC pool is more reduced in the *pgr5-1* background during induction (Results; Figure Figure 4b, 8a), which would tend to increase $[PC_r]$ and therefore increase k_{obs}^{P700} if $k_{2,\mathrm{eff}}^{P700}$ were unchanged (Eq. S1.14). The observation that k_{obs}^{P700} is instead smaller implies that $k_{2,\mathrm{eff}}^{P700}$ must be reduced, consistent with a slowdown in the productive association/encounter term:

Eq. S6.2 $$k_{2,\mathrm{eff}}^{PSI} \approx k_{\mathrm{on}} \;\Rightarrow\; k_{\mathrm{on}} \text{ is reduced in } \textit{pgr5-1}$$

This interpretation follows directly from the encounter-complex derivation of Section S1 and the fast intracomplex ET limit described by Haehnel *et al.* (1994), under which the effective second-order constant is dominated by productive association.

S6.2 Smoluchowski-style encounter framework for k_{on} (Hope 2000)

A mechanistic basis for variation in k_{on} is provided by encounter theory. Hope (2000) describes a Smoluchowski-style framework in which the association rate depends on diffusion, collision geometry, and long-range electrostatics. In compact form:

Eq. S6.2 $$k_{\mathrm{on}} \approx 4\pi N_A \,(D_{PC} + D_{partner})\, R \times f_{\mathrm{steric/orient}} \times f_{\mathrm{electrostatic}}$$

where R is the encounter distance (sum of effective radii), D terms are mutual diffusion coefficients, and the multiplicative factors capture steric/orientation constraints and the electric-field distribution that can enhance (or inhibit) productive encounters. This form applies generically to mobile carrier encounters in the lumen, including both $PC \rightarrow PSI$ and $Cytf \rightarrow PC$ interactions.

Within the lumen, the key experimentally supported differences between WT and *pgr5-1* relevant to these terms are (i) altered redox poise (more reduced PC and P700 pools) and (ii) lower ΔpH (and therefore a less acidic lumen during induction). Changes in lumen pH can alter protonation of amino-acid residues involved in docking on both PC and PSI, providing a plausible route to reduced electrostatic steering and/or altered docking orientation efficiency (Hope 2000). This framework therefore provides a mechanistically grounded explanation for why a slower k_{obs}^{P700} in *pgr5-1* need not imply a classical "Cytb_6f is slower" interpretation, but can instead reflect altered donor-side encounter kinetics under induction conditions.

S6.3 Factorization of $Cytf \rightarrow PC$ delivery into pH, diffusion, and electrostatic/docking terms

In the Discussion, we express the intrinsic $Cytf \rightarrow PC$ delivery capacity as a product of separable factors (Eq. 11), emphasizing that multiple physical constraints can contribute to an effective rate constant measured during induction. We write the intrinsic effective term as:

Eq. S6.3 $$\boxed{k_{f,\mathrm{eff}}^{Cytf} = k_f^0 \ \phi(\Delta pH) \ \psi(D) \ \chi(\mathrm{electrostatics})}$$

where:

- $\phi(\Delta pH)$ captures lumen acidification dependence,
- $\psi(D)$ captures effective diffusion/encounter limitation within the lumen,
- $\chi(\mathrm{electrostatics})$ captures local electrostatic steering and docking efficiency for productive $Cytf - PC$ interactions.

Equation (S6.3) is the explicit analogue, for $Cytf \rightarrow PC$, of the encounter-theory statement in Eq. (S6.2): the experimentally observed effective delivery constant can change because of altered lumen pH (affecting charge states and docking), altered diffusion/encounter constraints, and/or altered electrostatic steering, even if the underlying catalytic machinery of the complexes is unchanged. As argued in the Discussion, this factorized view clarifies why the early induction phenotype is difficult to explain by pH effects alone given the magnitude required relative to measured *pmf*, and motivates interpreting both PSI donor-side kinetics and $Cytf \rightarrow PC$ delivery through the same encounter-theory lens (Hope, 2000).

S7. Full species-level donor-side model with PC diffusion and Jacobian reduction

S7.1 Rationale

The simplified donor-side model presented above is useful for interpreting the observed shared rates between P700 and PC oxidation, but it does not show explicitly how diffusion enters the full kinetic system. As a result, the reduced formulation creates an apparent contradiction: if k_1 is shared, the simplified treatment seems to imply that $k_{2,\mathrm{eff}}\langle PC_r\rangle = k_{2,\mathrm{eff}}\langle P700\rangle$, which is not physically meaningful as written. The purpose of this section is to show that this contradiction is only apparent and arises from over-reduction of the full coupled system to a scalar form. When PC diffusion and the full donor-side reaction network are included, and the kinetics are interpreted through a linearized matrix formulation, the shared rates emerge naturally as properties of the coupled system eigenmodes (Kustin *et al.*, 1965). To make that clear, we begin with the full species-level formulation including Cyt*f* binding, PSI binding, electron transfer, and PC diffusion between the Cytb_6f and PSI domains. We then show how the Jacobian of the full nonlinear system defines the shared relaxation modes and finally reduce that description to the donor-side PSI block relevant to the measured DIRK kinetics. This makes explicit that the shared rates are first properties of the complete coupled system, and only afterward can be interpreted in reduced donor-side form.

S7.2 Species-level kinetic scheme

The full reaction scheme is

Eq. S7.1 $$\mathrm{Cyt}f_r + PC_o^C \underset{k_2}{\overset{k_1}{\rightleftharpoons}} X = \mathrm{Cyt}f_r{:}PC_o$$

Eq. S7.2 $$X \overset{k_{12}}{\rightarrow} \mathrm{Cyt}f_o + PC_r^C$$

Eq. S7.3 $$PC_r^C \overset{k_{\mathrm{d2}}}{\rightarrow} PC_r^P$$

Eq. S7.4 $$P700^+ + PC_r^P \underset{k_4}{\overset{k_3}{\rightleftharpoons}} Y = PC_r{:}P700^+$$

Eq. S7.5 $$Y \overset{k_{34}}{\rightarrow} P700 + PC_o^P$$

Eq. S7.6 $$PC_o^P \overset{k_{\mathrm{d1}}}{\rightarrow} PC_o^C$$

Here, the superscript C denotes the Cyt*f* domain and P denotes the PSI domain. The intermediate X is the Cyt*f* encounter complex, and Y is the PSI encounter complex. This full

system explicitly includes both forward and return PC diffusion steps which were missing from the initial derivations.

S7.3 State vector and nonlinear ODE system

Using the state ordering (S7.7):

$$
\begin{aligned}
x_1 &= X = \mathrm{Cyt}f_r{:}\,PC_o \\
x_2 &= Y = PC_r{:}\,P700^+ \\
x_3 &= [\mathrm{Cyt}f_r] \\
x_4 &= [\mathrm{Cyt}f_o] \\
x_5 &= [P700^+] \\
x_6 &= [P700] \\
x_7 &= [PC_o^C] \\
x_8 &= [PC_r^C] \\
x_9 &= [PC_r^P] \\
x_{10} &= [PC_o^P]
\end{aligned}
$$

Following the same method explained in Kustin *et al.* (1965), the full state vector is

Eq. S7.8 $$x = [x_1\ x_2\ x_3\ x_4\ x_5\ x_6\ x_7\ x_8\ x_9\ x_{10}]^T$$

The nonlinear ODE system (S7.9) is

$$
\begin{aligned}
\dot{x}_1 &= k_1 x_3 x_7 - (k_2 + k_{12}) x_1 \\
\dot{x}_2 &= k_3 x_5 x_9 - (k_4 + k_{34}) x_2 \\
\dot{x}_3 &= -k_1 x_3 x_7 + k_2 x_1 \\
\dot{x}_4 &= k_{12} x_1 \\
\dot{x}_5 &= -k_3 x_5 x_9 + k_4 x_2 \\
\dot{x}_6 &= k_{34} x_2 \\
\dot{x}_7 &= -k_1 x_3 x_7 + k_2 x_1 + k_{\mathrm{d}1} x_{10} \\
\dot{x}_8 &= k_{12} x_1 - k_{\mathrm{d}2} x_8 \\
\dot{x}_9 &= -k_3 x_5 x_9 + k_4 x_2 + k_{\mathrm{d}2} x_8 \\
\dot{x}_{10} &= k_{34} x_2 - k_{\mathrm{d}1} x_{10}
\end{aligned}
$$

This is the full donor-side reaction-diffusion model at the species level. It contains all factors considered here: Cyt*f* binding and ET, PSI binding and ET, oxidation and reduction of PC in distinct domains, and interdomain diffusion of reduced and oxidised PC.

S7.4 Full Jacobian matrix

Linearization of the nonlinear system around an operating point x^* gives

Eq. S7.10 $$\delta\dot{x} \approx J(x^*)\,\delta x$$

where the Jacobian (S7.11) is

$$J(x) = \begin{bmatrix} -(k_2+k_{12}) & 0 & k_1x_7 & 0 & 0 & 0 & k_1x_3 & 0 & 0 & 0 \\ 0 & -(k_4+k_{34}) & 0 & 0 & k_3x_9 & 0 & 0 & 0 & k_3x_5 & 0 \\ k_2 & 0 & -k_1x_7 & 0 & 0 & 0 & -k_1x_3 & 0 & 0 & 0 \\ k_{12} & 0 & 0 & 0 & 0 & 0 & 0 & 0 & 0 & 0 \\ 0 & k_4 & 0 & 0 & -k_3x_9 & 0 & 0 & 0 & -k_3x_5 & 0 \\ 0 & k_{34} & 0 & 0 & 0 & 0 & 0 & 0 & 0 & 0 \\ k_2 & 0 & -k_1x_7 & 0 & 0 & 0 & -k_1x_3 & 0 & 0 & k_{\mathrm{d1}} \\ k_{12} & 0 & 0 & 0 & 0 & 0 & 0 & -k_{\mathrm{d2}} & 0 & 0 \\ 0 & k_4 & 0 & 0 & -k_3x_9 & 0 & 0 & k_{\mathrm{d2}} & -k_3x_5 & 0 \\ 0 & k_{34} & 0 & 0 & 0 & 0 & 0 & 0 & 0 & -k_{\mathrm{d1}} \end{bmatrix}$$

The eigenvalues of $J(x^*)$ define the relaxation rates of the full system. Because each measured signal is a linear combination of state variables, the measured P700, PC, and Cyt*f* transients all inherit the same underlying eigenmodes of this Jacobian, even though their amplitudes differ.

S7.5 Why the full Jacobian implies shared rates

The linearized solution can be written as

Eq. S 7.12 $$\delta x(t) = \sum_i a_i\, v_i e^{\lambda_i t}$$

where λ_i are the eigenvalues of $J(x^*)$ and v_i are the corresponding eigenvectors. Any measured observable $y(t)$, such as a P700 or PC signal, is a projection of $\delta x(t)$ onto a measurement vector, so

Eq. S7.13 $$y(t) = \sum_i b_i\, e^{\lambda_i t}$$

Thus, P700 and PC do not need to obey identical scalar ODEs in order to share the same fitted rate constant. They only need to inherit the same dominant eigenmode from the coupled system. In this sense, the shared rate is first a property of the full Jacobian, not of any single reduced equation.

S7.6 Reduction to the PSI donor-side interaction block

To interpret the observed donor-side relaxation more directly, the relevant part of the full system is the PSI interaction block containing

$$Y = PC_r{:}\,P700^+$$
$$P700^+$$
$$PC_r^P$$

together with the diffusion-fed source term from PC_r^C. In terms of the full variable set, this means the dominant donor-side subsystem is built from $x_2\ x_5\ x_9\ x_8$.

Define the reduced donor-side state vector

$$z = [x_2\ x_5\ x_9\ x_8]^T$$

with dynamics

$$\dot{x}_2 = k_3 x_5 x_9 - (k_4 + k_{34}) x_2$$
$$\dot{x}_5 = -k_3 x_5 x_9 + k_4 x_2$$
$$\dot{x}_9 = -k_3 x_5 x_9 + k_4 x_2 + k_{\mathrm{diff2}} x_8$$
$$\dot{x}_8 = k_{12} x_1 - k_{\mathrm{diff2}} x_8$$

If the Cyt*f* side is treated locally as an upstream source over the fitting interval, then x_1 may be regarded as slowly varying or approximately constant to first order, so the PSI-side coupling is dominated by the interaction between complex formation, $P700^+$ consumption, local reduced PC availability, and diffusion delivery.

S7.7 PSI diffusion Jacobian

Linearizing this reduced subsystem around an operating point z^* gives

Eq. S7.14 $$\delta\dot{z} \approx J_{\mathrm{PSI+d}}(z^*)\,\delta z$$

With (S7.15)

$$J_{\mathrm{PSI+diff}}(z) = \begin{bmatrix} -(k_4 + k_{34}) & k_3 x_9 & k_3 x_5 & 0 \\ k_4 & -k_3 x_9 & -k_3 x_5 & 0 \\ k_4 & -k_3 x_9 & -k_3 x_5 & k_{\mathrm{d2}} \\ 0 & 0 & 0 & -k_{\mathrm{d2}} \end{bmatrix}$$

and therefore, at the operating point (aka measuring at a specific time point),

$$J_{\mathrm{PSI+diff}}(z^*) = \begin{bmatrix} -(k_4 + k_{34}) & k_3 x_9^* & k_3 x_5^* & 0 \\ k_4 & -k_3 x_9^* & -k_3 x_5^* & 0 \\ k_4 & -k_3 x_9^* & -k_3 x_5^* & k_{\mathrm{d2}} \\ 0 & 0 & 0 & -k_{\mathrm{d2}} \end{bmatrix}$$

This is the reduced Jacobian in which diffusion becomes mathematically visible as its own relaxation mode. It is this step that allows the donor-side slowdown to be interpreted in diffusion-limited terms.

S7.8 Diffusion eigenvalues and interpretation

The reduced PSI-plus-diffusion block now contains four characteristic modes:

$$\lambda_1 \sim k_{34}$$

as the very fast intracomplex ET mode,

$$\lambda_2 \sim k_3 x_9^*$$

as the pseudo-first-order association mode,

$$\lambda_3$$

as the coupled depletion or donor-side interaction mode, and

$$\lambda_4 \sim k_{\mathrm{d2}}$$

as the diffusion mode.

The exact eigenvalues depend on the operating point, but the important qualitative result is that diffusion is now part of the spectrum. If

$$k_{\mathrm{d2}} < k_3 x_9^*$$

which recent studies point to PC diffusion acting as the rate limiting step for P700 decay at steady state (Höhner *et al.*, 2020),

then the dominant donor-side relaxation can become diffusion-limited, such that

$$k_{\mathrm{obs}} \approx k_{\mathrm{d2}}$$

In that case, P700 relaxation slows even if the total reduced PC pool is high, because the limiting factor is no longer bulk reduction state alone, but effective delivery of reduced PC to the PSI reaction domain.

S7.9 Interpretation for the present study

This sequence of reductions makes the logic explicit. The shared observed rates first arise from the eigenmodes (the rates) of the full 10-variable Jacobian (Kustin *et al.*, 1965). The donor-side PSI interpretation is then obtained by reducing that full system to the relevant PSI interaction block. Once diffusion is retained in that reduced block, it becomes clear that the observed donor-side rate can reflect effective PC delivery rather than the intrinsic ET step alone.

Thus, the common fitted rate shared by P700 relaxation and the PSI-linked component of PC oxidation is best interpreted as the dominant donor-side eigenmode of the coupled system. In the presence of slowed delivery, that dominant mode can become diffusion-limited. The model now aligns with the observed data, that PC diffusion is rate limiting and defines the relaxation of P700 signals in vivo (Höhner *et al.*, 2020).

Chapter 4: Residual PGR5 protects *Setaria viridis pgrl1αβ* mutant under fluctuating light

Introduction

PROTON GRADIENT REGULATION 5 (PGR5) is necessary for sustaining the trans-thylakoid proton motive force (*pmf*) and photoprotective responses during rapid increases in irradiance, making it essential for the acclimation of *Setaria viridis* to fluctuating light (Woodford *et al.*, 2025b). The principal partner of PGR5 is PROTON GRADIENT REGULATION 5-LIKE 1 (PGRL1), a thylakoid membrane protein that interacts with PGR5 and regulates its activity (DalCorso *et al.*, 2008). The loss of PGRL1 in *Arabidopsis thaliana* also results in an absence of PGR5, making the phenotypes of *pgr5 and pgrl1ab* mutants in *A. thaliana* practically identical (DalCorso *et al.*, 2008; Rühle *et al.*, 2021; Penzler *et al.*, 2022). The reason for this is that another protein PGRL2 promotes PGR5 degradation in the absence of PGRL1 (Rühle *et al.*, 2021). Consistent with this, *pgrl1ab pgrl2* double knockout plants in *A. thaliana* retain PGR5 at approximately 60% of WT levels and display a partial rescue of the *pgrl1ab* phenotype; however, these plants are impaired under very low light, where φ_{NO} and φ_{NPQ} are significantly elevated and φ_{I} is significantly reduced (Rühle *et al.*, 2021), demonstrating that unregulated PGR5 activity is itself deleterious. Together, PGRL1 and PGRL2 modulate PGR5 activity to balance the photoprotective benefits against the apparently deleterious consequences of unregulated PGR5 activity. The latter is evidenced by observations that the strong overexpression of PGR5 under a 35S promoter in *A. thaliana* delayed chloroplast and cotyledon greening, and elevated NPQ under constant light conditions, but improved survival under high light and drought stress (Okegawa *et al.*, 2007; Long *et al.*, 2008). Additionally, as PGR5 abundance increased in *A. thaliana*, PSI photoprotection and growth under fluctuating light improved, but beyond an optimal level, F_V/F_M declined and photosynthetic performance deteriorated, further supporting that PGR5 activity must be precisely calibrated to avoid deleterious consequences (Tanigawa *et al.*, 2026).

Given an increase of PGR5 and PGRL1 abundance during C_4 evolution (Nakamura *et al.*, 2013; Munekage, 2016), it might be predicted that in C_4 grasses PGRL2 also became elevated. To answer this question, I performed a preliminary analysis on the mesophyll and bundle sheath expression patterns of *PGR5*, *PGRL1*, and *PGRL2* genes between *S. viridis* as the C_4 example and *Oryza sativa* as the C_3 representative grass species, using published data sets (John *et al.*, 2014; Hua *et al.*, 2021). In the mesophyll fraction, *PGRL1α*, *PGRL1β*, and *PGR5* transcript abundance were all significantly higher in *S. viridis* than in *O. sativa*, at 12-fold, 1.3-fold, and 3.5-fold higher respectively (Fig. 1a). In the bundle sheath fraction, the same

three genes were significantly elevated in *S. viridis* relative to *O. sativa*, at 16-fold, 5.7-fold, and 4.4-fold higher respectively (Fig. 1b). Interestingly, *PGRL2* transcript abundance was relatively low in both cell types and not different between *S. viridis* and *O. sativa* (Fig. 1a, b). Since expression of *PGRL2* did not increase alongside *PGR5* and *PGRL1* in C_4 evolution, the degradation of PGR5 by PGRL2 may be less significant in *S. viridis*. As PGR5 protein abundance is known to increase under high-light stress in *A. thaliana* (Flannery *et al.*, 2021), I hypothesised that under fluctuating light, a condition known to induce PGR5-dependent responses, stress-induced PGR5 expression might be maintained in a *S. viridis pgrl1αβ* mutant, in contrast to the complete loss of PGR5 observed in *A. thaliana pgrl1ab*.

In this chapter, *S. viridis pgrl1α* and *pgrl1β* single mutants were crossed to generate a *pgrl1αβ* double knockout, which was then characterised alongside *pgr5-1*. Indeed, 6% of WT level PGR5 was detected in *pgrl1αβ* when plants were grown under fluctuating light. Although this residual PGR5 was low and insufficient to prevent the significant decrease of PSI abundance observed in *pgr5-1* under fluctuating light, *pgrl1αβ-5* unexpectedly displayed a clear intermediate phenotype relative to *pgr5-1* and WT. These results indicate that PGR5 is required for a coordinated response to fluctuating light stress in *S. viridis* and even low amounts of this protein can have defined phenotypic effects.

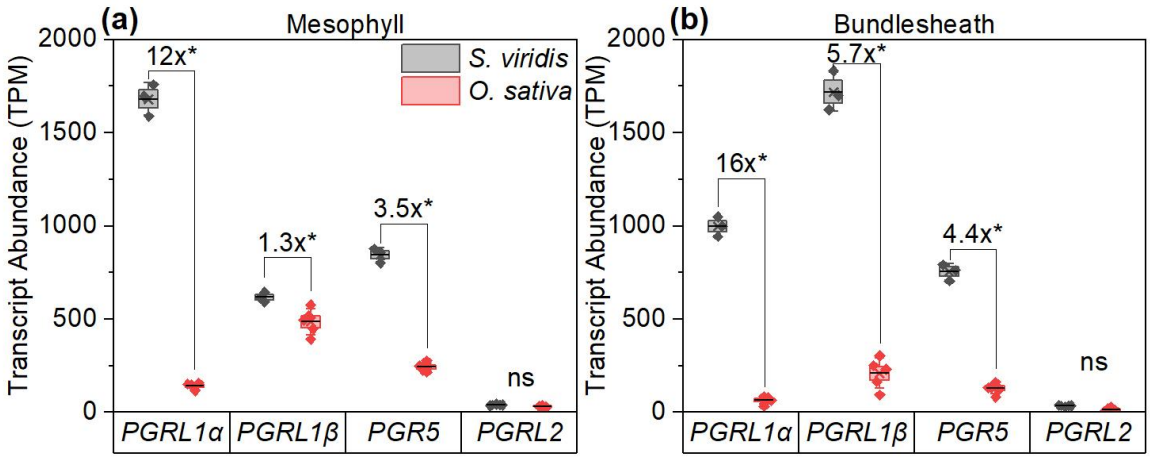

Fig. 1. Transcript abundance of *PGR5* and associated genes in mesophyll- and bundle sheath-enriched cell fractions of *S. viridis* and *O. sativa*. Transcript abundance is expressed in transcripts per million (TPM) for *PGRL1α*, *PGRL1β*, *PGR5*, and *PGRL2* in (**a**) mesophyll-enriched and (**b**) bundle sheath-enriched fractions. *S. viridis* data are from (John *et al.*, 2014); *O. sativa* data are from (Hua *et al.*, 2021). Fold changes shown above brackets represent the ratio of *S. viridis* to *O. sativa* mean TPM for each gene within each cell-type fraction. Significance was determined by Welch's t-test comparing *S. viridis* and *O. sativa* within each gene; *, $P < 0.05$; ns, not significant. Mean ± SE, n = 3 (*S. viridis*), n = 5 (*O. sativa*).

Materials and Methods

Generation and selection of *S. viridis pgrl1αβ* double mutant lines

S. viridis ecotype ME034V-1 *pgrl1* single mutant lines *pgrl1α3-38-1* and *pgrl1β1-61-1*, generated in Chapter 2, were manually crossed to generate the double mutant line referred to as *pgrl1αβ*. Unlike the A10 ecotype, ME034V-1 cannot be chemically emasculated according to Rizal *et al.* (2015) and instead requires manual removal of anthers. Emasculation was therefore performed manually during anthesis with the aid of a stereomicroscope and fine-point forceps to produce the maternal parent. Anthesis was monitored closely, and approximately 15 minutes after floret opening, when anthers had emerged from the floret but prior to pollen release, the anthers were plucked with forceps, and the emasculated floret was marked on the lemma with a permanent marker. An intact floret from the designated paternal parent (pollen donor) was then detached and tapped gently over the emasculated floret to deposit pollen onto the exposed style. Crossed florets were monitored throughout seed development to confirm successful fertilisation. When seed coats had hardened and darkened to indicate near-maturity, seeds were manually removed from the panicle.

To accelerate generation turnover and bypass the dormancy cycle characteristic of *S. viridis*, embryo rescue was performed on seeds from confirmed crosses. Seeds were bisected longitudinally with a scalpel, taking care not to damage the embryo. The embryo and surrounding endosperm tissue were excised from the seed coat and surface-sterilised in 1% (v/v) sodium hypochlorite solution containing 0.05% (v/v) Tween 20, then transferred to non-selective Murashige and Skoog (MS) medium containing 2.15 g L^{-1} Murashige and Skoog salts, 10 mL L^{-1} 100× Murashige and Skoog vitamins stock, 30 g L^{-1} sucrose, and 7 g L^{-1} Phytoblend (pH 5.7). Germinated seedlings were transferred to seed-raising mix (Debco, Tyabb, Australia) supplemented with 5 g L^{-1} slow-release fertiliser (Osmocote, Scotts, Bella Vista, Australia) once they had reached approximately 6 cm in height.

F1 progeny was screened for the presence of both the *pgrl1α3-38-1* and *pgrl1β1-61-1* mutations by Sanger sequencing, using the primers and protocols described in Chapter 2. Plants confirmed to carry both mutations were allowed to self-pollinate. F2 progeny was subsequently screened by Sanger sequencing with the same primers to identify plants with homozygous mutant alleles. To confirm the absence of PGRL1, protein extraction from leaf discs, SDS-PAGE, and immunoblotting were performed as described in Ermakova et al. (2019). Reactivity of PGRL1 antibody (1:5,000; AS19 4311, Agrisera, Vännäs, Sweden) with both PGRL1 paralogs was validated using WT and single mutants. PGR5 abundance was not assessed by immunoblot; the PGR5 antibody (AS16 3985, Agrisera, Vännäs, Sweden)

produced off-target bands in *S. viridis* leaf extracts and lacked sufficient sensitivity to detect PGR5 below 25% of WT abundance in our standard immunoblotting conditions. PGR5 quantification was therefore performed by targeted LC-MS/MS proteomics as described below.

Plant material and growth conditions

S. viridis ecotype ME034V-1 WT, *pgrl1αβ-5* and *pgr5-1,* reported by Woodford *et al.* (2025b), were used in this study. *S*eeds were germinated directly on soil in communal pots containing seed-raising mix (Debco, Tyabb, Australia) supplemented with 5 g L^{-1} of slow-release fertiliser (Osmocote, Scotts, Bella Vista, Australia). One week after germination, individual seedlings were transferred to 0.5 L pots containing the same soil and fertiliser mixture, with one plant per pot. For chlorophyll fluorescence, P700 spectroscopy and ECS measurements, plants were grown in a controlled environment chamber at 28°C day / 22°C night under a 16 h photoperiod, irradiance of 380 µmol photons m^{-2} s^{-1} and 60% humidity. Measurements were performed on the youngest fully expanded leaves of plants at 3–4 weeks of age. Tissue samples for proteomics were taken from plants 3 weeks post germination: leaf discs of 0.5 cm² from the mid-section of the first fully expanded leaf were snap-frozen in liquid.

For fluctuating light growth experiments, plants were germinated and grown for one week under the constant light conditions described above before being transferred to a growth chamber with a repeating cycle of 5 min at 250 µmol m^{-2} s^{-1} followed by 1 min at 1,000 µmol m^{-2} s^{-1}, for the duration of a 16 h photoperiod. This regime was designed to deliver the same total daily photon dose as the constant light condition. Leaf discs for proteomics were harvested from plants grown for two weeks under FL.

Chlorophyll fluorescence and P700 spectroscopy analysis

Chlorophyll fluorescence and P700 redox spectroscopy were measured concurrently using Dual KLAS-NIR (Heinz Walz GmbH, Effeltrich, Germany) and the deconvolution of near-infrared absorbance signals into PSI, Fd and PC was performed as described in Chapter 3. For light response curves, leaves were dark-adapted for 30 min. A saturating pulse was first applied to determine the maximum (F_M) and minimum (F_0) fluorescence levels, after which the maximal $P700^+$ signal (P_M) was recorded by applying a saturating pulse at the end of an 8-s far-red illumination (720 nm), with the minimal $P700^+$ signal (P_0) recorded directly following the saturating pulse. Leaves were then subjected to a 15 min induction period at 300 µmol photons m^{-2} s^{-1} before irradiance was increased stepwise through 72, 158, 352, 453, 716, 1,090, 1,327, and 1,724 µmol photons m^{-2} s^{-1}, with a saturating pulse applied at the end of each 120 s illumination step. At each step, the steady-state fluorescence level (F) and the maximum

fluorescence under actinic light (F_M') were recorded, along with the steady-state $P700^+$ signal (P) and the maximal $P700^+$ signal during the saturating pulse (P_M'). For PSII, the effective quantum yield was calculated as $\varphi_{II} = (F_M' - F)/F_M'$. The yields of regulated and non-regulated energy dissipation were calculated as $\varphi_{NPQ} = F/F_M' - F/F_M$ and $\varphi_{NO} = F/F_M$, respectively (Klughammer & Schreiber, 2008c). For PSI, the photochemical yield (φ_I) and the yields of non-photochemical reactions due to donor (φ_{ND})- or acceptor (φ_{NA})-side limitation were calculated as $\varphi_I = (P_M' - P)/(P_M - P_0)$, $\varphi_{ND} = (P - P_0)/(P_M - P_0)$, and $\varphi_{NA} = (P_M - P_M')/(P_M - P_0)$ (Klughammer & Schreiber, 2008a).

Thylakoid membrane energisation analysis

ECS measurements were performed using a Dual-PAM-100 (Heinz Walz, Effeltrich, Germany) equipped with the P515/535 emitter-detector module. ECS signal was recorded as absorbance changes between 550 and 520 nm and normalised to the amplitude of the ECS response to a 20 µs saturating pulse at 14,000 µmol m^{-2} s^{-1} applied to dark-adapted leaves (ECS_{ST}). Leaves were dark-adapted for 30 min prior to measurement, after which ECS_{ST} was recorded. Actinic irradiance was then stepped to 1,500 µmol photons m^{-2} s^{-1} for 50 s, with t = 0 defined as the irradiance transition. Dark intervals were applied every 1 s for the first 10 s following the irradiance step, then every 5 s thereafter. The amplitude of the fitted ECS decay was used as a relative estimate of proton motive force (*pmf*), and proton conductivity of the thylakoid membrane (g_{H^+}) was calculated as the inverse time constant of the decay (1/τ) (Cruz *et al.*, 2001). The initial rate of ECS relaxation at dark onset was calculated from the derivative of the fitted exponential at t = 0 and is reported here as v_{H^+} (Avenson *et al.*, 2005b).

MultispeQ analysis under constant and fluctuating light

Chlorophyll fluorescence parameters and relative chlorophyll content were measured non-destructively using a MultispeQ v2.0 handheld instrument (PhotosynQ, East Lansing, MI, USA) running the RIDES 2.0 protocol. Measurements were performed on the same day in both the constant light and fluctuating light growth cabinets. In the fluctuating light cabinet, measurements were taken during the low-light phase (250 µmol photons m^{-2} s^{-1}) of the fluctuating light cycle. All fluorescence parameters were therefore measured on leaves acclimated to their respective growth light conditions (Kuhlgert *et al.*, 2016). Relative chlorophyll content (SPAD) was estimated from absorbance measurements at 650 nm and 940 nm (Maas & Dunlap, 1989; Raymond Hunt Jr. & Daughtry, 2014).

Phenospex PlantEye measurements

Automated, non-destructive plant phenotyping was performed using the TraitFinder system (Phenospex B.V., Heerlen, Netherlands) equipped with a PlantEye F600 multispectral 3D scanner. The PlantEye F600 sensor captured 3D point clouds and multispectral reflectance data across five wavebands (blue, green, red, near-infrared, and 3D laser). Initial scans were performed 14 days after sowing, with subsequent scans conducted every four days thereafter. Data processing and trait extraction were performed using HortControl software (Phenospex, version 3.8). Morphological traits, including digital biomass, plant height, and 3D leaf area, were computed from the 3D processing pipeline. Physiological indices, including the Normalised Difference Vegetation Index (NDVI; Rouse *et al.*, 1973), the Normalised Pigment Chlorophyll Index (NPCI; Peñuelas *et al.*, 1994), and the Plant Senescence Reflectance Index (PSRI; Merzlyak *et al.*, 1999), were calculated by mapping multispectral reflectance data onto the 3D plant models. A height-based segmentation threshold was applied to exclude signal from the potting medium and surrounding surfaces.

Transcript abundance meta-analysis

To compare the relative expression of CEF-associated genes between C_4 *S. viridis* and C_3 *O. sativa*, transcript abundance data were obtained from previously published cell-type-enriched RNA-seq datasets. *S. viridis* mesophyll- and bundle sheath-enriched transcript data were sourced from (John *et al.*, 2014), and equivalent *O. sativa* data were sourced from (Hua *et al.*, 2021). Supplementary tables containing TPM values were downloaded directly from each publication, and no raw read reprocessing was performed. The following locus identifiers were used to extract transcript abundance for each gene of interest: *SvPGRL1α* (SEVIR.2G115600), *SvPGRL1β* (SEVIR.9G004600), *SvPGR5* (SEVIR.6G259600), and *SvPGRL2* (SEVIR.3G066800) in *S. viridis*; and *OsPGRL1α* (LOC_Os08g41460), *OsPGRL1β* (LOC_Os03g64020), *OsPGR5* (LOC_Os08g45190), and *OsPGRL2* (LOC_Os05g02010) in *O. sativa*. Pairwise comparisons between species within each cell-type fraction were performed using Welch's *t*-test, with n = 3 biological replicates for *S. viridis* and n = 5 for *O. sativa*, reflecting the original experimental designs of each study.

Protein extraction, quantification and digestion

Leaf disc were homogenised in an ice-cold glass homogeniser in 0.5 mL of extraction buffer containing 100 mM Tris-HCl (pH 7.8), 25 mM NaCl, 20 mM ethylenediaminetetraacetic acid (EDTA), 2% (w/v) sodium dodecyl sulphate (SDS), 10 mM dithiothreitol (DTT), and 2% (v/v) protease inhibitor cocktail (Sigma-Aldrich, St Louis, MO, USA). Extracts were incubated at 65°C for 10 min and then centrifuged at 16,000 × *g* for 5 min to obtain a clarified supernatant.

Protein concentration was determined using the DC Protein Assay Kit (Bio-Rad Laboratories, Hercules, CA, USA) following the manufacturer's instructions.

Proteins were digested using S-Trap Micro spin columns (ProtiFi, Huntington, NY, USA) following the manufacturer's protocol (document no. 20250417-08PRD-5021-BK-REV-A). Briefly, 10 µg of protein from prior extractions was brought up to a volume of 23 µL using the extraction buffer and sonicated to ensure complete solubilisation. Samples were reduced by addition of 1 µL tris(2-carboxyethyl)phosphine (TCEP) 120 mM and incubated at 55°C for 15 min. Cysteines were alkylated by addition of 1 µL chloroacetamide 500 mM and incubated at room temperature for 10 min in the dark. Samples were acidified to pH ≤ 1 by addition of 27.5% (v/v) phosphoric acid, combined with Binding/Wash Solution (100 mM Triethylammonium bicarbonate (TEAB) in 90% (v/v) methanol, pH 7.5), and loaded onto S-Trap Micro columns. Columns were washed three times with Binding/Wash Solution at 10,000 × *g* for 30 s per wash to remove SDS and other contaminants. Trypsin (Pierce MS-Grade Trypsin Protease, cat. no. 90057, Thermo Fisher Scientific, Waltham, MA, USA) was diluted in Digestion Solution (50 mM TEAB, pH 8.0) and applied to each column at a 1:50 (w/w) enzyme-to-protein ratio in a final volume of 20 µL. Columns were incubated overnight at 37°C in an heat block. Peptides were sequentially eluted with 40 µL Digestion Solution, 40 µL of 0.2% (v/v) formic acid, and 40 µL of 50% (v/v) acetonitrile in 0.2% (v/v) formic acid, each at 10,000 × *g* for 1 min. Combined eluates were dried by vacuum centrifugation.

LC-MS/MS data acquisition

Dried peptides were resuspended in 25 µL of 2% (v/v) acetonitrile, 0.1% (v/v) formic acid, yielding a concentration of approximately 0.4 µg μL^{-1}. A 5 µL injection (approximately 2 µg of total peptide) was loaded onto a Dionex Ultimate 3000 µ-flow UHPLC (Ultra-high-performance liquid chromatography) system coupled to a Thermo Orbitrap Fusion Tribrid mass spectrometer equipped with a nanospray electrospray ionisation (ESI) source, operated through the ANU Joint Mass Spectrometry Facility (Australian National University, Canberra, Australia). Data were acquired in data-dependent acquisition (DDA) mode.

To ensure detection of PGR5, which produces only a single reliably detectable peptide and is present at low abundance in *pgrl1αβ*, a targeted inclusion list was generated using Skyline v24.1 (MacCoss Lab, Department of Genome Sciences, University of Washington, Seattle, WA, USA; MacLean et al., 2010). The inclusion list was generated using the *S. viridis* reference proteome with the following parameters: Thermo Orbitrap instrument defaults, peptide length 4–35 amino acids, carbamidomethyl modification of cysteine, trypsin digestion, and a minimum precursor *m/z* of 350. The PGR5 target peptide GLFAPLVVVAR was added to the DDA inclusion list to prioritise its fragmentation during data acquisition. The inclusion

list was validated on WT and *pgr5-1* samples, in which GLFAPLVVVAR was consistently detected in WT and absent from *pgr5-1*. Manual inspection of the extracted ion chromatograms in Skyline confirmed a well-defined peptide peak in WT and its absence in *pgr5-1*.

Proteomics data analysis

Raw LC-MS/MS files were processed using MaxQuant v2.8.0.0 (Cox & Mann, 2008). Database searches were performed against a combined FASTA file comprising the *S. viridis* UniProt reference proteome (UP000298652) and a manually curated *S. viridis* chloroplast protein sequence file derived from the published chloroplast genome (GenBank KT289405), supplemented with the default MaxQuant contaminant database. Searches used trypsin/P as the digestion enzyme in specific mode with up to two missed cleavages permitted. Carbamidomethylation of cysteine was set as a fixed modification; oxidation of methionine and acetylation of protein N-termini were set as variable modifications. The minimum peptide length was seven amino acids. Precursor mass tolerances were 20 ppm for the first search and 4.5 ppm for the main search; MS/MS fragment ion tolerance was 20 ppm (FTMS). Match-between-runs was disabled to prevent false transfer of the low-abundance PGR5 peptide identification across samples. Label-free quantification (LFQ) and iBAQ calculation were both enabled. Each sample was assigned an individual experiment label; no grouping was applied within MaxQuant. The minimum ratio count for LFQ was reduced from the default of 2 to 1 to permit quantification of proteins represented by a single high-confidence peptide, specifically to enable inclusion of PGR5 in the quantified output. Peptide and protein false discovery rates were both maintained at 1%.

Raw data quality was assessed using the PTXQC R package v1.1.5 (Bielow *et al.*, 2016). All 22 raw files demonstrated consistent peptide intensity distributions (RSD = 1.9%, criterion < 5%), post-calibration mass accuracy within ±0.7 ppm standard deviation across all files, and contaminant intensity below 5% in all samples. One *pgrl1αβ-5* replicate (*pgrl1αβ-5-7*) was excluded prior to the MaxQuant search on quality grounds, resulting in n = 3 biological replicates for *pgrl1αβ-5* under fluctuating light. One WT replicate (WT 2) was identified as an outlier in the PTXQC principal component analysis of raw protein group intensities, where it separated markedly from the remaining WT constant light replicates along PC2, and was excluded from all constant light statistical analyses, resulting in n = 3 for WT under constant light.

Standard iBAQ values were recalculated using a custom observed iBAQ method to address the systematic underestimation of abundance for integral membrane proteins, whose hydrophobic tryptic peptides are frequently undetected under standard LC-MS/MS conditions.

For each protein in each sample, the sum of peptide intensities was divided by the number of peptides with intensity greater than zero in that sample, rather than by the theoretical count of tryptic peptides. Prior to counting, peptides were filtered to retain only those with zero missed cleavages, no methionine oxidation, and no decoy or contaminant assignments, with a minimum length of seven amino acids enforced by the MaxQuant search settings. Both the intensity sum and the observed peptide count were calculated independently per sample. Within each sample, observed iBAQ values were normalised to the sum of all observed iBAQ values in that sample and multiplied by 10^6 to yield relative iBAQ values expressed as parts per million (riBAQ ppm). To account for differences in total protein content per unit leaf area between samples, riBAQ ppm values were further scaled by the total protein concentration per unit leaf area determined from the DC assay, yielding leaf-area normalised riBAQ values (arbitrary units). Because the DC assay measures total protein including undetected proteins, these values represent a semi-quantitative estimate of protein abundance per unit leaf area rather than an absolute concentration and are reported as arbitrary units throughout. All recalculation and normalisation steps were implemented in custom Python scripts developed with the assistance of Claude (Anthropic, 2025a; Anthropic, 2025b).

Differential abundance between genotypes was assessed on $\log_2$-transformed leaf-area normalised riBAQ values using a limma empirical-Bayes moderated *t*-test (Smyth, 2004), implemented following Kammers *et al.* (2015) with prior variance estimated as a function of mean $\log_2$ abundance (trend = TRUE). A single three-group model was fitted across *pgrl1αβ*, WT, and *pgr5-1* simultaneously, and the three pairwise contrasts were extracted from the shared moderated variance estimate. Multiple testing correction was applied using the Storey q-value method (Storey, 2003); proteins were considered significantly differentially abundant at $q < 0.05$. No fold-change threshold was applied to significance calling; fold-change reference lines are shown in volcano plots for visual orientation only. All statistical analyses and visualisations were performed using custom Python scripts developed with the assistance of Claude Co-work (Anthropic, 2025a).

Functional annotation and pathway enrichment analysis

Functional annotation of all detected proteins was performed using the Mercator4 v8 web tool (Schwacke *et al.*, 2019), which assigns proteins to hierarchical MapMan functional bins based on sequence homology.

Pathway membership for each detected protein was additionally retrieved from the *S. viridis* metabolic network database SviridisCyc (Hawkins *et al.*, 2025) via the BioCyc REST API, querying the pathways-of-gene endpoint for each detected gene using Sevir v2.1 locus identifiers. Each protein was assigned to all pathways in which its gene product catalyses at

least one reaction; where a protein participates in multiple pathways, all pathway memberships were retained independently, following the approach recommended by Reimand *et al.* (2019).

Prior to enrichment testing, differentially abundant proteins were partitioned into six direction-status groups based on the direction of change (increased or decreased relative to the comparator) and genotype comparison (*pgrl1αβ-5* vs WT, *pgr5-1* vs WT, or shared between both). Over-representation of MapMan bins within each direction-status group was assessed using a one-tailed Fisher's exact test with the elim algorithm to account for the hierarchical structure of MapMan bin annotations (Alexa *et al.*, 2006); proteins assigned to significantly enriched child bins (raw $p < 0.01$) were removed from ancestor bin tests prior to scoring. Over-representation of SviridisCyc pathways was assessed using a one-tailed Fisher's exact test without hierarchy correction, as SviridisCyc pathway frames do not follow a strict hierarchy. The background for each test comprised all proteins detected in the fluctuating-light dataset that carried an annotation in the respective system (MapMan, 1,996 of 2,031 detected proteins; SviridisCyc, 493), rather than the whole *S. viridis* proteome. For both annotation systems, multiple testing correction was applied using the Benjamini-Hochberg procedure within each direction-status group. Where multiple SviridisCyc pathway frames mapped to the same pathway name, the frame with the lowest adjusted p-value was retained for display. Enrichment results are reported at $q < 0.05$. All enrichment analyses and visualisations were performed using custom Python scripts developed with the assistance of Claude Co-work (Anthropic, 2025a).

Statistical analysis

For growth, chlorophyll fluorescence, and Phenospex phenotyping data, pairwise comparisons between genotypes within each light condition were performed using one-way ANOVA with Tukey's honest significant difference post hoc test, with significance assessed at $p < 0.05$. For ECS and light response curve data, genotype differences at individual irradiance or time points were assessed using two-way repeated-measures ANOVA with Tukey's post hoc test, with significance assessed at $p < 0.05$. All analyses were performed in OriginPro (OriginLab, Northampton, MA, USA).

Results

Generation of the *pgrl1αβ* double mutant

The homozygous double mutant plants were confirmed by Sanger sequencing at both *SvPGRL1α* and *SvPGRL1β* loci, with insertions identical to those in the respective parental lines (Fig. 2a, b; see also Chapter 2). No PGRL1 was detected by immunoblotting in the double

mutant plants (Fig. 2c). Ponceau S staining of the Rubisco large subunit was used as a loading control.

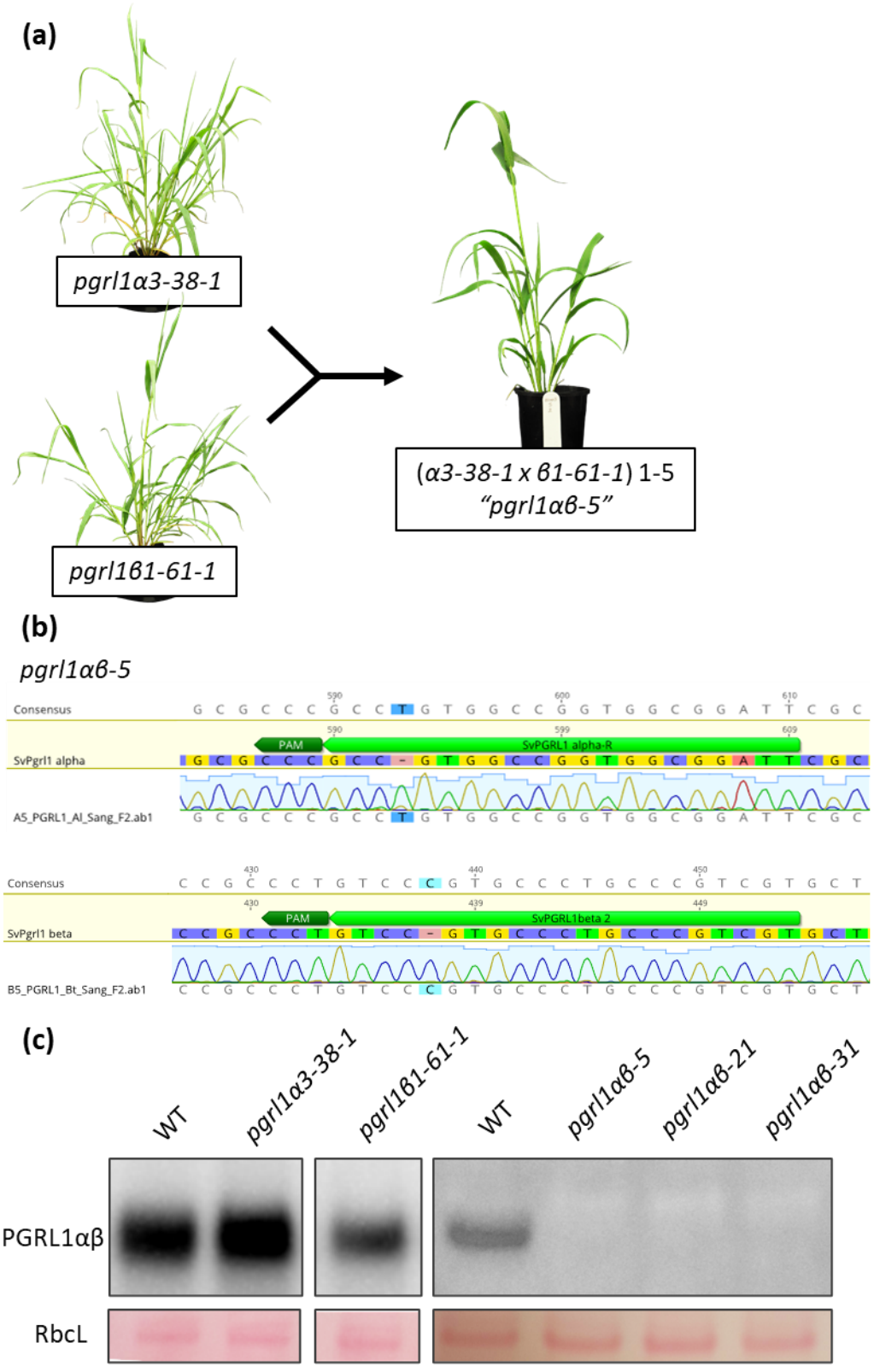

Fig. 2. Generation and confirmation of the *S. viridis pgrl1αβ* double mutant plants. (**a**) Crossing scheme used to generate the *pgrl1αβ* double mutant. (**b**) Sanger sequencing traces confirming homozygous CRISPR-induced insertions at both *PGRL1α* and *PGRL1β* loci in *pgrl1αβ-5*. (**c**) Immunoblot using a PGRL1 antibody recognising both paralogs. No detectable PGRL1 signal was observed in homozygous double mutant plants. Samples were loaded on a leaf-area basis; Ponceau S staining of RbcL is shown as a loading control. Panels are from separate blots/exposures; the immunoblot is qualitative (presence/absence).

Photosynthesis in plants grown under constant light

To determine whether loss of both PGRL1 paralogs results in a similar photosynthetic phenotype as the loss of PGR5, PSI, PSII photochemistry and thylakoid membrane energisation were assessed on plants grown under constant light. The *pgrl1αβ-5* and *pgr5-1* mutants showed similar PSII and PSI quantum yields at all irradiances (Fig. 3). φ_{II}, the PSII photochemical yield, was significantly lower in *pgrl1αβ-5* and *pgr5-1* than in WT at lower irradiances (Fig. 3a). φ_{NO}, the yield of non-regulated energy dissipation, was significantly higher in both mutants than in WT at all irradiances (Fig. 3b). φ_{NPQ}, the yield of non-photochemical quenching, was significantly lower in both mutants than in WT from moderate irradiances onward (Fig. 3c). The PSI photochemical yield, φ_I, was significantly lower in both mutants than in WT across all irradiances (Fig. 3d). φ_{ND}, the fraction of P700 which is oxidised, was significantly lower in both mutants than in WT from low irradiances onward (Fig. 3e). The PSI acceptor-side limitation, φ_{NA} reflecting the fraction of PSI which is reduced due to lack of acceptor, was significantly higher in both mutants than in WT at all irradiances (Fig. 3f).

Thylakoid membrane energisation was assessed by ECS during a step increase in irradiance from darkness to 1,500 µmol photons m^{-2} s^{-1} (Fig. 4). *pmf* was lower in both *pgrl1αβ-5* and *pgr5-1* than in WT during the induction, with no significant difference between the mutants at any time point (Fig. 4a). Proton conductivity of the thylakoid membrane (g_{H^+}) showed some differences between genotype at individual time points throughout the induction, but the overall genotype × time interaction was not significant between genotypes (Fig. 4b). v_{H^+} was not significantly different between genotype (Fig. 4c). However, it is worth mentioning, that the derivative of the ECS exponential decay is conventionally used to estimate the rate of proton flux under steady-state conditions (Avenson *et al.*, 2005b). Since this experiment was conducted during photosynthetic induction and not at steady-state, v_{H^+} here is the rate of proton efflux through the thylakoid membrane.

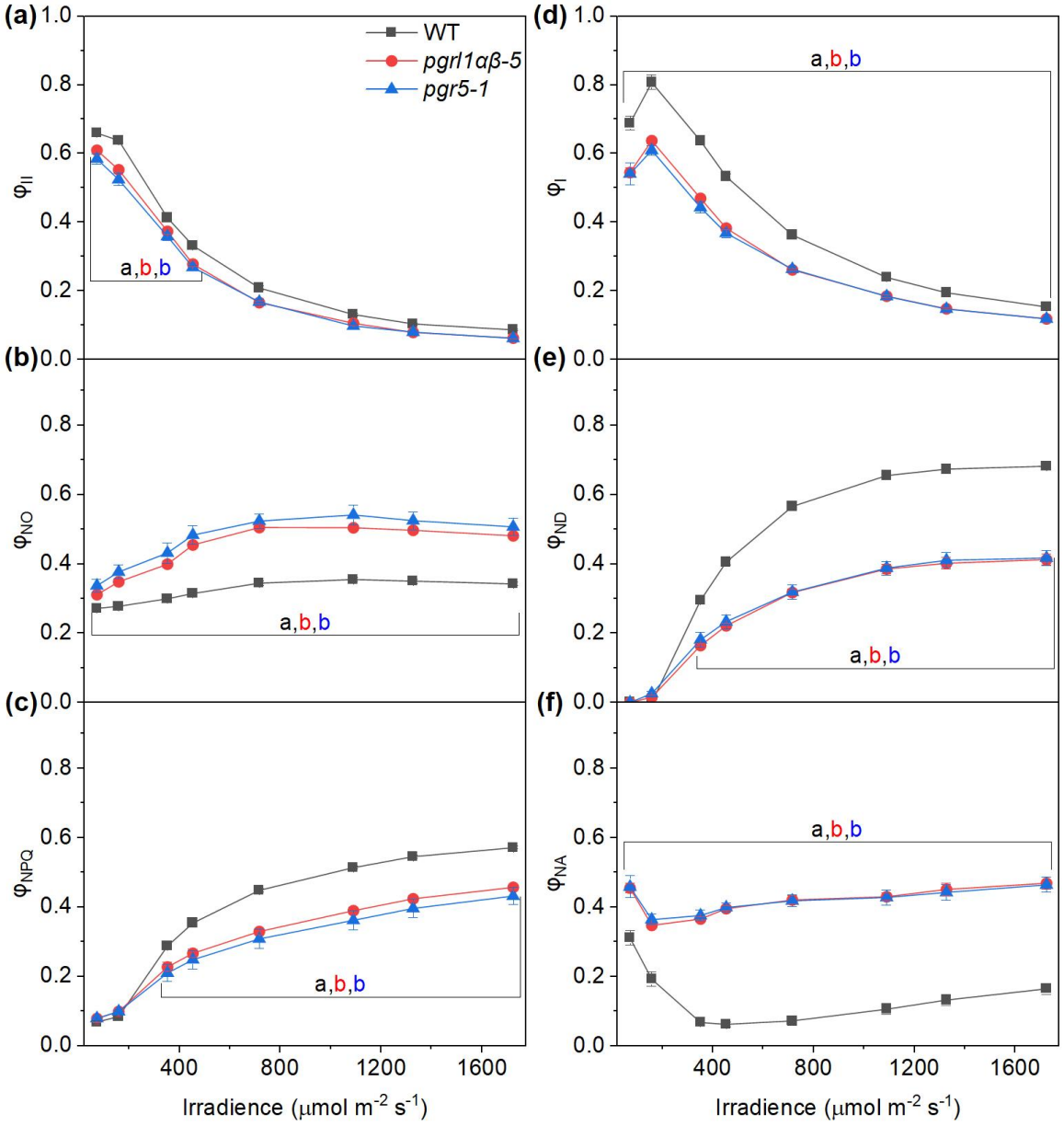

Fig. 3. Light response curves of PSII and PSI quantum yields in *S. viridis* WT, *pgrl1αβ-5*, and *pgr5-1* grown under constant light. (**a**) Photochemical yield of PSII (φ_{II}). (**b**) Quantum yield of non-regulated energy dissipation (φ_{NO}). (**c**) Quantum yield of non-photochemical quenching (φ_{NPQ}). (**d**) Photochemical yield of PSI (φ_{I}). (**e**) Donor-side limitation of PSI (φ_{ND}). (**f**) Acceptor-side limitation of PSI (φ_{NA}). Mean ± SE, n = 4 biological replicates. Letters denote significant differences between genotypes at selected irradiance points (two-way repeated-measures ANOVA with Tukey's post hoc test, $P = 0.05$); letter colour corresponds to genotype as indicated in the legend.

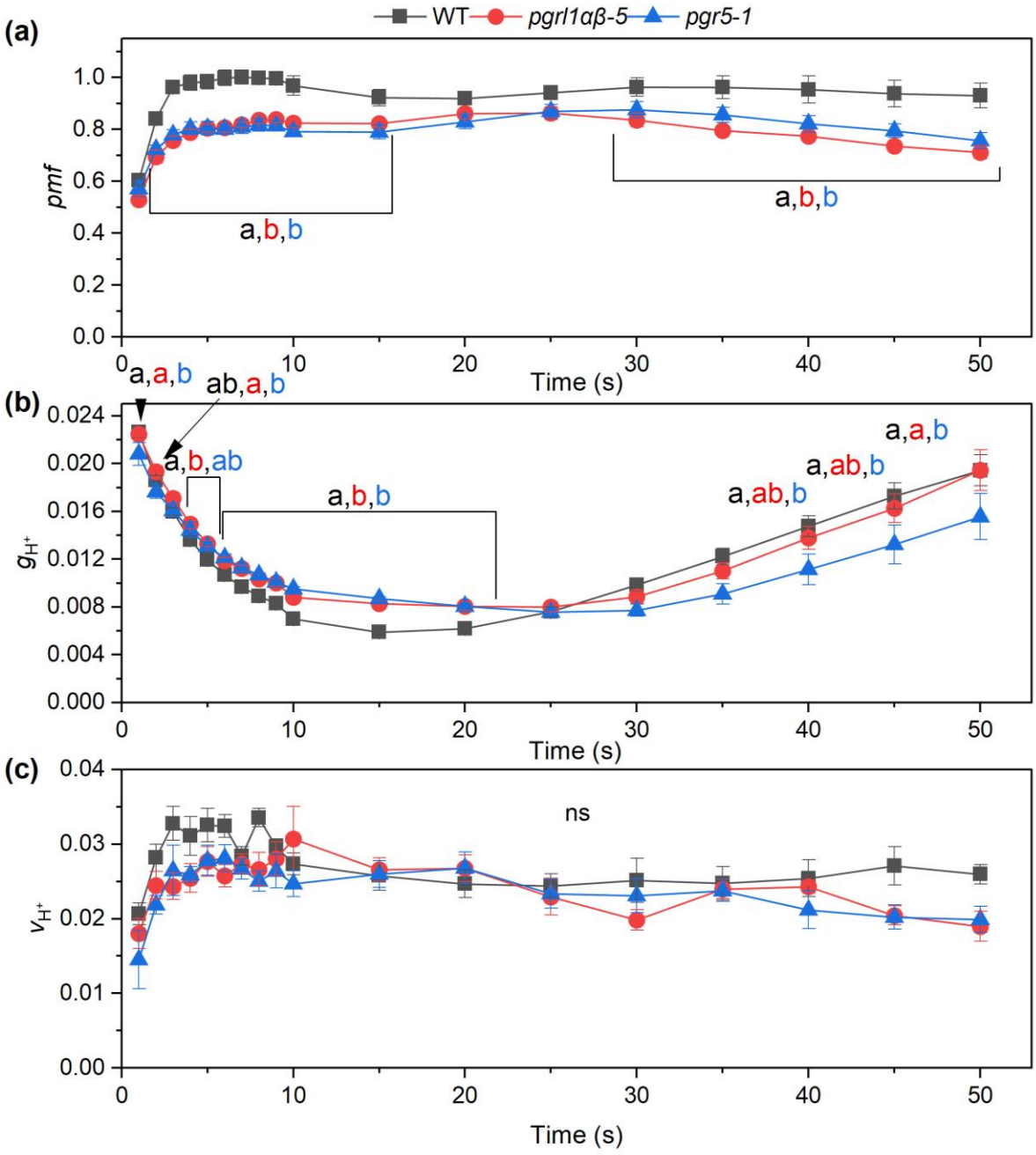

Fig. 4. Thylakoid membrane energisation in *S. viridis* WT, *pgrl1αβ-5*, and *pgr5-1* grown under constant light during the induction. Plants were dark-adapted for 30 minutes prior to measurement. At t = 0, actinic light (1,500 µmol m^{-2} s^{-1}) was applied. (**a**) *pmf*, proton motive force. (**b**) g_{H^+}, proton conductivity of the thylakoid membrane. (**c**) v_{H^+}, instantaneous proton efflux through the thylakoid membrane. Mean ± SE, n = 6 biological replicates. Letters denote significant differences between genotypes at selected time points (two-way repeated-measures ANOVA with Tukey's post hoc test, *P* = 0.05); letter colour corresponds to genotype as indicated in the legend; ns, not significant.

Growth phenotype under constant and fluctuating light

To determine whether loss of both PGRL1 paralogs affected plant growth and photosynthetic performance similarly to loss of PGR5, the growth and photosynthesis of WT, *pgrl1αβ-5*, and *pgr5-1* were compared under constant and fluctuating light. Under constant light, no visible differences were observed between genotypes (Fig. 5a). Under fluctuating light, *pgr5-1* showed the most severe reduction in growth and the greatest degree of chlorosis, and *pgrl1αβ-5* displayed an intermediate appearance relative to WT and *pgr5-1* (Fig. 5b).

Under constant light, no significant differences between genotypes were detected for φ_{II}, φ_{NPQ}, shoot biomass, tiller count, or SPAD (Fig. 5c, d, f, g, h). φ_{NO} was slightly higher in *pgr5-1* relative to WT but not different from *pgrl1αβ-5* (Fig. 5e). No significant differences in digital shoot biomass, Normalised Pigment Chlorophyll Index (NPCI; an index of total carotenoid to total chlorophyll ratio), Normalised Difference Vegetation Index (NDVI; an index of canopy chlorophyll concentration and photosynthetic biomass density), or Plant Senescence Reflectance Index (PSRI; an index of the onset of leaf senescence derived from the ratio of carotenoids to chlorophyll) were detected between genotypes under constant light by Phenospex scanning (Fig. 6a–d).

Under fluctuating light, all three genotypes were significantly different from one another for φ_{II}, φ_{NPQ}, and φ_{NO} (Fig. 5c–e). φ_{II} was highest in WT, lowest in *pgr5-1*, and intermediate in *pgrl1αβ-5* (Fig. 5c). φ_{NPQ} was lowest in WT, highest in *pgr5-1*, and intermediate in *pgrl1αβ-5* (Fig. 5d). φ_{NO} showed a distinct pattern: *pgrl1αβ-5* had the highest φ_{NO}, WT was intermediate, and *pgr5-1* had the lowest (Fig. 5e). SPAD was significantly lower in *pgr5-1* relative to both WT and *pgrl1αβ-5*, which were not significantly different from each other (Fig. 5f). Tiller count was significantly lower in both *pgrl1αβ-5* and *pgr5-1* relative to WT, with no significant difference between the two mutant genotypes (Fig. 5g). Shoot biomass was significantly different across all three genotypes, with WT highest, *pgr5-1* lowest, and *pgrl1αβ-5* intermediate (Fig. 5h). Digital shoot biomass and NDVI were significantly lower in both *pgrl1αβ-5* and *pgr5-1* than in WT, while NPCI and PSRI were significantly higher in both mutants than in WT Fig. 6a–d). In each case, the mean values of *pgrl1αβ-5* were intermediate between WT and *pgr5-1*.

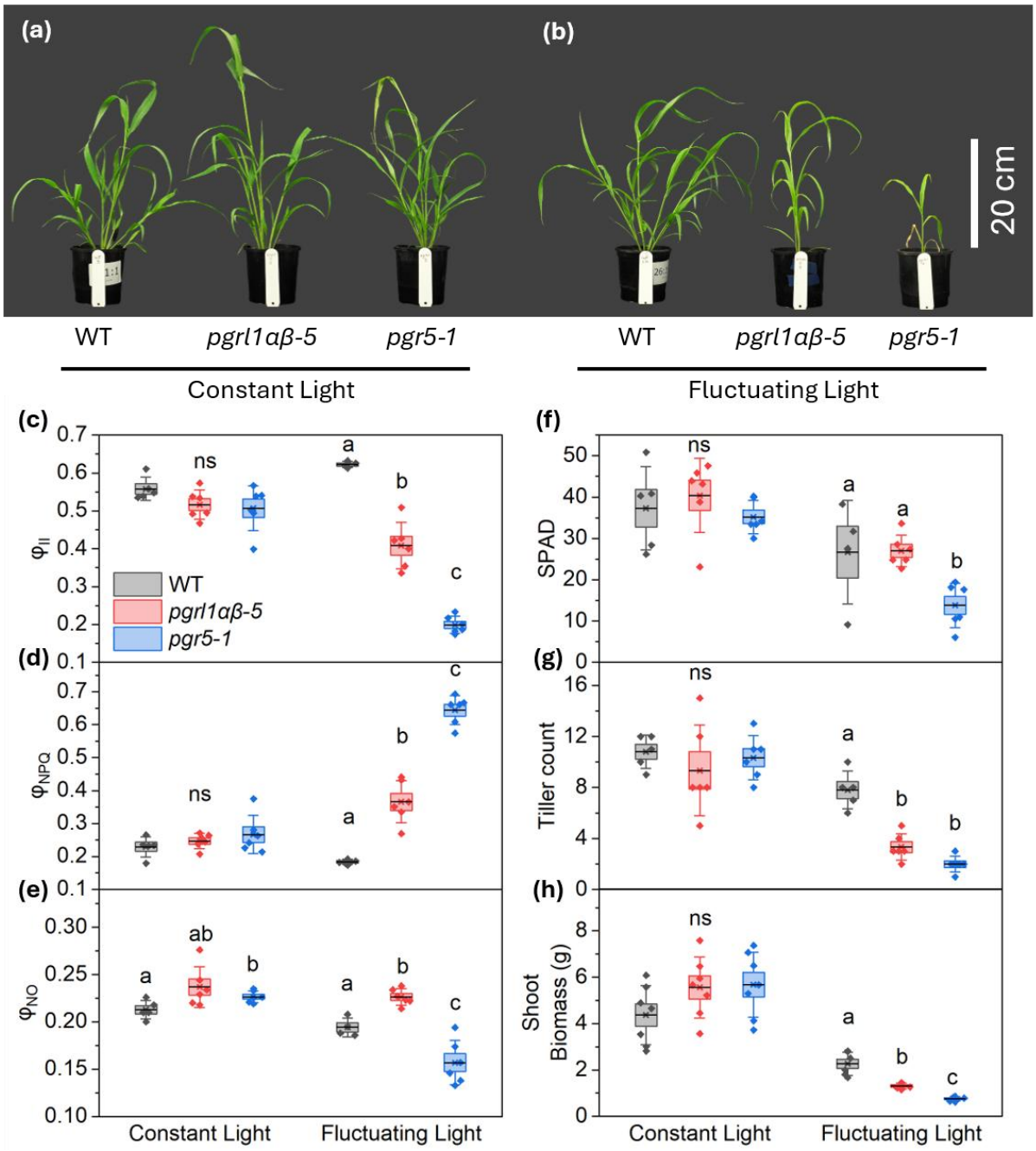

Fig. 5. Growth phenotype of *S. viridis* WT, *pgrl1aβ*, and *pgr5-1* grown under constant or fluctuating light. (**a, b**) Representative photographs of WT (left), *pgrl1aβ-5* (centre), and *pgr5-1* (right) grown under constant light or fluctuating light. Scale bar = 20 cm. (**c–e**) Photochemical yield of PSII (φ_{II}), quantum yield of non-regulated energy dissipation (φ_{NO}), and quantum yield of non-photochemical quenching (φ_{NPQ}) measured by MultispeQ under ambient light. (**f**) Relative chlorophyll content (SPAD). (**g**) Tiller count per plant. (**h**) Shoot biomass; DW, dry weight. Mean ± SE. For (**c–h**): WT n = 5, *pgrl1aβ-5* n = 6, *pgr5-1* n = 6, except WT under fluctuating light for (**c–f**) where n = 4. For (**h**): constant light n = 7 per genotype; fluctuating light WT n = 7, *pgrl1aβ-5* n = 6, *pgr5-1* n = 6. Statistics performed independently within each light condition. Letters denote significant genotype differences (one-way ANOVA with Tukey's post hoc test, P = 0.05); ns, not significant.

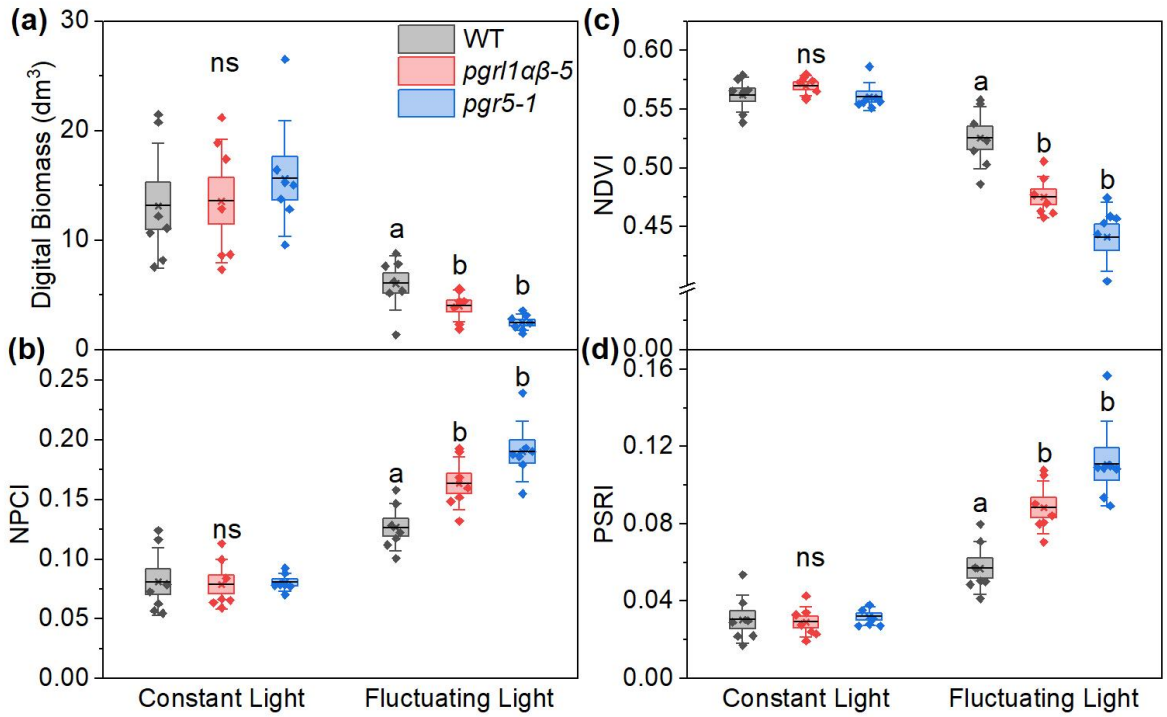

Fig. 6. Multispectral 3D phenotyping of *S. viridis* WT, *pgrl1αβ-5*, and *pgr5-1* grown under constant or fluctuating light. (**a**) Digital shoot biomass. (**b**) Normalised Pigment Chlorophyll Index (NPCI). (**c**) Normalised Difference Vegetation Index (NDVI). (**d**) Plant Senescence Reflectance Index (PSRI). Mean ± SE, n = 7 biological replicates. Statistics were performed independently within each light condition. Letters above boxplots denote significant differences between genotypes (one-way ANOVA with Tukey's post hoc test, *P* = 0.05); ns, not significant.

Targeted proteomics of PGR5 and PGRL1 paralogs

To quantify PGR5, targeted DDA proteomics was performed targeting the tryptic peptide GLFAPLVVVAR. Under constant light, PGR5 was undetectable in *pgrl1αβ-5* and *pgr5-1* across all replicates (Fig. 7). Under fluctuating light, PGR5 abundance in WT increased approximately three-fold relative to constant light (Fig. 7). In *pgrl1αβ-5*, PGR5 was detected in two of three replicates under fluctuating light, at approximately 5.8% of WT abundance under the same condition (Fig. 7).

PGRL1α abundance in WT was significantly lower under fluctuating light than under constant light ($q < 0.01$; Fig. 7), whereas PGRL1β abundance did not differ significantly between light conditions in WT (Fig. 7). Under fluctuating light, both PGRL1α and PGRL1β were significantly lower in *pgr5-1* than in WT ($q < 0.01$ and $q < 0.05$, respectively; Fig. 7). PGRL1α and PGRL1β were undetectable in *pgrl1αβ-5*. PGRL2 was also absent from the LC-MS/MS dataset across all genotypes and conditions, likely because its abundance falls below the detection threshold of the pipeline.

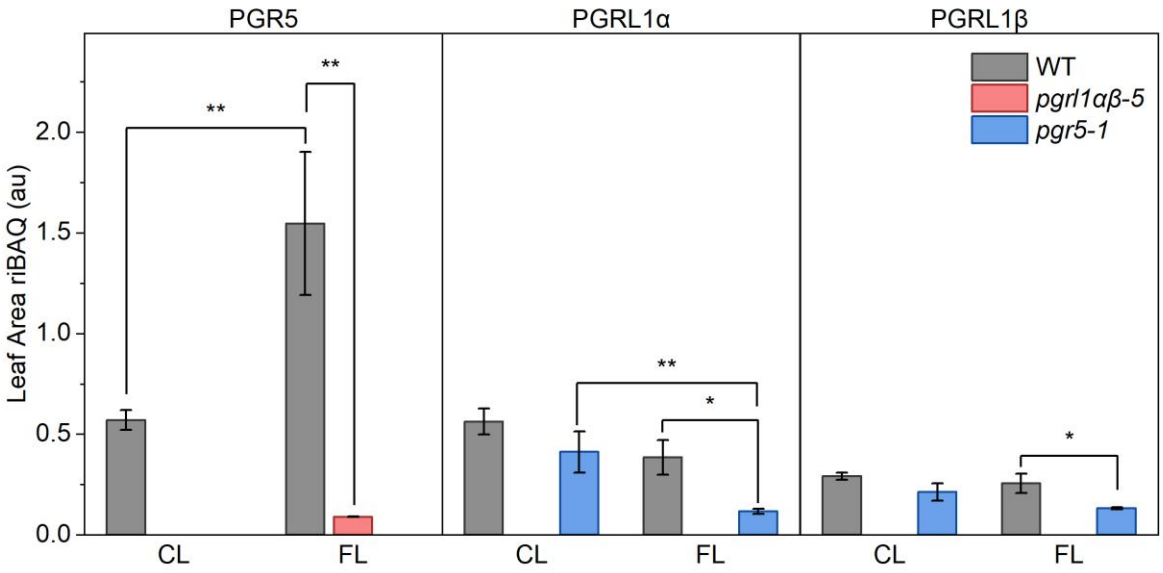

Fig. 7. Leaf-area normalised riBAQ abundance of PGR5, PGRL1α, and PGRL1β in *S. viridis* WT, *pgrl1αβ-5*, and *pgr5-1* grown under constant or fluctuating light. CL, constant light; FL, fluctuating light. Abundance is expressed as leaf-area normalised riBAQ (arbitrary units). Mean ± SE, n = 3–4 biological replicates; absent bars indicate that the protein was not detected. Significance brackets indicate pairwise comparisons assessed by limma empirical-Bayes moderated *t*-test with Storey q-value correction: **, $q < 0.01$; *, $q < 0.05$.

Quantitative leaf proteomics under constant and fluctuating light

To identify the reasons for distinct phenotypes of *pgrl1αβ-5* and *pgr5-1*, quantitative leaf proteomics was performed on WT, *pgrl1αβ-5*, and *pgr5-1* plants grown under constant or fluctuating light. Under constant light, no protein changes were detected in either the *pgrl1αβ-5* vs WT or the *pgr5-1* vs WT comparison (Fig. 8a, b). A single protein of unknown relevance to chloroplast function was significantly higher in *pgrl1αβ-5* vs *pgr5-1* (Fig. 8c).

Under fluctuating light, both mutants showed large numbers of significantly differentially abundant proteins relative to WT (Fig. 8d, e). While the majority of changes were shared between genotypes, a subset of proteins was different between mutants in the direct comparison (Figs. 8, 9a). Functional enrichment analysis revealed that proteins decreased in both mutants were enriched for photosynthetic electron transport categories, including PSI, NDH complex, Cytochrome b_6f Complex (Cytb_6f), and ATP synthase, reflecting shared overall reductions in chloroplast electron transport capacity (Fig. 9b, c). Proteins uniquely elevated in *pgrl1αβ-5* were enriched for C_4 carbon assimilation and nitrogen metabolism categories, while those uniquely decreased in *pgr5-1* were enriched for Calvin cycle and sucrose biosynthesis, indicating distinct metabolic responses between genotypes (Fig. 9b, c).

To further characterise the molecular differences between *pgrl1αβ-5* and *pgr5-1* under fluctuating light, all significantly differentially abundant proteins in the direct mutant comparison were identified (Table 1). Proteins significantly more abundant in *pgrl1αβ-5* than in *pgr5-1* included NDH complex subunits NdhI, NdhT, and PnsB3, light-harvesting antenna proteins LHCA1 and LHCB3, citrate cycle NAD-malic enzyme, C_4

cycle enzymes phosphoenolpyruvate carboxylase (PEPC) and carbonic anhydrase (CA), and Ferredoxin-dependent glutamate synthase (Fd-GOGAT) (Table 1). Proteins significantly less abundant in *pgrl1αβ-5* than in *pgr5-1*, included class III apoplastic peroxidase, caffeic acid 3-O-methyltransferase (COMT), and proline dehydrogenase (Table 1).

To contextualise the differential abundance of these proteins within the photosynthetic proteome, a heatmap of proteins involved to electron transport, carbon fixation, and photorespiration was examined (Fig. 10). Overall, subunits of PSI, PSII, Cytb_6f, and ATP synthase were similarly decreased in both mutants relative to WT, and there were no consistent differences between *pgrl1αβ-5* and *pgr5-1*. In contrast, NDH subunits were decreased in both mutants but to a different extent so that overall NDH abundance was increased in *pgrl1αβ-5* vs *pgr5-1* (Fig. 10). In addition to CA and PEPC, other enzymes of the

C_4 cycle were broadly elevated in *pgrl1αβ-5* relative to *pgr5-1* (Fig. 10) and the same general trend was observed for photorespiratory enzymes.

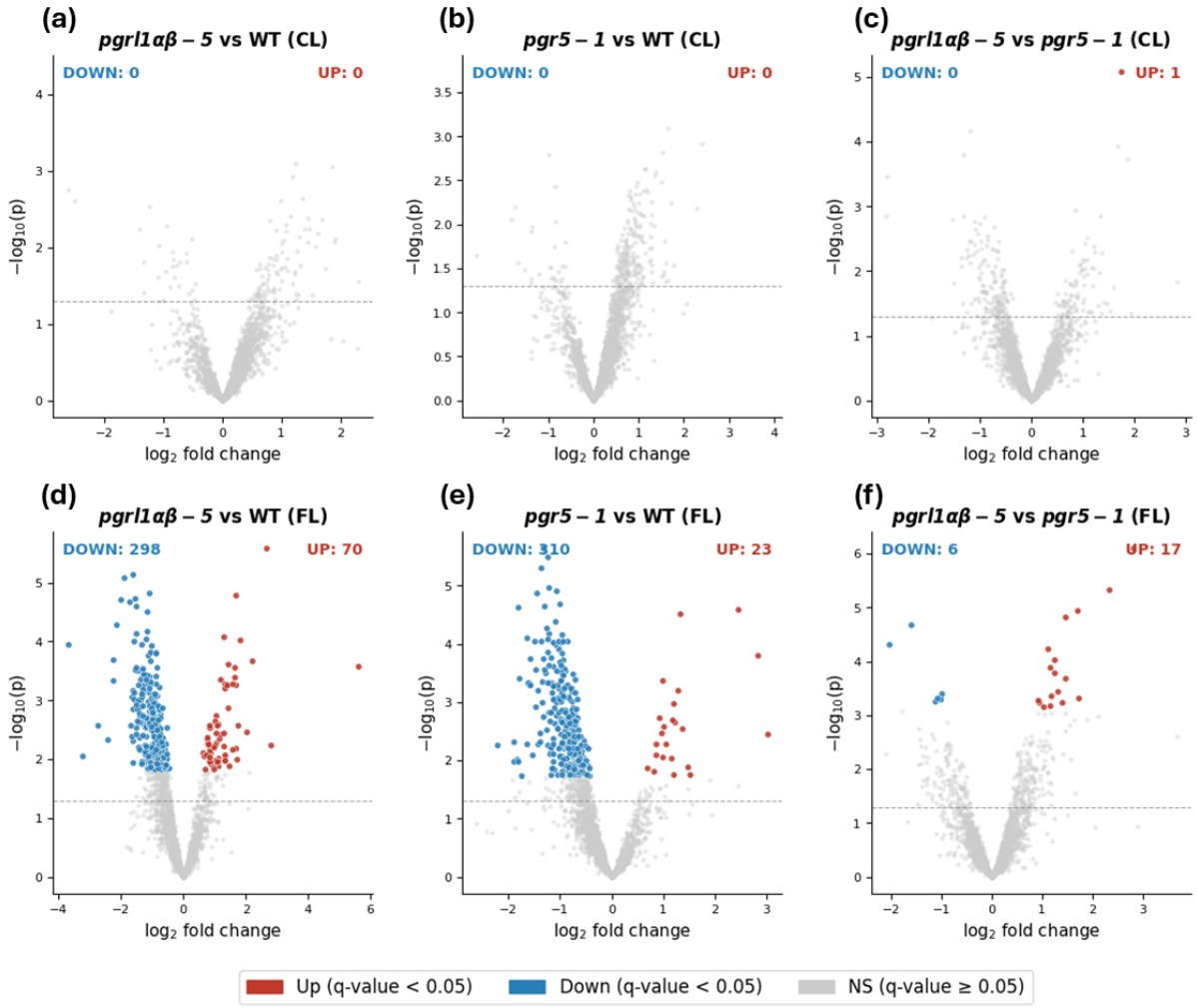

Fig. 8. Volcano plots of differentially abundant proteins in *S. viridis pgrl1αβ-5* and *pgr5-1* grown under constant or fluctuating light. Abundance values are leaf-area normalised riBAQ (log_2-transformed). The y-axis shows $-log_{10}$ of the uncorrected p-value; dot colour indicates significance based on the Storey q-value: red, significantly increased ($q < 0.05$); blue, significantly decreased ($q < 0.05$); grey, not significant ($q \geq 0.05$). The horizontal dashed line marks the uncorrected p-value corresponding to $q = 0.05$. Hit counts are annotated in the upper left (DOWN) and upper right (UP) of each panel. Top row: constant light (CL; n = *pgrl1αβ-5* 4, WT 3, *pgr5-1* 4; 2,397 proteins tested). (**a**) *pgrl1αβ-5* vs WT: 0 DOWN, 0 UP. (**b**) *pgr5-1* vs WT: 0 DOWN, 0 UP. (**c**) *pgrl1αβ-5* vs *pgr5-1*: 0 DOWN, 1 UP. Bottom row: fluctuating light (FL; n = *pgrl1αβ-5* 3, WT 3, *pgr5-1* 4; 2,031 proteins tested). (**d**) *pgrl1αβ-5* vs WT: 298 DOWN, 70 UP. (**e**) *pgr5-1* vs WT: 310 DOWN, 23 UP. (**f**) *pgrl1αβ-5* vs *pgr5-1*: 6 DOWN, 17 UP.

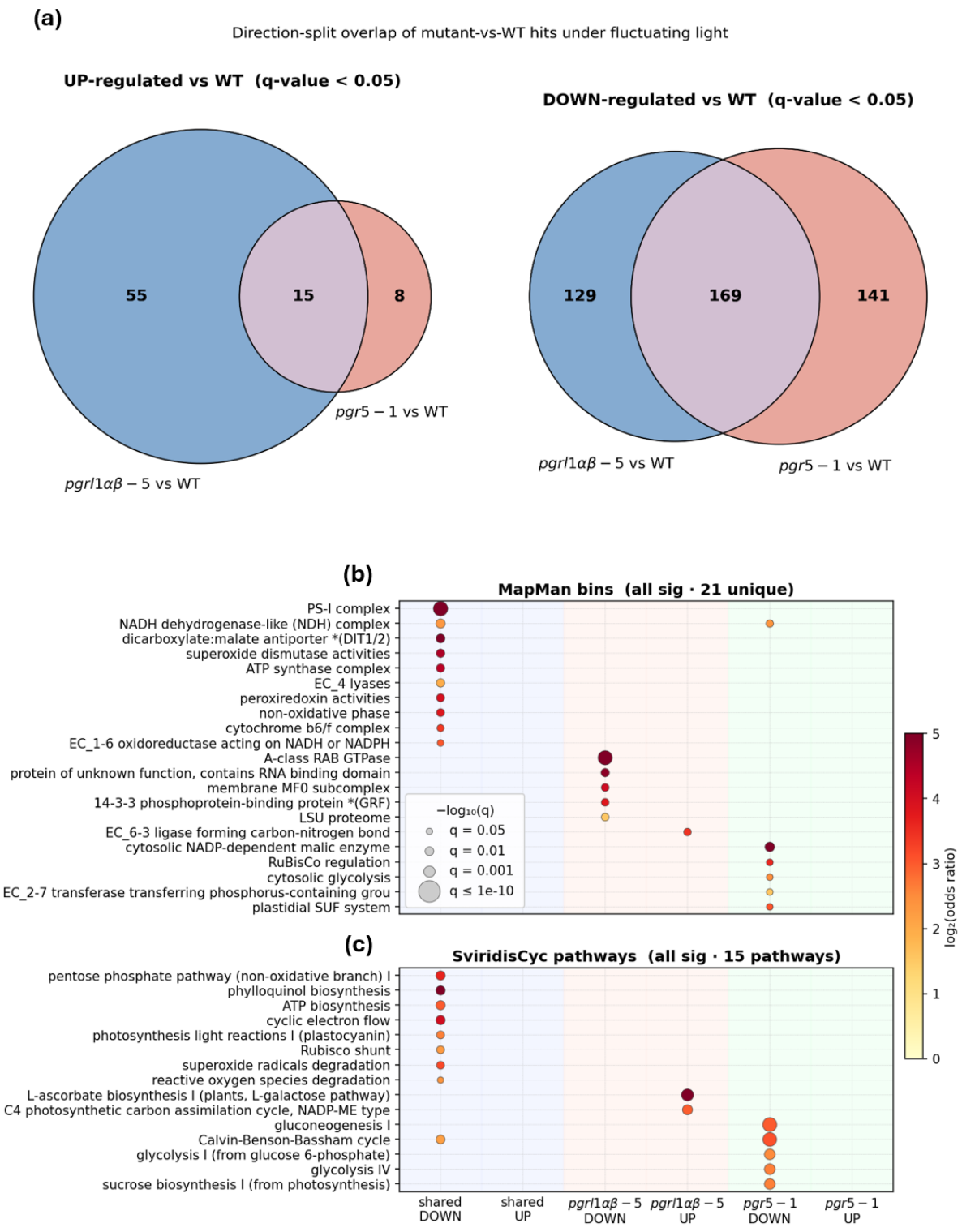

Fig. 9. Overlap and functional enrichment of differentially abundant proteins in *S. viridis pgrl1αβ-5* and *pgr5-1* grown under fluctuating light. (**a**) Venn diagrams showing the overlap of significantly increased (left) and significantly decreased (right) proteins between *pgrl1αβ-5* vs WT and *pgr5-1* vs WT comparisons. (**b**) MapMan functional bin enrichment dot plot across direction-status groups. Only bins enriched at q < 0.05 are shown. (**c**) SviridisCyc metabolic pathway enrichment dot plot across direction-status groups. Only pathways enriched at q < 0.05 are shown. In (**b**) and (**c**), dot size indicates $-\log_{10}(q)$ and dot colour

indicates $\log_2$(odds ratio), where darker red indicates greater over-representation of the functional category in that direction-status group; the six x-axis columns correspond to the direction-status groups defined in (**a**).

Table 1. Proteins significantly differentially abundant in *pgrl1αβ-5* vs *pgr5-1* under fluctuating light. Log_2FC values are derived from leaf-area normalised riBAQ abundance. Proteins are grouped by direction of change in *pgrl1αβ-5* relative to *pgr5-1*: ▲, significantly more abundant in *pgrl1αβ-5*; ▼, significantly less abundant in *pgrl1αβ-5* (Storey q < 0.05, limma moderated t-test). The WT comparison column indicates in which mutant(s) the protein was also significantly differentially abundant relative to WT (q < 0.05): '*pgrl1αβ-5*', '*pgr5-1*', 'both', or 'neither'. UniquePeptides, number of unique peptides contributing to protein quantification. n = *pgrl1αβ-5* 3, WT 3, *pgr5-1* 4.

Protein Description	**Complex / Pathway**	**log_2FC (*pgrl1αβ-5*/WT)**	**log_2FC (*pgr5-1*/WT)**	**log_2FC (*pgrl1αβ-5*/*pgr5-1*)**	**Storey q (*pgrl1αβ-5* vs *pgr5-1*)**	**WT comparison (q<0.05)**	**Unique Peptides**
▲ Higher in *pgrl1αβ-5* (FC > 0)							
NdhI	NDH Complex	0.615	-0.843	1.458	**0.0059**	*pgr5-1*	6
NdhT	NDH Complex	0.009	-1.16	1.169	**0.0429**	*pgr5-1*	8
PnsB3	NDH Complex	0.041	-0.981	1.022	**0.0476**	*pgr5-1*	5
PEPC	C_4 Cycle	0.829	-0.319	1.148	**0.0225**	*pgrl1αβ-5*	88
CA	C_4 Cycle	0.872	-0.381	1.253	**0.0185**	*pgrl1αβ-5*	23
ME – Cytosolic/Mitochondrial	Citrate Cycle	0.231	-1.069	1.3	**0.0429**	*pgr5-1*	11
Maltose excess protein 1	Starch Metabolism	0.127	-0.818	0.945	**0.0429**	*pgr5-1*	4
LHCA1	PSI Antenna	0.163	-0.996	1.159	**0.0476**	*pgr5-1*	11
LHCB3	PSII Antenna	0.679	-0.774	1.453	**0.0294**	*pgr5-1*	8
Fd-GOGAT (ferredoxin-glutamate synthase)	N Assimilation	1.688	0.454	1.234	**0.0259**	*pgrl1αβ-5*	73
Histidine-tRNA ligase	Amino Acid / tRNA	0.513	-0.892	1.406	**0.0429**	Neither	16

Sulfate adenylyltransferase	Sulfur Metabolism	0.086	-1.032	1.118	**0.0131**	*pgr5-1*	23
Tonoplast intrinsic protein (aquaporin)	Transport	2.677	-0.121	2.799	**0.0013**	*pgrl1αβ-5*	1
Sugar phosphate transporter domain protein	Carrier-mediated transport	1.287	-0.428	1.715	**0.0429**	*pgrl1αβ-5*	1
▼ Lower in *pgrl1αβ-5* (FC < 0)							
Cytochrome c domain protein (loc. 2)	Oxidative Stress	-1.509	-0.499	-1.01	**0.0429**	*pgrl1αβ-5*	1
Class III Apoplastic Peroxidase	Cell Wall Oxidative Stress	-0.008	0.986	-0.993	**0.0429**	*pgr5-1*	8
Proline dehydrogenase	Mitochondrial ETC	-1.888	-0.281	-1.607	**0.0067**	*pgrl1αβ-5*	4
Histone H2A	Chromatin	-1.731	-0.598	-1.133	**0.0429**	*pgrl1αβ-5*	4
Single-stranded DNA-binding protein	Chromatin	-1.023	0.05	-1.073	**0.0429**	*pgrl1αβ-5*	2
Caffeic acid 3-O-methyltransferase	monolignol biosynthesis	-1.379	0.668	-2.047	**0.0127**	*pgrl1αβ-5*	14

Proteomics — Leaf area normalised riBAQ

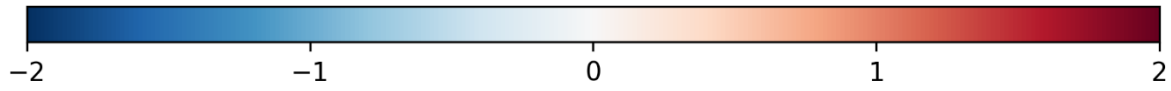

	pgrl1αβ vs *WT*	*pgr5* vs *WT*	*pgrl1αβ* vs *pgr5*
NDH			
NDH-A	-0.49	-0.27	-0.22
NDH-D	-0.09	-0.62	+0.53
NDH-F	-0.26	-0.68 *	+0.42
NDH-H	-0.57 *	-0.62 *	+0.05
NDH-I	+0.59	-0.86 *	+1.45 **
NDH-J	-0.40	-0.87 *	+0.47
NDH-K	-0.20	-0.95 **	+0.76
PnsL2	-0.96 *	-0.81 *	-0.15
PnsL3	-0.96 *	-0.87 *	-0.09
PnsB1	-0.07	-0.57 *	+0.49
PnsB2	-0.23	-0.64 *	+0.40
PnsB3	+0.02	-0.99 **	+1.01 *
PnsB4	-0.81 *	-1.38 **	+0.57
PnsB5	-0.49	-0.98 **	+0.49
NdhT	+0.02	-1.18 **	+1.20 *
Ndh-M	-0.33	-0.80 **	+0.47
Ndh-N	-0.86 *	-1.29 **	+0.43
Ndh-O	-0.15	-0.42	+0.26
Ndh-S	-0.60 *	-0.76 **	+0.16
Ndh-U	-0.77 *	-1.18 **	+0.40
Ndh-V	-0.18	-0.91 **	+0.73
PnsL1	-0.49	-0.69 *	+0.20
PnsL4	-0.03	-0.51 *	+0.48
PnsL5	+0.01	-0.28	+0.29
PSII			
PsbB/CP47	-0.59 *	-0.73 *	+0.14
PsbS	-0.48	-0.34	-0.15
PsbP	-0.36	-0.29	-0.08
PsbQ	-0.00	+0.03	-0.04
PsbR	-0.43	-0.29	-0.14
PsbA (D1)	-0.62 *	-0.51	-0.11
PsbD (D2)	-0.67 *	-0.51 *	-0.16
PsbC (CP43)	-0.55 *	-0.46 *	-0.09
PsbE (Cytb559-a)	-0.85 *	-0.66 *	-0.19
PSI			
PsaD	-1.09 *	-0.95 **	-0.14
PsaO	-1.30 *	-1.20 **	-0.10
PsaN	-0.73	-0.60	-0.13
PsaH	-1.52 *	-1.27 **	-0.25
PsaG	-0.56	-0.83 *	+0.27
PsaE	-0.79 *	-0.80 *	+0.01
PsaF	-1.16 *	-1.02 **	-0.14
PsaB	-0.86 *	-0.94 **	+0.08
PsaA	-0.70 *	-0.91 **	+0.21
PsaC (subVII)	-0.50	-0.56	+0.05
Cyt b_6f			
PetB (Cyt b6)	-0.66 *	-0.62 *	-0.04
PetC (Rieske)	-0.43	-0.85 **	+0.43
PetA (Cyt f)	-0.55 *	-0.73 **	+0.18

	pgrl1αβ vs *WT*	*pgr5* vs *WT*	*pgrl1αβ* vs *pgr5*
C_4 Cycle			
ADK	-0.25	-0.49	+0.25
CA	+0.88 *	-0.37	+1.25 *
NADP-ME	+0.07	-0.42 *	+0.49
PEPC	+0.84 *	-0.30	+1.14 *
PPDK	+0.80 *	+0.11	+0.69
PPDK-RP	+0.50	+0.12	+0.37
Calvin Cycle			
RPE	-0.87 *	-1.06 **	+0.18
GAPDH-A (loc.2)	-0.11	-0.45 *	+0.35
RCA	-0.19	-0.42 *	+0.24
GAPDH-A (loc.1)	-0.08	-0.44	+0.37
Aldolase	-0.84 *	-1.24 **	+0.40
GAPDH-B (NADP)	-0.53	-0.34	-0.19
SBPase	-0.80 *	-0.88 **	+0.08
Transketolase	-0.01	-0.57 *	+0.56
PGK	-0.44	-0.66 *	+0.21
RbcS (loc.1)	-0.91 *	-1.26 **	+0.35
RbcS (loc.2)	-1.02 *	-1.20 **	+0.18
TPI	+0.09	-0.14	+0.23
PRK	-0.49	-0.92 **	+0.43
RbcL	-0.46	-0.86 *	+0.40
Photorespiration			
SHMT	-0.37	-0.74 *	+0.37
PLGG1	-0.33	-0.56	+0.23
Catalase	+0.61	-0.04	+0.65
SHMT1	-0.26	-0.21	-0.06
PGLP1	+1.19 *	+0.92 *	+0.27
GDC-L	-0.35	-0.00	-0.34
GDC-P1	+0.47	-0.49	+0.95
GLYK	+0.01	-0.02	+0.02
GS2	+0.82 *	-0.10	+0.92
Fd-GOGAT	+1.70 **	+0.48	+1.21 *
Photoprotection			
OHP1	-0.60	-0.05	-0.55
ZEP3	+0.37	-0.15	+0.52
VDE	+0.15	-0.41	+0.56
LCNP	-0.49	-0.86 *	+0.38
ZEP Main	+0.52	-0.07	+0.59
OHP2	-0.69	-0.90	+0.22
PHT4;4	-0.70 *	-0.99 **	+0.28
ZEP2	-0.26	-0.53	+0.27
ATP Synthase			
AtpC (g; CF1)	-0.79 *	-1.01 **	+0.22
AtpD (d; CF1)	-0.84	-0.92 *	+0.08
AtpG (CF0-b)	-1.08 *	-1.31 **	+0.22
AtpI (CF0-IV)	-0.79	-0.62	-0.17
AtpF (CF0-I)	-0.57 *	-0.69 *	+0.12
AtpA (a; CF1)	-0.89 **	-1.08 **	+0.19
AtpE (e; CF1)	-0.60	-0.96 *	+0.36
AtpB (b; CF1)	-0.37	-0.80 *	+0.44

Fig. 10. Curated heatmap of leaf-area normalised riBAQ abundance for photosynthetic and metabolic proteins in *S. viridis pgrl1αβ-5*, WT, and *pgr5-1* grown under fluctuating light. Values represent $\log_2$(group mean / reference group mean) and are displayed on a diverging colour scale from −2 (blue, decreased relative to reference) to +2 (red, increased relative to reference). Storey q-value correction: **, q < 0.01; *, q < 0.05. *pgrl1αβ-5* n = 3, WT n = 3, *pgr5-1* n = 4. Protein abbreviations are in Table 2.

Table 2 Protein abbreviations

Abbreviation	Full Name
NDH Complex	
PnsB1	NDH-B subunit 1
PnsB2	NDH-B subunit 2
PnsB4	NDH-B subunit 4
PnsB5	NDH-B subunit 5
PnsL2	NDH-L subunit 2
PnsL3	NDH-L subunit 3
NDH-A	NAD(P)H dehydrogenase subunit A
NDH-D	NAD(P)H dehydrogenase subunit D
NDH-F	NAD(P)H dehydrogenase subunit F
NDH-H	NAD(P)H dehydrogenase subunit H
NDH-I	NAD(P)H dehydrogenase subunit I
NDH-J	NAD(P)H dehydrogenase subunit J
NDH-K	NAD(P)H dehydrogenase subunit K
PSII	
PsbA	D1 reaction centre protein
PsbB	CP47 chlorophyll a-binding protein
PsbC	CP43 chlorophyll a-binding protein
PsbD	D2 reaction centre protein
PsbE	Cytochrome b559 alpha subunit
PsbO	Manganese-stabilising protein
PsbR	10 kDa polypeptide
PsbS	22 kDa protein
PSI	
PsaA	Reaction centre subunit I
PsaB	Reaction centre subunit II
PsaC	Subunit VII

PsaD	Subunit II
PsaE	Subunit IV
PsaF	Subunit VI
PsaG	Subunit V
PsaH/L	Subunit III
PsaN	Subunit N
PsaO	Subunit O
Cytochrome b_6f	
PetA	Cytochrome *f*
PetB	Cytochrome b_6
PetC	Rieske iron-sulphur protein
ATP Synthase	
AtpA	Alpha subunit (CF_1)
AtpB	Beta subunit (CF_1)
AtpC	Gamma subunit (CF_1)
AtpD	Delta subunit (CF_1)
AtpE	Epsilon subunit (CF_1)
AtpF	Subunit b (CF_0-I)
AtpG	Subunit b' (CF_0-b)
AtpI	Subunit c (CF_0-IV)
C_4 Cycle	
ADK	Adenylate kinase
CA	Carbonic anhydrase
NADP-ME	NADP-dependent malic enzyme
PEPC	Phosphoenolpyruvate carboxylase
PPDK	Pyruvate orthophosphate dikinase
PPDK-RP	Pyruvate orthophosphate dikinase regulatory protein
Calvin Cycle	
Aldolase	Fructose-bisphosphate aldolase
GAPDH-A (loc.1/loc.2)	Glyceraldehyde-3-phosphate dehydrogenase A, loci 1 and 2
GAPDH-B (NADP)	NADP-dependent glyceraldehyde-3-phosphate dehydrogenase B
PGK	Phosphoglycerate kinase
PRK	Phosphoribulokinase

RbcL	Rubisco large subunit
RbcS (loc.1/loc.2)	Rubisco small subunit, loci 1 and 2
RCA	Rubisco activase
RPE	Ribulose-5-phosphate 3-epimerase
SBPase	Sedoheptulose-1,7-bisphosphatase
TPI	Triosephosphate isomerase
Photorespiration	
Catalase	Catalase
GLYK	Glycerate kinase
Fd-GOGAT	Ferredoxin-dependent glutamate synthase
GDC-L	Glycine decarboxylase complex L-protein (dihydrolipoamide dehydrogenase)
GDC-P1	Glycine decarboxylase complex P-protein
GS2	Glutamine synthetase 2 (Chloroplast localized)
PGLP1	2-Phosphoglycolate phosphatase 1
PLGG1	Plastidial glycolate/glycerate translocator 1
SHMT/SHMT1	Serine hydroxymethyltransferase isoforms
Photoprotection	
LCNP	Low chlorophyll NPQ protein
OHP1/OHP2	One-helix proteins 1 and 2
PHT4;4	Phosphate transporter 4;4
VDE	Violaxanthin de-epoxidase
ZEP Main/ZEP2/ZEP3	Zeaxanthin epoxidase isoforms

Discussion

PGR5 is required for the acclimation of *S. viridis* to fluctuating light, where it sustains the trans-thylakoid *pmf* and protects PSI during rapid increases in irradiance (Woodford *et al.*, 2025b). Because levels of PGRL2, which degrades PGR5 in the absence of PGRL1 (Rühle *et al.*, 2021) do not increase during C_4 evolutionary trajectory as PGR5 and PGRL1 do (Fig. 1), the capacity to degrade PGR5 might be comparatively low in *S. viridis*. Consistent with this, *pgrl1αβ-5* retained some PGR5, had higher photosystem II efficiency and grew faster compared to *pgr5-1* under fluctuating light (Fig. 4, Fig. 7). This was accompanied by elevated abundance of major enzymes of central carbon and nitrogen metabolism in *pgrl1αβ-5* relative to *pgr5-1* indicating that PGR5 is required for this metabolic response of C_4 plants to fluctuating light.

Under constant light, *pgrl1αβ-5* and *pgr5-1* were photosynthetically indistinguishable (Fig. 3, Fig. 4). Consistent with physiological observations, quantitative proteomics under constant light identified no PGR5 in either mutant and found no differentially abundant proteins in either *pgrl1αβ-5* or *pgr5-1* relative to WT. Interestingly, this was in contrast to the strong transcripts' responses detected in *pgr5-1* vs WT (Woodford *et al.*, 2025b) , indicating that the loss of PGR5 elicits a transcriptional response not reflected in the proteome. Discordance between transcript and protein abundance is well documented in plants and attributed to translational and post-translational regulation (Vélez-Bermúdez & Schmidt, 2014). Together, these data suggest that loss of both PGRL1 paralogs imposes no photosynthetic cost beyond the loss of PGR5 under non-stress conditions.

Under fluctuating light, *pgrl1αβ-5* retained approximately 6% of WT PGR5 levels but showed a consistent intermediate growth phenotype between WT and *pgr5-1* across every physiological parameter measured: biomass, tiller count, and relative chlorophyll content (Fig. 5, Fig. 6). PSII photochemical yield was higher in *pgrl1αβ-5* than in *pgr5-1* but lower than in WT, while the yield of NPQ was lower in *pgrl1αβ-5* than in *pgr5-1* but higher than in WT (Fig. 5c–e). It was recently shown that the elevated NPQ under fluctuating light in *pgr5-1* was due to the slower-relaxing zeaxanthin-dependent quenching (qZ), (Woodford *et al.*, 2025b). qZ is essential to provide photoprotection in during the high light phases of fluctuating light when qE and photosynthetic control are impaired in *pgr5-1*. However, because qZ relaxes slowly, it dissipates light energy that could otherwise drive photochemistry during the low light phases. The lower NPQ of *pgrl1αβ-5* vs *pgr5-1* (Fig. 5d), suggests less qZ engagement and, therefore, improved photochemistry during the low-light phase in *pgrl1αβ-5* vs *pgr5-1*.

Lower NPQ and corresponding higher PSII efficiency in *pgrl1αβ-5* vs *pgr5-1* has likely resulted in improved growth by sustaining greater photochemistry during the low-light phases.

However, since PSI, PSII, Cytb_6f, and ATP synthase were similarly decreased in both mutants relative to WT (Fig. 10), both mutants sustain comparable photodamage to PSI. Thus, the low abundance of residual PGR5 in *pgrl1αβ-5* did not provide greater protection of PSI from photodamage. Nevertheless, higher efficiency of PSI might be predicted in *pgrl1αβ-5* under fluctuating light but requires further investigation.

The only major thylakoid complex higher in abundance in *pgrl1αβ-5* vs *pgr5-1* was NDH (Table 1, Fig. 10). This indicated higher capacity of NDH-dependent CEF which enables ATP generation in BS cells (Ermakova *et al.*, 2024b). The intermediate growth phenotype of *pgrl1αβ-5* may therefore also relate to a greater capacity of ATP generation in bundle sheath. The exact mechanism of selective retaining NDH in *pgrl1αβ-5* under fluctuating light will require further investigation and might be related to an interplay between PGR5 and NDH in a chloroplast developmental context. Light-harvesting antenna proteins LHCA1 and LHCB3 were similarly retained in *pgrl1αβ-5* vs *pgr5-1* (Table 1), corresponding to the higher relative chlorophyll content in *pgrl1αβ-5* (Fig. 5, Fig. 6). This provides additional support for increased photochemical efficiency in *pgrl1αβ-5*, providing more energy for metabolic acclimation and growth.

Interestingly, the mesophyll-localised C_4 cycle enzymes PEPC and CA were elevated in *pgrl1αβ-5* vs *pgr5-1*, so much so that they were also significantly more abundant in *pgrl1αβ-5* vs WT, against the backdrop of lower abundance of most proteins on leaf area basis (Table 1, Fig. 10). While greater enzyme abundance against a background of reduced photosystem capacity does not by itself indicate higher C_4 flux; the most cautious interpretation is that *pgrl1αβ-5* mounts a compensatory increase in C_4 enzyme abundance in response to perceived inefficiency of CO_2 assimilation in the mesophyll imposed by an energy deficit resulting from the lower capacity of the mesophyll light reactions. That this response is absent in *pgr5-1* indicates a dependence, direct or indirect, on the residual PGR5 present in *pgrl1αβ-5*, although the mechanism for this regulation remains to be resolved.

Both mutants appear to engage higher photorespiratory flux under fluctuating light, but only *pgrl1αβ-5* additionally elevates nitrogen metabolism. PGLP1 was elevated relative to WT in both mutants (Fig. 10), indicating that both likely experience increased Rubisco oxygenation rates and an increased need to recycle photorespiratory products under fluctuating light. Photorespiration is strongly suppressed in C_4 plants (von Caemmerer & Furbank, 2003) but recycling of photorespiratory products is not dispensable. Serious growth defects result in a C_4 species from the knockdown of PGLP to 5% WT activities in a C_4, due to the inability to metabolise this photorespiratory product (Levey *et al.*, 2019). Intriguingly, it has also been suggested that imbalances between ATP and NADPH production and coordination of the C_4

and C_3 cycles during light transients can induce high photorespiratory flux in C_4 leaves through inefficiencies in the CO_2 concentrating mechanism (Fu & Walker, 2024). In contrast, Fd-GOGAT, involved in recycling photorespiratory ammonia and in primary N assimilation, was significantly more abundant in *pgrl1αβ-5* than in *pgr5-1* and was elevated above WT only in *pgrl1αβ-5* (Table 1; Fig. 10). Fd-GOGAT catalyses the transfer of the amide group of glutamine to 2-oxoglutarate to form two molecules of glutamate, the final step of the GS/GOGAT cycle (Kendall *et al.*, 1987; Coschigano *et al.*, 1998). In *S. viridis*, Fd-GOGAT is mesophyll-enriched at the transcript level, expressed approximately 11-fold higher in mesophyll vs bundle sheath cells yet still present in both cell types (John *et al.*, 2014), matching the pattern reported for Sorghum from Döring *et al.* (2016). It has been proposed that glutamine is produced in the bundle sheath cells during detoxification of photorespiratory ammonia and diffuses to mesophyll cells for conversion to glutamate. Together, the elevation of PGLP1 in both mutants indicates increased photorespiratory flux in bundle sheath cells under fluctuating light, while the selective elevation of Fd-GOGAT above WT and *pgr5-1* in *pgrl1αβ-5* indicates a greater capacity for re-assimilation of photorespiratory ammonia in these mutants.

The proteins selectively elevated above WT in *pgrl1αβ-5* (PEPC, CA, and Fd-GOGAT) are all mesophyll-localised or -enriched, supporting a mesophyll-specific acclimation response absent in *pgr5-1*. This pattern is also consistent with an inadequacy of the CO_2 concentrating mechanism under low irradiance to maintain high BS CO_2. $^{13}CO_2$ labelling kinetics reveal excess PEPC flux, increased CO_2 back-leakage, restriction of NADP-ME with a switch toward alternative decarboxylation routes, less effective use of metabolite pools to drive intercellular shuttles, and elevated photorespiration (Ubierna *et al.*, 2013; Kromdijk *et al.*, 2014; Medeiros *et al.*, 2022; Arrivault *et al.*, 2025). Fluctuating light represents a condition of both high-light stress and low irradiance, two conditions pgr5 mutants would struggle under, but only *pgrl1αβ-5* mounts a compensatory increase in mesophyll enzyme capacity. Together, the elevation of mesophyll-localised enzymes across both the C_4 cycle and the photorespiratory/nitrogen re-assimilation pathway in *pgrl1αβ-5* suggest a mesophyll-specific response to energy limitation that depends, directly or indirectly, on residual PGR5.

The six proteins more abundant in *pgr5-1* than in *pgrl1αβ-5* are consistent with higher stress in *pgr5-1* (Table 1). A class III peroxidase and COMT act together in a phenylpropanoid module in which COMT supplies monolignols and the peroxidase couples them using H_2O_2, a process linked both to stress-induced cell-wall fortification and to apoplastic ROS signalling (Passardi *et al.*, 2004; Shigeto & Tsutsumi, 2016), with COMT in particular induced under abiotic stress (Xu *et al.*, 2025). Proline dehydrogenase, the first enzyme of proline catabolism through the proline–P5C pathway, it too is reported to change in abundance in response to stress (Verslues & Sharma, 2010). The remaining two proteins, a histone H2A and a single-stranded

DNA-binding protein, have no clear known function, but neither have transit peptides and thus may contribute to modulating gene expression. Taken together, and consistent with the more severe growth and chlorosis phenotype of *pgr5-1*, these proteins further support the interpretation that *pgr5-1* is more stressed state than *pgrl1αβ-5* under fluctuating light.

The accumulation of residual PGR5 in *pgrl1αβ-5* under fluctuating light, but not under constant light, is most simply explained by a stoichiometric excess of PGR5 over PGRL2-mediated degradation capacity in the absence of PGRL1 (Fig. 7). PGR5 has been previously shown to be required for acclimation to fluctuating light (Woodford *et al.*, 2025b), but its abundance had not been directly compared between constant and fluctuating light. Here we show that PGR5 abundance in WT *S. viridis* increases approximately 3-fold under fluctuating light relative to constant light, interestingly, with no similar increase in PGRL1 paralogs (Fig. 7). This identifies PGR5, rather than PGRL1, as the light-regulated component of the pathway and indicates that under fluctuating light a more constitutive activity of PGR5 can be required in C_4 plants. This potentially unregulated by PGRL1 activity of PGR5 suggests either need for constitutive photoprotection of PSI or that additional activity of PGR5, potentially outside of PSI photoprotection, is needed under fluctuating light.

One possibility is that residual PGR5 acts outside PSI photoprotection, retaining a regulatory function even at an abundance insufficient for photoprotection itself. The 6% pool in *pgrl1αβ-5* was evidently below the threshold required for its bulk photoprotective function, as PSI abundance was decreased to the same extent as in *pgr5-1*, yet its presence correlates with the distinct metabolic acclimation described above. Similar phenomena have been observed where an uncoupling of a low-abundance regulatory role from bulk catalytic function that is well documented in other systems. An analogous uncoupling occurs for inositol polyphosphate multikinase (IPMK): severe knockdown abolishes its catalytic synthesis of inositol polyphosphates, yet its tight-affinity scaffolding of regulators such as mTORC1 and ULK1 persists at very low protein abundance, separating its catalytic role from its signalling role (Kim *et al.*, 2017; Guha *et al.*, 2019). By the same logic, a small PGR5 pool may nonetheless perform regulatory function that shapes the metabolic response to fluctuating light.

Future directions

The conclusion that residual PGR5 does not protect PSI in *pgrl1αβ-5* relies on equivalence of PSI abundance between the mutants, but the functional state of PSI was not measured under fluctuating light. Measuring the maximum oxidisable P700 (P_M) and PSI photochemical yields in plants grown under fluctuating light would establish whether abundance equates to efficiency. Similarly, detailed analysis of *pmf* and qE in plants grown under fluctuating light is

needed to reveal whether residual PGR5 can help induce some qE, this could be the reason why *pgrl1αβ-5* does not need to engage qZ.

The greater abundance of NDH subunits in *pgrl1αβ-5* was interpreted as a greater capacity for NDH-dependent CEF, but the functional activity of the complex was not measured. NDH-dependent CEF could be quantified in bundle sheath cells (Ermakova *et al.*, 2024b). Detailed gas exchange of plants grown under fluctuating light could clarify whether higher NDH abundance corresponds to greater chloroplast ATP supply and increased assimilation rates in *pgrl1αβ-5* vs *pgr5-1*. Furthermore, the CO_2 compensation point as a proxy for photorespiration, together with measurement of key metabolite pools such as 2-phosphoglycolate, would show whether the elevated C_4 and photorespiratory enzyme abundances in *pgrl1αβ-5* correspond to altered flux. The observation of elevated levels of mesophyll enzymes observed here in plants with low levels of PGR5 points toward a yet unidentified signalling pathway linking protein expression and PGR5. Examination of the components of this signalling may reveal novel ways of integrating metabolic flux with electron transport in C_4 plants.

Conclusion

This chapter shows that, unlike in *A. thaliana*, the loss of both PGRL1 paralogs in *S. viridis* does not phenocopy the loss of PGR5 under fluctuating light. Approximately 6% of WT-level PGR5 was retained in *pgrl1αβ-5* under fluctuating light, and this residual PGR5 was associated with an intermediate phenotype between WT and *pgr5-1* across growth, photosynthetic and proteomic measures. Because PSI, PSII, Cytb_6f and ATP synthase were reduced to the same extent in both mutants, this intermediate phenotype likely did not arise from greater photoprotection of PSI but from an improved metabolic response to fluctuating light: relative to *pgr5-1*, *pgrl1αβ-5* retained NDH and light-harvesting antenna, elevated C_4 and photorespiratory/nitrogen-metabolism enzymes, and lacked the oxidative-stress signature characteristic of *pgr5-1*. Consistent with a less stressed state, *pgrl1αβ-5* maintained lower NPQ and higher PSII photochemical efficiency than *pgr5-1* during the low-light phases of fluctuating light. Together, these results indicate that PGR5 contributes to the coordinated metabolic acclimation of *S. viridis* to fluctuating light and support a potential role for PGR5 in stress-acclimation in addition to its established function in PSI photoprotection.

Chapter 5: Conclusions and Future Directions

Regulation of the light reactions in C_4 photosynthesis is an elaborate process that requires cell specialisation to match the distinct metabolic energy demands of each cell type. Balancing energy supply and photoprotection against metabolic demand under fluctuating light depends on fast regulation of the light reactions, yet how C_4 plants achieve this has remained poorly defined. PGR5 and PGRL1 stood out as the principal candidates, accumulating to higher levels in C_4 species than in their C_3 relatives and enabling growth under fluctuating light (Munekage *et al.*, 2010; Kümpers *et al.*, 2017; Woodford *et al.*, 2025b). This thesis provided novel insights into evolution and function of the PGR5/PGRL1 system in C_4 grasses, showing that it is not simply inherited from C_3 plants, but it has specialised for regulatory needs of C_4 photosynthesis.

Through specialisation of PGRL1 paralogs in grasses, PGR5/PGRL1 constitutes a powerful photoprotective system, affording a more dynamic range of photoprotection than in dicots. In the C_4 NADP-ME grasses, this system is further co-opted in distinct cell types, correlating with the distinct energy demands. By expressing the paralog whose kinetics suit each cell: the fast PGRL1β in the bundle sheath, where rapid PSI oxidation is needed to sustain productive CEF via NDH, and the slower but better-sustained PGRL1α in the mesophyll where balanced LEF to CEF is required, each cell type can tune the speed and capacity of PSI photoprotection independently. This helps to balance PSI photoprotection with the contrasting CEF/LEF demands of mesophyll and bundle sheath cells contributing to overall fitness of leaf-level C_4 photosynthesis.

PGR5-regulated photoprotection acts within the first second of a low to high-light transition. This rapid response is mounted by a PGRL1β, which I propose arises from distinct grass-specific lumenal regulation of PGRL1β dimerisation. It follows that PGRL1 paralogs, even within the grass family, could carry additional substitutions that further tune the speed and capacity of PSI photoprotection. This positions PGRL1 as a main controller of PSI photoprotection, which could be tuned based on various chloroplast signals. If these properties can be predicted from sequence, then the natural diversity of PGRL1 across the grasses, and across photosynthetic organisms more widely, becomes a source to mine for alleles that could confer superior kinetics and/or regulation. Engineering PGRL1 to confer both faster and sustained photoprotection, or other useful properties, could hold real potential for improving crops. An immediate direct application would be to introduce the fast PGRL1β-type response into dicot crops, like canola, to test whether it can broaden the dynamic range of PSI photoprotection and improve yields under stress.

Critical importance of PGR5 for fluctuating-light acclimation is corroborated here through PGR5 abundance being upregulated three-fold under fluctuating light vs constant moderate light. This highlights the increased demand for rapid photoprotection during repetitive low to high light irradiance increases which are characteristic for grasses' open field habitats. Importantly, this work uncovers that, apart from the immediate role in photoprotection, PGR5 enables metabolic acclimation of C_4 plants to fluctuating light stress, likely through preserving the energy generated by the light reactions. This reinforces the importance of metabolic adaptation of C_4 photosynthesis to fluctuating light a known vulnerability of the C_4 system, whose metabolism adjusts slowly and can fall out of coordination under sudden shifts in irradiance, causing CO_2 leakage and loss of efficiency (Furbank & Walker, 1985; Arce Cubas *et al.*, 2023; Arrivault *et al.*, 2025).

As C_4 plants are rarely CO_2 limited but are more frequently limited by the energy generated by the light reactions, developing strategies to improve electron transport efficiency can provide vital for improving C_4 crop productivity. Overexpression of the Rieske FeS subunit of Cytb_6f, which raises Cytb_6f abundance, increased CO_2 assimilation in *S. viridis* (Ermakova *et al.*, 2019) and accelerated photosynthetic induction to increase biomass and grain yield in *Sorghum bicolor* (Ermakova *et al.*, 2023), demonstrating that boosting electron-transport capacity can enhance C_4 productivity. Furthermore, the expression of algal cytochrome c_6 alongside enhanced ribulose-1,5-bisphosphate regeneration improved assimilation and biomass in tobacco likely by increasing the acceptor side pool and improving electron transfer efficiency (López-Calcagno *et al.*, 2020). Therefore, increasing the abundance of the carriers flanking PSI, Cytb_6f and PC on the donor side, and Fd on the acceptor side, would enlarge the pool of available electron-transfer partners and raise flux through PSI, increasing ATP and NADPH production. Provided donor and acceptor capacity are expanded together, this added flux could be accommodated while keeping P700 oxidised, avoiding the over-reduction that generates ROS and so preserving the photosynthetic control that protects PSI. The mass action approach developed here provides ways of analysing such improvements to electron transfer.

There are several limitations of this work. The in vivo flux method developed in Chapter 3 was applied only to WT and *pgr5-1*, but there is no assessment of potential CEF flux in single PGRL1 mutants. Currently, the distinction between the speed of PGRL1β and the capacity of PGRL1α therefore rests on the kinetics of P700 oxidation. Resolving PC, Fd, and P700 redox kinetics and fluxes, along with lumenal pH reporters, would reveal whether the speed difference between PGRL1α and PGRL1β is regulated by lumen pH, as suggested by AlphaFold structural predictions in which PGRL1β is proposed to be insensitive to lumen pH while PGRL1α is proposed to require lumenal acidification to engage. Likewise, the claim that

the ~6% residual PGR5 pool does not provide significant PSI protection is inferred from the proteomics analysis, and will require analysis of the photochemically active amount of PSI. Therefore, P700 redox spectroscopy and the mass-action analysis of PC, Fd, and P700 rate constants and fluxes should be performed on WT, *pgr5-1* and *pgrl1αβ-5* plants under fluctuating light to establish whether the residual pool of PGR5 in *pgrl1αβ-5* promotes PSI photoprotection. Finally, the proteomic analysis of Chapter 4 was not cell-type resolved, so a mesophyll- and bundle sheath-enriched analysis under fluctuating light is needed to determine where the metabolic acclimation occurs.

Several lines of work follow directly from these limitations. The mass-action DIRK-NIR framework should also be validated against established mutants and phenotypes to confirm that this approach agrees with, or usefully clarifies, known results. Examples include but are not limited to the *A. thaliana pgr1* (a single point mutation (P194L) in the Rieske subunit of Cytb_6f that causing PCON to engage at a higher lumen pH; Okegawa *et al.,* 2005), *trol* (mutant lacking TROL which tethers FNR to the thylakoid near PSI, mutants show changes in balance between LEF and CEF; Vojta *et al.,* 2015), *pgrl1ab-pgrl2* (Rühle *et al.*, 2021), and *S. viridis ndho* (Ermakova *et al.*, 2024b) and *ndhO*/*pgr5* mutants. Finally, extending the mass-action and spectral-unmixing framework to cytochrome *f*, *b* hemes, and ideally the plastoquinone pool would yield a system capable of resolving fluxes through both LEF and CEF. Further extending this to mesophyll and bundle sheath enrichment would pull apart the cell specific fluxes and regulations as well.

This thesis has revealed that PGR5/PGRL1 is a central and specialised regulator of C_4 photosynthesis under fluctuating light, extending the knowledge beyond what's been known from C_3 plants. The duplication of PGRL1 broadened the kinetic range of PSI photoprotection across cell types, the *in vivo* flux analysis exposed a donor-side role for PGR5 in regulating electron flow, and the abundance of PGR5 emerged as a tuneable set-point that also drives metabolic acclimation to fluctuating light stress. In conclusion, these findings not only refine the mechanistic understanding of how PGR5 and PGRL1 act but also identify new directions and priority targets for engineering improved electron transfer in C_4 crops in field environments.

References

Abramson J, Adler J, Dunger J, Evans R, Green T, Pritzel A, Ronneberger O, Willmore L, Ballard AJ, Bambrick J, et al. 2024. Accurate structure prediction of biomolecular interactions with AlphaFold 3. *Nature* **630**(8016): 493–500.

Adler L, Díaz-Ramos A, Mao Y, Pukacz KR, Fei C, McCormick AJ. 2022. New horizons for building pyrenoid-based CO_2-concentrating mechanisms in plants to improve yields. *Plant Physiology* **190**(3): 1609–1627.

Alexa A, Rahnenführer J, Lengauer T. 2006. Improved scoring of functional groups from gene expression data by decorrelating GO graph structure. *Bioinformatics* **22**(13): 1600–1607.

Allen M 2017. Errors of measurement: attenuation. *The SAGE Encyclopedia of Communication Research Methods*: SAGE Publications, Inc. 430–433.

Almagro Armenteros JJ, Salvatore M, Emanuelsson O, Winther O, von Heijne G, Elofsson A, Nielsen H. 2019. Detecting sequence signals in targeting peptides using deep learning. *Life Science Alliance* **2**(5): e201900429.

Alvarez CE, Bovdilova A, Höppner A, Wolff C-C, Saigo M, Trajtenberg F, Zhang T, Buschiazzo A, Nagel-Steger L, Drincovich MF, et al. 2019. Molecular adaptations of NADP-malic enzyme for its function in C_4 photosynthesis in grasses. *Nature Plants* **5**(7): 755–765.

Ang WSL, How JA, How JB, Mueller-Cajar O. 2023. The stickers and spacers of Rubiscondensation: assembling the centrepiece of biophysical CO_2-concentrating mechanisms. *Journal of Experimental Botany* **74**(2): 612–626.

Anthropic 2025a. Claude Opus 4.7. *Large language model*.

Anthropic 2025b. Claude Sonnet 4.6. *Large language model*.

Appel J, Craig S, Theune M, Hüren V, Künzel S, Forberich B, Bryan S, Gutekunst K. 2022. Evidence for Electron Transfer from the Bidirectional Hydrogenase to the Photosynthetic Complex I (NDH-1) in the Cyanobacterium *Synechocystis sp.* PCC 6803. *Microorganisms* **10**(8): 1617.

Arce Cubas L, Rodrigues Gabriel Sales C, Vath RL, Bernardo EL, Burnett AC, Kromdijk J. 2023. Lessons from relatives: C_4 photosynthesis enhances CO_2 assimilation during the low-light phase of fluctuations. *Plant Physiology* **193**(2): 1073–1090.

Arrivault S, Medeiros DB, Sales CRG, Guenther M, Kromdijk J, Fernie AR, Stitt M. 2025. Metabolite profiling reveals slow and uncoordinated adjustment of C_4 photosynthesis to sudden changes in irradiance. *Plant Physiology* **199**(3).

Asada K. 1999. THE WATER-WATER CYCLE IN CHLOROPLASTS: Scavenging of Active Oxygens and Dissipation of Excess Photons. *Annual Review of Plant Biology* **50**(Volume 50, 1999): 601–639.

Ashton AR, Burnell JN, Furbank RT, Jenkins CLD, Hatch MD 1990. 3 - Enzymes of C_4 Photosynthesis. In: Lea PJ ed. *Methods in Plant Biochemistry*: Academic Press, 39–72.

Avenson TJ, Cruz JA, Kanazawa A, Kramer DM. 2005a. Regulating the proton budget of higher plant photosynthesis. *Proc Natl Acad Sci U S A* **102**(27): 9709–9713.

Avenson TJ, Kanazawa A, Cruz JA, Takizawa K, Ettinger WE, Kramer DM. 2005b. Integrating the proton circuit into photosynthesis: progress and challenges. *Plant, Cell & Environment* **28**(1): 97–109.

Bauwe H, Hagemann M, Fernie AR. 2010. Photorespiration: players, partners and origin. *Trends in Plant Science* **15**(6): 330–336.

Bellasio C, Ermakova M. 2022. Reduction of bundle sheath size boosts cyclic electron flow in C_4 *Setaria viridis* acclimated to low light. *Plant Journal* **111**(5): 1223–1237.

Bielow C, Mastrobuoni G, Kempa S. 2016. Proteomics Quality Control: Quality Control Software for MaxQuant Results. *Journal of Proteome Research* **15**(3): 777–787.

Borba AR, Reyna-Llorens I, Dickinson PJ, Steed G, Gouveia P, Górska AM, Gomes C, Kromdijk J, Webb AAR, Saibo NJM, et al. 2023. Compartmentation of

photosynthesis gene expression in C_4 maize depends on time of day. *Plant Physiology* **193**(4): 2306–2320.

Cacefo V, Ribas AF, Zilliani RR, Neris DM, Domingues DS, Moro AL, Vieira LGE. 2019. Decarboxylation mechanisms of C_4 photosynthesis in *Saccharum spp.*: increased PEPCK activity under water-limiting conditions. *BMC Plant Biology* **19**(1): 144.

Cardona T, Sánchez-Baracaldo P, Rutherford AW, Larkum AW. 2019. Early Archean origin of Photosystem II. *Geobiology* **17**(2): 127–150.

Cassan N, Lagoutte B, Sétif P. 2005. Ferredoxin-$NADP^+$ Reductase: Kinetics of electron transfer, transient intermediates, and catalytic activities studied by flash-absorption spectroscopy with isolated photosystem I and ferredoxin. *Journal of Biological Chemistry* **280**(28): 25960–25972.

Chan KX, Phua SY, Crisp P, McQuinn R, Pogson BJ. 2016. Learning the Languages of the Chloroplast: Retrograde Signaling and Beyond. *Annual Review of Plant Biology* **67**(Volume 67, 2016): 25–53.

Chapman KSR, Berry JA, Hatch MD. 1980. Photosynthetic metabolism in bundle sheath cells of the C_4 species *Zea mays*: Sources of ATP and NADPH and the contribution of photosystem II. *Archives of Biochemistry and Biophysics* **202**(2): 330–341.

Chaturvedi AK, Dym O, Levin Y, Fluhr R. 2024. PGR5-LIKE PHOTOSYNTHETIC PHENOTYPE1A redox states alleviate photoinhibition during changes in light intensity. *Plant Physiology* **194**(2): 1059–1074.

Chaux F, Burlacot A, Mekhalfi M, Auroy P, Blangy S, Richaud P, Peltier G. 2017. Flavodiiron Proteins Promote Fast and Transient O_2 Photoreduction in Chlamydomonas *Plant Physiology* **174**(3): 1825–1836.

Chotewutmontri P, Barkan A. 2021. Ribosome profiling elucidates differential gene expression in bundle sheath and mesophyll cells in maize. *Plant Physiology* **187**(1): 59–72.

Concordet J-P, Haeussler M. 2018. CRISPOR: intuitive guide selection for CRISPR/Cas9 genome editing experiments and screens. *Nucleic Acids Research* **46**(W1): W242–W245.

Coschigano KT, Melo-Oliveira R, Lim J, Coruzzi GM. 1998. Arabidopsis *gls* Mutants and Distinct Fd-GOGAT Genes: Implications for Photorespiration and Primary Nitrogen Assimilation. *The Plant Cell* **10**(5): 741–752.

Courteille A, Vesa S, Sanz-Barrio R, Cazalé A-C, Becuwe-Linka N, Farran I, Havaux M, Rey P, Rumeau D. 2012. Thioredoxin m4 Controls Photosynthetic Alternative Electron Pathways in Arabidopsis *Plant Physiology* **161**(1): 508–520.

Cox J, Mann M. 2008. MaxQuant enables high peptide identification rates, individualized p.p.b.-range mass accuracies and proteome-wide protein quantification. *Nature Biotechnology* **26**(12): 1367–1372.

Croce R, Carmo-Silva E, Cho YB, Ermakova M, Harbinson J, Lawson T, McCormick AJ, Niyogi KK, Ort DR, Patel-Tupper D, et al. 2024. Perspectives on improving photosynthesis to increase crop yield. *The Plant Cell* **36**(10): 3944–3973.

Cruz JA, Sacksteder CA, Kanazawa A, Kramer DM. 2001. Contribution of Electric Field ($\Delta\psi$) to Steady-State Transthylakoid Proton Motive Force (*pmf*) in Vitro and in Vivo. Control of pmf Parsing into $\Delta\psi$ and ΔpH by Ionic Strength. *Biochemistry* **40**(5): 1226–1237.

DalCorso G, Pesaresi P, Masiero S, Aseeva E, Schunemann D, Finazzi G, Joliot P, Barbato R, Leister D. 2008. A complex containing PGRL1 and PGR5 is involved in the switch between linear and cyclic electron flow in Arabidopsis. *Cell* **132**(2): 273–285.

Danila FR, Quick WP, White RG, von Caemmerer S, Furbank RT. 2019. Response of plasmodesmata formation in leaves of C_4 grasses to growth irradiance. *Plant, Cell & Environment* **42**(8): 2482–2494.

Das K, Roychoudhury A. 2014. Reactive oxygen species (ROS) and response of antioxidants as ROS-scavengers during environmental stress in plants. *Frontiers in Environmental Science* **Volume 2 - 2014**.

Davis GA, Kramer DM. 2020. Optimization of ATP Synthase c–Rings for Oxygenic Photosynthesis. *Frontiers in Plant Science* **Volume 10 - 2019**.

Davis GA, Rutherford AW, Kramer DM. 2017. Hacking the thylakoid proton motive force for improved photosynthesis: modulating ion flux rates that control proton motive force partitioning into $\Delta\psi$ and ΔpH. *Philosophical Transactions of the Royal Society B: Biological Sciences* **372**(1730): 20160381.

Degen GE, Jackson PJ, Proctor MS, Zoulias N, Casson SA, Johnson MP. 2023a. High cyclic electron transfer via the PGR5 pathway in the absence of photosynthetic control. *Plant Physiology* **192**(1): 370–386.

Degen GE, Johnson MP. 2024. Photosynthetic control at the cytochrome b_6f complex. *The Plant Cell* **36**(10): 4065–4079.

Degen GE, Pastorelli F, Johnson MP. 2023b. Proton Gradient Regulation 5 is required to avoid photosynthetic oscillations during light transitions. *Journal of Experimental Botany* **75**(3): 947–961.

Denton AK, Maß J, Külahoglu C, Lercher MJ, Bräutigam A, Weber APM. 2017. Freeze-quenched maize mesophyll and bundle sheath separation uncovers bias in previous tissue-specific RNA-Seq data. *Journal of Experimental Botany* **68**(2): 147–160.

Döring F, Streubel M, Bräutigam A, Gowik U. 2016. Most photorespiratory genes are preferentially expressed in the bundle sheath cells of the C_4 grass *Sorghum bicolor*. *Journal of Experimental Botany* **67**(10): 3053–3064.

Edgar RC. 2022. Muscle5: High-accuracy alignment ensembles enable unbiased assessments of sequence homology and phylogeny. *Nature Communications* **13**(1): 6968.

Ehleringer J, Pearcy RW. 1983. Variation in Quantum Yield for CO_2 Uptake among C_3 and C_4 Plants. *Plant Physiology* **73**(3): 555–559.

Eisenhut M, Roell M-S, Weber APM. 2019. Mechanistic understanding of photorespiration paves the way to a new green revolution. *New Phytologist* **223**(4): 1762–1769.

Engler C, Youles M, Gruetzner R, Ehnert T-M, Werner S, Jones JDG, Patron NJ, Marillonnet S. 2014. A Golden Gate Modular Cloning Toolbox for Plants. *ACS Synthetic Biology* **3**(11): 839–843.

Ermakova M, Arrivault S, Giuliani R, Danila F, Alonso-Cantabrana H, Vlad D, Ishihara H, Feil R, Guenther M, Borghi GL, et al. 2021a. Installation of C_4 photosynthetic pathway enzymes in rice using a single construct. *Plant Biotechnology Journal* **19**(3): 575–588.

Ermakova M, Bellasio C, Fitzpatrick D, Furbank RT, Mamedov F, von Caemmerer S. 2021b. Upregulation of bundle sheath electron transport capacity under limiting light in C_4 *Setaria viridis*. *Plant Journal* **106**(5): 1443–1454.

Ermakova M, Fitzpatrick D, Larkum AWD. 2024a. Cyclic electron flow and Photosystem II-less photosynthesis. *Functional Plant Biology* **51**(11).

Ermakova M, Lopez-Calcagno PE, Raines CA, Furbank RT, von Caemmerer S. 2019. Overexpression of the Rieske FeS protein of the Cytochrome b_6f complex increases C_4 photosynthesis in Setaria viridis. *Communications Biology* **2**(1): 314.

Ermakova M, Sharwood RE, Furbank RT. 2026. Tuning the C_4 supercharger: improving photosynthesis and yield in C_4 crops. *New Phytologist* **249**(1): 76–92.

Ermakova M, Woodford R, Fitzpatrick D, Nix SJ, Zwahlen SM, Farquhar GD, von Caemmerer S, Furbank RT. 2024b. Chloroplast NADH dehydrogenase-like complex-mediated cyclic electron flow is the main electron transport route in C_4 bundle sheath cells. *New Phytologist* **243**(6): 2187–2200.

Ermakova M, Woodford R, Taylor Z, Furbank RT, Belide S, von Caemmerer S. 2023. Faster induction of photosynthesis increases biomass and grain yield in glasshouse-grown transgenic *Sorghum bicolor* overexpressing Rieske FeS. *Plant Biotechnology Journal* **21**(6): 1206–1216.

Fan Y, Noble DWA, Medlyn BE, Monson RK, Sage RF, Smith NG, Ainsworth EA, Busch FA, Danila FR, Ermakova M, et al. 2025. Environmental factors have a greater

influence on photosynthetic capacity in C_4 plants than biochemical subtypes or growth forms. *New Phytologist* **248**(3): 1205–1224.

Flannery SE, Hepworth C, Wood WHJ, Pastorelli F, Hunter CN, Dickman MJ, Jackson PJ, Johnson MP. 2021. Developmental acclimation of the thylakoid proteome to light intensity in *Arabidopsis*. *The Plant Journal* **105**(1): 223–244.

Flothow CEM, Küffner AM. 2026. Architectural and biochemical advances in understanding microbial CO_2 concentrating mechanisms. *The Plant Journal* **126**(3): e70913.

Friso G, Majeran W, Huang M, Sun Q, van Wijk KJ. 2010. Reconstruction of Metabolic Pathways, Protein Expression, and Homeostasis Machineries across Maize Bundle Sheath and Mesophyll Chloroplasts: Large-Scale Quantitative Proteomics Using the First Maize Genome Assembly. *Plant Physiology* **152**(3): 1219–1250.

Fu X, Walker BJ. 2024. Photorespiratory glycine contributes to photosynthetic induction during low to high light transition. *Scientific Reports* **14**(1): 19365.

Furbank R, Jenkins C, Hatch M. 1990. C_4 Photosynthesis: Quantum Requirement, C_4 and Overcycling and Q-Cycle Involvement. *Australian Journal of Plant Physiology* **17**(1): 1–7.

Furbank RT. 2011. Evolution of the C_4 photosynthetic mechanism: are there really three C_4 acid decarboxylation types? *Journal of Experimental Botany* **62**(9): 3103–3108.

Furbank RT, Badger J. 1983. Photorespiratory Characteristics of Isolated Bundle Sheath Strands of C_4 Monocotyledons. *Australian Journal of Plant Physiology* **10**: 451–458.

Furbank RT, Stitt M, Foyer CH. 1985. Intercellular compartmentation of sucrose synthesis in leaves of *Zea mays* L. *Planta* **164**(2): 172–178.

Furbank RT, Walker DA. 1985. Photosynthetic induction in C_4 leaves. *Planta* **163**(1): 75–83.

Furumoto T, Izui K, Quinn V, Furbank RT, von Caemmerer S. 2007. Phosphorylation of Phosphoenolpyruvate Carboxylase Is Not Essential for High Photosynthetic Rates in the C_4 Species *Flaveria bidentis*. *Plant Physiology* **144**(4): 1936–1945.

Furutani R, Makino A, Suzuki Y, Wada S, Shimakawa G, Miyake C. 2020. Intrinsic Fluctuations in Transpiration Induce Photorespiration to Oxidize P700 in Photosystem I. *Plants* **9**(12): 1761.

Geneious 2024. Geneious Prime 2025.0.1: GraphPad Software LLC d.b.a Geneious.

Ghannoum O, Evans JR, von Caemmerer S 2011. Chapter 8 Nitrogen and Water Use Efficiency of C_4 Plants. In: Raghavendra AS, Sage RF eds. *C_4 Photosynthesis and Related CO_2 Concentrating Mechanisms*. Dordrecht: Springer Netherlands, 129–146.

Goldman Sachs R. 2026. How Will the Iran Conflict Impact Oil Prices?

Goodstein DM, Shu S, Howson R, Neupane R, Hayes RD, Fazo J, Mitros T, Dirks W, Hellsten U, Putnam N, et al. 2011. Phytozome: a comparative platform for green plant genomics. *Nucleic Acids Research* **40**(D1): D1178–D1186.

Gowik U, Westhoff P. 2011. The Path from C_3 to C_4 Photosynthesis. *Plant Physiology* **155**(1): 56–63.

Guha P, Tyagi R, Chowdhury S, Reilly L, Fu C, Xu R, Resnick AC, Snyder SH. 2019. IPMK Mediates Activation of ULK Signaling and Transcriptional Regulation of Autophagy Linked to Liver Inflammation and Regeneration. *Cell Reports* **26**(10): 2692–2703.e2697.

Haehnel W, Jansen T, Gause K, Klösgen RB, Stahl B, Michl D, Huvermann B, Karas M, Herrmann RG. 1994. Electron transfer from plastocyanin to photosystem I. *The EMBO Journal* **13**(5): 1028–1038.

Hald S, Nandha B, Gallois P, Johnson GN. 2008. Feedback regulation of photosynthetic electron transport by NADP(H) redox poise. *Biochimica et Biophysica Acta (BBA) - Bioenergetics* **1777**(5): 433–440.

Hall CC, Cruz J, Wood M, Zegarac R, DeMars D, Carpenter J, Kanazawa A, Kramer D 2013. Photosynthetic Measurements with the Idea Spec: an Integrated Diode Emitter Array Spectrophotometer/Fluorometer. Berlin, Heidelberg: Springer Berlin Heidelberg. 184–188.

Hardy EC, Balcerowicz M. 2024. Untranslated yet indispensable—UTRs act as key regulators in the environmental control of gene expression. *Journal of Experimental Botany* **75**(14): 4314–4331.

Hatch MD. 1987. C_4 photosynthesis: a unique elend of modified biochemistry, anatomy and ultrastructure. *Biochimica et Biophysica Acta (BBA)* **895**(2): 81–106.

Hawkins C, Xue B, Yasmin F, Wyatt G, Zerbe P, Rhee Seung Y. 2025. Plant Metabolic Network 16: expansion of underrepresented plant groups and experimentally supported enzyme data. *Nucleic Acids Research* **53**(D1): D1606–D1613.

Hepworth C, Wood WHJ, Emrich-Mills TZ, Proctor MS, Casson S, Johnson MP. 2021. Dynamic thylakoid stacking and state transitions work synergistically to avoid acceptor-side limitation of photosystem I. *Nature Plants* **7**(1): 87–98.

Hertle Alexander P, Blunder T, Wunder T, Pesaresi P, Pribil M, Armbruster U, Leister D. 2013. PGRL1 Is the Elusive Ferredoxin-Plastoquinone Reductase in Photosynthetic Cyclic Electron Flow. *Molecular Cell* **49**(3): 511–523.

Höhner R, Pribil M, Herbstová M, Lopez LS, Kunz H-H, Li M, Wood M, Svoboda V, Puthiyaveetil S, Leister D, et al. 2020. Plastocyanin is the long-range electron carrier between photosystem II and photosystem I in plants. *Proceedings of the National Academy of Sciences* **117**(26): 15354–15362.

Hope AB. 2000. Electron transfers amongst cytochrome *f*, plastocyanin and photosystem I: kinetics and mechanisms. *Biochimica et Biophysica Acta (BBA) - Bioenergetics* **1456**(1): 5–26.

Hope AB, Valente P, Matthews DB. 1994. Effects of pH on the kinetics of redox reactions in and around the cytochrome *bf* complex in an isolated system. *Photosynthesis Research* **42**(2): 111–120.

Hotto AM, Salesse-Smith C, Lin M, Busch FA, Simpson I, Stern DB. 2021. Rubisco production in maize mesophyll cells through ectopic expression of subunits and chaperones. *Journal of Experimental Botany* **72**(13): 4930–4937.

Hua L, Stevenson SR, Reyna-Llorens I, Xiong H, Kopriva S, Hibberd JM. 2021. The bundle sheath of rice is conditioned to play an active role in water transport as well as sulfur assimilation and jasmonic acid synthesis. **107**(1): 268–286.

Hubáček M, Wey LT, Kourist R, Malihan-Yap L, Nikkanen L, Allahverdiyeva Y. 2024. Strong heterologous electron sink outcompetes alternative electron transport pathways in photosynthesis. *The Plant Journal* **119**(5): 2500–2513.

Huffine CA, Zhao R, Tang YJ, Cameron JC. 2023. Role of carboxysomes in cyanobacterial CO_2 assimilation: CO_2 concentrating mechanisms and metabolon implications. *Environmental Microbiology* **25**(2): 219–228.

IEA. 2025. Renewables 2025: Analysis and Forecast to 2030. Paris, France: International Energy Agency (IEA).

Imaizumi K, Ifuku K. 2025. Photosystem II: commonality and diversity with emphasis on the extrinsic subunits. *Plant and Cell Physiology* **66**(11): 1536–1561.

Ishikawa N, Takabayashi A, Noguchi K, Tazoe Y, Yamamoto H, von Caemmerer S, Sato F, Endo T. 2016. NDH-Mediated Cyclic Electron Flow Around Photosystem I is Crucial for C_4 Photosynthesis. *Plant and Cell Physiology* **57**(10): 2020–2028.

Jahns P, Holzwarth AR. 2012. The role of the xanthophyll cycle and of lutein in photoprotection of photosystem II. *Biochimica et Biophysica Acta (BBA) - Bioenergetics* **1817**(1): 182–193.

Jo S, Kim T, Iyer VG, Im W. 2008. CHARMM-GUI: A web-based graphical user interface for CHARMM. *Journal of Computational Chemistry* **29**(11): 1859–1865.

John CR, Smith-Unna RD, Woodfield H, Covshoff S, Hibberd JM. 2014. Evolutionary Convergence of Cell-Specific Gene Expression in Independent Lineages of C4 Grasses *Plant Physiology* **165**(1): 62–75.

Johnson JE, Berry JA. 2021. The role of Cytochrome b_6f in the control of steady-state photosynthesis: a conceptual and quantitative model. *Photosynthesis Research* **148**(3): 101–136.

Johnson MP. 2016. Photosynthesis. *Essays in Biochemistry* **60**: 255–273.

Joliot P, Johnson GN. 2011. Regulation of cyclic and linear electron flow in higher plants. *Proceedings of the National Academy of Sciences* **108**(32): 13317–13322.
Kadota K, Furutani R, Makino A, Suzuki Y, Wada S, Miyake C. 2019. Oxidation of P700 Induces Alternative Electron Flow in Photosystem I in Wheat Leaves. *Plants* **8**(6): 152.
Kai Y, Matsumura H, Inoue T, Terada K, Nagara Y, Yoshinaga T, Kihara A, Tsumura K, Izui K. 1999. Three-dimensional structure of phosphoenolpyruvate carboxylase: A proposed mechanism for allosteric inhibition. *Proceedings of the National Academy of Sciences* **96**(3): 823–828.
Kammers K, Cole RN, Tiengwe C, Ruczinski I. 2015. Detecting significant changes in protein abundance. *EuPA Open Proteomics* **7**: 11–19.
Kappel S, Thiele W, Gefen-Treves S, Henze A, Armbruster U, Schöttler MA. 2023. A congestion downstream of PSI causes the over-reduction of the electron transport chain in *pgr5* independent of membrane energization. *bioRxiv*: 2023.2009.2001.555968.
Katoh K, Misawa K, Kuma Ki, Miyata T. 2002. MAFFT: a novel method for rapid multiple sequence alignment based on fast Fourier transform. *Nucleic Acids Research* **30**(14): 3059–3066.
Katoh K, Standley DM. 2013. MAFFT Multiple Sequence Alignment Software Version 7: Improvements in Performance and Usability. *Molecular Biology and Evolution* **30**(4): 772–780.
Kendall AC, Bright SWJ, Hall NP, Keys AJ, Lea PJ, Turner JC, Wallsgrove RM 1987. Barley Photorespiration Mutants. In: Biggins J ed. *Progress in Photosynthesis Research: Volume 3 Proceedings of the VIIth International Congress on Photosynthesis Providence, Rhode Island, USA, August 10–15, 1986*. Dordrecht: Springer Netherlands, 629–632.
Kim E, Beon J, Lee S, Park SJ, Ahn H, Kim MG, Park JE, Kim W, Yuk J-M, Kang S-J, et al. 2017. Inositol polyphosphate multikinase promotes Toll-like receptor–induced inflammation by stabilizing TRAF6. *Science Advances* **3**(4): e1602296.
Kimata-Ariga Y, Chikuma Y, Saitoh T, Miyata M, Yanagihara Y, Yamane K, Hase T. 2019. NADP(H) allosterically regulates the interaction between ferredoxin and ferredoxin-$NADP^+$ reductase. *FEBS Open Bio* **9**(12): 2126–2136.
Klughammer C, Schreiber U. 2008a. Complementary PS II quantum yields calculated from simple fluorescence parameters measured by PAM fluorometry and the Saturation Pulse method. *PAM Application Notes* **1**: 27–35.
Klughammer C, Schreiber U. 2008b. New accessory for the DUAL-PAM-100: The P515/535 module and examples of its application. *PAM Application Notes* **1**: 1–10.
Klughammer C, Schreiber U. 2008c. Saturation Pulse method for assessment of energy conversion in PS I. *PAM Application Notes* **1**: 11–14.
Klughammer C, Schreiber U. 2016. Deconvolution of ferredoxin, plastocyanin, and P700 transmittance changes in intact leaves with a new type of kinetic LED array spectrophotometer. *Photosynthesis Research* **128**(2): 195–214.
Kok B, Forbush B, McGloin M. 1970. Cooperation of charges in photosynthetic O_2 evolution–I. A linear four step mechanism. *Photochemistry and Photobiology* **11**(6): 457–475.
Kono M, Yamori W, Suzuki Y, Terashima I. 2017. Photoprotection of PSI by Far-Red Light Against the Fluctuating Light-Induced Photoinhibition in *Arabidopsis thaliana* and Field-Grown Plants. *Plant and Cell Physiology* **58**(1): 35–45.
Kramer DM, Cruz JA, Kanazawa A. 2003. Balancing the central roles of the thylakoid proton gradient. *Trends in Plant Science* **8**(1): 27–32.
Kramer DM, Evans JR. 2011. The importance of energy balance in improving photosynthetic productivity. *Plant Physiology* **155**(1): 70–78.
Kramer DM, Johnson G, Kiirats O, Edwards GE. 2004. New Fluorescence Parameters for the Determination of Q_A Redox State and Excitation Energy Fluxes. *Photosynthesis Research* **79**(2): 209–218.
Kramer DM, Sacksteder CA, Cruz JA. 1999. How acidic is the lumen? *Photosynthesis Research* **60**(2): 151–163.

Krishnan-Schmieden M, Konold PE, Kennis JTM, Pandit A. 2021. The molecular pH-response mechanism of the plant light-stress sensor PsbS. *Nature Communications* **12**(1): 2291.

Kromdijk J, Ubierna N, Cousins AB, Griffiths H. 2014. Bundle-sheath leakiness in C_4 photosynthesis: a careful balancing act between CO_2 concentration and assimilation. *Journal of Experimental Botany* **65**(13): 3443–3457.

Kuhlgert S, Austic G, Zegarac R, Osei-Bonsu I, Hoh D, Chilvers MI, Roth MG, Bi K, TerAvest D, Weebadde P, et al. 2016. MultispeQ Beta: a tool for large-scale plant phenotyping connected to the open PhotosynQ network. *Royal Society Open Science* **3**(10).

Kümpers BMC, Burgess SJ, Reyna-Llorens I, Smith-Unna R, Boursnell C, Hibberd JM. 2017. Shared characteristics underpinning C_4 leaf maturation derived from analysis of multiple C_3 and C_4 species of *Flaveria*. *Journal of Experimental Botany* **68**(2): 177–189.

Kustin K, Shear D, Kleitman D. 1965. Theory of relaxation spectra; the kinetics of coupled chemical reactions. *Journal of Theoretical Biology* **9**(2): 186–212.

Letunic I, Bork P. 2021. Interactive Tree Of Life (iTOL) v5: an online tool for phylogenetic tree display and annotation. *Nucleic Acids Research* **49**(W1): W293–W296.

Levey M, Timm S, Mettler-Altmann T, Luca Borghi G, Koczor M, Arrivault S, PM Weber A, Bauwe H, Gowik U, Westhoff P. 2019. Efficient 2-phosphoglycolate degradation is required to maintain carbon assimilation and allocation in the C_4 plant *Flaveria bidentis*. *Journal of Experimental Botany* **70**(2): 575–587.

Levy S, Kafri M, Carmi M, Barkai N. 2011. The competitive advantage of a dual-transporter system. *Science* **334**(6061): 1408–1412.

Li X-P, Gilmore AM, Caffarri S, Bassi R, Golan T, Kramer D, Niyogi KK. 2004. Regulation of photosynthetic light harvesting involves intrathylakoid lumen pH sensing by the PsbS protein. *Journal of Biological Chemistry* **279**(22): 22866–22874.

Lima-Melo Y, Kılıç M, Aro E-M, Gollan PJ. 2021. Photosystem I Inhibition, Protection and Signalling: Knowns and Unknowns. *Frontiers in Plant Science* **Volume 12 - 2021**.

Lomize MA, Pogozheva ID, Joo H, Mosberg HI, Lomize AL. 2011. OPM database and PPM web server: resources for positioning of proteins in membranes. *Nucleic Acids Research* **40**(D1): D370–D376.

Long SP. 2025. Needs and opportunities to future-proof crops and the use of crop systems to mitigate atmospheric change. *Philosophical Transactions of the Royal Society B: Biological Sciences* **380**(1927): 20240229.

Long SP, Taylor SH, Burgess SJ, Carmo-Silva E, Lawson T, De Souza AP, Leonelli L, Wang Y. 2022. Into the Shadows and Back into Sunlight: Photosynthesis in Fluctuating Light. *Annual Review of Plant Biology* **73**(Volume 73, 2022): 617–648.

Long TA, Okegawa Y, Shikanai T, Schmidt GW, Covert SF. 2008. Conserved role of PROTON GRADIENT REGULATION 5 in the regulation of PSI cyclic electron transport. *Planta* **228**(6): 907–918.

López-Calcagno PE, Brown KL, Simkin AJ, Fisk SJ, Vialet-Chabrand S, Lawson T, Raines CA. 2020. Stimulating photosynthetic processes increases productivity and water-use efficiency in the field. *Nature Plants* **6**(8): 1054–1063.

Love MI, Huber W, Anders S. 2014. Moderated estimation of fold change and dispersion for RNA-seq data with DESeq2. *Genome Biology* **15**(12): 550.

Lyons E, Freeling M. 2008. How to usefully compare homologous plant genes and chromosomes as DNA sequences. *The Plant Journal* **53**(4): 661–673.

Lyu H, Lazár D. 2017. Modeling the light-induced electric potential difference $\Delta\Psi$ across the thylakoid membrane based on the transition state rate theory. *Biochimica et Biophysica Acta (BBA) - Bioenergetics* **1858**(3): 239–248.

Ma P-F, Liu Y-L, Jin G-H, Liu J-X, Wu H, He J, Guo Z-H, Li D-Z. 2021. The *Pharus latifolius* genome bridges the gap of early grass evolution. *The Plant Cell* **33**(4): 846–864.

Maas SJ, Dunlap JR. 1989. Reflectance, Transmittance, and Absorptance of Light by Normal, Etiolated, and Albino Corn Leaves. *Agronomy Journal* **81**(1): 105–110.

Maekawa S, Ohnishi M, Wada S, Ifuku K, Miyake C. 2024. Enhanced Reduction of Ferredoxin in PGR5-Deficient Mutant of *Arabidopsis thaliana* Stimulated Ferredoxin-Dependent Cyclic Electron Flow around Photosystem I. *International Journal of Molecular Sciences* **25**(5): 2677.

Majeran W, van Wijk KJ. 2009. Cell-type-specific differentiation of chloroplasts in C_4 plants. *Trends in Plant Science* **14**(2): 100–109.

Majeran W, Zybailov B, Ytterberg AJ, Dunsmore J, Sun Q, van Wijk KJ. 2008. Consequences of C_4 Differentiation for Chloroplast Membrane Proteomes in Maize Mesophyll and Bundle Sheath Cells. *Molecular & Cellular Proteomics* **7**(9): 1609–1638.

Malnoë A. 2018. Photoinhibition or photoprotection of photosynthesis? Update on the (newly termed) sustained quenching component qH. *Environmental and Experimental Botany* **154**: 123–133.

Malone LA, Proctor MS, Hitchcock A, Hunter CN, Johnson MP. 2021. Cytochrome b_6f – Orchestrator of photosynthetic electron transfer. *Biochimica et Biophysica Acta (BBA) - Bioenergetics* **1862**(5): 148380.

Mayerhöfer TG, Popp J. 2020. Beyond Beer's Law: Spectral Mixing Rules. *Applied Spectroscopy* **74**(10): 1287–1294.

Medeiros DB, Ishihara H, Guenther M, Rosado de Souza L, Fernie AR, Stitt M, Arrivault S. 2022. $^{13}CO_2$ labeling kinetics in maize reveal impaired efficiency of C_4 photosynthesis under low irradiance. *Plant Physiology* **190**(1): 280–304.

Meierhoff K, Westhoff P. 1993. Differential Biogenesis of Photosystem-II in Mesophyll and Bundle-Sheath Cells of Monocotyledonous NADP-Malic Enzyme-Type C_4 Plants - the Nonstoichiometric Abundance of the Subunits of Photosystem-II in the Bundle-Sheath Chloroplasts and the Translational Activity of the Plastome-Encoded Genes. *Planta* **191**(1): 23–33.

Merzlyak MN, Gitelson AA, Chivkunova OB, Rakitin VY. 1999. Non-destructive optical detection of pigment changes during leaf senescence and fruit ripening. *Physiologia Plantarum* **106**(1): 135–141.

Miyake C. 2010. Alternative Electron Flows (Water–Water Cycle and Cyclic Electron Flow Around PSI) in Photosynthesis: Molecular Mechanisms and Physiological Functions. *Plant and Cell Physiology* **51**(12): 1951–1963.

Müller P, Li X-P, Niyogi KK. 2001. Non-Photochemical Quenching. A Response to Excess Light Energy. *Plant Physiology* **125**(4): 1558.

Munekage Y, Hojo M, Meurer J, Endo T, Tasaka M, Shikanai T. 2002. PGR5 Is Involved in Cyclic Electron Flow around Photosystem I and Is Essential for Photoprotection in Arabidopsis. *Cell* **110**(3): 361–371.

Munekage YN. 2016. Light harvesting and chloroplast electron transport in NADP-malic enzyme type C_4 plants. *Current Opinion in Plant Biology* **31**: 9–15.

Munekage YN, Eymery F, Rumeau D, Cuiné S, Oguri M, Nakamura N, Yokota A, Genty B, Peltier G. 2010. Elevated Expression of PGR5 and NDH-H in Bundle Sheath Chloroplasts in C_4 *Flaveria* Species. *Plant and Cell Physiology* **51**(4): 664–668.

Munekage YN, Taniguchi YY. 2016. Promotion of Cyclic Electron Transport Around Photosystem I with the Development of C_4 Photosynthesis. *Plant and Cell Physiology* **57**(5): 897–903.

Murchie EH, Niyogi KK. 2011. Manipulation of Photoprotection to Improve Plant Photosynthesis. *Plant Physiology* **155**(1): 86–92.

Nakamura A, Ogawa T, Shimakawa G, Kobayashi R, Shikanai T, Munekage YN. 2026. Cyclic electron flow around photosystem I provides energy production and photoprotection in C_4 plants. *Plant Physiology* **201**(1).

Nakamura N, Iwano M, Havaux M, Yokota A, Munekage YN. 2013. Promotion of cyclic electron transport around photosystem I during the evolution of NADP–malic enzyme-type C_4 photosynthesis in the genus *Flaveria*. *New Phytologist* **199**(3): 832–842.

Nandha B, Finazzi G, Joliot P, Hald S, Johnson GN. 2007. The role of PGR5 in the redox poising of photosynthetic electron transport. *Biochimica et Biophysica Acta (BBA) - Bioenergetics* **1767**(10): 1252–1259.

Nikkanen L, Toivola J, Trotta A, Diaz MG, Tikkanen M, Aro E-M, Rintamäki E. 2018. Regulation of cyclic electron flow by chloroplast NADPH-dependent thioredoxin system. *Plant Direct* **2**(11): e00093.

Nikkanen L, Wey LT, Woodford R, Mustila H, Ermakova M, Rintamäki E, Allahverdiyeva Y. 2024. PGR5 is needed for redox-dependent regulation of ATP synthase both in chloroplasts and in cyanobacteria. *bioRxiv*: 2024.2011.2003.621747.

Nilkens M, Kress E, Lambrev P, Miloslavina Y, Müller M, Holzwarth AR, Jahns P. 2010. Identification of a slowly inducible zeaxanthin-dependent component of non-photochemical quenching of chlorophyll fluorescence generated under steady-state conditions in *Arabidopsis*. *Biochimica et Biophysica Acta (BBA) - Bioenergetics* **1797**(4): 466–475.

Nishikawa Y, Yamamoto H, Okegawa Y, Wada S, Sato N, Taira Y, Sugimoto K, Makino A, Shikanai T. 2012. PGR5-Dependent Cyclic Electron Transport Around PSI Contributes to the Redox Homeostasis in Chloroplasts Rather Than CO2 Fixation and Biomass Production in Rice. *Plant and Cell Physiology* **53**(12): 2117–2126.

Niu Y, Lazár D, Holzwarth AR, Kramer DM, Matsubara S, Fiorani F, Poorter H, Schrey SD, Nedbal L. 2023. Plants cope with fluctuating light by frequency-dependent nonphotochemical quenching and cyclic electron transport. *New Phytologist* **239**(5): 1869–1886.

Ogawa T, Kobayashi K, Taniguchi YY, Shikanai T, Nakamura N, Yokota A, Munekage YN. 2023. Two cyclic electron flows around photosystem I differentially participate in C_4 photosynthesis. *Plant Physiology* **191**(4): 2288–2300.

Ohnishi M, Maekawa S, Wada S, Ifuku K, Miyake C. 2023. Evaluating the Oxidation Rate of Reduced Ferredoxin in *Arabidopsis thaliana* Independent of Photosynthetic Linear Electron Flow: Plausible Activity of Ferredoxin-Dependent Cyclic Electron Flow around Photosystem I. *International Journal of Molecular Sciences* **24**(15): 12145.

Okegawa Y, Long TA, Iwano M, Takayama S, Kobayashi Y, Covert SF, Shikanai T. 2007. A Balanced PGR5 Level is Required for Chloroplast Development and Optimum Operation of Cyclic Electron Transport Around Photosystem I. *Plant and Cell Physiology* **48**(10): 1462–1471.

Okegawa Y, Motohashi K. 2020. M-Type Thioredoxins Regulate the PGR5/PGRL1-Dependent Pathway by Forming a Disulfide-Linked Complex with PGRL1. *The Plant Cell* **32**(12): 3866–3883.

Okegawa Y, Tsuyama M, Kobayashi Y, Shikanai T. 2005. The *pgr1* Mutation in the Rieske Subunit of the Cytochrome b_6f Complex Does Not Affect PGR5-dependent Cyclic Electron Transport around Photosystem I. *Journal of Biological Chemistry* **280**(31): 28332–28336.

Om K, Arias NN, Jambor CC, MacGregor A, Rezachek AN, Haugrud C, Kunz H-H, Wang Z, Huang P, Zhang Q, et al. 2022. Pyruvate, phosphate dikinase regulatory protein impacts light response of C_4 photosynthesis in *Setaria viridis*. *Plant Physiology* **190**(2): 1117–1133.

Ortega-Martínez P, Nikkanen L, Wey LT, Florencio FJ, Allahverdiyeva Y, Díaz-Troya S. 2024. Glycogen synthesis prevents metabolic imbalance and disruption of photosynthetic electron transport from photosystem II during transition to photomixotrophy in *Synechocystis sp.* PCC 6803. *New Phytologist* **243**(1): 162–179.

Osborn HL, Alonso-Cantabrana H, Sharwood RE, Covshoff S, Evans JR, Furbank RT, von Caemmerer S. 2016. Effects of reduced carbonic anhydrase activity on CO_2 assimilation rates in *Setaria viridis*: a transgenic analysis. *Journal of Experimental Botany* **68**(2): 299–310.

Pan X, Cao D, Xie F, Xu F, Su X, Mi H, Zhang X, Li M. 2020. Structural basis for electron transport mechanism of complex I-like photosynthetic NAD(P)H dehydrogenase. *Nature Communications* **11**(1): 610.

Passardi F, Longet D, Penel C, Dunand C. 2004. The class III peroxidase multigenic family in rice and its evolution in land plants. *Phytochemistry* **65**(13): 1879–1893.

Peñuelas J, Gamon JA, Fredeen AL, Merino J, Field CB. 1994. Reflectance indices associated with physiological changes in nitrogen- and water-limited sunflower leaves. *Remote Sensing of Environment* **48**(2): 135–146.

Penzler J-F, Marino G, Reiter B, Kleine T, Naranjo B, Leister D. 2022. Commonalities and specialties in photosynthetic functions of PROTON GRADIENT REGULATION5 variants in Arabidopsis. *Plant Physiology* **190**(3): 1866–1882.

Peterson RB, Schultes NP, McHale NA, Zelitch I. 2016. Evidence for a Role for NAD(P)H Dehydrogenase in Concentration of CO_2 in the Bundle Sheath Cell of *Zea mays* *Plant Physiology* **171**(1): 125–138.

Phillips JC, Hardy DJ, Maia JDC, Stone JE, Ribeiro JV, Bernardi RC, Buch R, Fiorin G, Hénin J, Jiang W, et al. 2020. Scalable molecular dynamics on CPU and GPU architectures with NAMD. *The Journal of Chemical Physics* **153**(4).

Pick TR, Bräutigam A, Schulz MA, Obata T, Fernie AR, Weber APM. 2013. *PLGG1*, a plastidic glycolate glycerate transporter, is required for photorespiration and defines a unique class of metabolite transporters. *Proceedings of the National Academy of Sciences* **110**(8): 3185–3190.

Raines CA. 2003. The Calvin cycle revisited. *Photosynthesis Research* **75**(1): 1–10.

Rao X, Lu N, Li G, Nakashima J, Tang Y, Dixon RA. 2016. Comparative cell-specific transcriptomics reveals differentiation of C_4 photosynthesis pathways in switchgrass and other C_4 lineages. *Journal of Experimental Botany* **67**(6): 1649–1662.

Raymond Hunt Jr. E, Daughtry CST. 2014. Chlorophyll Meter Calibrations for Chlorophyll Content Using Measured and Simulated Leaf Transmittances. *Agronomy Journal* **106**(3): 931–939.

Reimand J, Isserlin R, Voisin V, Kucera M, Tannus-Lopes C, Rostamianfar A, Wadi L, Meyer M, Wong J, Xu C, et al. 2019. Pathway enrichment analysis and visualization of omics data using g:Profiler, GSEA, Cytoscape and EnrichmentMap. *Nature Protocols* **14**(2): 482–517.

Rieseberg LH, Willis JH. 2007. Plant Speciation. *Science* **317**(5840): 910–914.

Rizal G, Karki S, Garcia R, Larazo N, Alcasid M, Quick WP. 2015. The Use of Maleic Hydrazide for Effective Hybridization of *Setaria viridis*. *PLOS ONE* **10**(4): e0125092.

Rouse JW, Jr., Haas RH, Schell JA, Deering DW. 1973. Monitoring the vernal advancement and retrogradation (green wave effect) of natural vegetation. College Station, TX, United States: Texas A&M University.

Ruban AV. 2016. Nonphotochemical Chlorophyll Fluorescence Quenching: Mechanism and Effectiveness in Protecting Plants from Photodamage. *Plant Physiology* **170**(4): 1903–1916.

Rühle T, Dann M, Reiter B, Schünemann D, Naranjo B, Penzler J-F, Kleine T, Leister D. 2021. PGRL2 triggers degradation of PGR5 in the absence of PGRL1. *Nature Communications* **12**(1): 3941.

Rumberg B, Siggel U. 1969. pH changes in the inner phase of the thylakoids during photosynthesis. *Naturwissenschaften* **56**(3): 130–132.

Sacksteder CA, Kramer DM. 2000. Dark-interval relaxation kinetics (DIRK) of absorbance changes as a quantitative probe of steady-state electron transfer. *Photosynthesis Research* **66**(1): 145–158.

Sage RF. 2004. The evolution of C_4 photosynthesis. *New Phytologist* **161**(2): 341–370.

Sage RF, Christin P-A, Edwards EJ. 2011. The C_4 plant lineages of planet Earth. *Journal of Experimental Botany* **62**(9): 3155–3169.

Sage RF, Kubien DS. 2007. The temperature response of C_3 and C_4 photosynthesis. *Plant, Cell & Environment* **30**(9): 1086–1106.

Sage RF, Sage TL, Kocacinar F. 2012. Photorespiration and the Evolution of C_4 Photosynthesis. *Annual Review of Plant Biology* **63**(Volume 63, 2012): 19–47.

Sales CRG, Wang Y, Evers JB, Kromdijk J. 2021. Improving C_4 photosynthesis to increase productivity under optimal and suboptimal conditions. *Journal of Experimental Botany* **72**(17): 5942–5960.

Sánchez-Baracaldo P, Cardona T. 2020. On the origin of oxygenic photosynthesis and Cyanobacteria. *New Phytologist* **225**(4): 1440–1446.

Sarewicz M, Pintscher S, Pietras R, Borek A, Bujnowicz Ł, Hanke G, Cramer WA, Finazzi G, Osyczka A. 2021. Catalytic Reactions and Energy Conservation in the Cytochrome bc_1 and b_6f Complexes of Energy-Transducing Membranes. *Chemical Reviews* **121**(4): 2020–2108.

Sato Y, Antonio B, Namiki N, Motoyama R, Sugimoto K, Takehisa H, Minami H, Kamatsuki K, Kusaba M, Hirochika H, et al. 2011. Field transcriptome revealed critical developmental and physiological transitions involved in the expression of growth potential in *japonica* rice. *BMC Plant Biology* **11**(1): 10.

Sato Y, Takehisa H, Kamatsuki K, Minami H, Namiki N, Ikawa H, Ohyanagi H, Sugimoto K, Antonio BA, Nagamura Y. 2012. RiceXPro Version 3.0: expanding the informatics resource for rice transcriptome. *Nucleic Acids Research* **41**(D1): D1206–D1213.

Satoh H, Ohara Y, Hanke G, Ifuku K, Shimakawa G, Suzuki Y, Makino A, Morigaki K, Miyake C. 2025. The regulation of PSI cyclic electron transport by both plastoquinone and ferredoxin redox states: correlation with the rate of proton motive force utilization. *Frontiers in Plant Science* **Volume 16 - 2025**.

Schrodinger, LLC 2015. The PyMOL Molecular Graphics System, Version 3.0.

Schwacke R, Ponce-Soto GY, Krause K, Bolger AM, Arsova B, Hallab A, Gruden K, Stitt M, Bolger ME, Usadel B. 2019. MapMan4: A Refined Protein Classification and Annotation Framework Applicable to Multi-Omics Data Analysis. *Molecular Plant* **12**(6): 879–892.

Schwanhäusser B, Busse D, Li N, Dittmar G, Schuchhardt J, Wolf J, Chen W, Selbach M. 2011. Global quantification of mammalian gene expression control. *Nature* **473**(7347): 337–342.

Seetharam AS, Yu Y, Bélanger S, Clark LG, Meyers BC, Kellogg EA, Hufford MB. 2021. The *Streptochaeta* Genome and the Evolution of the Grasses. *Frontiers in Plant Science* **12**.

Shigeto J, Tsutsumi Y. 2016. Diverse functions and reactions of class III peroxidases. *New Phytologist* **209**(4): 1395–1402.

Shikanai T. 2014. Central role of cyclic electron transport around photosystem I in the regulation of photosynthesis. *Current Opinion in Biotechnology* **26**: 25–30.

Shikanai T, Munekage Y, Shimizu K, Endo T, Hashimoto T. 1999. Identification and Characterization of *Arabidopsis* Mutants with Reduced Quenching of Chlorophyll Fluorescence. *Plant and Cell Physiology* **40**(11): 1134–1142.

Slattery RA, Walker BJ, Weber APM, Ort DR. 2018. The Impacts of Fluctuating Light on Crop Performance. *Plant Physiology* **176**(2): 990–1003.

Smyth GK. 2004. Linear Models and Empirical Bayes Methods for Assessing Differential Expression in Microarray Experiments. *Statistical Applications in Genetics and Molecular Biology* **3**(1).

Sonoike K. 2011. Photoinhibition of photosystem I. *Physiologia Plantarum* **142**(1): 56–64.

Soriano GM, Guo L-W, de Vitry C, Kallas T, Cramer WA. 2002. Electron Transfer from the Rieske Iron-Sulfur Protein (ISP) to Cytochrome *f* in Vitro: IS A GUIDED TRAJECTORY OF THE ISP NECESSARY FOR COMPETENT DOCKING? *Journal of Biological Chemistry* **277**(44): 41865–41871.

South PF, Walker BJ, Cavanagh AP, Rolland V, Badger M, Ort DR. 2017. Bile Acid Sodium Symporter BASS6 Can Transport Glycolate and Is Involved in Photorespiratory Metabolism in *Arabidopsis thaliana* *The Plant Cell* **29**(4): 808–823.

Stamatakis A. 2014. RAxML version 8: a tool for phylogenetic analysis and post-analysis of large phylogenies. *Bioinformatics* **30**(9): 1312–1313.

Storey JD. 2003. The positive false discovery rate: a Bayesian interpretation and the *q*-value. *The Annals of Statistics* **31**(6): 2013–2035, 2023.

Storti M, Segalla A, Mellon M, Alboresi A, Morosinotto T. 2020. Regulation of electron transport is essential for photosystem I stability and plant growth. *New Phytologist* **228**(4): 1316–1326.

Strand DD, Fisher N, Kramer DM. 2017. The higher plant plastid NAD(P)H dehydrogenase-like complex (NDH) is a high efficiency proton pump that increases ATP production by cyclic electron flow. *Journal of Biological Chemistry* **292**(28): 11850–11860.

Strand DD, Walker BJ. 2023. Energetic considerations for engineering novel biochemistries in photosynthetic organisms. *Frontiers in Plant Science* **Volume 14 - 2023**.

Sujak A, Drepper F, Haehnel W. 2004. Spectroscopic studies on electron transfer between plastocyanin and cytochrome b_6f complex. *Journal of Photochemistry and Photobiology B: Biology* **74**(2): 135–143.

Sun T, Bonthala VS, Stich B, Luginbuehl LH, Hibberd JM. 2026. Conserved spatial patterning of gene expression in independent lineages of C_4 plants. *New Phytologist* **249**(1): 24–38.

Suorsa M, Järvi S, Grieco M, Nurmi M, Pietrzykowska M, Rantala M, Kangasjärvi S, Paakkarinen V, Tikkanen M, Jansson S, et al. 2012. PROTON GRADIENT REGULATION5 Is Essential for Proper Acclimation of *Arabidopsis* Photosystem I to Naturally and Artificially Fluctuating Light Conditions. *The Plant Cell* **24**(7): 2934–2948.

Suorsa M, Rossi F, Tadini L, Labs M, Colombo M, Jahns P, Kater Martin M, Leister D, Finazzi G, Aro E-M, et al. 2016. PGR5-PGRL1-Dependent Cyclic Electron Transport Modulates Linear Electron Transport Rate in *Arabidopsis thaliana*. *Molecular Plant* **9**(2): 271–288.

Takagi D, Miyake C. 2018. PROTON GRADIENT REGULATION 5 supports linear electron flow to oxidize photosystem I. *Physiologia Plantarum* **164**(3): 337–348.

Tanigawa K, Kodama H, Okegawa Y, Shikanai T, Yamori W. 2026. Moderate overexpression of *PROTON GRADIENT REGULATION 5* improves photosynthetic performance and plant growth under fluctuating low light in *Arabidopsis thaliana*. *bioRxiv*: 2026.2004.2021.719829.

Tazoe Y, Ishikawa N, Shikanai T, Ishiyama K, Takagi D, Makino A, Sato F, Endo T. 2020. Overproduction of PGR5 enhances the electron sink downstream of photosystem I in a C_4 plant, *Flaveria bidentis*. *Plant Journal* **103**(2): 814–823.

Tello-Ruiz MK, Jaiswal P, Ware D 2022. Gramene: A Resource for Comparative Analysis of Plants Genomes and Pathways. In: Edwards D ed. *Plant Bioinformatics: Methods and Protocols*. New York, NY: Springer US, 101–131.

Theune ML, Hildebrandt S, Steffen-Heins A, Bilger W, Gutekunst K, Appel J. 2021. In-vivo quantification of electron flow through photosystem I – Cyclic electron transport makes up about 35% in a cyanobacterium. *Biochimica et Biophysica Acta (BBA) - Bioenergetics* **1862**(3): 148353.

Tikhonov AN. 2013. pH-Dependent regulation of electron transport and ATP synthesis in chloroplasts. *Photosynthesis Research* **116**(2): 511–534.

Tikhonov AN. 2014. The cytochrome b_6f complex at the crossroad of photosynthetic electron transport pathways. *Plant Physiology and Biochemistry* **81**: 163–183.

Tikkanen M, Aro E-M. 2014. Integrative regulatory network of plant thylakoid energy transduction. *Trends in Plant Science* **19**(1): 10–17.

Tikkanen M, Grieco M, Kangasjärvi S, Aro E-M. 2010. Thylakoid Protein Phosphorylation in Higher Plant Chloroplasts Optimizes Electron Transfer under Fluctuating Light *Plant Physiology* **152**(2): 723–735.

Tikkanen M, Mekala NR, Aro E-M. 2014. Photosystem II photoinhibition-repair cycle protects Photosystem I from irreversible damage. *Biochimica et Biophysica Acta (BBA) - Bioenergetics* **1837**(1): 210–215.

Tovar-Méndez A, Mújica-Jiménez C, Muñoz-Clares RA. 2000. Physiological Implications of the Kinetics of Maize Leaf Phosphoenolpyruvate Carboxylase. *Plant Physiology* **123**(1): 149–160.

Turina P, Petersen J, Gräber P. 2016. Thermodynamics of proton transport coupled ATP synthesis. *Biochimica et Biophysica Acta (BBA) - Bioenergetics* **1857**(6): 653–664.

Ubierna N, Sun W, Kramer DM, Cousins AB. 2013. The efficiency of C_4 photosynthesis under low light conditions in *Zea mays*, *Miscanthus x giganteus* and *Flaveria bidentis*. *Plant, Cell & Environment* **36**(2): 365–381.

Uflewski M, Rindfleisch T, Korkmaz K, Tietz E, Mielke S, Correa Galvis V, Dünschede B, Luzarowski M, Skirycz A, Schwarzländer M, et al. 2024. The thylakoid proton antiporter KEA3 regulates photosynthesis in response to the chloroplast energy status. *Nature Communications* **15**(1): 2792.

van Dijk M, Morley T, Rau ML, Saghai Y. 2021. A meta-analysis of projected global food demand and population at risk of hunger for the period 2010–2050. *Nature Food* **2**(7): 494–501.

Vélez-Bermúdez IC, Schmidt W. 2014. The conundrum of discordant protein and mRNA expression. Are plants special? *Frontiers in Plant Science* **Volume 5 - 2014**.

Verslues PE, Sharma S. 2010. Proline Metabolism and Its Implications for Plant-Environment Interaction. *The Arabidopsis Book* **2010**(8).

Vojta L, Carić D, Cesar V, Antunović Dunić J, Lepeduš H, Kveder M, Fulgosi H. 2015. TROL-FNR interaction reveals alternative pathways of electron partitioning in photosynthesis. *Scientific Reports* **5**(1): 10085.

von Caemmerer S. 2021. Updating the steady-state model of C_4 photosynthesis. *Journal of Experimental Botany* **72**(17): 6003–6017.

von Caemmerer S, Furbank RT. 2003. The C_4 pathway: an efficient CO_2 pump. *Photosynthesis Research* **77**(2): 191.

von Caemmerer S, Furbank RT. 2016. Strategies for improving C_4 photosynthesis. *Current Opinion in Plant Biology* **31**: 125–134.

Waage P, Gulberg CM. 1864; 1986. Translation of: Studies concerning affinity. *Journal of Chemical Education* **63**(12): 1044.

Walker BJ, Kramer DM, Fisher N, Fu X. 2020. Flexibility in the Energy Balancing Network of Photosynthesis Enables Safe Operation under Changing Environmental Conditions. *Plants* **9**(3): 301.

Walker RP, Acheson RM, Técsi LI, Leegood RC. 1997. Phosphoenolpyruvate Carboxykinase in C_4 Plants: Its Role and Regulation. *Australian Journal of Plant Physiology* **24**(4): 459–468.

Wang Y, Bräutigam A, Weber APM, Zhu X-G. 2014. Three distinct biochemical subtypes of C_4 photosynthesis? A modelling analysis. *Journal of Experimental Botany* **65**(13): 3567–3578.

Wang Y, Chan KX, Long SP. 2021. Towards a dynamic photosynthesis model to guide yield improvement in C_4 crops. *The Plant Journal* **107**(2): 343–359.

Wang Y, Stutz SS, Bernacchi CJ, Boyd RA, Ort DR, Long SP. 2022. Increased bundle-sheath leakiness of CO_2 during photosynthetic induction shows a lack of coordination between the C_4 and C_3 cycles. *New Phytologist* **236**(5): 1661–1675.

Wei Y, Qiu F, An H, Zhang X, Li C, Guo X. 2024. Exogenous oil supply shocks and global agricultural commodity prices: The role of biofuels. *International Review of Economics & Finance* **92**: 394–414.

William Schopf J. 2011. The paleobiological record of photosynthesis. *Photosynthesis Research* **107**(1): 87–101.

Wilson S, Johnson MP, Ruban AV. 2021. Proton motive force in plant photosynthesis dominated by ΔpH in both low and high light. *Plant Physiology* **187**(1): 263–275.

Wiśniewski JR, Zougman A, Nagaraj N, Mann M. 2009. Universal sample preparation method for proteome analysis. *Nature Methods* **6**(5): 359–362.

Wójtowicz J, Mazur R, Jakubauskas D, Sokolova A, Garvey C, Mortensen K, Jensen PE, Kirkensgaard JJK, Kowalewska Ł. 2025. Shrink or expand? Just relax! Bidirectional grana structural dynamics as early light-induced regulator of photosynthesis. *New Phytologist* **246**(6): 2580–2596.

Woo KC, Anderson JM, Boardman NK, Downton WJS, Osmond CB, Thorne SW. 1970. Deficient Photosystem II in Agranal Bundle Sheath Chloroplasts of C_4 Plants. *Proceedings of the National Academy of Sciences* **67**(1): 18–25.

Woodford R, Ermakova M, Furbank RT, von Caemmerer S. 2025a. Fitting photosynthetic carbon dioxide and irradiance response curves for C_4 leaves. *bioRxiv*: 2025.2006.2003.657559.

Woodford R, Watkins J, Moore M, Nix SJ, Yee S, Chan KX, Pogson B, von Caemmerer S, Furbank RT, Ermakova M. 2025b. PROTON GRADIENT REGULATION 5 enables efficient C_4 photosynthesis under fluctuating light. *Plant Physiology* **199**(2).

Wu C, Guo D. 2023. Identification of Two Flip-Over Genes in Grass Family as Potential Signature of C_4 Photosynthesis Evolution. *International Journal of Molecular Sciences* **24**(18): 14165.

Wu EL, Cheng X, Jo S, Rui H, Song KC, Dávila-Contreras EM, Qi Y, Lee J, Monje-Galvan V, Venable RM, et al. 2014. CHARMM-GUI Membrane Builder toward realistic biological membrane simulations. *Journal of Computational Chemistry* **35**(27): 1997–2004.

Xie K, Minkenberg B, Yang Y. 2015. Boosting CRISPR/Cas9 multiplex editing capability with the endogenous tRNA-processing system. *Proceedings of the National Academy of Sciences* **112**(11): 3570–3575.

Xu J, Liu T, Lin H, Huang R, Chen M, Fang P, Niu X. 2025. Comprehensive analysis of the Caffeic acid O-methyltransferase gene family in kenaf (*Hibiscus cannabinus L.*) and their expression characteristics in response to salinity stress. *Frontiers in Plant Science* **Volume 16 - 2025**.

Yamamoto H, Shikanai T. 2018. PGR5-Dependent Cyclic Electron Flow Protects Photosystem I under Fluctuating Light at Donor and Acceptor Sides. *Plant Physiology* **179**(2): 588–600.

Yamamoto H, Takahashi S, Badger MR, Shikanai T. 2016. Artificial remodelling of alternative electron flow by flavodiiron proteins in Arabidopsis. *Nature Plants* **2**(3): 16012.

Yamori W, Makino A, Shikanai T. 2016. A physiological role of cyclic electron transport around photosystem I in sustaining photosynthesis under fluctuating light in rice. *Sci Rep* **6**(1): 20147.

Yamori W, Shikanai T. 2016. Physiological Functions of Cyclic Electron Transport Around Photosystem I in Sustaining Photosynthesis and Plant Growth. *Annual Review of Plant Biology* **67**(Volume 67, 2016): 81–106.

Zhang C, Shuai J, Ran Z, Zhao J, Wu Z, Liao R, Wu J, Ma W, Lei M. 2020. Structural insights into NDH-1 mediated cyclic electron transfer. *Nature Communications* **11**(1): 888.

Zhang Q, Tian S, Chen G, Tang Q, Zhang Y, Fleming AJ, Zhu X-G, Wang P. 2024. Regulatory NADH dehydrogenase-like complex optimizes C_4 photosynthetic carbon flow and cellular redox in maize. *New Phytologist* **241**(1): 82–101.

Zhang T, Huang W, Zhang L, Li D-Z, Qi J, Ma H. 2024. Phylogenomic profiles of whole-genome duplications in Poaceae and landscape of differential duplicate retention and losses among major Poaceae lineages. *Nature Communications* **15**(1): 3305.

Zhu X-G, Wang Y, Ort DR, Long SP. 2013. e-photosynthesis: a comprehensive dynamic mechanistic model of C_3 photosynthesis: from light capture to sucrose synthesis. *Plant, Cell & Environment* **36**(9): 1711–1727.

Zimmer E, Poppitz C, Klähn S, Selim KA. 2026. Functional and structural insights into cyanobacterial CO_2 concentrating mechanisms: from compartmentalization to regulation. *The Plant Journal* **126**(5): e70974.